



# THÈSE

**En vue de l'obtention du**  
DOCTORAT DE L'UNIVERSITÉ DE TOULOUSE

**Délivré par:** Institut National des Sciences Appliquées de Toulouse  
**Cotutelle internationale avec:** University of Thessaly, Volos, Greece

---

**Présentée et soutenue par:** LAJOS SZALMÁS

**Le:** 18 Juin 2012

**Titre:** FLOWS OF GAS MIXTURES IN MICROCHANNELS

---

**École doctorale et discipline ou specialite:**

ED MEGEP : Dynamique des fluides

**Unité de recherche:**

INSA de Toulouse, Institut Clément Ader

**Directeur(s) de Thèse:**

Prof. Dimitris Valougeorgis and Prof. Stéphane Colin

**Rapporteurs :**

Prof. Irina Graur and Prof. Gian Luca Morini

**Autre(s) membre(s) du jury:**

Prof. Dimitris Valougeorgis, Prof. Stéphane Colin,

Prof. Vasilis Bontozoglou, Dr. Lucien Baldas and

Dr. Nikos Andritsos

**- draft version -**

# Acknowledgment

The author would like to thank Prof. Dimitris Valougeorgis (University of Thessaly, Department of Mechanical Engineering) and Prof. Stéphane Colin (Université de Toulouse, Institut National des Sciences Appliquées, Institut Clément Ader) for the supervision of the Ph.D. thesis. Financial support of the European Community's Seventh Framework Programme (FP7/2007-2013) under grant agreement no 215504 is acknowledged.

Lajos Szalmás

# Abstract

The scope of the thesis is the computational and experimental study of flows of gaseous mixtures in microchannels. These flows have attracted considerable attention in the last years in the scientific community. They can be found in numerous applications, such as micro-electromechanical systems and vacuum devices. Microflows differ from macroscopic flows, which are described by the equations of fluid dynamics. As the size of the device approaches the micro-scale, the molecular details of the flows should be considered in the description. The characterization of the flows requires the consideration of the distribution function of the molecular velocity and the Boltzmann or other kinetic equations.

Previous works have almost focused on the flows of single gases. The behaviour of the flows has been studied theoretically and experimentally. Model kinetic equations have been solved for flows of single gases in various channels. Experimental studies have been performed in order to measure the flow rate in the device. Unlike single gases, there are very few works on gaseous mixtures. However, in applications, we almost encounter gaseous mixtures. For this reason, it is useful to study these flows.

The thesis has numerical and experimental parts. The flows are studied in long and short microchannels. The two types of flow require two different theoretical approaches in the description. Flows in long channels are described by linearized kinetic models, while flows in short channels are characterized by non-linear kinetic equations. In the numerical part of the thesis, both types of flow are simulated, while in the experimental part, only flows in long microchannels are studied.

# 1. Computational study of flows of gaseous mixtures in microchannels

## 1.1. Simulation of flows in long microchannels

The flows of gaseous mixtures are simulated on the basis of the McCormack linearized kinetic model. Since the speed of the flow is small compared to the characteristic speed of the molecules in long channels, the linearized description can be used. The McCormack model is considered as the most advanced method among others. All transport coefficients can be adjusted for an arbitrary intermolecular potential. In the thesis, the experimental transport is captured by the realistic potential.

The simulation is divided into two parts because of the geometrical symmetry. First, the McCormack model is solved locally at a particular cross section of the channel for a wide range of parameters, the rarefaction of the gas and the concentration. The solution is carried out by the discrete velocity method. An accelerated discrete velocity method is developed for single gases on triangular grids. It is shown by a stability analysis that the accelerated method provides faster solution near the hydrodynamic region. Two accelerated codes are developed for flows of gas mixtures through triangular and trapezoidal channels on the basis of the McCormack model. The codes are used to simulate flows of  $Ne/Ar$ ,  $He/Xe$ ,  $He/Ar$  and  $He/Kr$  mixtures at various flow parameters. The simulations provide the kinetic coefficients and other local macroscopic quantities of the flow.

Secondly, the global behavior of the flow, involving the flow rates and the distribution of the pressure and concentration in the microchannel, is deduced. The mass and molar flow rates are different for gaseous mixtures because of the gaseous separation. The light component travels faster than the heavy species in the channel. First, formulas are derived for estimating the flow rate by neglecting the separation. Then, a calculator of the molar

flow rate is developed. This latter method takes into account the gaseous separation exactly. Representative results are obtained from the simulations. The flow exhibits the gaseous separation. The distribution of the concentration is not uniform in the channel, even if the downstream and upstream concentrations are the same.

## 1.2. Simulation of flows in short microchannels

Flows of gaseous mixtures in short microchannels are described by the non-linear Boltzmann equation. For short channels, the speed of the flow can be in the range of the characteristic speed of the molecules, and the non-linear kinetic equations need to be considered. The simulation is carried out by the direct simulation Monte Carlo (DSMC). The DSMC is a gaseous model. The motion of model particles is simulated in the real geometry of the flow. In the thesis, advanced codes are developed for the simulations. The codes use weighting zones in order to increase the efficiency of the method. In addition, they use three-level distribution of the grid near the channels for a better resolution. The codes are applied for the simulation of flows through orifices, short tubes and slits. *Ne/Ar* and *He/Xe* mixtures are considered in these studies. Results are obtained for a wide range of gaseous rarefaction, different concentrations and pressure ratios. The flow rates and the axial distribution of the macroscopic quantities are analyzed. The mixture exhibits the gaseous separation. At high rarefaction, the relative flow rate is larger for the lighter species than the heavier one. The macroscopic quantities exhibit strong variations near the channel. The velocity of the gas can be as high as the characteristic molecular speed. There is a drop of the temperature near the outlet of the channel.

## 2. Experimental study of flows of gaseous mixtures in long microchannels and comparison to kinetic calculation

The flow rate of gaseous mixtures in long microchannels is measured. The experiment is based on the constant volume method. A bunch of microchannels is connected to upstream and downstream reservoirs. The reservoirs are filled up with the gaseous mixtures at different pressures. The difference of the pressure drives the flow through the microchannels. The experiment is carried out under isothermal conditions. The flow rate is determined from the variations of the pressure in the upstream and downstream containers. Experiments are performed for flows of  $He/Ar$  and  $He/Kr$  gaseous mixtures through rectangular and trapezoidal microchannels in the transition and early transition regions.

The experimental flow rates are compared to the solution of the McCormack model. The kinetic results are obtained by the method, which is developed in the numerical part of the thesis. An excellent agreement between the numerical and experimental flow rates is obtained. The difference between the results is less than the experimental uncertainty. The distribution of the pressure and the concentration is deduced from the numerical simulations.

## 3. Conclusions

In the thesis, flows of gaseous mixtures are studied numerically and experimentally. In the numerical part, a method is developed for the simulation of flows in long microchannels on the basis of the McCormack model. The flows in short channels are simulated by the DSMC method. In the experimental part, the flow rate of gaseous mixtures is measured in long microchannels.

The experimental results are compared to the kinetic calculation. Good agreement is obtained between the two approaches. It can be concluded that the McCormack model can be viewed as a viable tool for the description of isothermal flows of gas mixtures considered in the present work.

# Περίληψη<sup>1</sup>

## 1. Εισαγωγή

Ο στόχος της διατριβής είναι η αριθμητική και πειραματική μελέτη ροών αερίων μιγμάτων σε μικροαγωγούς. Αυτές οι ροές έχουν προσελκύσει μεγάλο ενδιαφέρον τα τελευταία χρόνια στην επιστημονική κοινότητα. Μπορούν να βρεθούν σε πολλές εφαρμογές, όπως μικρο-ηλεκτρομηχανολογικά συστήματα και συσκευές κενού. Οι μικροροές διαφέρουν από τις μακροσκοπικές ροές, οι οποίες περιγράφονται από τις εξισώσεις της κλασικής ρευστοδυναμικής. Όμως καθώς μέγεθος της συσκευής προσεγγίζει την μικροκλίμακα ή καθώς η πίεση λειτουργίας μειώνεται σημαντικά κάτω από την ατμοσφαιρική πίεση, οι μοριακές λεπτομέρειες των ροών θα πρέπει να συμπεριλαμβάνονται στην περιγραφή. Ο χαρακτηρισμός των ροών απαιτεί την εξέταση της συνάρτησης κατανομής της μοριακής ταχύτητας και της εξίσωσης Boltzmann ή άλλων κινητικών εξισώσεων.

Η συμπεριφορά των μικροροών σε απλά αέρια έχει μελετηθεί θεωρητικά και πειραματικά. Κινητικές εξισώσεις έχουν λυθεί για τις ροές των μεμονωμένων αερίων σε διάφορα κανάλια, ενώ πειραματικές μελέτες έχουν πραγματοποιηθεί προκειμένου να μετρηθεί η παροχή ροής στη συσκευή. Σε αντίθεση με μεμονωμένα αέρια, υπάρχουν πολύ λίγα απορελέσματα σε αέρια μίγματα. Όμως, στις εφαρμογές, συναντάμε πολύ συχνά αέρια μίγματα. Για το λόγο αυτό, είναι χρήσιμο και απαραίτητο να μελετηθούν ροές αερίων μιγμάτων.

Η διατριβή περιλαμβάνει αριθμητική και πειραματική μελέτη. Μελετώνται ροές σε μικροαγωγούς μικρού και μεγάλου μήκους. Οι δύο τύποι ροής απαιτούν δύο διαφορετικές θεωρητικές προσεγγίσεις στην περιγραφή. Οι ροές σε μικρο-

---

<sup>1</sup>Greek abstract

αγωγούς μεγάλου μήκους περιγράφονται από τα γραμμικά κινητικά μοντέλα, ενώ οι ροές σε σύντομη κανάλια χαρακτηρίζονται από μη-γραμμικές κινητικές εξισώσεις. Στο αριθμητικό μέρος της διατριβής προσομοιώνονται και οι δύο τύποι ροής, ενώ στο πειραματικό μέρος μόνο οι ροές σε μικροκανάλια μεγάλου μήκους.

## 2. Υπολογιστική μελέτη ροής αερίων μιγμάτων σε μικροαγωγούς

### 2.1. Προσομοίωση ροής σε μικροαγωγούς μεγάλου μήκους

Επειδή η ταχύτητα της ροής είναι μικρή σε σύγκριση με την χαρακτηριστική ταχύτητα των μορίων εφαρμόζεται η γραμμική κινητική θεωρία και συγκεκριμένα το γραμμικό κινητικό μοντέλο McCormack που θεωρείται ως το πλέον αποτελεσματικό και ακριβές κινητικό μοντέλο στη περίπτωση των αερίων μιγμάτων. Είναι ιδιαίτερα σημαντικό ότι με το μοντέλο Μερμαςκ όλοι οι συντελεστές μεταφοράς μπορούν να προσαρμοστούν για ένα αυθαίρετο δυναμικό μοριακής αλληλεπίδρασης. Στη διατριβή εφαρμόζεται το πραγματικό ενδομοριακό δυναμικό όπως αυτό προκύπτει από πειράματα.

Η προσομοίωση χωρίζεται σε δύο μέρη, λόγω της γεωμετρικής συμμετρίας. Αρχικά, το μοντέλο McCormack επιλύεται τοπικά σε μια συγκεκριμένη εγκάρσια διατομή του καναλιού για ένα ευρύ φάσμα παραμέτρων αραιοποίησης και συγκέντρωσης μίγματος. Η επίλυση πραγματοποιείται με τη μέθοδο των διακριτών ταχυτήτων. Στο πλαίσιο της διατριβής η μέθοδος αυτή έχει αναβαθμιστεί αναπτύσσοντας έναν αλγόριθμο επιτάχυνσης σε τριγωνικά πλέγματα. Η βελτιωμένη έκδοση της μεθόδου παρέχει ταχύτερη λύση κοντά στην υδροδυναμική περιοχή. Αναπτύχθηκαν κώδικες για αγωγούς τριγωνικής και τραπεζοειδούς διατομής. Οι κώδικες χρησιμοποιούνται για την επίλυση του μοντέλου McCor-

mack για διάφορες παραμέτρους αραιοποίησης και συγκέντρωσης. Εξετάζονται τα μίγματα Ne/Ar, He/Xe, He/Ar και He/Kr. Οι προσομοιώσεις υπολογίζουν τους ονομαζόμενους κινητικούς συντελεστές και τις τοπικές μακροσκοπικές ποσότητες της ροής. Στο πρώτο στάδιο όλα τα μεγέθη είναι σε αδιάστατη μορφή.

Στο δεύτερο στάδιο, εξάγεται η συνολική συμπεριφορά της ροής που περιλαμβάνει τη παροχή και τη κατανομή πίεσης και συγκέντρωσης κατά μήκος του μικροκαναλιού. Σημειώνεται ότι η μοριακή μάζα του αερίου αλλάζει κατά μήκος του αγωγού λόγω της μεταβολής της συγκέντρωσης του μίγματος που οφείλεται στο γεγονός ότι το ελαφρύ συστατικό ταξιδεύει πιο γρήγορα από το βαρύ συστατικό στο μικροκάνάλι. Για το λόγο αυτό οι υπολογισμοί βασίζονται τον υπολογισμό των γραμμομοριακών παροχών (αριθμός σωματιδίων) που παραμένει σταθερός κατά μήκος του καναλιού. Έχουν αναπτυχθεί δύο μεθοδολογίες: η πρώτη δεν λαμβάνει υπόψη τον διαχωρισμό ενώ η δεύτερη που είναι η πλήρης και περισσότερο ακριβής συμπεριλαμβάνει το φαινόμενο του διαχωρισμού στους υπολογισμούς. Αντιπροσωπευτικά αποτελέσματα παρουσιάζονται για ένα μεγάλο εύρος παραμέτρων. Τονίζεται ότι η κατανομή της συγκέντρωσης είναι η μη ομοιόμορφη στο κανάλι, ακόμα και αν οι συγκεντρώσεις είναι οι ίδιες στην είσοδο και έξοδο.

## 2.2. Προσομοίωση ροής σε μικροαγωγούς μικρού μήκους

Οι ροές αερίων μιγμάτων σε μικροαγωγούς μικρού μήκους χαρακτηρίζονται από υψηλές ταχύτητες όπου η ταχύτητα της ροής μπορεί να είναι εντός του εύρους των χαρακτηριστικών ταχυτήτων των μορίων. Η επίλυση απαιτεί την μοντελοποίηση με μη-γραμμικές κινητικές εξισώσεις (εξίσωση Boltzmann) ή εναλλακτικά την εφαρμογή της μεθόδου άμεσης προσομοίωσης Monte Carlo (DSMC). Στη παρούσα διατριβή εφαρμόζεται η δεύτερη προσέγγιση. Η μέθοδος DSMC προσομοιώνει τη ροή με έναν αριθμό υπολογιστικών μορίων που είναι μεγάλος αλλά πολύ μικρότερος από τον πραγματικό αριθμό. Στη συνέχεια εξετάζεται

η κίνηση των μορίων και οι συγκρούσεις μεταξύ τους και με τα τοιχώματα. Η πρώτη διαδικασία προσομοιώνεται ντετερμινιστικά ενώ η δεύτερη στοχαστικά. Στη διατριβή, αναπτύσσονται προηγμένοι κώδικες για τη προσομοίωση ροών σε κυλινδρικούς αγωγούς, στόμια και σχισμές. Οι κώδικες χρησιμοποιούν τις ζώνες στάθμισης, ώστε να αυξηθεί την αποτελεσματικότητα της μεθόδου και τρία επίπεδα του πλέγματος κοντά στα κανάλια για μια καλύτερη ανάλυση. Οι κώδικες χρησιμοποιούνται για την προσομοίωση της ροής μέσα από κυλινδρικούς μικροαγωγούς με διάφορα μήκη και σχισμές. Εξετάζονται τα μίγματα Ne/Ar και He/Xe. Τα αποτελέσματα λαμβάνονται για ευρύ φάσμα της παραμέτρου αραιώσης του αερίου, για διαφορετικές συγκεντρώσεις και αναλογίες πίεσης. Αναλύονται οι ροές και η αξονική κατανομή των μακροσκοπικών ποσοτήτων. Και στη περίπτωση αυτή το μίγμα υπόκειται στο φαινόμενο του διαχωρισμού. Σε υψηλή αραιώση, η σχετική ροή είναι μεγαλύτερη για το ελαφρύ σε σχέση με το συστατικό. Οι μακροσκοπικές ποσότητες έχουν ισχυρές παραλλαγές κοντά στο κανάλι. Η ταχύτητα του αερίου μπορεί να είναι τόσο υψηλή όσο η χαρακτηριστική μοριακή ταχύτητα. Υπάρχει μια πτώση της θερμοκρασίας κοντά στην έξοδο του καναλιού.

### 3. Πειραματική μελέτη ροής σε μικροαγωγούς μεγάλου μήκους και σύγκριση με υπολογιστικά αποτελέσματα

Μετράται η παροχή αερίων μιγμάτων σε μικροαγωγούς μεγάλου μήκους. Το πείραμα βασίζεται στην ονομαζόμενη μέθοδο «σταθερού όγκου». Μια δέσμη των μικροκαναλιών συνδέεται με ανάντη και κατόντη δεξαμενές. Αρχικά οι δεξαμενές γεμίζουν με τα αέρια μίγματα σε διαφορετικές πιέσεις και ίδιες συγκεντρώσεις. Η διαφορά της πίεσης οδηγεί την ροή μέσα από τα μικροκανάλια. Το πείραμα πραγματοποιείται σε ισόθερμοκρασιακές συνθήκες. Η ροή καθορίζεται

από τις παραλλαγές της πίεσης στα ανάντη και κατόντη δοχεία. Τα πειράματα γίνονται για τις ροές των αερίων μιγμάτων He/Ar και He/K μέσω μικροαγωγών με ορθογώνια και τραπεζοειδή διατομή. Το εύρος του αριθμού Knudsen περιλαμβάνει τη περιοχή ολίσθησης και τμήμα της μεταβατικής περιοχής.

Τα πειραματικά αποτελέσματα συγκρίνονται με τα αντίστοιχα υπολογιστικά όπως αυτά προκύπτουν από την επίλυση του μοντέλου McCormack. Τα κινητικά αποτελέσματα λαμβάνονται από την μέθοδο, η οποία αναπτύσσεται στο αριθμητικό μέρος της διατριβής. Η συμφωνία μεταξύ των αριθμητικών και πειραματικών ροών είναι πολύ καλή. Η διαφορά μεταξύ των αποτελεσμάτων είναι μικρότερη από την πειραματική αβεβαιότητα που εκτιμάται στο 4%. Η κατανομή της πίεσης και της συγκέντρωσης εξάγεται από τις αριθμητικές προσομοιώσεις.

## 4. Συμπεράσματα

Στη παρούσα διατριβή, οι ροές αερίων μιγμάτων μελετώνται αριθμητικά και πειραματικά. Στο αριθμητικό μέρος, αναπτύσσεται μια μέθοδος για την προσομοίωση της ροής σε μικροαγωγούς μεγάλου μήκους με βάση το μοντέλο McCormack. Οι ροές σε μικροαγωγούς μικρού μήκους προσομοιώνονται από την μέθοδο DSMC. Στο πειραματικό μέρος, η ροή αερίων μιγμάτων μετράται σε μικροαγωγούς μεγάλου μήκους ορθογώνιας και τραπεζοειδούς διατομής. Τα πειραματικά αποτελέσματα συγκρίνονται με τα αντίστοιχα υπολογιστικά που βασίζονται στη γραμμική κινητική θεωρία. Πολύ καλή συμφωνία επιτυγχάνεται μεταξύ των δύο προσεγγίσεων. Το μοντέλο McCormack μπορεί να θεωρηθεί ως ένα ιδιαίτερα αποτελεσματικό μοντέλο για την περιγραφή ισοθερμοκρασιακών ροών των μικροαγωγών με διαφορά πίεσης.

# Résumé français<sup>1</sup>

## 1. Introduction

La sujet de la thèse est l'étude numérique et expérimentale des écoulements des mélanges gazeux dans les microcanaux. L'écoulement gazeux dans les microsystèmes a attiré une attention considérable ces dernières années dans les communautés de gaz raréfié et de dynamique des fluides. Ces écoulements peuvent être trouvés dans des nombreuses applications, telles que les systèmes électromécaniques, des équipements de vide ou la métrologie de gaz. La caractéristique avantageuse de minimiser les systèmes mécaniques ou électromécaniques est de réduire la consommation. Les écoulements dans les microsystèmes sont différents des écoulements décrits par les équations de dynamique des fluides. Comme la taille de l'appareil s'approche de l'échelle microscopique, la moyenne du libre parcours des molécules devient comparable à la taille caractéristique de l'appareil, telle que le diamètre du microcanal. Selon leur taille, les canaux peuvent être classés en nanocanaux, microcanaux et minicanaux avec des diamètres inférieurs à 1 micromètre, entre 1 et 10 micromètres et supérieurs à 10 micromètres, respectivement.

La description théorique du micro-écoulement exige l'examen de la fonction de distribution de la vitesse moléculaire et les équations de Boltzmann ou d'autres équations cinétiques. En comparant les résultats des approches cinétiques avec les résultats des expériences, les modèles théoriques peuvent être testés et évalués. La description du micro-écoulement peut être divisée en deux types, selon la longueur des microcanaux. Dans des conditions normales de fonctionnement, si le canal est long, la vitesse d'écoulement est

---

<sup>1</sup>French abstract

faible comparée à la vitesse caractéristique des molécules. En conséquence, les modèles linéarisés cinétiques peuvent être utilisés pour décrire l'écoulement. Si le canal est court, la vitesse de l'écoulement peut être aussi élevée que la vitesse caractéristique, et l'équation de Boltzmann non linéaire doit être résolue.

Dans la littérature, les écoulements de gaz seul dans les microsystèmes sont presque connus. Ils ont été étudiés théoriquement et expérimentalement. Toutefois, il y a très peu de travaux sur les mélanges gazeux. En conséquence, il est utile d'étudier ces écoulements. Dans la thèse, les écoulements dans les canaux longs et courts sont considérés. La thèse a des parties numériques et expérimentales, où la simulation numérique des écoulements et la mesure de débit du mélange de gaz dans les microcanaux sont effectuées.

Dans la partie calculatoire de la thèse, la description de l'écoulement dans les microcanaux longs est effectuée en utilisant le modèle linéarisé cinétique de McCormack. Dans cette approche, l'opérateur de collision de l'équation de Boltzmann est remplacé par un modèle de collision, qui a une expression polynomiale des vitesses moléculaires. Dans le modèle de McCormack, tous les coefficients de transport du mélange gazeux peuvent être ajustés pour les valeurs d'un potentiel d'interaction arbitraire. L'avantage du modèle est notamment que les coefficients expérimentaux de transport peuvent être retrouvés. La solution du modèle est une tâche ambitieuse. Dans la thèse, une méthodologie de calcul, une méthode accélérée de vitesse discrète, est développée pour résoudre le modèle de McCormack sur des grilles triangulaires. Ces réseaux sont adaptés à la description de l'écoulement dans les microcanaux avec des sections transversales triangulaires et trapézoïdales. En utilisant la méthode, les écoulements de mélange gazeux sont simulés pour différents paramètres de l'écoulement. Ces simulations fournissent des quantités macroscopiques dans une section transversale particulière du microcanal. Les quantités globales de l'écoulement, les débits et les distributions de pression et de concentration

le long de l'axe du canal, jouent un rôle important dans la caractérisation et la compréhension des comportements de l'écoulement. Pour déduire ces quantités globales, un calcul du débit d'écoulement est développé. Il résout le problème sur la base des informations locales sur une section transversale. Le calcul est utilisé pour déduire les débits des différentes configurations. Il est démontré que le mélange se sépare dans le canal. Les différentes composantes s'écoulent avec des vitesses différentes. Les écoulements de mélanges gazeux dans les microcanaux courts sont simulés en utilisant la simulation directe Monte Carlo. Des codes avancés avec des zones de pondération et des grilles multi-niveaux sont développés. Les codes sont utilisés pour simuler l'écoulement de mélanges de gaz nobles dans les microcanaux courts pour des paramètres différents, impliquant la composition du gaz, la concentration, le rapport de pression et la raréfaction du gaz.

La partie expérimentale de la thèse est axée sur la mesure des débits dans les microcanaux longs. Les résultats expérimentaux sont comparés aux résultats obtenus par la solution du modèle McCormack. La méthode de vitesse discrète est appliquée pour résoudre le modèle à une section transversale particulière. Ensuite, ces informations sont utilisées pour déduire le débit par le calcul. La mesure de débit est basée sur la méthode de volume constant. C'est la technique la plus appropriée pour les microcanaux parce que les débits relativement faibles dans les microsystèmes peuvent être mesurés commodément par la méthode. L'appareil expérimental se compose des réservoirs en amont et en aval et du microsystème. Pendant la mesure, le gaz circule du conteneur en amont au conteneur en aval à travers les microcanaux. Pendant la mesure, les variations de la pression dans les deux réservoirs sont mesurées et détectées. A partir de la pression, le débit à travers le microsystème est déterminé en utilisant l'équation d'état. Des mesures dans les microcanaux rectangulaires et trapézoïdaux pour les mélanges de gaz nobles sont effectuées. Les débits sont comparés à des calculs cinétiques. La raré-

faction correspond au régime de glissement et de début de transition. Mais les résultats expérimentaux à plus haute raréfaction sont également utilisés pour la comparaison. L'écart est inférieur à l'incertitude expérimentale, mais il peut la dépasser pour les cas de raréfaction élevée. Globalement, un très bon accord entre les débits théoriques et expérimentaux est obtenu. Le bon accord démontre l'utilité du modèle de McCormack pour décrire l'écoulement isotherme dans les microcanaux pour les valeurs de paramètres considérés.

Dans les sections suivantes, les résultats de la thèse sont résumés.

## 2. Simulation des écoulements des gaz binaires raréfiés dans les microcanaux

### 2.1. Les écoulements dans les microcanaux longs

Dans la thèse, les écoulements de gaz binaires dans des microcanaux longs ayant des sections transversales rectangulaires, triangulaires ou trapézoïdales sont étudiés. L'axe du canal se trouve le long de la direction  $z'$ , tandis que la section transversale est dans le plan  $(x', y')$ . Le canal est situé entre les réservoirs en amont A et en aval B, qui contiennent le gaz aux pressions  $P_A, P_B$  et aux concentrations  $C_A, C_B$  d'entrée et de sortie. Les pressions en amont et en aval sont différentes,  $P_A > P_B$ , mais les concentrations correspondantes sont les mêmes. Par conséquent, la différence de pression entraîne la circulation de l'entrée du canal à sa sortie. Le gaz est dans des conditions isothermes. L'écoulement est caractérisé par le paramètre de raréfaction

$$\delta = \frac{PL_C}{\mu v_0}, \quad (1)$$

où  $P$  est la pression,  $L_C$  est la longueur caractéristique du problème, telle que le diamètre hydraulique du canal,  $\mu$  est la viscosité et  $v_0$  est la vitesse caractéristique moléculaire. L'inverse du paramètre de raréfaction est le nombre

de Knudsen,  $Kn = 1/\delta$ , comme défini ici. L'étude se réfère à l'ensemble du spectre de raréfaction du gaz. Dans ces conditions, le comportement de l'écoulement, la vitesse locale du gaz, le débit à travers le microcanal et les distributions de la pression et de la concentration, sont déterminés.

Pour les écoulements dans les canaux longs, la vitesse du gaz est faible par rapport à la vitesse caractéristique moléculaire. En conséquence, la description linéarisée peut être utilisée. En outre, les coordonnées dans la section transversale locale du canal peuvent être séparées de la coordonnée axiale en raison de la géométrie spécifique. En conséquence, l'analyse de l'écoulement est divisée en deux parties. Tout d'abord, l'écoulement est calculé dans une section transversale particulière du canal en supposant connues les forces motrices locales. Deuxièmement, le comportement global de l'écoulement, y compris les débits et les distributions de la pression et de la concentration, est résolu.

Pour le problème considéré, l'écoulement gazeux est piloté par les gradients locaux de pression et de concentration

$$X_P = \frac{\partial P}{\partial z} \frac{1}{P}, \quad X_C = \frac{\partial C}{\partial z} \frac{1}{C}, \quad (2)$$

où  $z = z'/L_C$  est la coordonnée sans dimension. Deux flux thermodynamiques  $J_P$  et  $J_C$  sont introduits pour décrire les débits par

$$J_P = - \iint (n_1 u'_1 + n_2 u'_2) dx' dy', \quad (3)$$

$$J_C = -n_1 \iint (u'_1 - u'_2) dx' dy', \quad (4)$$

où  $n_\alpha$  et  $u'_\alpha$  sont la densité molaire et la composante axiale de la vitesse de l'espèce  $\alpha$ , et l'intégration se réfère à la section transversale du canal. Ces flux sont reliés aux gradients par

$$J_P = \Lambda_{PP} X_P + \Lambda_{PC} X_C, \quad J_C = \Lambda_{CP} X_C + \Lambda_{CC} X_C. \quad (5)$$

Ici,  $\lambda_{PP}$ ,  $\lambda_{PC}$ ,  $\lambda_{CP}$  et  $\lambda_{CC}$  sont les coefficients cinétiques. Ils dépendent de la concentration locale du gaz et du paramètre de raréfaction. A partir des flux

thermodynamiques, les débits molaires des composants peuvent être calculés par

$$J_1 = -CJ_P + (1 - C)J_C, \quad J_2 = -(1 - C)(J_P - J_C). \quad (6)$$

Les débits molaires sont des quantités importantes dans l'étude globale. Pour les obtenir, l'écoulement dans une section transversale particulière du canal doit être résolu. Le calcul donne les coefficients cinétiques. Le calcul est effectué pour toute la gamme de la concentration de gaz et de raréfaction. Il est à noter que les coefficients  $\lambda_{PP}$ ,  $\lambda_{PC}$  ou  $\lambda_{CP}$ ,  $\lambda_{CC}$  sont obtenus à partir d'un écoulement piloté par la pression ou la concentration. Par conséquent, dans le calcul, les écoulements locaux générés par les distributions de pression et de concentration sont calculés séparément.

La modélisation du problème de l'écoulement est réalisée à l'échelle cinétique. Comme la vitesse du gaz est petite, des équations cinétiques linéarisées sont utilisées. La variable principale à l'échelle cinétique est la fonction de distribution de la vitesse moléculaire, qui est donnée par  $f_\alpha(\mathbf{v}, \mathbf{r})$  pour l'espèce  $\alpha$  dans des conditions stables, où le processus est indépendant du temps. Ici,  $\mathbf{v}$  et  $\mathbf{r}$  désignent la vitesse moléculaire et la coordonnée. La fonction de distribution est linéarisée selon  $f_\alpha(\mathbf{v}, \mathbf{r}) = f_\alpha^0[1 + h_\alpha(\mathbf{v}, \mathbf{r})]$ , où  $f_\alpha^0$  est la distribution à l'équilibre et  $h_\alpha(\mathbf{v}, \mathbf{r})$  représente l'écart à l'équilibre. Les quantités macroscopiques du gaz peuvent être calculées comme les moments de la fonction de distribution. La fonction de distribution obéit à des équations cinétiques, qui sont des équations aux dérivées partielles.

Le mélange gazeux est décrit par le modèle linéarisé McCormack cinétique. L'équation cinétique pour un écoulement généré par une pression ( $X_P = 1, X_C = 0$ ) ou une concentration ( $X_P = 0, X_C = 1$ ) uniforme dans la section transversale du canal est donnée par

$$c_{\alpha x} \frac{\partial h_\alpha^{(i)}}{\partial x} + c_{\alpha y} \frac{\partial h_\alpha^{(i)}}{\partial y} = \omega_\alpha \sum_{\beta=1}^2 L_{\alpha\beta} h_\beta^{(i)} - c_{\alpha z} \eta_\alpha^{(i)}. \quad (7)$$

Ici,  $L_{\alpha\beta}$  est l'opérateur de collision de McCormack,  $x = x'/L_C, y = y'/L_C$  sont les coordonnées sans dimension,  $c_{\alpha x}, c_{\alpha y}$  et  $c_{\alpha z}$  sont les composantes selon  $x, y$  et  $z$  de la vitesse moléculaire sans dimension, l'indice  $i$  est égal à  $P$  ou  $C$  pour les écoulements générés par gradient de pression ou de concentration et

$$\omega_\alpha = \sqrt{\frac{m_\alpha}{m}} \left[ \frac{C}{\gamma_1} + \frac{1-C}{\gamma_2} \right] \delta, \quad (8)$$

où  $m_\alpha, m$  sont la masse molaire des espèces et la masse moyenne, tandis que  $\gamma_\alpha$  est une fréquence de collision pour l'espèce  $\alpha$ . De plus,  $\eta_1^{(P)} = 1, \eta_2^{(P)} = 1$  et  $\eta_1^{(C)} = 1, \eta_2^{(C)} = -C/(1-C)$  pour les deux types d'écoulement. Le terme de collision dans le modèle de McCormack dépend de la vitesse, du tenseur de pression et du flux de chaleur des espèces gazeuses. Ces quantités sont obtenues comme les moments de la fonction de perturbation.

Afin d'obtenir les quantités locales hydrodynamiques du gaz et les coefficients cinétiques, le modèle de McCormack est résolu par la méthode de vitesse discrète.

### 2.1.1. La méthode accélérée de vitesse discrète

Dans la méthode de vitesse discrète, la solution de l'équation cinétique est obtenue en rendant faisant les espaces de vitesses moléculaires et coordonnées spatiales discrets. Les équations discrètes résultantes sont ensuite résolues numériquement. Dans la thèse, une méthode accélérée de vitesse discrète est développée sur des grilles triangulaires pour un calcul efficace. Ces grilles peuvent être utilisées pour décrire les écoulements dans des canaux de sections transversales triangulaire et trapézoïdale. Le schéma accéléré est différent de la méthode standard dans le sens qu'il fournit une solution plus rapide près de la région hydrodynamique peu raréfiée. L'accélération peut augmenter considérablement l'efficacité de la méthode. La méthode accélérée est développée pour les gaz seuls et les mélanges de gaz. Dans la suite, la

méthode pour le cas du gaz seul est brièvement décrite et le cas du mélange de gaz est alors considéré.

L'écoulement de gaz simple généré par pression est considéré dans une section transversale particulière du canal triangulaire. La coordonnée spatiale dans la section transversale du canal est notée  $\mathbf{x} = (x_1, x_2)$ . Le gaz est modélisé par l'équation cinétique Bhatnagar-Gross-Krook par

$$\mathbf{c} \cdot \nabla f^{(t+1/2)}(c, \theta, \mathbf{x}) + \delta f^{(t+1/2)}(c, \theta, \mathbf{x}) = \delta F_{0,0}^{(t)}(\mathbf{x}) + S(\mathbf{x}) \quad (9)$$

Ici,  $f^{(t+1/2)}(c, \theta, \mathbf{x})$  désigne la fonction de distribution réduite,  $\mathbf{c} = (c, \theta)$  est la vitesse moléculaire donnée en coordonnées polaires,  $F_{0,0}^{(t)}(\mathbf{x})$  est la vitesse du gaz le long de l'axe du canal,  $S(\mathbf{x})$  est un terme source, qui vaut  $-1/2$  pour les écoulements générés par pression et  $t$  est l'indice d'itération dans le calcul de vitesse discrète. Il est à noter que la fonction de distribution réduite peut être obtenue à partir de la fonction de perturbation en éliminant la vitesse axiale moléculaire afin de simplifier le problème. La vitesse macroscopique du gaz est obtenue comme le moment de la fonction de distribution

$$F_{0,0}^{(t+1)}(\mathbf{x}) = \frac{1}{\pi} \int_0^{2\pi} \int_0^\infty f^{(t+1/2)}(c, \theta, \mathbf{x}) \exp(-c^2) c d c d \theta. \quad (10)$$

Une condition aux limites diffuse est appliquée à la paroi et le débit est calculé lors de la simulation. Le problème est résolu de manière itérative comme indiqué par l'indice  $t$ . En supposant connue la vitesse du membre droit de l'équation cinétique, la fonction de distribution est calculée à partir du membre gauche. En utilisant la deuxième équation, la vitesse est alors déduite pour la prochaine étape de l'itération. L'itération est terminée si la différence entre les valeurs suivantes du débit est inférieure à une valeur donnée.

L'approche ci-dessus est l'itération standard et peut être lente à faible niveau de raréfaction (grand  $\delta$ ). Afin d'accélérer la solution, une équation de

moment supplémentaire est introduite selon

$$\begin{aligned} \Delta F_{0,0}^{(t+1)}(\mathbf{x}) = \\ - \frac{1}{2} \partial_{x_1}^2 F_{2,0}^{(t+1/2)}(\mathbf{x}) - \frac{1}{2} \partial_{x_2}^2 F_{0,2}^{(t+1/2)}(\mathbf{x}) - \partial_{x_1} \partial_{x_2} F_{1,1}^{(t+1/2)}(\mathbf{x}) - \delta S(\mathbf{x}), \end{aligned} \quad (11)$$

où les quantités  $F_{2,0}$ ,  $F_{0,2}$  et  $F_{1,1}$  sont les moments d'Hermite de la fonction de distribution. Dans l'itération améliorée, les moments d'Hermite sont calculés à partir de la fonction de distribution donnée par la première équation. Ensuite, la vitesse pour la prochaine étape d'itération est obtenue par la solution de la troisième équation.

La solution particulière des équations ci-dessus est effectuée en discrétisant les espaces de vitesse moléculaire et de coordonnées. Les équations discrètes sont résolues numériquement par un ordinateur. Les valeurs de la fonction de distribution et les moments macroscopiques pertinents sur les points du maillage sont stockés dans la mémoire. Dans chaque étape d'itération, les équations différentielles réelles sont résolues. L'itération est répétée jusqu'à ce que le résultat final soit atteint.

L'itération améliorée accélère considérablement le processus de la solution. Afin de montrer l'amélioration du processus d'itération, une analyse de stabilité est développée pour les équations cinétiques discrètes. L'analyse examine l'évolution des modes de Fourier dans le processus d'itération. Il est montré théoriquement que le schéma accéléré a un meilleur comportement de convergence par rapport à l'itération standard dans le cas des grandes valeurs du paramètre de raréfaction. Des simulations sur ordinateur pour des écoulements dans des canaux triangulaires équilatéraux sont exécutées aussi pour étudier la performance d'itération. Il est constaté que le nombre d'itérations nécessaire pour obtenir un résultat convergent est plus petit à faible niveau de raréfaction pour la méthode accélérée. En règle générale, pas plus d'une centaine d'itérations est nécessaire pour obtenir des résultats typiques en utilisant le schéma accéléré. Au contraire, le nombre requis d'itérations peut

être de plusieurs milliers pour  $\delta = 50$  en appliquant la méthode standard. Le temps de calcul requis peut être de quelques milliers de secondes pour la méthode accélérée, mais il peut être plus grand que cent mille secondes pour la méthode standard pour  $\delta = 50$ .

Les méthodes accélérées de vitesse discrète sont développées aussi pour la solution du modèle de McCormack. Dans ce cas, les équations de moments supplémentaires sont introduites d'une manière semblable que pour le modèle Bhatnagar-Gross-Krook. En particulier, deux codes pour canaux triangulaires et trapézoïdaux sont développés. Ces codes sont utilisés pour résoudre le modèle cinétique de McCormack pour les écoulements des mélanges  $Ne/Ar$  et  $He/Xe$  générés par pression et concentration dans toute la gamme de concentration et de raréfaction du gaz pour les sections transversales triangulaires et trapézoïdales. Ces calculs fournissent des quantités de dynamique des fluides dans la section transversale du canal et les coefficients cinétiques. Des simulations similaires sont menées pour les mélanges  $He/Ar$  et  $He/Kr$ . Ces résultats sont utilisés dans la partie expérimentale de la thèse pour faire la comparaison entre théorie et expérience.

### **2.1.2. Les débits et le comportement global**

Dans les applications, les débits à travers le système sont des quantités importantes. Le débit peut être défini comme le débit massique ou molaire. Ces deux quantités adimensionnelles sont identiques pour les gaz seuls, puisque la masse du gaz est proportionnelle au nombre de moles. Toutefois, les deux quantités sont différentes pour les mélanges gazeux en raison de la séparation du gaz. Les différentes espèces du gaz s'écoulent avec des vitesses moyennes différentes dans le canal. Habituellement, les espèces plus légères ont des vitesses plus grandes. En raison de la séparation du gaz, les débits massiques et molaires ne sont pas simplement proportionnels comme dans le cas d'un gaz seul. La séparation du gaz entraîne la non-uniformité de la concentration

du gaz dans le canal. Même si les concentrations à l'entrée et la sortie sont les mêmes, la concentration varie le long de l'axe du canal.

Dans la thèse, d'abord, des formules approximatives sont développées pour déduire le débit massique pour les écoulements générés par pression ou concentration. Dans l'écoulement généré par pression, les effets de diffusion, donc la variation de concentration, sont négligés. Pour l'écoulement généré par concentration, la variation de pression le long de l'axe du canal est négligée. La formule est fondée sur les flux thermodynamiques  $J_P$  et  $J_C$ . Les gradients locaux sont remplacés par les différences globales de pression ou de concentration entre l'entrée et la sortie du canal. De cette façon, les coefficients cinétiques moyens sont introduits et utilisés dans la formule du débit massique.

Deuxièmement, une méthodologie exacte est développée afin de déduire le débit molaire des espèces à travers le canal en tenant compte de la séparation du gaz. En utilisant les flux thermodynamiques  $J_P$  et  $J_C$ , les débits molaires des espèces sont exprimés par les gradients locaux de pression et de concentration. En conséquence, les débits molaires peuvent être écrits par

$$J_1 = -\frac{PA'L_C}{m(C)v_0(C)L} \times \left[ (C\Lambda_{PP} + (1-C)\Lambda_{CP}) \frac{\partial P}{\partial \hat{z}} \frac{1}{P} + (C\Lambda_{PC} + (1-C)\Lambda_{CC}) \frac{\partial C}{\partial \hat{z}} \frac{1}{C} \right], \quad (12)$$

$$J_2 = -\frac{PA'L_C}{m(C)v_0(C)L} \times (1-C) \left[ (\Lambda_{PP} - \Lambda_{CP}) \frac{\partial P}{\partial \hat{z}} \frac{1}{P} + (\Lambda_{PC} - \Lambda_{CC}) \frac{\partial C}{\partial \hat{z}} \frac{1}{C} \right], \quad (13)$$

où  $A'$  est la surface de la section transversale du canal,  $L$  la longueur du canal et  $\hat{z} = z'/L$  la coordonnée sans dimension le long de l'axe du canal. En raison de la conservation du nombre de particules, les débits molaires sont constants.

Les deux équations ci-dessus forment un système d'équations différentielles ordinaires pour les distributions de pression et de concentration. Les

pressions et les concentrations à l'entrée et la sortie constituent des conditions aux limites. L'équation ci-dessus est résolue pour les configurations d'écoulement particulier en utilisant la base de données des coefficients cinétiques obtenue à partir de la solution du modèle cinétique de McCormack. Il se trouve que pour un débit généré par pression, le mélange présente une distribution de concentration non uniforme. Ainsi, le débit est affecté par la séparation gazeuse. Le calcul fournit aussi la distribution de pression, qui suit presque le comportement typique d'un gaz seul généré par pression. Lorsque la raréfaction est élevée, le profil de pression est presque linéaire, tandis que lorsqu'elle est faible, il est non-linéaire à cause des effets de compressibilité. Le calcul de débit est aussi utilisé pour la comparaison entre théorie et expérience.

## 2.2. Les écoulements dans les microcanaux courts

Les écoulements de gaz binaires raréfiés dans les microcanaux courts sont analysés. L'axe du canal se trouve le long de la direction  $x'$ , tandis que la section transversale est située dans le plan  $(y', z')$ . Le microcanal est placé entre les réservoirs en amont A et en aval B contenant un mélange gazeux aux pressions et concentrations  $P_A, P_B$  et  $C_A, C_B$ , respectivement. Il y a une différence de pression entre les deux réservoirs,  $P_A > P_B$ , ce qui entraîne l'écoulement dans le microcanal, mais les concentrations sont égales dans les deux réservoirs. La température du gaz  $T_0$  est maintenue constant dans les réservoirs et sur les parois du canal.

Le paramètre de raréfaction  $\delta$  est introduit aussi pour décrire l'écoulement de la même manière que pour le canal long. Le paramètre de raréfaction  $\delta_A$  et la concentration  $C_A$  en amont sont utilisés comme valeurs de référence pour caractériser l'écoulement. Dans ces conditions, nous nous intéressons

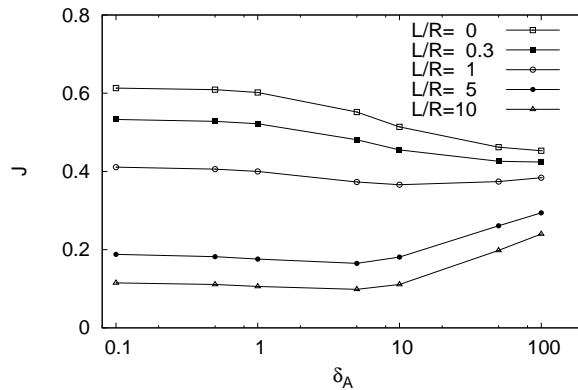
aux débits sans dimension des espèces gazeuses à travers le canal

$$J_\alpha = \frac{1}{n_0 v_0 A'} \iint n_\alpha u_{\alpha x} dy' dz', \quad (14)$$

où  $n_0$  est la densité molaire totale dans le réservoir amont et l'intégration se réfère à la section transversale du canal. Les quantités macroscopiques de dynamique des fluides, la densité, la vitesse et la température, sont déduites aussi de l'étude. Dans le cas du canal court, lorsque la longueur du canal est comparable à son diamètre hydraulique, la vitesse du gaz peut être dans la même gamme que la vitesse caractéristique moléculaire. Dans ce cas, l'équation de Boltzmann non linéaire doit être utilisée pour décrire l'écoulement. L'équation de Boltzmann est résolue par l'application de la méthode de simulation directe de Monte Carlo (DSMC). Dans la DSMC, le mouvement de particules modèles est modélisé dans le domaine de l'écoulement. Le domaine spatial est divisé en une série de cellules. Le transport des particules est modélisé selon des phases de mouvement et de collision. Dans l'étape de mouvement, les particules modèles se déplacent le long de trajectoires droites, conformément à leur vitesse. Dans l'étape de collision, la collision entre les particules est simulée. Il y a aussi une étape d'échantillonnage, lorsque les quantités macroscopiques sont calculées dans les cellules. La DSMC donne un modèle du gaz. L'avantage de la méthode est sa simplicité. Elle peut être utilisée avec succès pour les écoulements à haute vitesse, lorsque la dispersion statistique des quantités macroscopiques est relativement faible.

Dans la thèse, des codes avancés de DSMC sont développés pour simuler l'écoulement de gaz binaires raréfiés dans des tubes courts avec différentes longueurs et à travers des fentes. Ces codes appliquent des zones de pondération afin de réduire la dispersion statistique et utilisant des distributions de grille à trois niveaux à proximité du canal pour une meilleure résolution. Le modèle de collision de sphère dure est mis en œuvre dans les codes.

Des simulations sont réalisées pour des écoulements de mélanges  $Ne/Ar$  et  $He/Xe$  à travers des microtubes et des fentes dans une large gamme de



Le débit total sans dimension de  $He/Xe$  en fonction de  $\delta_A$  pour  $C_A = 0.5$ ,  $P_B/P_A = 0.1$  et différentes valeurs de  $L/R$ .

raréfaction du gaz et de concentration du mélange et à des valeurs différentes du rapport de pression  $P_B/P_A$ . Les débits des espèces gazeuses et du mélange et la distribution axiale de densité, de vitesse et de température sont déduits des simulations.

Des résultats intéressants sont obtenus à partir de ces études. L'effet de séparation du gaz est observé sur les débits des espèces. Lorsque la raréfaction augmente, les espèces du gaz deviennent plus indépendantes en raison de la réduction des collisions intermoléculaires, et le débit de l'espèce légère devient plus grand que celui de l'espèce lourde. Les mélanges avec un rapport de masses plus grand présentent une séparation du gaz plus forte. Dans la Fig. 0, le débit total  $J = J_1 + J_2$  est représenté en fonction du paramètre de raréfaction pour des valeurs différentes du rapport  $L/R$  de la longueur de canal sur le rayon, pour les écoulements de mélange  $He/Xe$  dans des microtubes. On remarque que pour les tubes courts le débit augmente lorsque le paramètre de raréfaction décroît, mais pour les tubes plus longs le débit s'approche des courbes typiques de canaux longs. Pour les plus longs tubes, le minimum de Knudsen se présente à une valeur particulière de la raréfaction.

La distribution axiale de densité, de vitesse et de température du gaz est aussi analysée. De cette étude, on peut conclure que les quantités macroscopiques montrent de fortes variations près du canal. Les profils de densité dépendent des espèces, ce qui est la preuve de la séparation du gaz. Les vitesses axiales sont non nulles dans la région du canal. Pour un niveau de raréfaction fini, la vitesse de l'espèce légère est plus grande que celle de l'espèce lourde. La vitesse augmente avec la chute de pression, et elle peut dépasser la vitesse caractéristique moléculaire. Il y a une chute de température près de la sortie du canal, qui est causée par la détente rapide du gaz dans le réservoir aval. Pour résumer, les simulations des écoulements de gaz binaires raréfiés dans les microtubes courts donnent une idée du comportement de ces écoulements.

### **3. Étude expérimentale des écoulements de mélanges gazeux dans des microcanaux longs et comparaison avec le calcul cinétique**

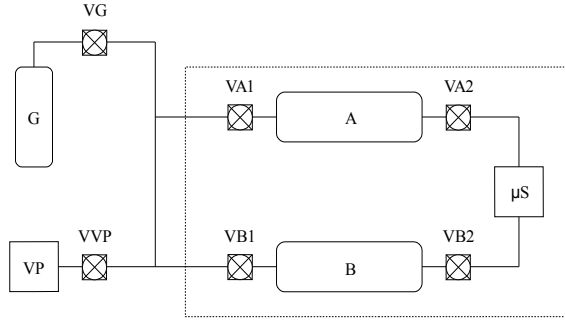
Les écoulements des mélanges gazeux dans les microcanaux longs sont étudiés expérimentalement. Le débit du gaz à travers le microsystème est mesuré et comparé aux résultats du modèle de McCormack. La mesure du débit est basée sur la méthode de volume constant. La configuration de l'écoulement est la même que celle décrite dans le paragraphe sur la simulation de canaux longs. La disposition de l'appareillage expérimental est montrée sur la Fig. 0. Le dispositif expérimental compare les réservoirs amont A et aval B, et le microsystème  $\mu S$ . Le microsystème est raccordé aux réservoirs par les vannes VA2 et VB2. L'ensemble est situé dans une chambre plastique isolée thermiquement. Des modules Peltier sont utilisés pour maintenir des conditions isothermes à l'intérieur de la chambre. La température est surveillée en permanence. La pression dans les réservoirs est mesurée par des

capteurs capacitifs Inficon. Les signaux de température et de pression sont relevés par un ordinateur pendant la mesure. Le débit dans le microsysteme est entraîné par la différence de pression entre les réservoirs amont et aval. Dans la méthode de volume constant, le débit est déterminé par la variation de pression dans les réservoirs.

La mesure réelle du débit est un processus en trois étapes. Avant la mesure, l'ensemble du circuit peut être mis au vide par une pompe à vide VP. Dans la première étape, le circuit est rempli avec le mélange gazeux à la pression de sortie  $P_B$ , issue d'une bouteille du gaz comprimé G. Ensuite, la vanne VA2 est fermée et le débit éventuel de fuite ou de dégazage dans le circuit B est mesuré. Le récipient A est rempli avec le gaz à la pression d'entrée  $P_A$ . Une fois la régulation thermique atteinte, la vanne VA2 est ouverte et le gaz s'écoule à travers les microcanaux. Dans cette étape, le débit est déterminé. Enfin, le circuit est rempli avec le gaz à la pression d'entrée  $P_A$ . La vanne VB2 est fermée et le débit éventuel de fuite ou de dégazage est mesuré dans le circuit A. Les débits de fuite ou de dégazage dans les première et troisième étapes sont utilisés pour corriger le débit obtenu dans la deuxième étape. De cette façon, l'effet éventuel des fuites ou du dégazage est pris en compte dans le résultat. Le débit final expérimental considéré est la moyenne de la valeur corrigée des débits en amont et en aval.

Dans l'expérience, les deux débits  $J_A^e$  et  $J_B^e$  sont déterminés à partir de la variation de la pression dans les réservoirs A et B. Ils sont déduits de l'équation d'état. En conséquence, le débit peut être calculé à partir de la dérivée temporelle de la pression. L'incertitude globale expérimentale de la mesure est de  $\pm 4\%$ . Cependant, cette valeur est modifiée à raréfaction élevée ( $P_B = 2kPa$ ), lorsque l'effet de fuite ou de dégazage n'est pas négligeable.

Le débit des mélanges gazeux  $He/Ar$  et  $He/Kr$  dans des microcanaux rectangulaires et trapézoïdaux longs est mesuré. Le microsysteme est constitué d'une série de microcanaux parallèles afin d'augmenter le débit. Pour le



La disposition du banc d'essais pour la mesure du débit.

mélange  $He/Ar$ , des expériences avec les concentrations de 10%, 30%, 50%, 70%, 90% et avec les gaz seuls  $He$ ,  $Ar$  sont réalisées. Pour le mélange  $He/Kr$ , la concentration est de 50%. Les expériences sont réalisées avec les pressions fixées en aval mais à des valeurs différentes du rapport de pression. Les pressions aval sont  $15.2kPa$ ,  $8kPa$  et  $15.1kPa$ ,  $8.05kPa$  pour les canaux rectangulaires et trapézoïdaux, respectivement. Les débits expérimentaux sont comparés aux résultats du calcul cinétique. Une étude comparative avec d'autres résultats expérimentaux est également faite pour les mélanges  $He/Ar$ . Dans ce cas, la pression en aval est  $15kPa$  et  $2kPa$ .

Afin d'illustrer les résultats expérimentaux et l'étude comparative, les débits sont indiqués pour un microcanal rectangulaire de hauteur  $H = 1,15\mu m$ , de largeur  $W = 21\mu m$  et de longueur  $L = 5mm$  dans les tableaux 0 et 0 pour  $P_B = 15.2kPa$  et  $P_B = 8kPa$ , respectivement, pour des mélanges  $He/Ar$  et  $He/Kr$ . Dans ces tableaux, les colonnes présentent dans l'ordre les pressions d'entrée et de sortie, le rapport de pression, le nombre de Knudsen moyen, le débit expérimental d'entrée et de sortie, le débit final expérimental, la différence  $\Delta_e = (1 - J_A^e/J_B^e)$  entre les débits d'entrée et de sortie, le débit numérique, et l'écart  $\Delta = 100(1 - J^e/J)$  entre les débits numériques et ex-

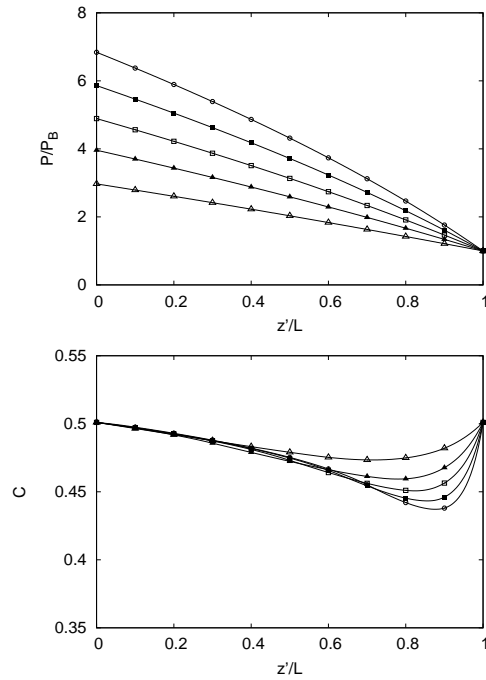
Débits de mélange  $He/Ar$  à différentes valeurs de la concentration (en haut) et  $He/Kr$  à  $C_A = 0.5010$  (en bas) en fonction du rapport de pressions à  $P_B = 15.2kPa$ .

$P_A(kPa)$	$P_B(kPa)$	$P_A/P_B$	$Kn_0$	$J_A^e(mol/s)$	$J_B^e(mol/s)$	$J^e(mol/s)$	$\Delta^e$	$J(mol/s)$	$\Delta$
$C_A = 0.0$									
45908	15200	3.02	0.23	2.26e-11	2.24e-11	2.25e-11	-1.02	2.25e-11	-0.03
59198	15200	3.89	0.19	3.60e-11	3.47e-11	3.53e-11	-3.69	3.46e-11	-2.12
73582	15200	4.84	0.16	4.91e-11	4.88e-11	4.89e-11	-0.45	4.94e-11	0.86
89571	15200	5.89	0.13	7.18e-11	6.94e-11	7.06e-11	-3.45	6.79e-11	-3.94
104238	15200	6.86	0.12	8.95e-11	8.89e-11	8.92e-11	-0.62	8.69e-11	-2.65
$C_A \simeq 0.1$									
45809	15201	3.01	0.24	2.40e-11	2.34e-11	2.37e-11	-2.84	2.40e-11	1.31
59232	15200	3.90	0.20	3.71e-11	3.75e-11	3.73e-11	1.01	3.68e-11	-1.56
73603	15200	4.84	0.17	5.13e-11	5.12e-11	5.13e-11	-0.06	5.20e-11	1.47
89424	15199	5.88	0.14	7.26e-11	7.09e-11	7.17e-11	-2.52	7.08e-11	-1.26
104225	15202	6.86	0.12	9.33e-11	9.27e-11	9.30e-11	-0.67	9.04e-11	-2.82
$C_A \simeq 0.3$									
44327	15199	2.92	0.28	2.59e-11	2.54e-11	2.56e-11	-2.27	2.63e-11	2.62
59292	15200	3.90	0.23	4.36e-11	4.21e-11	4.28e-11	-3.43	4.19e-11	-2.27
74553	15200	4.90	0.19	6.19e-11	6.17e-11	6.18e-11	-0.28	5.95e-11	-3.88
89629	15200	5.90	0.16	8.17e-11	7.90e-11	8.03e-11	-3.43	7.87e-11	-2.12
104034	15200	6.84	0.14	9.84e-11	9.82e-11	9.83e-11	-0.22	9.88e-11	0.47
$C_A \simeq 0.5$									
45217	15200	2.97	0.33	3.13e-11	3.06e-11	3.09e-11	-2.51	3.22e-11	3.93
60197	15201	3.96	0.26	4.86e-11	4.78e-11	4.82e-11	-1.81	4.98e-11	3.23
74279	15201	4.89	0.22	6.59e-11	6.60e-11	6.60e-11	0.27	6.79e-11	2.90
89125	15200	5.86	0.19	9.00e-11	8.90e-11	8.95e-11	-1.13	8.86e-11	-1.09
104034	15200	6.84	0.16	1.13e-10	1.11e-10	1.12e-10	-1.26	1.11e-10	-0.80
$C_A \simeq 0.7$									
45823	15200	3.01	0.39	3.92e-11	3.79e-11	3.85e-11	-3.36	4.00e-11	3.72
59504	15200	3.91	0.32	5.82e-11	5.67e-11	5.74e-11	-2.61	5.89e-11	2.53
74071	15200	4.87	0.27	7.97e-11	7.80e-11	7.89e-11	-2.11	8.05e-11	1.99
89356	15200	5.88	0.23	1.02e-10	1.00e-10	1.01e-10	-1.63	1.05e-10	3.72
104103	15200	6.85	0.20	1.30e-10	1.27e-10	1.29e-10	-2.57	1.30e-10	1.05
$C_A \simeq 0.9$									
45671	15199	3.00	0.51	4.95e-11	4.77e-11	4.86e-11	-3.74	5.05e-11	3.80
59550	15200	3.92	0.42	7.22e-11	7.21e-11	7.22e-11	-0.18	7.47e-11	3.35
74267	15199	4.89	0.35	1.03e-10	1.00e-10	1.02e-10	-2.67	1.02e-10	0.20
90106	15200	5.93	0.29	1.37e-10	1.37e-10	1.37e-10	-0.52	1.33e-10	-3.27
104329	15201	6.86	0.26	1.65e-10	1.61e-10	1.63e-10	-2.63	1.62e-10	-0.19
$C_A = 1.0$									
45673	15200	3.00	0.64	5.68e-11	5.73e-11	5.71e-11	0.87	5.81e-11	1.79
59241	15200	3.90	0.52	8.89e-11	8.60e-11	8.75e-11	-3.35	8.58e-11	-1.99
74048	15200	4.87	0.43	1.20e-10	1.19e-10	1.20e-10	-1.29	1.18e-10	-1.67
89282	15200	5.87	0.37	1.60e-10	1.54e-10	1.57e-10	-3.67	1.52e-10	-3.07
103915	15200	6.84	0.33	1.96e-10	1.90e-10	1.93e-10	-2.91	1.88e-10	-2.86
$C_A \simeq 0.5$									
45278	15199	2.98	0.26	2.60e-11	2.52e-11	2.56e-11	-3.08	2.64e-11	3.19
59797	15200	3.93	0.21	4.07e-11	4.05e-11	4.06e-11	-0.59	4.04e-11	-0.44
73618	15204	4.84	0.18	5.70e-11	5.51e-11	5.60e-11	-3.56	5.47e-11	-2.40
87696	15201	5.77	0.15	7.29e-11	7.07e-11	7.18e-11	-3.03	7.05e-11	-1.83
104033	15200	6.84	0.13	9.42e-11	9.11e-11	9.27e-11	-3.46	9.08e-11	-2.02

Débits de mélange  $He/Ar$  à différentes valeurs de la concentration (en haut) et  $He/Kr$  à  $C_A = 0.5010$  (en bas) en fonction du rapport de pressions à  $P_B = 8kPa$ .

$P_A(kPa)$	$P_B(kPa)$	$P_A/P_B$	$Kn_0$	$J_A^e(mol/s)$	$J_B^e(mol/s)$	$J^e(mol/s)$	$\Delta^e$	$J(mol/s)$	$\Delta$
$C_A = 0.0$									
31822	8000	3.98	0.35	1.57e-11	1.62e-11	1.60e-11	3.14	1.56e-11	2.23
40113	8000	5.01	0.29	2.26e-11	2.29e-11	2.27e-11	1.44	2.20e-11	-3.17
47964	8000	6.00	0.25	3.00e-11	2.95e-11	2.97e-11	-1.80	2.86e-11	-3.88
55969	8002	6.99	0.22	3.52e-11	3.39e-11	3.46e-11	-3.78	3.59e-11	3.55
$C_A \simeq 0.1$									
31989	8000	4.00	0.37	1.70e-11	1.65e-11	1.67e-11	-3.04	1.72e-11	2.85
40346	8000	5.04	0.31	2.46e-11	2.42e-11	2.44e-11	-1.76	2.41e-11	-1.55
47949	8000	5.99	0.27	3.10e-11	3.06e-11	3.08e-11	-1.48	3.07e-11	-0.20
56125	8000	7.02	0.23	3.91e-11	3.84e-11	3.87e-11	-1.86	3.84e-11	-0.85
$C_A \simeq 0.3$									
31977	8000	4.00	0.42	2.05e-11	2.00e-11	2.02e-11	-2.76	2.07e-11	2.10
40290	8000	5.04	0.35	2.79e-11	2.82e-11	2.81e-11	1.26	2.83e-11	1.00
47968	8000	6.00	0.30	3.52e-11	3.40e-11	3.46e-11	-3.28	3.58e-11	3.23
56000	8000	7.00	0.26	4.50e-11	4.35e-11	4.38e-11	-3.34	4.39e-11	0.41
$C_A \simeq 0.5$									
31781	7997	3.97	0.49	2.53e-11	2.46e-11	2.49e-11	-3.11	2.49e-11	-0.18
40109	8000	5.01	0.41	3.30e-11	3.19e-11	3.25e-11	-3.52	3.38e-11	3.85
47854	8000	5.98	0.35	4.10e-11	4.06e-11	4.08e-11	-1.04	4.24e-11	3.70
55934	8000	6.99	0.31	5.04e-11	4.97e-11	5.01e-11	-1.32	5.16e-11	2.84
$C_A \simeq 0.7$									
31909	8000	3.99	0.60	3.07e-11	3.00e-11	3.02e-11	-2.58	3.11e-11	2.70
40266	8001	5.03	0.49	4.08e-11	3.93e-11	4.01e-11	-3.97	4.17e-11	3.95
48003	8000	6.00	0.42	5.10e-11	4.98e-11	5.04e-11	-2.38	5.20e-11	2.96
55984	8000	7.00	0.37	6.22e-11	6.02e-11	6.12e-11	-3.21	6.28e-11	2.64
$C_A \simeq 0.9$									
31947	8000	3.99	0.78	3.92e-11	3.80e-11	3.86e-11	-3.18	3.95e-11	2.22
40176	8000	5.02	0.64	5.35e-11	5.19e-11	5.27e-11	-3.15	5.39e-11	2.29
47888	8000	5.99	0.56	6.62e-11	6.54e-11	6.58e-11	-1.25	6.59e-11	0.17
55820	8000	6.98	0.49	7.71e-11	7.81e-11	7.76e-11	1.17	7.96e-11	2.55
$C_A = 1.0$									
31691	8000	3.96	0.98	4.47e-11	4.37e-11	4.42e-11	-2.19	4.46e-11	0.86
40047	8000	5.01	0.81	6.32e-11	6.24e-11	6.28e-11	-1.36	6.07e-11	-3.50
47739	8000	5.97	0.70	7.64e-11	7.68e-11	7.66e-11	0.50	7.59e-11	-0.91
55917	8000	6.99	0.61	9.36e-11	9.69e-11	9.53e-11	3.43	9.25e-11	-3.00
$C_A \simeq 0.5$									
31914	8000	3.99	0.40	2.06e-11	2.11e-11	2.08e-11	2.40	2.07e-11	-0.54
40232	8000	5.03	0.33	2.74e-11	2.64e-11	2.69e-11	-3.67	2.78e-11	3.27
48055	8000	6.01	0.28	3.43e-11	3.32e-11	3.37e-11	-3.40	3.48e-11	3.02
55928	8000	6.99	0.25	4.27e-11	4.30e-11	4.28e-11	0.67	4.20e-11	-2.03

périmentaux. Le débit est présenté pour un canal individuel. On constate un très bon accord entre les résultats expérimentaux et numériques. La différence entre ces résultats est inférieure à l'incertitude expérimentale. Il est également constaté que la différence  $\Delta_e$  est toujours inférieure à l'incertitude



Distributions de pression (en haut) et de concentration (en bas) pour le mélange  $He/Ar$  avec  $C_A = 0.5010$  pour  $P_B = 15.2kPa$ . Les symboles  $\Delta, \blacktriangle, \square, \blacksquare, \circ$  représentent les résultats pour  $P_A/P_B = [2.97, 3.96, 4.89, 5.86, 6.84]$ .

expérimentale. Cela justifie que l'effet éventuel de fuite ou de dégazage est correctement pris en compte. Telle est la situation pour toutes les expériences.

Les distributions de pression et de concentration le long de l'axe du canal sont également déduites du calcul cinétique. Afin d'illustrer les résultats, les profils de pression et de concentration sont présentés pour les écoulements de mélange  $He/Ar$  avec la concentration  $C_A = 0.5010$  et une pression de sortie  $P_B = 15.2kPa$  sur la Fig. 0. On peut voir que les profils de pression sont relativement non-linéaires en raison des effets de compressibilité. En outre, la concentration n'est pas uniforme. Il y a une baisse de concentration près de la sortie du canal. Ceci est la preuve évidente de la séparation gazeuse. La baisse de la concentration augmente lorsque le rapport de pression décroît.

L'étude comparative montre que la différence entre les résultats expérimentaux et numériques est inférieure à l'incertitude expérimentale pour tous les cas mesurés dans le cadre de la thèse. Une comparaison avec des résultats expérimentaux de la littérature est également faite. Dans ce cas, la différence entre les débits des deux approches peut dépasser l'incertitude expérimentale, mais l'accord est toujours considéré comme très bon. Pour conclure, il est constaté que le modèle de McCormack est un outil viable pour décrire les écoulements des mélanges gazeux générés par pression à pour les valeurs des paramètres considérées.

## 4. Conclusions

Dans la thèse, les écoulements des mélanges gazeux dans des microcanaux sont étudiés numériquement et expérimentalement. Dans la partie numérique, différents traitements sont utilisés pour les microcanaux longs et courts. Pour les microcanaux longs, une méthode accélérée de vitesse discrète est développée pour des grilles triangulaires. La méthode est utilisée pour résoudre le modèle cinétique de McCormack. De plus, un calcul de débit est développé pour déduire le comportement global de l'écoulement. Des résultats illustratifs sont obtenus pour les mélanges  $Ne/Ar$  et  $He/Xe$ . Dans le cas des microcanaux courts, des codes avancés de DSMC sont développés pour simuler l'écoulement gazeux. Ces codes sont utilisés pour les simulations pratiquées pour étudier le comportement des mélanges  $Ne/Ar$  et  $He/Xe$  dans des configurations d'écoulements différents. Dans la partie expérimentale, la méthode de volume constant est appliquée pour la mesure des débits dans les microcanaux longs. Les mesures sont effectuées pour les microcanaux rectangulaires et trapézoïdaux. Les débits des mélanges  $He/Ar$  et  $He/Kr$  sont mesurés et comparés aux calculs cinétiques sur la base du modèle de McCormack. Un très bon accord entre les résultats numériques et

expérimentaux est atteint. Cela montre que le modèle de McCormack peut être utilisé avec succès pour décrire l'écoulement isotherme de gaz binaires générés par pression dans les microsystèmes.

# Contents

<b>1</b>	<b>Introduction</b>	<b>1</b>
1.1	Kinetic theory of gases . . . . .	1
1.2	The Boltzmann equation . . . . .	4
1.2.1	Collision invariants . . . . .	9
1.2.2	H-theorem . . . . .	10
1.2.3	Linearized Boltzmann equation . . . . .	11
1.2.4	Model collision operators . . . . .	12
1.2.5	Boundary conditions . . . . .	13
1.2.6	Fluid dynamic description . . . . .	14
1.3	Characteristics of gaseous micro-flows . . . . .	16
1.4	Objectives and novelty of the thesis . . . . .	21
<b>2</b>	<b>Literature survey on rarefied and micro-gas flows</b>	<b>23</b>
2.1	Kinetic description of gaseous mixtures . . . . .	23
2.1.1	Sirovich model . . . . .	24
2.1.2	Hamel-Morse model . . . . .	26
2.1.3	McCormack model . . . . .	28
2.1.4	Recent approaches . . . . .	30
2.2	Gas microfluidics – General . . . . .	34
2.3	Modeling of rarefied gas flows . . . . .	34
2.3.1	Extended hydrodynamics . . . . .	34

2.3.2	Kinetic description – Flows in long channels . . . . .	35
2.3.3	Kinetic description – Flows in short channels . . . . .	36
2.4	Experimental studies on rarefied flows . . . . .	37
2.4.1	Flows through long channels . . . . .	37
2.4.2	Flows through short channels . . . . .	38
2.5	Gaseous separation . . . . .	38
<b>3</b>	<b>Simulation of binary gas flows through long microchannels of triangular and trapezoidal cross sections</b>	<b>40</b>
3.1	Introduction . . . . .	40
3.2	Flow configuration and formulation . . . . .	41
3.3	The McCormack model . . . . .	46
3.4	Accelerated discrete velocity algorithm in triangular lattices .	51
3.4.1	General . . . . .	51
3.4.2	Single gases . . . . .	52
3.4.3	Gaseous mixtures . . . . .	73
3.5	Kinetic coefficients . . . . .	76
3.6	Flow rates . . . . .	81
3.6.1	General expressions . . . . .	81
3.6.2	Pressure driven flow . . . . .	83
3.6.3	Concentration driven flow . . . . .	84
3.6.4	Separation effect . . . . .	86
<b>4</b>	<b>Simulation of binary gas flows through microchannels of fi- nite length</b>	<b>93</b>
4.1	Introduction . . . . .	93
4.2	Flow configuration . . . . .	94
4.2.1	Flow through short tubes . . . . .	94
4.2.2	Flow through slits . . . . .	96
4.3	The DSMC algorithm for binary gas flows . . . . .	97

4.3.1	General considerations . . . . .	97
4.3.2	Computational domain and grid . . . . .	99
4.3.3	Moving . . . . .	100
4.3.4	Boundary conditions . . . . .	101
4.3.5	Collision modeling . . . . .	102
4.3.6	Sampling of macroscopic quantities . . . . .	108
4.3.7	Computational details . . . . .	109
4.4	Results and discussions . . . . .	110
4.4.1	Flows through short tubes and orifices . . . . .	110
4.4.2	Flows through slits . . . . .	126
<b>5</b>	<b>Experimental study of binary gas flows through long microchannels and comparison to kinetic calculation</b>	<b>137</b>
5.1	Introduction . . . . .	137
5.2	Definition of the problem . . . . .	138
5.3	The experimental approach . . . . .	139
5.3.1	Experimental setup . . . . .	139
5.3.2	Determination of the flow rates . . . . .	141
5.3.3	Specification of microchannels . . . . .	143
5.4	Kinetic calculation of the flow rates . . . . .	144
5.5	Comparative study for binary gas flows in rectangular and trapezoidal channels . . . . .	146
5.5.1	Flow rates for channel R1 . . . . .	146
5.5.2	Distribution of macroscopic quantities for R1 . . . . .	150
5.5.3	Flow rates for channel R2 . . . . .	151
5.5.4	Distribution of macroscopic quantities for R2 . . . . .	156
5.5.5	Flow rates for channel T1 . . . . .	158
5.5.6	Distribution of macroscopic quantities for T1 . . . . .	161
<b>6</b>	<b>Conclusions</b>	<b>164</b>

<b>Appendices</b>	<b>167</b>
<b>A Collision integrals and viscosity function</b>	<b>167</b>
A.1 Collision integrals . . . . .	167
A.2 Viscosity function . . . . .	168

# List of Figures

3.1	The cross sections of the triangular and the trapezoidal channels. . . . .	42
3.2	The triangular grid used in the discretization of the spatial coordinates. . . . .	56
3.3	The computational cell for one node on the triangular grid. . . . .	57
3.4	Eigenvalues $\omega(\mathbf{k})$ as a function of the wave number $\mathbf{k}$ at different values of the rarefaction parameter $\delta$ . . . . .	68
3.5	Eigenvalues $\omega(\mathbf{k})$ as a function of the wave number $\mathbf{k}$ at different values of spatial resolution $h$ . . . . .	69
3.6	Eigenvalues $\omega(\mathbf{k})$ as a function of the wave number $\mathbf{k}$ at different values of the angular resolution $M \times N$ . . . . .	70
3.7	Number of iterations versus convergence criterion ( $\epsilon$ ). . . . .	72
3.8	CPU time in seconds versus convergence criterion ( $\epsilon$ ). . . . .	72
3.9	Concentration distribution along the isosceles triangular channel for the $He/Xe$ mixture with $C_I = C_{II} = 0.5$ . . . . .	89
3.10	Concentration distribution along the isosceles triangular channel for the $He/Xe$ mixture with $C_I = C_{II} = 0.8$ . . . . .	89
3.11	Pressure distribution along the isosceles triangular channel for the $He/Xe$ mixture with $C_I = C_{II} = 0.5$ . . . . .	90
3.12	Pressure distribution along the isosceles triangular channel for the $He/Xe$ mixture with $C_I = C_{II} = 0.8$ . . . . .	90

4.1	The computational domain and the weighting zones for the short tube problem. . . . .	100
4.2	The computational domain and the weighting zones for the slit flow problem. . . . .	101
4.3	Dimensionless total flow rate for $He/Xe$ as a function of $\delta_A$ for $C_A = 0.5$ , $P_B/P_A = 0.1$ and various values of $L/R$ for short tubes. . . . .	119
4.4	Axial distributions of the density of each species of $He/Xe$ for $C_A = 0.5$ , $P_B/P_A = 0.1$ , $\delta_A = (0.1, 1, 10)$ and $L/R = (1, 5, 10)$ for short tubes. . . . .	120
4.5	Axial distributions of the density of each species of $He/Xe$ for $L/R = 1$ , $\delta_A = 1$ , $P_B/P_A = 0.1$ and $C_A = (0.25, 0.75)$ for short tubes. . . . .	121
4.6	Axial distributions of the density of each species of $He/Xe$ and $Ne/Ar$ for $C_A = 0.5$ , $L/R = 0.3$ , $\delta_A = 1$ and $P_B/P_A = (0.1, 0.4, 0.7)$ for short tubes. . . . .	122
4.7	Distributions of axial velocities of each species of $He/Xe$ for $C_A = 0.5$ , $P_B/P_A = 0.1$ , $\delta_A = (0.1, 1, 10)$ and $L/R = (1, 5, 10)$ for short tubes. . . . .	123
4.8	Distributions of axial velocities of each species of $He/Xe$ and $Ne/Ar$ for $C_A = 0.5$ , $L/R = 0.3$ , $\delta_A = 5$ and $P_B/P_A = (0.1, 0.4, 0.7)$ for short tubes. . . . .	124
4.9	Axial distribution of the temperature of $He/Xe$ for $C_A = 0.5$ , $P_B/P_A = 0.1$ , $\delta_A = (0.1, 1, 10)$ and $L/R = (1, 5, 10)$ for short tubes. . . . .	125
4.10	Axial distributions of the local rarefaction parameter and the Mach number of $He/Xe$ for $C_A = 0.5$ , $L/R = 0.3$ , $\delta_A = 1$ and $P_B/P_A = (0.1, 0.4, 0.7)$ for short tubes. . . . .	126

4.11	The distribution of the density for <i>He/Xe</i> and <i>Ne/Ar</i> mixtures with $C_A = 0.5$ and $P_B/P_A = 0$ at different values of the rarefaction parameter for slit flows. . . . .	131
4.12	The distribution of the density for <i>He/Xe</i> mixture with $C_A = (0.25, 0.75)$ and $\delta_A = 10$ at $P_B/P_A = 0.1$ for slit flows. . . . .	132
4.13	The distribution of the density for <i>He/Xe</i> and <i>Ne/Ar</i> mixtures with $C_A = 0.5$ and $\delta_A = 1$ at different values of the pressure ratio for slit flows. . . . .	132
4.14	The distribution of the axial velocity for <i>He/Xe</i> and <i>Ne/Ar</i> mixtures with $C_A = 0.5$ and $P_B/P_A = 0$ at different values of the rarefaction parameter for slit flows. . . . .	133
4.15	The distribution of the axial velocity for <i>He/Xe</i> and <i>Ne/Ar</i> mixtures with $C_A = 0.5$ and $\delta_A = 1$ at different values of the pressure ratio for slit flows. . . . .	133
4.16	The distribution of the temperature for <i>He/Xe</i> and <i>Ne/Ar</i> mixtures with $C_A = 0.5$ and $P_B/P_A = 0$ at different values of the rarefaction parameter for slit flows. . . . .	134
4.17	The distribution of the temperature for <i>He/Xe</i> and <i>Ne/Ar</i> mixtures with $C_A = 0.5$ and $\delta_A = 1$ at different values of the pressure ratio for slit flows. . . . .	134
4.18	Normalized rarefaction parameter and Mach number for <i>He/Xe</i> mixture with $C_A = 0.5$ and $P_B/P_A = 0$ at different values of rarefaction parameter for slit flows. . . . .	135
5.1	The layout of the flow rate setup. . . . .	140
5.2	Distributions of the pressure and concentration for <i>He/Ar</i> mixture with $C_A = 0.5010$ along the axis of the channel for $P_B \simeq 15kPa$ and $P_B \simeq 2kPa$ for channel R1. . . . .	150

5.3	Distributions of the pressure and the concentration for <i>He/Ar</i> and <i>He/Kr</i> mixtures with $C_A = 0.5010$ along the axis of the channel at $P_B \simeq 15.2kPa$ for channels R2. . . . .	156
5.4	Distributions of the pressure and the concentration for <i>He/Ar</i> and <i>He/Kr</i> mixtures with $C_A = 0.5010$ along the axis of the channel at $P_B \simeq 8kPa$ for channels R2. . . . .	157
5.5	Distributions of the pressure and the concentration for <i>He/Ar</i> and <i>He/Kr</i> mixtures with $C_A = 0.5010$ along the axis of the channel for $P_B \simeq 15.1kPa$ for channels T1. . . . .	162
5.6	Distributions of the pressure and the concentration for <i>He/Ar</i> and <i>He/Kr</i> mixtures with $C_A = 0.5010$ along the axis of the channel for $P_B \simeq 8.05kPa$ for channels T1. . . . .	163

# List of Tables

3.1	Discrete spectral radius $\sigma_S$ of the accelerated scheme. . . . .	67
3.2	Computational performance of the standard and accelerated schemes. . . . .	71
3.3	Kinetic coefficients for the isosceles triangular channel ( $\omega = 54.74^0$ ). . . . .	77
3.4	Kinetic coefficients for the isosceles trapezoidal channel ( $\omega = 54.74^0, b/h = 0.5$ ). . . . .	78
3.5	Kinetic coefficients for the isosceles trapezoidal channel ( $\omega = 54.74^0, b/h = 3$ ). . . . .	79
3.6	Geometrical effects on the kinetic coefficients, $He/Xe$ mixture with $C = 0.5$ . . . . .	80
3.7	The Poiseuille number for triangular and trapezoid channels as a function of $Kn_v$ for a single gas ( $C = 0$ ). . . . .	81
3.8	Normalized fluxes and mass flow rates with and without separation effects ( $He/Xe, C_I = C_{II} = 0.5$ ). . . . .	91
3.9	Normalized fluxes and mass flow rates with and without separation effects ( $He/Xe, C_I = C_{II} = 0.8$ ). . . . .	92
4.1	Dimensionless flow rates of $He/Xe$ through short tubes in terms of $\delta_A$ for $P_B/P_A = 0.1, L/R = 1$ and $C_A = (0.25, 0.5, 0.75)$ . . . . .	113
4.2	Dimensionless flow rates of $He/Xe$ through short tubes in terms of $\delta_A$ for $P_B/P_A = 0.1, L/R = (5, 10)$ . . . . .	114

4.3	Dimensionless flow rates of $He/Xe$ through short tubes in term of $\delta_A$ for $C_A = 0.5$ , $P_B/P_A = 0.4$ and $L/R = 1$ . . . . .	114
4.4	Dimensionless flow rates through short tubes for $He/Xe$ and $Ne/Ar$ in terms of $\delta_A$ for $C_A = 0.5$ , $P_B/P_A = (0.1, 0.4, 0.7)$ and $L/R = 0.3$ . . . . .	115
4.5	Dimensionless flow rates through orifices for $He/Xe$ in terms of $\delta_A$ for various values of $C_A$ and $P_B/P_A = 0.1$ . . . . .	116
4.6	Dimensionless flow rates through orifices for $He/Xe$ in terms of $\delta_A$ for $C_A = 0.5$ and $P_B/P_A = 0.4$ . . . . .	117
4.7	Dimensionless flow rate through orifices for $He/Xe$ in terms of $P_B/P_A$ for $\delta_A = 1$ and $C_A = 0.5$ . . . . .	117
4.8	Dimensionless flow rates through orifices for $Ne/Ar$ in terms of $\delta_A$ for $C_A = 0.5$ and $P_B/P_A = 0.1$ . . . . .	117
4.9	Flow rates through slits for $He/Xe$ mixture at different values of the concentration and $P_B/P_A = 0$ . . . . .	128
4.10	Flow rates through slits for $Ne/Ar$ mixture at $C_A = 0.5$ and $P_B/P_A = 0$ . . . . .	128
4.11	Flow rates through slits for $He/Xe$ and $Ne/Ar$ mixture at $C_A = 0.5$ and $P_B/P_A = (0.4, 0.7)$ . . . . .	129
5.1	Flow rates for $He/Ar$ mixture at different values of the concentration and pressure ratio at $P_B \simeq 15kPa$ through channels R1. . . . .	147
5.2	Flow rates for $He/Ar$ mixture at different values of the concentration and pressure ratio at $P_B \simeq 2kPa$ through channels R1. . . . .	148
5.3	Flow rates for $He/Ar$ at different values of the concentration as the function of the pressure ratio at $P_B \simeq 15.2kPa$ through channels R2. . . . .	152

5.4	Flow rates for $He/Kr$ at $C_A = 0.5010$ as the function of the pressure ratio at $P_B \simeq 15.2kPa$ through channels R2. . . . .	153
5.5	Flow rates for $He/Ar$ at different values of the concentration as the function of the pressure ratio at $P_B \simeq 8kPa$ through channels R2. . . . .	154
5.6	Flow rates for $He/Kr$ at $C_A = 0.5010$ as the function of the pressure ratio at $P_B \simeq 8kPa$ through channels R2. . . . .	155
5.7	Flow rates of $He$ and $Ar$ gases as the function of the pressure ratio at $P_B \simeq 4.1kPa$ through rectangular channels R2. . . . .	155
5.8	Flow rates for $He/Ar$ at different values of the concentration as the function of the pressure ratio at $P_B \simeq 15.1kPa$ through channels T1. . . . .	159
5.9	Flow rates for $He/Kr$ at $C_A = 0.5010$ as the function of the pressure ratio at $P_B \simeq 15.1kPa$ through channels T1. . . . .	160
5.10	Flow rates for $He/Ar$ at different values of the concentration as the function of the pressure ratio at $P_B \simeq 8.05kPa$ through channels T1. . . . .	160
5.11	Flow rates for $He/Kr$ at $C_A = 0.5010$ as the function of the pressure ratio at $P_B \simeq 8.05kPa$ through channels T1. . . . .	161
A.1	Viscosity of $He/Ar$ and $He/Kr$ mixtures at different helium concentrations $C$ . . . . .	169

# Chapter 1

## Introduction

### 1.1 Kinetic theory of gases

The born of the kinetic theory of gases can be dated back to Daniel Bernoulli, who published *Hydrodynamica* in 1738. Bernoulli established the basic principles of gas kinetics. In his theory, the gas consists of a large number of elastic molecules moving in all directions with relatively high speed. These molecules collide with each other, dictated by the law of mechanics. Bernoulli was able to explain the pressure of the gas as the force exerted by the molecules on the walls of the container during collisions. This idea was tempting for other physicists since it included the law of energy conservation. Even though his theory is true in principle, as we know now, the development of kinetic theory lasted many years, because there was no idea for handling the motion of the huge number of particles.

In 1857, Rudolf Clausius refining others' idea contributed to the kinetic theory of gases by establishing a gas kinetic model, which took into account the translational, rotational and vibrational motion of the molecules. The main achievement of Clausius in the field was the introduction of the idea of the mean free path, the average distance travelling by one molecule in

the gas between two subsequent collisions. He first stated the second law of thermodynamics and introduced the idea of entropy on phenomenological grounds.

One of the major contributors to the kinetic theory of gases was James Clerk Maxwell (1831-1879). The original theory of Bernoulli was advanced and cast into a consistent mathematical formulation. Although there were other contributors in that time, Maxwell can be considered as a cardinal investigator in kinetic theory. He appeared as a mathematician and also as an experimentalist in the field. One of the major achievements of Maxwell was the introduction of the distribution function, a statistical description of the very large amount of particles of the gas. The invention and the establishment of mathematical background of the distribution function can be considered as the born of statistical mechanics. He derived the equilibrium distribution function and introduced a transfer equation for the distribution function and the so-called Maxwell potential for describing the interactions between the molecules. Another contribution of Maxwell was establishing a gas-surface interaction law, which is now called as the Maxwell boundary condition. With the assumption of the diffuse reflection of gas molecules on a solid wall, he derived a slip boundary condition for the macroscopic velocity field. Also, he was able to calculate the viscosity of the model gas with the Maxwell interaction. He found that the viscosity of the gas is independent of its density. Generally speaking, he can be considered as the most cardinal scientist in the 19. Century, contributing to the modern theory of physics. His influence on physics is indeed decisive.

Another important, or maybe the most substantial, contributor for the kinetic theory of gases was Ludwig Boltzmann (1844-1906). He can be considered as one of the founders of statistical mechanics and statistical thermodynamics. Also, he advocated atomistic theory in that time when the existence of atoms was not generally accepted. Boltzmann itself in this the-

ory successfully presupposed atoms and molecules. In principle, he followed the way of Maxwell. One of his main contributions to the kinetic theory of gases is the establishment of the Boltzmann equation (BE), a transport equation for the one-particle distribution function. Since the invention of the original BE by Boltzmann itself, similar equations have been proposed to a large class of transport phenomena, including neutron transport relevant to nuclear energy, charged particle transport in solids, such as semiconductors or metals, particle transport in plasmas, radiative transfer. His main achievement was formulating the collision term in the BE. For rarefied gases, he introduced the molecular chaos assumption for describing the collisions between the molecules. Another important contribution of Boltzmann for kinetic theory and statistical mechanics was the introduction of the entropy, as a statistical concept. He was able to incorporate the notion of irreversibility into the BE. He introduced the H-function, a functional of the distribution function, which monotonically decreases in time in accordance of the BE. Finally, this made the statistical definition of the temperature possible.

After Boltzmann, the interests of scientists turned towards the BE in kinetic theory. Much effort has been devoted for solving the Boltzmann equation. On the other hand, the relationship between the kinetic and the fluid dynamic descriptions, which later operates with macroscopic quantities such as density, velocity and temperature, was not exactly clear. For example, the expression of the transport coefficients, such as the viscosity and the thermal conductivity, was missing.

First, Hilbert proposed a perturbative solution method for the Boltzmann equation. His solution method was formal. He expanded the distribution function and the macroscopic quantities into power series of a small parameter related to the Knudsen number. The Knudsen number is the ratio of the mean free path and the relevant macroscopic size of the physical system. He obtained a series of equations, but the transport coefficients could not

be deduced. Although the method remained formal, it was the first attempt to solving the BE and inspired several scientists in the future. Following Hilbert, Chapman and Enskog proposed another expansion technique, which is now generally referred as the Chapman-Enskog method [15]. On the contrary of Hilbert's approach, only the distribution function is expanded in a series of the Knudsen number. In this way, it was possible to obtain an approximated solution of the BE, which consists of the spatial derivatives of the macroscopic quantities. However, the method is only applicable in the low Knudsen number, hydrodynamic limit. With using this approach, the transport coefficients can be calculated. Another approximated solution method was suggested by Grad [24]. He expanded the distribution function in the microscopic velocity variable into special polynomials, more closely Hermite polynomials. He obtained a series of macroscopic moment equations. With the aid of the Grad approach, it is possible to obtain an approximate solution of the BE in the hydrodynamic limit.

In recent decades, the developments related to solving the BE have been fuelled by the emergence of computational science. It is impossible to solve the Boltzmann equation analytically, and solution only exists in special cases. However, there is still much interest in transport theory and BE like equations. The notion of the kinetic theory of gases and the Boltzmann equation has been extended for many kinds of applications. Solution methods for the Boltzmann equation are clearly needed. With the developments of numerical and computational techniques, this task has become achievable.

## 1.2 The Boltzmann equation

In order to describe the motion of the large number of particles in the gas, statistical considerations are taken into account. The state of the gas in a given physical point  $\boldsymbol{x}$  of the spatial coordinate system and time  $t$  can be

described by the one-particle distribution function  $f_\alpha(\mathbf{v}, \mathbf{x}, t)$ , where  $\mathbf{v}$  is the microscopic velocity vector of the particles and  $\alpha$  denotes the components of the gas. For general purposes, it is assumed that the gas is a mixture and consists of  $n_c$  components. The one-particle distribution function is defined such that

$$dN_\alpha = f_\alpha(\mathbf{v}, \mathbf{x}, t) d\mathbf{v} d\mathbf{x} \quad (1.1)$$

is the number of molecules from component  $\alpha$  in the phase element  $d\mathbf{v} d\mathbf{x}$  at time  $t$ . This description allows defining the macroscopic quantities of the gas, i.e. the number density  $n_\alpha$ , the velocity  $\mathbf{u}_\alpha$ , the pressure tensor  $p_{\alpha ab}$  and the internal energy density  $\epsilon_\alpha$  of the components

$$n_\alpha = \int f_\alpha(\mathbf{v}, \mathbf{x}, t) d\mathbf{v}, \quad (1.2)$$

$$n_\alpha \mathbf{u}_\alpha = \int \mathbf{v}_\alpha f_\alpha(\mathbf{v}, \mathbf{x}, t) d\mathbf{v}, \quad (1.3)$$

$$p_{\alpha ab} = m_\alpha \int (v_a - u_{\alpha a})(v_b - u_{\alpha b}) f_\alpha(\mathbf{v}, \mathbf{x}, t) d\mathbf{v}, \quad (1.4)$$

$$\epsilon_\alpha = m_\alpha \int \frac{(v - u_\alpha)^2}{2} f_\alpha(\mathbf{v}, \mathbf{x}, t) d\mathbf{v}. \quad (1.5)$$

The pressure exerted by component  $\alpha$  is obtained from the trace of the pressure tensor

$$P_\alpha = \frac{1}{3} \sum_{a=1}^3 p_{\alpha aa}. \quad (1.6)$$

The total density  $n$  and the total pressure  $P$  are the sums of the component quantities  $n = \sum_{\alpha=1}^{n_c} n_\alpha$ ,  $P = \sum_{\alpha=1}^{n_c} P_\alpha$  and connected to each other by  $P = nkT$ , where  $k$  is the Boltzmann constant and  $T$  is the temperature. As it follows from the above definitions, the internal energy density is related to pressure such that

$$\epsilon_\alpha = \frac{3}{2} P_\alpha. \quad (1.7)$$

In order to describe the dynamics of the gas, the time evolution of the distribution function in the considered spatial domain should be known. Hence, a transport equation for the distribution function, which accounts for its spatial and temporal variations, is needed. The change of the distribution function is caused by two factors: particle movement and collision.

Without molecular collisions, the transport equation of the distribution function takes the following form

$$\frac{\partial f_\alpha}{\partial t} + v_a \frac{\partial f_\alpha}{\partial x_a} + a_b \frac{\partial f_\alpha}{\partial v_b} = 0, \quad (1.8)$$

where  $\mathbf{a}$  is an optional external force per unit mass. Automatic summation is applied for the repeated coordinate indices in the thesis if it is not stated on the contrary. The external force rarely appears in rarefied gas dynamics; hence, it is neglected in the future. This equation describes the free motion of the molecules obeying the laws of mechanics. It is often referred as the collision-less Boltzmann equation. The first two terms on the left hand side of Eq. (1.8) characterize the advection term of the BE.

In order to handle the effect of the molecular collisions, Eq. (1.8) is supplemented with a collision term. The number of molecules which depart from and arrive to the  $d\mathbf{v}d\mathbf{x}$  phase element between time  $t$  and  $t + dt$  is counted. These molecules represent the gain and loss terms in the Boltzmann equation. In this way, the governing equation can be written by

$$\frac{\partial f_\alpha}{\partial t} + v_a \frac{\partial f_\alpha}{\partial x_a} + a_b \frac{\partial f_\alpha}{\partial v_b} = I_{IN} - I_{OUT}, \quad (1.9)$$

where  $I_{IN}$  and  $I_{OUT}$  are the above mentioned gain and loss terms, respectively. In order to find the expressions of  $I_{IN}$  and  $I_{OUT}$ , the details of the molecular collision process are needed. In the kinetic theory of gases, it is assumed that the collision process is two-body, which follows from the relatively rare atmosphere of the gas phase. This is one of the important assumptions of the Boltzmann equation.

The collision between two particles can be described by scattering theory, which defines the differential collision cross section  $\sigma(\theta)$ , a basic quantity of the collision process. The essence of the cross section is described as follows. Suppose that there is a molecular ray consisting of a large number of particles, with intensity  $I$ . The number of particles  $dN$  crossing a surface element  $dA$  perpendicular to the ray in time interval  $dt$  is  $dN = IdAdt$ . By considering a scattering ray with intensity  $I$  on a potential, the number of molecules scattering into the spherical angle element  $d\Omega$  around the scattering angle  $\theta$  in time interval  $dt$  is given by

$$dN = I\sigma(\theta)d\Omega dt. \quad (1.10)$$

As it can be seen, the number of scattered particles is proportional the spherical angle element and the differential cross section. The total collision cross section  $\sigma_T$ , which accounts for the total number of collisions, is also introduced by

$$\sigma_T = 2\pi \int \sigma(\theta) \sin(\theta) d\theta, \quad (1.11)$$

where the relationship  $d\Omega = 2\pi \sin(\theta)d\theta$  has been used. The differential collision cross section can be calculated for particular interactions, such as power law, Lennard-Jones or other model interactions. One of the often used collision models is the hard-sphere interaction, of which differential cross section is written by

$$\sigma_{\alpha\beta}(\theta) = \left( \frac{d_\alpha + d_\beta}{2} \right)^2, \quad (1.12)$$

where  $d_\alpha, d_\beta$  are the diameters of the colliding molecules for components  $\alpha, \beta$ . These diameters may not be equal for mixtures. As it can be seen, the hard-sphere differential collision cross section is independent of the scattering angle. This collision process is isotropic.

Now, the Boltzmann equation is discussed. It is supposed that the molecules have velocity  $\mathbf{v}'_1, \mathbf{v}'_2$  before collision and  $\mathbf{v}_1, \mathbf{v}_2$  after collision. In

order to evaluate the gain and loss terms in the BE, Boltzmann introduced the key idea, the so-called molecular chaos assumption, which supposes that the number of colliding molecules is proportional to the two distribution functions  $f_\alpha(\mathbf{v}'_1)$  and  $f_\beta(\mathbf{v}'_2)$ . The molecular chaos assumption rests on the condition that the gas is rarefied, the collisions are two-body and there is no correlation between the particles. Following this idea, the gain term can be expressed as

$$I_{IN} = \sum_{\beta=1}^{n_c} \iint \sigma_{\alpha\beta}(\theta) |\mathbf{v}'_1 - \mathbf{v}'_2| f_\alpha(\mathbf{v}'_1) f_\beta(\mathbf{v}'_2) d\Omega d\mathbf{v}_2, \quad (1.13)$$

where the integration goes over all possible post-collisional velocity  $\mathbf{v}_2$  and spherical scattering angle  $\Omega$ . The loss term can be obtained in a similar fashion

$$I_{OUT} = - \sum_{\beta=1}^{n_c} \iint \sigma_{\alpha\beta}(\theta) |\mathbf{v}_1 - \mathbf{v}_2| f_\alpha(\mathbf{v}_1) f_\beta(\mathbf{v}_2) d\Omega d\mathbf{v}_2. \quad (1.14)$$

These two integrals can be cast into a common form, because the relative velocities,  $|\mathbf{v}'_1 - \mathbf{v}'_2|$  and  $|\mathbf{v}_1 - \mathbf{v}_2|$ , before and after collisions are the same. Following Eq. (1.9), the Boltzmann equation can be obtained by

$$\frac{\partial f_\alpha(\mathbf{v})}{\partial t} + v_a \frac{\partial f_\alpha(\mathbf{v})}{\partial x_a} = \sum_{\beta=1}^{n_c} \iint \sigma_{\alpha\beta}(\theta) |\mathbf{v} - \mathbf{v}_2| [f_\alpha(\mathbf{v}'_1) f_\beta(\mathbf{v}'_2) - f_\alpha(\mathbf{v}) f_\beta(\mathbf{v}_2)] d\Omega d\mathbf{v}_2. \quad (1.15)$$

Finally, it is noted that the velocities after and before the collisions are related via the collision process. The pre-collisional velocities can be completely determined from  $\mathbf{v}, \mathbf{v}_2$  and  $\Omega$ , as dictated by the energy and momentum conservations. In fact, only the orientation of the relative velocity changes during the collision. The Boltzmann equation may be rewritten into the

following form

$$\frac{\partial f_\alpha}{\partial t} + v_a \frac{\partial f_\alpha}{\partial x_a} = \sum_{\beta=1}^{n_c} \iint B_{\alpha\beta}(\theta, V) [f_\alpha(\mathbf{v}'_1) f_\beta(\mathbf{v}'_2) - f_\alpha(\mathbf{v}) f_\beta(\mathbf{v}_2)] d\Omega d\mathbf{v}_2. \quad (1.16)$$

where  $B_{\alpha\beta}(\theta, V) = \sigma_{\alpha\beta}(\theta)V$  is a function and  $V = |\mathbf{v} - \mathbf{v}_2|$  is the relative velocity.

### 1.2.1 Collision invariants

There are several important properties of the Boltzmann equation. One of these is the so-called collision invariants, which is the direct evidence of the rules of the conservation of the collision process. In the following, only single component gases are considered and the component indices are omitted.

The right hand side of the Boltzmann equation contains the bilinear expression

$$Q(f, f) = \iint B(\theta, V) [f(\mathbf{v}'_1) f(\mathbf{v}'_2) - f(\mathbf{v}) f(\mathbf{v}_2)] d\Omega d\mathbf{v}_2. \quad (1.17)$$

This is usually called as the collision term or the collision integral of the Boltzmann equation. The velocity moments of the collision term have great importance. These moments are defined by

$$\int \Psi(\mathbf{v}) Q(f, f) d\mathbf{v} = \frac{1}{4} \iiint B(\theta, V) [\Psi(\mathbf{v}) + \Psi(\mathbf{v}_2) - \Psi(\mathbf{v}'_1) - \Psi(\mathbf{v}'_2)] \times [f(\mathbf{v}'_1) f(\mathbf{v}'_2) - f(\mathbf{v}) f(\mathbf{v}_2)] d\Omega d\mathbf{v}_2 d\mathbf{v}, \quad (1.18)$$

where  $\Psi(\mathbf{v})$  is an arbitrary polynomial of the velocity variable. It can be shown that the moments are zero if and only if, see e.g. Cercignani [13],

$$\Psi(\mathbf{v}) + \Psi(\mathbf{v}_2) - \Psi(\mathbf{v}'_1) - \Psi(\mathbf{v}'_2) = 0. \quad (1.19)$$

The functions satisfying this equation are usually called the collision invariants. In fact, the collision invariants can be expressed as

$$\Psi(\mathbf{v}) = a + \mathbf{b}\mathbf{v} + c\mathbf{v}^2, \quad (1.20)$$

where  $a$ ,  $\mathbf{b}$  and  $c$  are arbitrary scalar, vector and scalar, respectively.

The expression of the collision invariants follows from the particle, momenta and energy conservation of the collision process. The collision invariants have an important role in deriving fluid dynamic, macroscopic equations from the BE.

For mixtures, the total particle, momenta and energy are the conserved quantities, and there can be exchange of momenta and energy between the components. If chemical reaction is involved, there is also exchange between the particle numbers.

### 1.2.2 H-theorem

There is a clear phenomenological evidence that a closed but perturbed gaseous system evolves towards an equilibrium state. The irreversible nature of the gas is mathematically manifested by the H-theorem introduced by Boltzmann. For a single component gas, the H-function of the distribution function is defined according to

$$H(f) = \int f \log(f) d\mathbf{v}. \quad (1.21)$$

By using the Boltzmann equation, it can be shown that this function monotonically decreases in time  $dH(t)/dt \leq 0$  [13]. It reaches its minimum in the equilibrium state. The corresponding equilibrium distribution function can be parametrized by the local macroscopic quantities of the gas, the density  $n$ , the gas velocity  $\mathbf{u}$  and the temperature  $T$  such that

$$f^0(\mathbf{v}) = n \left( \frac{2\pi kT}{m} \right)^{-3/2} \exp \left( -\frac{m(\mathbf{v} - \mathbf{u})^2}{2kT} \right). \quad (1.22)$$

By using the H-function, the entropy is defined according to  $S = -NkH(f)$ , where  $N$  is the total number of molecules. The irreversibility of the gas can also be characterized by the relation  $dS(t)/dt \geq 0$ .

### 1.2.3 Linearized Boltzmann equation

If the gas is not far from absolute equilibrium, the Boltzmann equation can be linearized. In this situation, the departure of the macroscopic quantities from absolute values are small. A typical example can be slow flows, where the macroscopic gas velocity can be neglected in comparison with the characteristic microscopic velocity  $u_\alpha \ll \sqrt{2kT/m_\alpha}$ .

By linearizing around absolute equilibrium, the distribution function can be written by

$$f_\alpha(\mathbf{v}, \mathbf{x}, t) = f_\alpha^0(\mathbf{v}) [1 + h_\alpha(\mathbf{v}, \mathbf{x}, t)], \quad (1.23)$$

where  $h_\alpha(\mathbf{v})$  is the perturbation function and the equilibrium distribution is given by

$$f_\alpha^0(\mathbf{v}) = n_{0\alpha} \left( \frac{2\pi kT_0}{m_\alpha} \right)^{-3/2} \exp \left( -\frac{m_\alpha v_\alpha^2}{2kT_0} \right) \quad (1.24)$$

with  $n_{0\alpha}$  and  $T_0$  denoting the reference densities and temperature.

Using this ansatz, the Boltzmann equation may be written in the following form

$$\frac{\partial h_\alpha}{\partial t} + v_a \frac{\partial h_\alpha}{\partial x_a} = \sum_{\beta=1}^{n_c} \mathcal{L}_{\alpha\beta}, \quad (1.25)$$

where  $\mathcal{L}_{\alpha\beta}$  is the linearized collision term. Its particular form of the collision term depends on the molecular interactions.

Finally, it is noted that it is also possible to linearize the Boltzmann equation around local equilibrium. This is sometimes used in rarefied gas dynamics, when the flow is driven by the gradients of the macroscopic quantities, for example the density or the concentration. In this case, the form of the linearized Boltzmann equation is the same as above, but driving forces appear in the equation.

## 1.2.4 Model collision operators

The Boltzmann collision integral has a complex mathematical structure, which may be simplified by using a suitable collision model. However, the collision integral can still be more simplified by introducing relaxation approximations. In this case, the collision operator contains an equilibrium function, toward which the system evolves. In principle, this advocates irreversibility in a simplified manner.

An often used collision term is the Bhatnagar-Gross-Krook (BGK) single relaxation time approximation [7]. In this case, the collision term in the BE for a single gas is represented by

$$Q(f, f) = -\frac{1}{\tau} [f(\mathbf{v}, \mathbf{x}, t) - f^0(\mathbf{v}, \mathbf{x}, t)], \quad (1.26)$$

where  $\tau$  is the relaxation time and  $f^0(\mathbf{v}, \mathbf{x}, t)$  is the local Maxwell distribution. The relaxation time measures the rate of the relaxation toward the equilibrium. Larger (or smaller) relaxation time results into slower (or faster) relaxation.

The BGK collision term provides relatively good results for isothermal rarefied gas flows. One shortcoming of this model is that it fixes the Prandtl number, the ratio of the viscosity and the thermal conductivity, to an unrealistic value. For thermal problems, the Shakov (S) model may be applied [61]. This can be considered as the modification of the BGK model with two relaxation times, but the second one is fixed to yield the correct Prandtl number.

Several kinetic models have been developed for replacing the Boltzmann collision operator for gaseous mixtures as well. The aim of these approaches is to provide a more simpler equation for the mixture while preserving its main properties. These models are especially useful for computational purposes because the kinetic models may be solved in a more efficient manner in this way. Since these models are closely related to the scope of the thesis, they

are discussed in detail in the chapter of the literary review.

## 1.2.5 Boundary conditions

In order to define the kinetic problem, the Boltzmann equation needs to be supplemented by boundary conditions. The boundary condition is important in rarefied gas dynamics. It can affect the overall behaviour of the rarefied flow. The flow is often bounded by solid walls. This is especially the case for flows in microsystems.

The diffuse-reflection boundary condition is often used in rarefied gas dynamics. In this case, the molecules colliding with the solid walls reflect in accordance with the local equilibrium distribution function. The method needs to be supplemented by the condition of the conservation of the particle number. It is assumed that the particles do not adsorb onto the surface. As a consequence, the flow rate of the particles toward the wall is zero. Accordingly, the diffuse-reflection boundary condition can be written by

$$f_\alpha(\mathbf{v}, \mathbf{x}_b) = f_\alpha^0(\mathbf{v}) \frac{\int_{\mathbf{v}' \cdot \mathbf{n} < 0} |\mathbf{v}'_n| f_\alpha(\mathbf{v}', \mathbf{x}_b) d\mathbf{v}'}{\int_{\mathbf{v}' \cdot \mathbf{n} < 0} |\mathbf{v}'_n| f_\alpha^0(\mathbf{v}') d\mathbf{v}'}, \quad (1.27)$$

for  $\mathbf{v} \cdot \mathbf{n} > 0$ . Here,  $\mathbf{n}$  is the wall normal vector pointing towards the interior part of the domain,  $\mathbf{x}_b$  is the wall coordinate and  $\mathbf{v}'_n$  is the normal component of the microscopic velocity. The diffuse boundary condition can be extended further by the inclusion of specularly reflecting particles. In the specular-reflection boundary condition, only the normal component of the microscopic velocity changes. The resulting diffuse-specular boundary condition can be written by

$$f_\alpha(\mathbf{v}, \mathbf{x}_b) = \sigma f_\alpha^0(\mathbf{v}) \frac{\int_{\mathbf{v}' \cdot \mathbf{n} < 0} |\mathbf{v}'_n| f_\alpha(\mathbf{v}', \mathbf{x}_b) d\mathbf{v}'}{\int_{\mathbf{v}' \cdot \mathbf{n} < 0} |\mathbf{v}'_n| f_\alpha^0(\mathbf{v}') d\mathbf{v}'} + (1 - \sigma) f_\alpha(\mathbf{v}_S, \mathbf{x}_b), \quad (1.28)$$

where  $S$  denotes the specularly reflected microscopic velocity and  $\sigma$  is the accommodation coefficient, which describes the amount of the diffusely reflected particles. Comparison between theory and experiments shows that for

several materials the diffuse boundary condition,  $\sigma = 1$ , can be considered adequate.

### 1.2.6 Fluid dynamic description

The Boltzmann equation describes an N-body weakly interacting system, where the number of molecules N is very large. This description corresponds to the kinetic level, which accounts for the molecular density in the six-dimensional phase space spanned by the microscopic and coordinate spaces. However, it is known that at the macroscopic level the fluid media can be described by much fewer, the so-called fluid dynamic quantities introduced previously. In kinetic theory, much effort has been devoted for establishing the relationship between kinetic and macroscopic descriptions for a long time. If the gas is sufficiently dense, it can be described by hydrodynamic, such as the Euler or Navier-Stokes, equations. The key issue is the reduction of the large number of variables and the establishment of the physical conditions under which the hydrodynamic description may be applicable. In the following, the relationship between the kinetic and fluid dynamic descriptions are considered for the case of single gases for demonstrative purposes.

The magnitude of the collision term of the BE can be estimated by the lost term according to

$$I_{OUT} = - \iint \sigma(\theta) |\mathbf{v} - \mathbf{v}_2| f(\mathbf{v}) f(\mathbf{v}_2) d\Omega d\mathbf{v}_2 \sim -n\sigma_T \sqrt{\frac{2kT}{m}} f(\mathbf{v}). \quad (1.29)$$

Here, the relative velocity has been estimated by the average molecular velocity. As one can see, the magnitude of the collision integral is proportional to  $n\sigma_T$ , the total value of the scattering surface per unit volume. This quantity is related to the mean-free path, which is defined as the average distance travelled by the molecule between two subsequent collision. As an example,

the mean-free path for a hard-sphere gas can be written as

$$\lambda_{HS} = \frac{1}{\sqrt{2}\pi d^2 n}. \quad (1.30)$$

By using the total cross section for hard-spheres,  $\sigma_T = \pi d^2$ , the following estimate is obtained

$$I_{OUT} \sim -\frac{1}{\lambda_{HS}} \sqrt{\frac{2kT}{m}} f(\mathbf{v}). \quad (1.31)$$

By comparing this term to the left hand side of the BE, where the spatial gradients are related to the macroscopic size of the problem  $L$ , it can be deduced that the magnitude of the collision integral is  $L/\lambda$ , the inverse of the Knudsen number  $Kn = \lambda/L$ , which is a basic dimensionless similarity number in rarefied gas dynamics. The solution of the Boltzmann equation can be classified by the Knudsen number: the region  $Kn < 0.1$  is regarded as hydrodynamic, the domain  $Kn > 10$  can be considered free-molecular, while the transition region lies midway  $0.1 < Kn < 10$ .

The fluid dynamic description are valid in the small Knudsen number limit, where the mean free path is relatively small compared to the macroscopic sizes. The fluid dynamic equations can be obtained as the velocity moments of the BE. In this way, for the density  $n$  and the momenta  $n\mathbf{u}$ , the following equations can be obtained

$$\frac{\partial n}{\partial t} + \frac{\partial nu_a}{\partial x_a} = 0, \quad (1.32)$$

$$\frac{\partial(nu_a)}{\partial t} + \frac{\partial(nu_a u_b)}{\partial x_b} + \frac{1}{m} \frac{\partial p_{ab}}{\partial x_b} = 0, \quad (1.33)$$

These equations are not closed because of the appearance of the pressure tensor, as a higher moment, in the second equation. In order to obtain a closed form for the equations, a closure relation is needed for the pressure tensor.

The expression of the pressure can be obtained from the Chapman-Enskog expansion of the distribution function in terms of the Knudsen number [15],

[75]. In the zero-order approximation, the solution of the BE is just the local Maxwellian equilibrium, which yields the pressure tensor for the Euler fluid such that

$$p_{ab} = P\delta_{ab}, \quad (1.34)$$

where  $\delta_{ab}$  is the unit matrix. In the first-order approximation, there is an additional contribution to the local Maxwell distribution, which results in the extension of the pressure

$$p_{ab} = P\delta_{ab} + \sigma_{ab}, \quad (1.35)$$

where the second term is called as the stress tensor and given by

$$\sigma_{ab} = \mu \left( \frac{\partial u_a}{\partial x_b} + \frac{\partial u_b}{\partial x_a} - \frac{2\delta_{ab}}{3} \sum_{c=1}^3 \frac{\partial u_c}{\partial x_c} \right) \quad (1.36)$$

with  $\mu$  denoting the dynamic viscosity of the gas.

### 1.3 Characteristics of gaseous micro-flows

Over the last decades, a new field of study, the so-called gaseous micro-flows (or micro-gas flows), has been emerged in the scientific community and engineering applications. Micro-flows refer to the gas flow in small micron-size objects. This field has attracted huge attention because of its engineering and technological importance. Gaseous flows in micron-size devices can be found in almost everywhere in technological applications, i.e. micro-electromechanical devices (MEMS), pressure gauges, micro-sensors, air-bearings or micro-actuators. Generally speaking, the emergence of micro-flows has been stimulated by the increasing miniaturization in technology. Devices in this way may operate with less consumption and more effectively than macroscopic ones.

Gaseous flows at the micro-scale show special physical behaviours, which are not found in the usual continuum hydrodynamics. Even if the micro-device operates with atmospheric pressure, the small size of the device causes large mean-free path object size ratio. As a result, the flow can not be considered continuum. For the proper description of micro-flows, kinetic approaches should be applied. In order to characterize the flow in the micro-device, three important similarity numbers of hydrodynamics can be introduced. These are the Knudsen  $Kn$ , Reynolds  $Re$  and Mach  $Ma$  numbers. The Knudsen number, as it has already been mentioned, is the ratio of the mean free path  $\lambda$  and the characteristic size of the device  $L$ , e.g. the hydrodynamic diameter of the micro-channel,

$$Kn = \frac{\lambda}{L}. \quad (1.37)$$

However, the definition of the mean free path is not unique for specific situations. There are collision models in the Boltzmann equation for which the expression of the mean-free path may not be obtainable. For example, relaxation models operate with relaxation times or collision frequencies and the meaning of the mean-free path is not included. On the other hand, in experiments, it would be difficult to define the mean-free path. In order to find a unique definition, an equivalent mean-free path and Knudsen number are usually introduced on the basis of the viscosity. In this way, different models and methods can be compared to each other. This so-called viscosity based mean-free path is defined by  $\lambda = (\mu/P)/\sqrt{2kT/m}$ . The corresponding Knudsen number is given by

$$Kn = \frac{\mu}{PL} \sqrt{\frac{2kT}{m}}, \quad (1.38)$$

The rarefaction parameter is also introduced for measuring the degree of the rarefaction. The rarefaction parameter is defined as the inverse of the

Knudsen number

$$\delta = \frac{1}{Kn}. \quad (1.39)$$

Another important dimensionless similarity number is the Reynolds number defined by

$$Re = \frac{\rho Lu}{\mu}, \quad (1.40)$$

where  $u$  stands for a characteristic flow velocity in the device. Finally, the Mach number is the ratio of the flow velocity and the characteristic molecular speed, such as the sound speed or the average molecular velocity in our case,

$$Ma = u \sqrt{\frac{m}{2kT}}. \quad (1.41)$$

It is mentioned that the similarity numbers are not independent of each other. They are connected via the relation  $Ma \sim KnRe$ .

Generally speaking, the flow in a micro-device is usually in the low-Reynolds number region. As a consequence, the flow can be considered laminar. In addition, the main flow parameter is the Knudsen number. The local rarefaction can vary in a wide range even for the same experiment. Micro-flows are usually in the low Mach number region. As a consequence, the flow is slow and linearization of the kinetic equations can be used. However, there can be situations when the Mach number is higher. An example is gaseous flow through short channels, where the flow velocity may be comparable to the average microscopic velocity.

### **Rarefaction effects in micro-flows**

If the Knudsen number is finite, the flow in the device increasingly departs from the hydrodynamic pattern. In the low Knudsen number region  $Kn < 0.1$ , the hydrodynamic description, the Navier-Stokes equations, can be used with the modification of the boundary condition at the solid walls. The first

observable rarefaction effect on the flow as the Knudsen number becomes larger is the slip or the jump of the macroscopic quantities at the walls, e.g. velocity slip. Consequently, the equations are supplemented by slip or jump boundary conditions. The low Knudsen number domain  $Kn < 0.1$  is usually called as the slip region.

With regarding the velocity slip, the first-order slip boundary condition can be expressed by

$$u_S = u_y - u_w = \alpha \frac{\partial u_y}{\partial x} \lambda, \quad (1.42)$$

where  $u_S$ ,  $u_y$  and  $u_w$  are the tangential slip velocity, the actual gas velocity at the wall and the tangential wall velocity, respectively. The coordinates  $x, y$  are along the normal and tangential directions of the wall. In addition,  $\alpha$  is the first-order slip coefficient, which has the value of  $\alpha \sim 1$  for the diffuse reflection boundary condition. In fact, the first-order slip coefficients can be calculated by solving the Boltzmann equation for a given model and gas-surface interaction [78], [69], [65] or measured [3], [18], [19], [5]. The calculated value of the coefficient depends on the collision model. The first-order slip boundary condition can be extended to higher Knudsen numbers. This new boundary condition is referred as the second-order slip model. The second-order slip boundary condition can be written by

$$u_S = \alpha \frac{\partial u_y}{\partial x} \lambda + \beta \frac{\partial^2 u_y}{\partial x^2} \lambda^2. \quad (1.43)$$

Here,  $\beta$  is the second-order slip coefficient, of which value can also be calculated or measured experimentally [16], [44]. The second-order slip boundary condition can be used approximately up to the Knudsen number  $Kn = 0.2 - 0.3$  to predict the flow rate.

By considering a pressure driven gaseous flow in a micro-channel, the flow rate exhibits the so-called Knudsen-minimum phenomenon. This means that the flow rate has a minimum as a function of the Knudsen number in

the transition region. It is mentioned that the Knudsen minimum is a true rarefaction effect. In the framework of the Navier-Stokes equation, neither the no-slip assumption nor the first-order slip boundary condition is able to capture this effect. Just the second-order slip boundary condition can describe qualitatively the Knudsen minimum. Of course, the kinetic description captures well the effect. In addition to the Knudsen minimum, there is a non-zero heat flow for pressure driven flows. This behaviour is completely missing in macroscopic flows, but appears for rarefied gases.

The slip boundary condition is applied for the temperature field as well. In that case, the boundary condition is referred as the temperature jump condition, where the normal gradient of the temperature causes a jump on the wall [65]. For thermal problems, there is another rarefaction effect, the thermal creep or thermal slip. In this situation, the tangential temperature gradient results into a slip velocity near the wall. The flow is directed from the colder place to the hotter one. This behaviour is used for the so-called Knudsen compressors. The thermal slip has been solved numerically in Refs. [70], [75], [65].

There are also rarefaction effects in gaseous mixtures. In addition to the above mentioned effects, there is the so-called diffusion slip, which accounts for a tangential velocity slip if there is a concentration gradient in the tangential direction near the wall. The diffusion slip velocity can be written by

$$u_{DS} = \sigma_C \frac{\mu}{\rho C} \frac{\partial C}{\partial y}, \quad (1.44)$$

where  $\sigma_C$  is the diffusion slip coefficient,  $\rho$  is the mass density of the gas and  $C$  is the concentration. The coordinate  $y$  is along the tangential direction related to the wall. In accordance with the velocity slip, there is a non-zero average mixture velocity if the flow is through a channel. This is an interesting rarefaction effect, which is not described by hydrodynamic equations. The diffusion slip coefficient has also been calculated for kinetic models [71],

[78], [65].

## 1.4 Objectives and novelty of the thesis

The goal of the thesis is the computational and experimental study of flows of gaseous mixtures in microsystems. The study refers to flows through long and short channels. For long channels, the speed of the flow is relatively small compared to the characteristic molecular speed; as a result, the linearized description can be applied. In the present work, the McCormack kinetic model is utilized and solved for specific channel geometries. For short channels, the full non-linear Boltzmann equation with the assumption of hard-sphere molecules is solved. The work includes the specific development of the computational methodology for the solution of the problems. For long channels, the discrete velocity methodology in an accelerated version, while for short channels, the direct simulations Monte Carlo method is developed. In the experimental part of the thesis, the flow rate through various long microchannels are measured by using the constant volume method. The experimental results are compared to the kinetic calculation. By the aid of the comparative study, the validity of the theoretical approaches used for computation can be tested and evaluated.

The novelty of the thesis is to provide detailed study of the flows of gaseous mixtures in microchannels. While the properties of single component gases are already well-known in the literature, there are relatively few works on gas mixtures. For mixtures, the flow is affected by the gas separation, e.g. the different components tend to flow through the system with different speeds. This phenomenon is yet not explored well in the literature. Throughout this study, its effect is experimentally verified. In addition, new computational methodologies are presented in the thesis. A synthetic type accelerated discrete velocity method has been developed for triangular grids

for efficient calculation. The improved computational performance is verified by a stability analysis. In the present work, the stability analysis is extended for discrete kinetic equations. With regard to the direct simulation Monte Carlo, new, upgraded codes have been developed for gaseous mixtures, which extends the state-of-art of probabilistic calculation of rarefied flows.

# Chapter 2

## Literature survey on rarefied and micro-gas flows

### 2.1 Kinetic description of gaseous mixtures

In the numerical part of the thesis, the McCormack kinetic model is used for describing the flow. For this reason, it is useful to consider a literature review on kinetic modelling of gaseous mixtures. In the scientific community, much effort has been made to develop kinetic models for rarefied gases. The goal of these models is their simplicity compared to the original Boltzmann equation, while their physical properties are similar to the BE. Because of the simpler mathematical structure of the kinetic models, their solution can be obtained easier. This especially becomes advantageous in numerical calculations allowed by modern computers. For binary mixtures, several kinetic models have been proposed. Here, the Sirovich, Hamel, Morse, McCormack models and the collision operator of Garzo et al., Andries et al. and Kosuge are discussed.

### 2.1.1 Sirovich model

The Sirovich model [79] was established in 1962. This model was one of the first approaches for gaseous mixtures. The kinetic equation can be written by

$$\begin{aligned} \partial_t F + \xi_a \partial_{x_a} F + \Phi_a \partial_{\xi_a} F = & \Gamma(F_0 - F) - \frac{\mu F_0}{NkT} (U_a - u_a) C_a - \\ & \frac{3\nu F_0}{2NkT} \left( \frac{C^2}{2RT} - 1 \right) (T - \tau) + \\ & \frac{\mu_M F_0}{NkT} (U - u)^2 \left( \frac{C^2}{2RT} - 1 \right), \end{aligned} \quad (2.1)$$

$$\begin{aligned} \partial_t f + \xi_a \partial_{x_a} f + \Phi_a \partial_{\xi_a} f = & \gamma(f_0 - f) - \frac{\mu f_0}{nk\tau} (u_a - U_a) c_a - \\ & \frac{3\nu f_0}{2nk\tau} \left( \frac{c^2}{2r\tau} - 1 \right) (\tau - T) + \\ & \frac{\mu_m f_0}{nk\tau} (U - u)^2 \left( \frac{c^2}{2r\tau} - 1 \right). \end{aligned} \quad (2.2)$$

Here,  $F, f, F_0, f_0, \xi_a, \Phi_a, \phi_a, U_a, u_a, C_a, c_a, T, \tau, N, n, k, M, m, R$  and  $r$  are the distribution functions, the equilibrium distribution functions, the molecular velocity, the external forces, the gas velocities, the peculiar velocities, the temperatures, the number densities, the Boltzmann constant, the masses and the gas constants. The capitalized and small letters refer to the same quantities but for the first and second components, respectively. In addition,

$$\mu_M = \frac{\mu MNmn}{\rho} \left[ \frac{1}{MN} - \frac{\epsilon(n - N)}{nN(m + M)} \right], \quad (2.3)$$

$$\mu_m = \frac{\mu MNmn}{\rho} \left[ \frac{1}{mn} - \frac{\epsilon(N - n)}{nN(m + M)} \right]. \quad (2.4)$$

In these equations,  $\Gamma, \gamma, \mu, \nu, \epsilon$  are the collision frequencies and  $\rho$  is the total mass density. The idea of Sirovich came from the Bhatnagar-Gross-Krook single relaxation time approximation. In the BGK model, the collision operator is replaced by a simple relaxation term, which ensures evolution toward the local equilibrium. The BGK operator itself is well-suited for single gases.

The model of Sirovich is built on the idea of a three stage relaxation. First, the lighter component relaxes to its equilibrium state, next the heavier component approaches its equilibrium state and finally the mixture as a whole relaxes toward to global mixture equilibrium. In this framework, the BGK operator is extended with additional terms providing the correct transport equations for the mixture. There are four terms on the right hand sides of the transport equations. The first one describes relaxation toward the component equilibrium like in the case of the BGK operator. The second and third terms describe the coupling between the species with regard to the macroscopic velocities and the temperatures of the components. The final term covers some additional interaction between the components. In the Sirovich approach, the conservation property for the mass, the momenta and the energy is automatically satisfied. Macroscopic transport equations for the mixture momenta, the energy and the diffusion are derived. The transport coefficients, the viscosity, the thermal conductivity and the diffusion coefficient can be obtained from the model. One apparent shortcoming of the model is the lack of thermal diffusion, but it may be included into the formalism. Sirovich provided a formal derivation of the approach from the Boltzmann equation by assuming Maxwell molecules. Finally, it is mentioned that the model describes small departure from the global mixture equilibrium state. As a consequence, it can be used when the velocity and the temperature differences are small between the components. The Sirovich model has inspired the development of other kinetic models, but it has rarely been used in rarefied gas calculations. The collision integrals of the Sirovich model were investigated by Walker et al. [103]. They found that the integrals are generally not those given by the Boltzmann equation. On the basis of the approach, a lattice Boltzmann method has been established [43]. However, that approach has been improved by other models later.

### 2.1.2 Hamel-Morse model

Another model, the Hamel model [28], appeared in 1965. It can also be viewed as a modification of the BGK operator. The model reads such that

$$\partial_t f_\alpha + v_{\alpha a} \partial_{x_a} f_\alpha = J_\alpha, \quad (2.5)$$

where

$$J_\alpha = n_\alpha \kappa_{\alpha\alpha} \left[ -f_\alpha + n_{\alpha\alpha} \left( \frac{m_\alpha}{2\pi k T_{\alpha\alpha}} \right)^{1/2} \exp \left( -\frac{m_\alpha (v_\alpha - V_{\alpha\alpha})^2}{2k T_{\alpha\alpha}} \right) \right] + n_\beta \kappa_{\alpha\beta} \left[ -f_\alpha + n_{\alpha\beta} \left( \frac{m_\alpha}{2\pi k T_{\alpha\beta}} \right)^{1/2} \exp \left( -\frac{m_\alpha (v_\alpha - V_{\alpha\beta})^2}{2k T_{\alpha\beta}} \right) \right]. \quad (2.6)$$

In the above equations,  $f_\alpha$ ,  $v_{\alpha a}$ ,  $J_\alpha$  are the distribution function, the molecular velocity and the collision term for component  $\alpha$ . In addition,  $n_{\alpha\alpha} = n_{\alpha\beta} = n_\alpha$ ,  $V_{\alpha\alpha} = V_\alpha$ ,  $T_{\alpha\alpha} = T_\alpha$ , where the quantities on the right hand sides are the densities, the velocities and the temperatures of the components, and

$$T_{\alpha\beta} = T_\alpha + \mu_\alpha \mu_\beta \left[ 2(T_\beta - T_\alpha) + (V_\alpha - V_\beta)^2 \frac{\mu_\beta m_0}{3k} \right], \\ \kappa_{\alpha\alpha} = 2.906(p_{\alpha\alpha} m_\alpha)^{1/2}, \quad \kappa_{\alpha\beta} = 2.906(p_{\alpha\beta} m_0)^{1/2}. \quad (2.7)$$

Other quantities,  $\mu_\alpha$ ,  $m_\alpha$ ,  $m_0$ ,  $k$ ,  $p_{\alpha\alpha}$  and  $p_{\alpha\beta}$ , are the reduced mass, the mass of the components, the total mass of the two components, the Boltzmann constant and the coefficients in the intermolecular force law. As it can be seen, in the method, there are two coupled relaxation terms on the right hand side of the balance equation of the distribution function. The idea of this approach is to distinguish between self relaxation and relaxation between the components. This is similar to the Sirovich method, but in the Hamel model all terms express relaxation, and linearization is not used. In the two BGK like terms of the Hamel model, there are densities, velocities and temperatures as parameters. In addition, the four relaxation times are additional unknown quantities. The definition of these quantities are based on the fulfillment of the conservation of mass, momenta and energy for the mixture

and some additional constraints for recovery the transport of momenta and energy between the components. These transport relations are chosen as dictated by the Maxwell molecule interaction. By using the constraints, the unknown densities, velocities, temperatures and the collision frequencies are determined in the method. Hamel derived the expression of the viscosity, the thermal conductivity and the diffusion coefficient from the method. The method gives the correct value of the diffusion coefficient similarly to the Chapman-Enskog (CE) theory. The viscosity is only in qualitative agreement with the CE theory. The Prandtl number is found to be unity in the method. Hamel derived the linearized versions of the method. Two types of linearization is considered. One is a linearization around the absolute equilibrium, and another one is a linearization in the mass ratio. The Hamel model has the advantageous feature that it goes beyond the Sirovich model, which can be used for small departure from the global mixture equilibrium. The approach of Hamel can be used for mixtures with disparate masses. The Hamel model has been used for rarefied gas calculation. The Poiseuille flow [12], Couette flow [97] of binary mixtures have been calculated on the basis of the model. In addition, lattice Boltzmann methods have been constructed on the basis of the Hamel model [83].

The approach of Morse [50] was published in 1964. This work is the same as the Hamel model so that the formulation is omitted. Practically, Morse did a similar deviation as Hamel. However, the paper of Hamel was submitted earlier as the Morse's one. In addition, the Hamel model already appeared in his PhD thesis. The Morse's approach starts with the non-linear BGK operator for binary mixtures. The relaxation terms contain four equilibrium distribution function with local densities, velocities and temperatures. In addition, there are four relaxation times, each one attached to each term. By using the constraints of the conservation of the mass, the momentum and the energy, the number of independent parameters in the operator can be

reduced. The approach applies the constraint for the exchange of momenta and energy between the particles as defined by the Maxwell molecule system. This constraint further reduces the number of unknown parameters, and finally the operator results in the one provided by Hamel. It is stated that Hamel applied the cut-off of the Maxwell potential, but this is explicitly not needed in the work of Morse.

### 2.1.3 McCormack model

A different approach was established by McCormack [45] in 1973. The McCormack model belongs to linearized kinetic theory. The goal of the model is to capture all transport coefficients appearing in gaseous mixtures. The linearized kinetic model is given by

$$\partial_t \Phi_\alpha + v_a \partial_{x_a} \Phi_\alpha = \sum_\beta L_{\alpha\beta}. \quad (2.8)$$

Here,  $\Phi_\alpha$ ,  $v_a$  and  $L_{\alpha\beta}$  are the perturbation function of the species, the molecular velocity and the collision term written by

$$\begin{aligned} L_{\alpha\beta}(c_{\alpha i}) = & -\gamma_{\alpha\beta} \Phi_\alpha + \gamma_{\alpha\beta} \nu_\alpha + \\ & 2 \left\{ \gamma_{\alpha\beta} u_{\alpha i} - \left[ u_{\alpha i} - \left( \frac{m_\alpha}{m_\beta} \right)^{1/2} u_{\beta i} \right] \nu_{\alpha\beta}^{(1)} - \left[ q_{\alpha i} - \left( \frac{m_\alpha}{m_\beta} \right)^{3/2} q_{\beta i} \right] \nu_{\alpha\beta}^{(2)} \right\} c_{\alpha i} + \\ & \left[ \gamma_{\alpha\beta} T_\alpha - 2 \frac{m_0}{m_\beta} (T_\alpha - T_\beta) \nu_{\alpha\beta}^{(1)} \right] \left( c_\alpha^2 - \frac{3}{2} \right) + \\ & 2 [(\gamma_{\alpha\beta} - \nu_{\alpha\beta}^{(3)}) P_{\alpha ij} + P_{\beta ij} \nu_{\alpha\beta}^{(4)}] c_{\alpha i} c_{\alpha j} + \\ & \frac{8}{5} \left\{ (\gamma_{\alpha\beta} - \nu_{\alpha\beta}^{(5)}) q_{\alpha i} + q_{\beta i} \nu_{\alpha\beta}^{(6)} - \frac{5}{8} \left[ u_{\alpha i} - \left( \frac{m_\alpha}{m_\beta} \right)^{1/2} u_{\beta i} \right] \nu_{\alpha\beta}^{(2)} \right\} \times \\ & c_{\alpha i} \left( c_\alpha^2 - \frac{5}{2} \right). \end{aligned} \quad (2.9)$$

In this formalism,  $c_{\alpha i}$  is the dimensionless molecular velocity defined by  $c_{\alpha i} = v_i (m_\alpha / 2kT)^{1/2}$  with  $m_\alpha, k, T$  denoting the mass of the components,

the Boltzmann constant and the temperature. In addition,  $\nu_{\alpha\beta}^{(k)}, \gamma_{\alpha\beta}, \nu_{\alpha}, u_{\alpha i}, T_{\alpha}, P_{\alpha ij}, q_{\alpha i}$  and  $m_0$  are the two types of collision frequencies, the densities, the velocities, the temperatures, the pressures, the heat fluxes and the reduced mass. The kinetic model is formulated in terms of the departure from equilibrium. McCormack developed a complete procedure to derive the method. The idea is to divide the collision term into loss and gain terms. The expression of the loss term is similar to the linearized framework, that is proportional to the distribution function with a proportionality constant, a collisional frequency. The gain term consists of the polynomial expression of the molecular velocity multiplied with some weights related to the moments of the distribution function. Particularly, the McCormack model is a general third-order polynomial model in the microscopic velocity variable. The polynomials are the eigenfunctions of the Maxwell molecule system. But, the overall model can be used for arbitrary interaction potential. The unknown coefficients in the polynomial expansion is determined by a constraints for the collisional moments. In this way, the hydrodynamic behavior of the approach is exactly the same as for the true Boltzmann equation. The same collisional moments are used as in the CE theory. They depend on the so-called omega-integrals, which can be computed for an arbitrary interaction potential. The construction of the model is relatively simple. The useful feature of the approach is that it generally describes all transport processes in gaseous mixtures well. The method is extended for polyatomic gases as well. In that case, the same polynomial procedure is applied as for the mixture model. Another property of the McCormack model is that the H-theorem can exactly be proved for that. During the last years, the McCormack model has been used to model and calculate binary rarefied gas flows. Although the model is relatively simple, it has been found that it is well-suited for the description of gas mixtures in a wide-range of the rarefaction. Recently, a large class of flows of gaseous mixtures in channels [53], [54], [68],[66], [67],

[77], [90], [87] or half space problems [69], [70], [71], [78] has been modeled and solved by using the McCormack model. It is emphasized again that all transport coefficients can be adjusted in the model. It is expected that this model provides the most accurate results compared to the true Boltzmann equation.

#### 2.1.4 Recent approaches

The collision operator of Garzo et al. [23] appeared in 1989. It is similar to the approaches of Sirovich and Hamel. However, the operator of Garzo et al. was developed to overcome a shortcoming of these two methods. The collision term can be used to describe mechanically identical molecules, but the model of Sirovich and Hamel can not be applied for this purpose. The goal of the Garzo et al. approach is to model self-diffusion and describe mixtures consisting of species with nearly the same masses. The model is written by

$$\partial_t f_\alpha + v_a \partial_{x_a} f_\alpha = K_{\alpha\alpha} + \sum_{\beta \neq \alpha}^n K_{\alpha\beta}, \quad (2.10)$$

where  $f_\alpha$ ,  $v_a$ ,  $K_{\alpha\alpha}$  and  $K_{\alpha\beta}$  are the distribution function for component  $\alpha$ , the molecular velocity, the self and cross collision terms. These collision terms can be written as

$$K_{\alpha\beta} = -\xi_{\alpha\beta}(f_\alpha - f_{\alpha\beta}^R), \quad (2.11)$$

where the reference distribution function is defined by

$$f_{\alpha\beta}^R = n_\alpha \left( \frac{m_\alpha}{2\pi kT} \right)^{3/2} \exp \left( -\frac{m_\alpha V^2}{2kT} \right) (1 + A_{\alpha\beta} + B_{\alpha\beta a} V_a + C_{\alpha\beta} V^2). \quad (2.12)$$

Here,  $n_\alpha$ ,  $m_\alpha$ ,  $k$ ,  $T$  and  $V_a$  are the densities, the masses, the Boltzmann constant, the temperature and the peculiar velocity of components. The un-

known coefficients are given by

$$\begin{aligned}
A_{\alpha\beta} &= -\frac{3kT}{m_\alpha}C_{\alpha\beta}, \\
B_{\alpha\beta a} &= \frac{m_\alpha}{kT}(u_{\alpha\beta a} - u_a), \\
C_{\alpha\beta} &= \frac{m_\alpha}{2kT} \left[ \frac{T_{\alpha\beta} - T}{T} + \frac{m_\alpha}{3kT}(u_{\alpha\beta} - u)^2 \right]
\end{aligned} \tag{2.13}$$

with

$$\begin{aligned}
u_{\alpha\beta a} &= \frac{m_\alpha u_{\alpha a} + m_\beta u_{\beta a}}{m_\alpha + m_\beta}, \\
T_{\alpha\beta} &= T_\alpha + \frac{2m_\alpha m_\beta}{(m_\alpha + m_\beta)^2} \left[ (T_\beta - T_\alpha) + \frac{m_\beta}{6k}(u_\alpha - u_\beta)^2 \right].
\end{aligned} \tag{2.14}$$

where  $u_{\alpha a}, T_\alpha$  are the velocities and the temperatures of the species. The construction of the model is similar to the Hammel one. It is based on the BGK operator. The collisions between the molecules are described by relaxation terms. In the relaxation terms, the distribution function evolves to a fictitious reference distribution function, which differs from the exponential form of the BGK or the Hamel models. It is a special combination of an exponential term multiplied with a polynomial expression of the molecular velocity. The unknown coefficients in the fictitious reference function are related to the macroscopic quantities. In addition, the collision frequencies are also unknown in the relaxation terms. All unknown quantities are determined under the constraints dictated by the conservation of mass, momenta, energy and the forms of the transport equations. For the latter constraint, the collisional moments defined by the Maxwell molecules are used. By adding together the kinetic equations of the separate, but mechanically identical components, the kinetic equation of the single-gas case is obtained. The viscosity, the thermal conductivity and the diffusion coefficient were derived for the model. They have a similar structure as obtained from the Boltzmann equation for Maxwell molecules. For the transport properties, the Onsager relation is found to be hold. The approach can be used to describe mixtures

consisting of components with nearly equal masses. It can be considered as a complement to previous relaxation time approaches.

Next, the approach of Andries et al. [1] is discussed. The model appeared in 2002. It is similar to the previous relaxation approaches [79], [28], [50], [23]. The kinetic model is written by

$$\partial_t f_\alpha + \xi_a \partial_{x_a} f_\alpha = \nu_\alpha [M_\alpha - f_\alpha]. \quad (2.15)$$

Here,  $f_\alpha$ ,  $\xi_a$ ,  $\nu_\alpha$  and  $M_\alpha$  are the distribution function for species  $\alpha$ , the molecular velocity, the collision frequency and the reference distribution function defined by

$$M_\alpha = n_\alpha \left( \frac{m_\alpha}{2\pi k T_\alpha} \right)^{3/2} \exp \left( -\frac{m_\alpha (\xi - v)^2}{2k T_\alpha} \right), \quad (2.16)$$

where  $n_\alpha$ ,  $m_\alpha$  are the density and the molecular mass. In addition, the velocity  $v_\alpha$  and the temperature  $T_\alpha$  are defined to recover the exchange relation of the momenta and the energy between the components. The component collision frequency is defined by

$$\nu_\alpha = \sum_{\beta=1}^n \nu_{\alpha\beta} n_\beta \quad (2.17)$$

with  $\nu_{\alpha\beta}$  denoting the collision frequencies deduced from the interaction potential. The goal of the approach is to ameliorate the shortcomings of the mentioned previous relaxation models. The following properties are satisfied: positivity of the distribution function, correct exchange coefficients, entropy inequality and indifferentiability principle. In the models of [79], [23], the positivity is not hold since they use linearization in terms of the departure from the equilibrium state. The entropy inequality was not shown for [79], [28], [50], [23]. The indifferentiability principle, i.e. the kinetic equation reduces into the single gas case with mixtures having mechanically identical particles, is covered only in the model of [23]. In the method of Andries et

al., the collision operator is built from a single relaxation term for the whole mixture. This choice can ensure the indifferentiability principle. There are fictitious quantities related to the macroscopic densities in the equilibrium distribution. All these quantities and the unknown collision frequencies are determined from the constraints of the collisional invariants and the moment transport between the components. The model also applies the Maxwell molecule system. The entropy inequality was shown to hold for the model. In addition, the macroscopic limit of the kinetic equation together with the transport coefficients was derived. To summarize, it is mentioned that the method of [1] is rather a mathematically refined version of previous relaxation approaches. The model has been used in Ref. [36] to test different approaches in practical calculations.

Finally, the model proposed by Kosuge in 2009 [36] is presented. This approach is similar to the McCormack model but non-linear. The model reads such that

$$\partial_t f_\alpha + \xi_a \partial_{x_a} f_\alpha = \sum_{\beta} J_{\beta\alpha} \quad (2.18)$$

where  $f_\alpha$ ,  $\xi_a$  and  $J_{\beta\alpha}$  are the distribution function for component  $\alpha$ , the molecular velocity and the collision operator given by

$$J_{\beta\alpha} = \left( \frac{m_\alpha}{2\pi kT} \right)^{3/2} \exp\left(-\frac{m_\alpha}{2kT}(\xi - u)^2\right) \Phi_{\beta\alpha} - K_M^{\beta\alpha} n_\beta f_\alpha, \quad (2.19)$$

where  $m_\alpha$ ,  $k$ ,  $T$ ,  $u_a$  and  $n_\beta$  are the molecular mass, the Boltzmann constant, the temperature, the mixture velocity and the component density. In addition,  $\Phi_{\beta\alpha}$  is a polynomial function defined by

$$\begin{aligned} \Phi_{\beta\alpha} = & K_M^{\beta\alpha} n_\beta n_\alpha + 2\zeta_{\alpha i} \Phi_{\beta\alpha i}^{(1)} + \left( \zeta_\alpha^2 - \frac{3}{2} \right) \Phi_{\beta\alpha}^{(2)} + \\ & \zeta_{\alpha i} \zeta_{\alpha j} \Phi_{\beta\alpha ij}^{(3)} + \frac{4}{5} \zeta_{\alpha i} \left( \zeta_\alpha^2 - \frac{5}{2} \right) \Phi_{\beta\alpha i}^{(4)} \end{aligned} \quad (2.20)$$

where  $\zeta_{\alpha i} = (m_\alpha/2kT)^{1/2}(\xi_i - u_i)$ ,  $K_M^{\beta\alpha}$ ,  $\Phi_{\beta\alpha i}^{(1)}$ ,  $\Phi_{\beta\alpha}^{(2)}$ ,  $\Phi_{\beta\alpha ij}^{(3)}$  and  $\Phi_{\beta\alpha i}^{(4)}$  are the dimensionless peculiar velocity and the coefficients in the collision term. The

collision operator in the kinetic equation is split into gain and loss terms. The gain term consists of the multiplication of a velocity polynomial and an equilibrium distribution function, while the lost term is proportional with distribution function. The unknown constants in the velocity polynomial are functions of the macroscopic quantities. The explicit expressions of the unknown functions are determined by some constraints for the collision operator. The first few moments of the operator are the same as the true Boltzmann collision operator with using the Grad distribution function, the 13 moment approximation. The model can be applied to arbitrary molecular interaction. The interaction affects the collision frequencies. The model can be used as the modification of the McCormack operator for non-linear flows. However, unlike the McCormack case, the H theorem was not proved for this model. Kosuge has used the approach in simulation of a real problem, condensation of the vapor of a gaseous mixture [36].

## **2.2 Gas microfluidics – General**

The field of microfluidics emerged in the 90s. It has attracted much attention during the forthcoming years in the scientific community. Review articles and books providing an introduction into the subject have been published. Here, we mention the review article of Ho et al. [30], the book of Karniadakis et al. [34] and the contribution of Kandlikar et al. [33].

## **2.3 Modeling of rarefied gas flows**

### **2.3.1 Extended hydrodynamics**

The description of the flow in a microsystem may be carried out by extended hydrodynamics at small Knudsen numbers. In this case, the Navier-Stokes equation is still considered valid, but an appropriate modification of the

boundary conditions is introduced to describe the slip and the jump of the macroscopic quantities. The validity and the usefulness of extended hydrodynamics have been studied by various researches [41], [40], [42]. The corresponding equations for gas flows through specific microchannels have also been solved [48], [49]. Lattice kinetic models, notably the Lattice Boltzmann method, have been developed and applied for modeling gaseous flows at finite rarefactions [81], [82], [84]. While extended hydrodynamics is valid at small or moderate rarefaction, kinetic theory is necessary for the whole spectrum of the rarefaction.

### 2.3.2 Kinetic description – Flows in long channels

For an overview of the general kinetic theory, the interested reader may refer to the books of Cercignani [13], [14] or Chapman and Cowling [15]. When the flow is through long channels, the speed of the flow is small and the linearized description can be applied. The linearized Boltzmann equation and available linearized kinetic models for both single gases and mixtures have been solved by many researchers for various flow configurations by using the discrete velocity method, which is a common tool for solving kinetic equations [2], [95], [46]. For single gases, the BGK model has been solved for rectangular [63], [98], [99], circular [99], elliptical [25], annular [10], triangular [52], [99] and trapezoidal [99] ducts. Accelerated discrete velocity schemes have been developed for single gases [98], [38] and mixtures [55]. An accelerated discrete velocity method has been developed for triangular grids [91]. The McCormack model describing gaseous mixtures has been solved for flows between two parallel plates [53], through rectangular [55], [54] and circular [68] channels, Couette flow [66] and heat flux between two plates [67]. Recently, the model has been solved for flows through triangular and trapezoidal channels [90], [89]. The analytical discrete ordinate method, which is very accurate but can be used only for one-dimensional problems, has also been applied

to solve the McCormack kinetic model for specific flow configurations [77]. The slip coefficients have also been calculated by the method [78]. Binary gas flows with the rigid-sphere interaction have been solved by the analytical discrete velocity method as well [21], [22].

### 2.3.3 Kinetic description – Flows in short channels

For flows through short channels, the speed of the flow can be in the range of the characteristic molecular speed. In this case, the full non-linear Boltzmann equation should be considered for describing the flow. The solution of the non-linear Boltzmann equation can conveniently be made by the direct simulation Monte Carlo (DSMC) method. Although the idea of the Monte Carlo technique was known previously, Bird developed and worked out the comprehensive simulation strategy, known as the DSMC, for rarefied gas flows [8]. Later, it was revealed that the DSMC solves the Boltzmann equation [102].

In the DSMC, the motion of model particles is simulated in the real geometry by splitting between free streaming and collision. The selection of particles for collision can be made by the widely used No Time Counter scheme [8]. In this approach, there is constant time step and the particle selection can be derived from the Boltzmann equation. On the contrary, the Mayorant Frequency Scheme applies random time step and selection is derived from the master kinetic equation [31]. The collisions treatment between the particles may be defined by supposing hard-sphere, variable hard-sphere [8] and variable soft-sphere interactions [37], which are the most popular approaches. Other versions of the DSMC have also appeared at a later stage [17], [9]. Recently, the DSMC has been applied for modelling pressure and concentration driven flows of gaseous mixtures between two parallel plates [85].

The flows through short channels were first examined theoretically by

Hanks and Weissberg [29]. They considered flows through circular capillaries and developed a flow rate formula in the hydrodynamic region by taking into account the slip effect at the walls. The DSMC method was used to compute supersonic free jets through orifices by Usami and Okuyama [96]. Shinagawa et al. studied the flow of rarefied gases through short tubes by using the DSMC method [76]. Experiments were also carried out in that work. Then, Lilly et al. simulated rarefied gas flow through short channels by using the DSMC method [39]. They examined the effect of the channel length on the flow. Sharipov computed the flow through an orifice by the DSMC [64]. Later, rarefied gas flow through short tubes into vacuum [100] and at arbitrary pressure ratio [101] was investigated by the DSMC method. Flows through slits into vacuum [73] and at arbitrary pressure drop [74] have also been studied by using the DSMC.

## **2.4 Experimental studies on rarefied flows**

Experimental work on gas flows through channels has almost been referred to the measurement of the flow rate. Generally, the constant volume method, the bubble-tacking method and the direct measurement of the pressure drop at constant flow rates have been applied. For low-flow rates, the constant volume method can be considered as the most appropriate.

### **2.4.1 Flows through long channels**

Previous works for long channels have mainly focused on single component gases. In early years, Bergoglio et al. measured and reported the flow rate through metal capillaries [6]. Arkilic et al. measured the mass flow rate through microchannels and determined the tangential accommodation coefficient [3]. Higher-order boundary conditions have been proposed and validated for circular and rectangular microchannels by Aubert et al. [4] and

Colin et al. [16]. The mass-flow rate was measured through circular and plane channels by Zohar et al., and the results have been compared to analytical results in the hydrodynamic limit [105]. The second-order slip coefficient was determined for shallow rectangular microchannels by Maurer et al. [44]. Ewart et al. measured the flow rate through circular and rectangular microchannels [18], [19]. Bentz et al. reported results for the viscosity, the slip and accommodation coefficients by using a spinning rotor gauge [5]. The experimental flow rates through long circular channels have been measured and compared to the numerical solution of the BGK model [99]. Recently, Pitakarnnop et al. have measured the flow rate of binary gases through microchannels [58].

#### **2.4.2 Flows through short channels**

The flow rate through short circular tubes was measured by Sreekanth in the slip and transition region [80]. Borisov et al. [11] and Porodnov et al. [59] carried out flow rate measurements for orifices. That works focused on small pressure drop, but a wide range of gas rarefaction was covered. Fujimoto et al. measured the flow rate through short tubes in a wide range of rarefaction by applying an unsteady experimental technique [20].

### **2.5 Gaseous separation**

In addition to the previous sections, an overview of the gas separation in mixtures is provided. In specific flow configurations, the components of the gas may separate due to the diffusion of the gas. This effect can be important in applications, such as composite membrans and meshes [27], [26], where the goal is the separation of different species. Another application can be gas chromatography, where the different gas components separate by flowing through capillaries.

The gaseous separation in long capillaries in the free molecular and slip regime has been discussed theoretically in Ref. [104]. Recently, the separation in long channels has been examined in the whole range of the gas rarefaction on the basis of linearized kinetic description by Sharipov and Kalempa [72],[32] and Szalmas and Valougeorgis [90]. The separation also occurs in flows through short channels. Previously, a few theoretical and numerical work has been devoted to address the separation effect in these channels. Raghuparan and Davidovits estimated the velocity profiles in free jet expansion on the basis of the Hamel model [60]. They found the evidence of the velocity difference between the components. Nanbu using the thirteen moment equations with the assumption of Maxwell molecules [51] and Mitra et al. using a two-fluid model in the viscous limit [47] investigated nozzle flow of helium-argon mixture. The difference between the axial component velocities was confirmed in both cases.

# Chapter 3

## Simulation of binary gas flows through long microchannels of triangular and trapezoidal cross sections

### 3.1 Introduction

In the present chapter, the computational investigation of flows of gaseous mixtures through long microchannels is performed. The study is based on the kinetic description of the flow; as a result, it is valid in the whole range of the gas rarefaction. The investigated model problem consists of a long channel connected to upstream and downstream reservoirs. The gas flows through the channel, driven by pressure or concentration gradients, which is practically achieved by setting the pressures and the concentrations at the inlet and the outlet of the channel. For long channels, even if the pressure difference between the inlet and outlet cross sections is finite, the speed of the flow is small compared to the characteristic molecular velocity; as a

consequence, the linearized description can be used.

The calculation of the flow through the channel is divided into two stages. In the first step, the local properties of the flow are calculated by assuming the local driving forces. The McCormack kinetic model [45] is utilized to describe the gas. Accelerated discrete velocity methods have been developed for solving the resulting kinetic equations [91], [90].

In the second step of the analysis, the global flow properties, such as the flow rate, are deduced on the basis of the local information. A flow calculator for the rarefied gas has been developed to achieve this goal [90]. It provides the flow rates and the pressure and concentration distributions along the channel. It is noted that the flow of the gaseous mixture is affected by the so-called separation phenomenon [72], [32], [90]. The different gas components have different velocities in the channel; as a result, the gas tends to separate. This can result into a non-uniform concentration distribution of the mixture along the axis of the channel. It is noted that even if the mixture is driven by the pressure difference between the inlet and the outlet of the channel, the separation phenomenon can have a significant impact on the flow. The effect of the separation on the flow is investigated in the present work.

## 3.2 Flow configuration and formulation

The flow of gaseous mixtures through long triangular and trapezoidal microchannels is calculated. These cross section shapes can be found in engineering applications. The microchannels etched by KOH in silicon wafer can have triangular and trapezoidal cross sections.

In the description of the geometry, Cartesian coordinates are used. The axis of the channel lies along the  $z'$  coordinate direction, while the cross section is located in the  $x', y'$  coordinate sheet. The characteristic length of

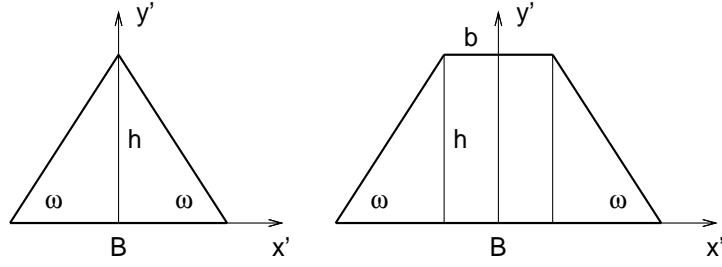


Figure 3.1: The cross sections of the triangular and the trapezoidal channels.

the problem is defined as the hydrodynamic diameter of the channel

$$D_h = \frac{4A'}{\Gamma}, \quad (3.1)$$

where  $A'$  and  $\Gamma$  denote the area and the perimeter of the cross section, respectively. Dimensionless coordinates are introduced as  $x = x'/D_h, y = y'/D_h$  and  $z = z'/D_h$ . The length of the channel is denoted by  $L$ . The condition of the long channel corresponds to  $L \gg D_h$ . The triangular and trapezoidal cross sections are presented in Figure 3.1. The geometrical shapes are characterized by the angle  $\omega$  on the base (or large base) and the ratio of the small base to the height  $b/h$ . It is noticed that the triangular cross section is recovered by the trapezoidal one by setting  $b/h = 0$ . The computational methodology developed here refers to arbitrary  $\omega$ . However, there are particular importance of the angle  $54.74^\circ$ , which is a special value for the microchannels etched by KOH.

The gaseous mixture consists of two components  $\alpha = 1, 2$ . The molar masses and the molar densities of the components are denoted by  $m_\alpha$  and  $n_\alpha$ , respectively. The total density is introduced by  $n = n_1 + n_2$ . To characterize the mixture, the concentration of the first component is introduced as

$$C = \frac{n_1}{n}. \quad (3.2)$$

The concentration is a varying quantity in the channel. Its value at the inlet and the outlet of the channel is denoted by  $C_A$  and  $C_B$ , respectively. The pressure of the gas is denoted by  $P$ . Its inlet and outlet value is given by  $P_A$  and  $P_B$ . The rarefaction degree of the gas is characterized by the rarefaction parameter

$$\delta = \frac{PD_h}{\mu(C)v_0(C)}. \quad (3.3)$$

Here,  $\mu(C)$  is the viscosity of the mixture and  $v_0(C)$  is the characteristic molecular speed defined by

$$v_0(C) = \sqrt{\frac{2kT_0}{m(C)}}, \quad (3.4)$$

where  $k$  and  $T_0$  are the Boltzmann constant and the temperature of the gas. In addition, the average mass of the mixture is given by

$$m(C) = Cm_1 + (1 - C)m_2. \quad (3.5)$$

The flow is driven by the local pressure and concentration gradients along the axis of the channel

$$X_P = \frac{\partial P}{\partial z} \frac{1}{P}, \quad X_C = \frac{\partial C}{\partial z} \frac{1}{C}. \quad (3.6)$$

The pressure gradient drives both components in the same direction, while the concentration gradient tends to move the gas components in opposite directions. These driving forces are given in dimensionless forms. Since the channel is long,  $X_P \ll 1$  and  $X_C \ll 1$ . These relations imply that the driving terms are small; hence, the linearized description is applicable.

One of the interests of this work is in the macroscopic velocity of the gas components  $\mathbf{u}'_\alpha$ . The velocity has only  $z$  component for the long channel  $\mathbf{u}'_\alpha(x, y) = [0, 0, u'_\alpha(x, y)]$ . Dimensionless macroscopic velocity is introduced according to  $\mathbf{u}_\alpha = \mathbf{u}'_\alpha/v_0(C)$ .

Another quantity, which has major practical importance, is the dimensionless flow rate of the components

$$G_\alpha = -\frac{2}{A} \iint u_\alpha dx dy = -2\bar{u}_\alpha, \quad (3.7)$$

where  $A$  is the dimensionless area of the cross section and the overline denotes the spatial average of the velocity over the cross section.

Since linearized description is applied in the present problem, the macroscopic velocity is a linear function of the driving terms. Since there are two driving terms, the velocity field can be decomposed as

$$u_\alpha = u_\alpha^{(P)} X_P + u_\alpha^{(C)} X_C, \quad (3.8)$$

where  $u_\alpha^{(P)}$  and  $u_\alpha^{(C)}$  are the velocity profiles caused by either unity pressure or unity concentration gradients. In the same manner, the flow rates can also be decomposed such that

$$G_\alpha = G_\alpha^{(P)} X_P + G_\alpha^{(C)} X_C. \quad (3.9)$$

Here,  $G_\alpha^{(P)}$  and  $G_\alpha^{(C)}$  denote the flow rates for the pressure and concentration driven flows with unity driving terms.

For later purposes, two thermodynamic fluxes, the particle  $J_P$  and diffusion  $J_C$  fluxes, [68] are introduced as

$$J_P = -n_1 \iint (C u'_1 + (1 - C) u'_2) dx' dy', \quad (3.10)$$

$$J_C = -n_1 \iint (u'_1 - u'_2) dx' dy'. \quad (3.11)$$

The particle flux is related to the total flow rate of the mixture, while the diffusion flux describes the difference of the flow rates between the components.

In addition, the dimensional molar flow rates of the components  $J_\alpha$  and the total mass flow rate  $\dot{M}$  are introduced as

$$J_\alpha = \iint n_\alpha u'_\alpha dx' dy', \quad (3.12)$$

and

$$\dot{M} = \iint (m_1 n_1 u'_1 + m_2 n_2 u'_2) dx' dy'. \quad (3.13)$$

There are relationships among the introduced flow rates. The  $J_\alpha$  and  $\dot{M}$  flow rates can be expressed by using the  $J_P$  and  $J_C$  fluxes such that

$$J_1 = -C J_P + (1 - C) J_C, \quad (3.14)$$

$$J_2 = -(1 - C)(J_P - J_C) \quad (3.15)$$

and

$$\dot{M} = -m(C) J_P + (m_2 - m_1)(1 - C) J_C. \quad (3.16)$$

In this way, the physically interesting flow rates are determined by  $J_P$  and  $J_C$ , which are first determined in the calculation.

The  $J_P$  and  $J_C$  thermodynamic fluxes are connected to the driving forces via the so-called kinetic coefficients  $\Lambda'_{PP}$ ,  $\Lambda'_{CP}$ ,  $\Lambda'_{CP}$  and  $\Lambda'_{CC}$  [68] such that

$$J_P = \Lambda'_{PP} X_P + \Lambda'_{PC} X_C, \quad (3.17)$$

$$J_C = \Lambda'_{CP} X_P + \Lambda'_{CC} X_C. \quad (3.18)$$

This relationship expresses a linear dependence of the flow rates on the driving terms. It is noted that the kinetic coefficients are not independent. The cross coefficients are connected to each other via the Onsager reciprocity law such that  $\Lambda'_{PC} = \Lambda'_{CP}$  [62]. For later purposes, the dimensionless kinetic coefficients are introduced by

$$\Lambda_{ij} = \frac{2}{nA'v_0(C)} \Lambda'_{ij} \quad (3.19)$$

with  $i, j = [P, C]$ .

The kinetic coefficients completely characterize the system from the viewpoint of the flow rates. If the coefficients are known, the component, total and

mass flow rates can be calculated. The kinetic coefficients can be obtained by considering pressure and concentration driven flows.

One of the main objectives of the research is the calculate and tabulate the kinetic coefficients for a wide range of the gas rarefaction and concentration for specific mixtures. In order to obtain the coefficients, the local flow problem needs to be solved. The solution is based on the kinetic level. The kinetic coefficients can be obtained from the previously introduced dimensionless flow rates  $G_\alpha^{(P)}$  and  $G_\alpha^{(C)}$  such that

$$\Lambda_{PP} = CG_1^{(P)} + (1 - C)G_2^{(P)}, \quad \Lambda_{CP} = C(G_1^{(P)} - G_2^{(P)}) \quad (3.20)$$

for a pressure driven flow and

$$\Lambda_{PC} = CG_1^{(C)} + (1 - C)G_2^{(C)}, \quad \Lambda_{CC} = C(G_1^{(C)} - G_2^{(C)}). \quad (3.21)$$

for a concentration driven flow.

### 3.3 The McCormack model

The McCormack linearized kinetic model [45] is used to describe the flow configuration at the kinetic level. The basic quantity of the description is the one-particle distribution function  $f_\alpha(\mathbf{c}_\alpha, x, y, z)$  for gas components  $\alpha = 1, 2$ . Here,  $\mathbf{c}_\alpha$  is the non-dimensional microscopic velocity vector defined by  $\mathbf{c}_\alpha = \mathbf{v}_\alpha(m_\alpha/2kT_0)^{1/2}$  with  $\mathbf{v}_\alpha$  being the microscopic velocity. The system is close to equilibrium, hence the distribution function is linearized according to

$$f_\alpha(\mathbf{c}_\alpha, x, y, z) = f_\alpha^{(0)}(\mathbf{c}_\alpha, z)(1 + h_\alpha^{(P)}(\mathbf{c}_\alpha, x, y)X_P + h_\alpha^{(C)}(\mathbf{c}_\alpha, x, y)X_C). \quad (3.22)$$

Here, the perturbation from the equilibrium state is decomposed from the functions  $h_\alpha^{(i)}(\mathbf{c}_\alpha, x, y)$  with  $i = [P, C]$  for pressure or concentration driven

flows  $i = [P, C]$ . The equilibrium distribution function  $f_\alpha^{(0)}(\mathbf{c}_\alpha, z)$  is given by

$$f_\alpha^{(0)}(\mathbf{c}_\alpha, z) = n_\alpha(z) \left( \frac{m_\alpha}{2\pi kT_0} \right)^{3/2} e^{-c_\alpha^2}. \quad (3.23)$$

The perturbation function obeys the McCormack kinetic model [45]

$$c_{\alpha x} \frac{\partial h_\alpha^{(i)}}{\partial x} + c_{\alpha y} \frac{\partial h_\alpha^{(i)}}{\partial y} = \omega_\alpha \sum_{\beta=1}^2 L_{\alpha\beta} h_\beta^{(i)} - c_{\alpha z} \eta_\alpha^{(i)}. \quad (3.24)$$

On the right hand side of this equation,  $L_{\alpha\beta} h_\beta^{(i)}$  denotes the McCormack collision term, the quantity  $\omega_\alpha$  is defined by

$$\omega_\alpha = \sqrt{\frac{m_\alpha}{m}} \left[ \frac{C}{\gamma_1} + \frac{1-C}{\gamma_2} \right] \delta \quad (3.25)$$

and

$$\eta_1^{(P)} = 1, \quad \eta_2^{(P)} = 1, \quad (3.26)$$

$$\eta_1^{(C)} = 1, \quad \eta_2^{(C)} = -\frac{C}{1-C} \quad (3.27)$$

for the pressure  $i = P$  or concentration  $i = C$  driven flow, respectively.

The McCormack collision term for the present problem is written by

$$\begin{aligned} L_{\alpha\beta} h_\beta = & -\gamma_{\alpha\beta} h_\alpha + \\ & 2\sqrt{\frac{m_\alpha}{m}} \left[ \gamma_{\alpha\beta} u_\alpha - \nu_{\alpha\beta}^{(1)}(u_\alpha - u_\beta) - \frac{1}{2}\nu_{\alpha\beta}^{(2)} \left( q_\alpha - \frac{m_\alpha}{m_\beta} q_\beta \right) \right] c_{\alpha z} + \\ & 4[(\gamma_{\alpha\beta} - \nu_{\alpha\beta}^{(3)})p_{\alpha x z} + \nu_{\alpha\beta}^{(4)}p_{\beta x z}]c_{\alpha z}c_{\alpha x} + \\ & 4[(\gamma_{\alpha\beta} - \nu_{\alpha\beta}^{(3)})p_{\alpha y z} + \nu_{\alpha\beta}^{(4)}p_{\beta y z}]c_{\alpha z}c_{\alpha y} + \\ & \frac{4}{5}\sqrt{\frac{m_\alpha}{m}} \left[ (\gamma_{\alpha\beta} - \nu_{\alpha\beta}^{(5)})q_\alpha + \nu_{\alpha\beta}^{(6)}\sqrt{\frac{m_\beta}{m_\alpha}}q_\beta - \frac{5}{4}\nu_{\alpha\beta}^{(2)}(u_\alpha - u_\beta) \right] \times \\ & c_{\alpha z} \left( c_\alpha^2 - \frac{5}{2} \right). \end{aligned} \quad (3.28)$$

In the present situation, the involved macroscopic quantities are the non-dimensional velocity  $u_\alpha$ , heat flow  $q_\alpha$  and traceless pressure tensor  $p_{\alpha ij}$ . The

last two quantities can also be decomposed for the two types of flow as the velocity such that

$$q_\alpha = q_\alpha^{(P)} X_P + q_\alpha^{(C)} X_C, \quad (3.29)$$

$$p_{\alpha jz} = p_{\alpha jz}^{(P)} X_P + p_{\alpha jz}^{(C)} X_C, \quad (3.30)$$

where the index  $j$  refers to the coordinates  $x$  or  $y$ . All macroscopic quantities are defined as the moments of the perturbation function. More particularly, the velocity, the heat flow vectors and the pressure tensor are obtained by

$$u_\alpha^{(i)} = \pi^{-3/2} \left( \frac{m}{m_\alpha} \right)^{1/2} \int_{-\infty}^{\infty} h_\alpha^{(i)} c_{\alpha z} e^{-c_\alpha^2} d\mathbf{c}_\alpha, \quad (3.31)$$

$$q_\alpha^{(i)} = \pi^{-3/2} \left( \frac{m}{m_\alpha} \right)^{1/2} \int_{-\infty}^{\infty} h_\alpha^{(i)} c_{\alpha z} \left( c_\alpha^2 - \frac{5}{2} \right) e^{-c_\alpha^2} d\mathbf{c}_\alpha, \quad (3.32)$$

$$p_{\alpha jz}^{(i)} = \pi^{-3/2} \int_{-\infty}^{\infty} h_\alpha^{(i)} c_{\alpha j} c_{\alpha z} e^{-c_\alpha^2} d\mathbf{c}_\alpha. \quad (3.33)$$

In McCormack model, the  $\nu_{\alpha\beta}^{(k)}$ ,  $\gamma_\alpha$  and  $\gamma_{\alpha\beta}$  quantities are the collision frequencies. These quantities are related to the Chapman-Cowling integrals  $\Omega_{\alpha\beta}^{ij}$  such that

$$\nu_{\alpha\beta}^{(1)} = \frac{16}{3} \frac{m_{\alpha,\beta}}{m_\alpha} n_\beta \Omega_{\alpha\beta}^{11}, \quad (3.34)$$

$$\nu_{\alpha\beta}^{(2)} = \frac{64}{15} \left( \frac{m_{\alpha,\beta}}{m_\alpha} \right)^2 n_\beta \left( \Omega_{\alpha\beta}^{12} - \frac{5}{2} \Omega_{\alpha\beta}^{11} \right), \quad (3.35)$$

$$\nu_{\alpha\beta}^{(3)} = \frac{16}{5} \left( \frac{m_{\alpha,\beta}}{m_\alpha} \right)^2 \frac{m_\alpha}{m_\beta} n_\beta \left( \frac{10}{3} \Omega_{\alpha\beta}^{11} + \frac{m_\beta}{m_\alpha} \Omega_{\alpha\beta}^{22} \right), \quad (3.36)$$

$$\nu_{\alpha\beta}^{(4)} = \frac{16}{5} \left( \frac{m_{\alpha,\beta}}{m_\alpha} \right)^2 \frac{m_\alpha}{m_\beta} n_\beta \left( \frac{10}{3} \Omega_{\alpha\beta}^{11} - \Omega_{\alpha\beta}^{22} \right), \quad (3.37)$$

$$\nu_{\alpha\beta}^{(5)} = \frac{64}{15} \left( \frac{m_{\alpha,\beta}}{m_\alpha} \right)^2 \frac{m_\alpha}{m_\beta} n_\beta \Gamma_{\alpha\beta}^{(5)}, \quad (3.38)$$

$$\nu_{\alpha\beta}^{(6)} = \frac{64}{15} \left( \frac{m_{\alpha,\beta}}{m_\alpha} \right)^2 \left( \frac{m_\alpha}{m_\beta} \right)^{3/2} n_\beta \Gamma_{\alpha\beta}^{(6)}, \quad (3.39)$$

where

$$\Gamma_{\alpha\beta}^{(5)} = \Omega_{\alpha\beta}^{22} + \left( \frac{15m_\alpha}{4m_\beta} + \frac{25m_\beta}{8m_\alpha} \right) \Omega_{\alpha\beta}^{11} - \left( \frac{m_\beta}{2m_\alpha} \right) (5\Omega_{\alpha\beta}^{12} - \Omega_{\alpha\beta}^{13}), \quad (3.40)$$

$$\Gamma_{\alpha\beta}^{(6)} = -\Omega_{\alpha\beta}^{22} + \frac{55}{8}\Omega_{\alpha\beta}^{11} - \frac{5}{2}\Omega_{\alpha\beta}^{12} + \frac{1}{2}\Omega_{\alpha\beta}^{13}. \quad (3.41)$$

The Chapman-Cowling integrals can be defined for a particular interaction potential. Throughout this work, the realistic potential of Kestin et al. [35] is used. The procedure of deducing the collision integrals is presented in Appendix A.1. The realistic potential was derived from the experimental measurements of transport coefficients, and it is suitable for comparative purposes between theory and experiment.

To complete the formulation of the McCormack model, the reduced mass is defined as

$$m_{\alpha,\beta} = \frac{m_\alpha m_\beta}{m_\alpha + m_\beta}. \quad (3.42)$$

The  $\gamma_{\alpha\beta}$  collision frequencies appear in the combination  $\gamma_\alpha = \gamma_{\alpha\alpha} + \gamma_{\alpha\beta}$  and they are given by

$$\gamma_\alpha = \frac{S_\alpha S_\beta - \nu_{\alpha\beta}^{(4)} \nu_{\beta\alpha}^{(4)}}{S_\beta + \nu_{\alpha\beta}^{(4)}}, \quad (3.43)$$

where  $S_\alpha = \nu_{\alpha\alpha}^{(3)} - \nu_{\alpha\alpha}^{(4)} + \nu_{\alpha\beta}^{(3)}$ . In the expressions of  $\gamma_\alpha$  and  $S_\alpha$ ,  $\alpha, \beta = [1, 2]$  and  $\alpha \neq \beta$ .

The kinetic equation is supplemented with the boundary condition for the perturbation function. In the present work, the diffuse-specular boundary condition is assumed at the channel walls for the incoming populations

$$h_\alpha^{(i)}(\mathbf{c}_\alpha) = (1 - \sigma)h_\alpha^{(i)}(\mathbf{c}'_\alpha), \quad (3.44)$$

where  $\sigma$  is the accommodation coefficient and  $\mathbf{c}'_\alpha$  denotes the specularly reflecting counterpart of the incoming velocity  $\mathbf{c}_\alpha$ .

It is recalled that the configuration of the channel flow is two-dimensional and the flow is perpendicular to the cross section. Under these circumstances, the kinetic problem can be simplified by introducing two reduced distribution functions according to

$$\Phi_\alpha^{(i)} = \frac{1}{\sqrt{\pi}} \sqrt{\frac{m}{m_\alpha}} \int_{-\infty}^{\infty} \int_{-\infty}^{\infty} h_\alpha^{(i)} c_{\alpha z} e^{-c_{\alpha z}^2} dc_{\alpha z}, \quad (3.45)$$

$$\Psi_\alpha^{(i)} = \frac{1}{\sqrt{\pi}} \sqrt{\frac{m}{m_\alpha}} \int_{-\infty}^{\infty} \int_{-\infty}^{\infty} h_\alpha^{(i)} c_{\alpha z}^3 e^{-c_{\alpha z}^2} dc_{\alpha z}. \quad (3.46)$$

It follows from the McCormack kinetic model that these functions obey the following four equations

$$c_{\alpha x} \frac{\partial \Phi_\alpha^{(i)}}{\partial x} + c_{\alpha y} \frac{\partial \Phi_\alpha^{(i)}}{\partial y} + \gamma_\alpha \omega_\alpha \Phi_\alpha^{(i)} = -\frac{1}{2} \sqrt{\frac{m}{m_\alpha}} \eta_\alpha^{(i)} + \omega_\alpha \sum_{\beta=1}^2 \left[ A_{\alpha\beta}^{(i)} + 2B_{\alpha\beta x}^{(i)} c_{\alpha x} + 2B_{\alpha\beta y}^{(i)} c_{\alpha y} + \frac{2}{5} C_{\alpha\beta}^{(i)} (c_{\alpha x}^2 + c_{\alpha y}^2 - 1) \right] \quad (3.47)$$

and

$$c_{\alpha x} \frac{\partial \Psi_\alpha^{(i)}}{\partial x} + c_{\alpha y} \frac{\partial \Psi_\alpha^{(i)}}{\partial y} + \gamma_\alpha \omega_\alpha \Psi_\alpha^{(i)} = -\frac{3}{4} \sqrt{\frac{m}{m_\alpha}} \eta_\alpha^{(i)} + \omega_\alpha \sum_{\beta=1}^2 \left[ \frac{3}{2} A_{\alpha\beta}^{(i)} + 3B_{\alpha\beta x}^{(i)} c_{\alpha x} + 3B_{\alpha\beta y}^{(i)} c_{\alpha y} + \frac{3}{5} C_{\alpha\beta}^{(i)} (c_{\alpha x}^2 + c_{\alpha y}^2) \right], \quad (3.48)$$

where  $\alpha = 1, 2$  for the two components. The coefficients  $A_{\alpha\beta}^{(i)}$ ,  $B_{\alpha\beta j}^{(i)}$  and  $C_{\alpha\beta}^{(i)}$  in these equations are related to the macroscopic quantities according to

$$A_{\alpha\beta}^{(i)} = \gamma_{\alpha\beta} u_\alpha^{(i)} - \nu_{\alpha\beta}^{(1)} (u_\alpha^{(i)} - u_\beta^{(i)}) - \frac{1}{2} \nu_{\alpha\beta}^{(2)} \left( q_\alpha^{(i)} - \frac{m_\alpha}{m_\beta} q_\beta^{(i)} \right), \quad (3.49)$$

$$B_{\alpha\beta j}^{(i)} = (\gamma_{\alpha\beta} - \nu_{\alpha\beta}^{(3)}) \sqrt{\frac{m}{m_\alpha}} p_{\alpha j z}^{(i)} + \nu_{\alpha\beta}^{(4)} \sqrt{\frac{m}{m_\alpha}} p_{\beta j z}^{(i)}, \quad (3.50)$$

$$C_{\alpha\beta}^{(i)} = (\gamma_{\alpha\beta} - \nu_{\alpha\beta}^{(5)}) q_\alpha^{(i)} + \nu_{\alpha\beta}^{(6)} \sqrt{\frac{m_\beta}{m_\alpha}} q_\beta^{(i)} - \frac{5}{4} \nu_{\alpha\beta}^{(2)} (u_\alpha^{(i)} - u_\beta^{(i)}). \quad (3.51)$$

In the reduced description, the macroscopic velocity and heat flow vectors and the pressure tensor are given by

$$u_\alpha^{(i)} = \frac{1}{\pi} \int_{-\infty}^{\infty} \int_{-\infty}^{\infty} \Phi_\alpha^{(i)} e^{-c_{\alpha x}^2 - c_{\alpha y}^2} dc_{\alpha x} dc_{\alpha y}, \quad (3.52)$$

$$q_\alpha^{(i)} = \frac{1}{\pi} \int_{-\infty}^{\infty} \int_{-\infty}^{\infty} \left[ \Psi_\alpha^{(i)} + \left( c_{\alpha x}^2 + c_{\alpha y}^2 - \frac{5}{2} \right) \Phi_\alpha^{(i)} \right] e^{-c_{\alpha x}^2 - c_{\alpha y}^2} dc_{\alpha x} dc_{\alpha y}, \quad (3.53)$$

$$p_{\alpha jz}^{(i)} = \frac{1}{\pi} \sqrt{\frac{m}{m_\alpha}} \int_{-\infty}^{\infty} \int_{-\infty}^{\infty} c_{\alpha j} \Phi_\alpha^{(i)} e^{-c_{\alpha x}^2 - c_{\alpha y}^2} dc_{\alpha x} dc_{\alpha y}. \quad (3.54)$$

For the reduced distribution functions, the diffuse-reflection boundary condition is given by

$$\Phi^{(i)}(+)= (1 - \sigma)\Phi^{(i)}(-), \quad \Psi^{(i)}(+)= (1 - \sigma)\Psi^{(i)}(-), \quad (3.55)$$

where the + and – arguments denote the incoming population and its specular counterpart with regard to the wall, respectively.

## 3.4 Accelerated discrete velocity algorithm in triangular lattices

### 3.4.1 General

The integro-differential equations of the McCormack model are solved by the discrete velocity method (DVM). The DVM can be used to solve various kinetic equations appearing in rarefied gas dynamics [2], [95], [46]. Both the microscopic velocity variable and the spatial coordinates are discretized in the method. The resulting discrete equations are solved numerically. The DVM has been successfully used in the past in rarefied gas dynamics. However, it is known that the method becomes slow in the hydrodynamic domain. This shortcoming can be improved by the synthetic-type accelerated DVM.

In the present work, an accelerated DVM has been developed for triangular lattices [91], which are applied for the description of flows through chan-

nels with triangular and trapezoidal cross sections. In the accelerated DVM, the kinetic equations are supplemented with additional moment equations. These equations are derived from the kinetic ones. Both types of equations are solved in a coupled iteration in the DVM. This process results into a better computational performance in the hydrodynamic limit and speeds up the DVM. In addition, a discrete stability analysis is developed in order to examine the convergence behavior of the method. The stability analysis proves that the accelerated DVM has a better iteration performance.

In the following, the development of the accelerated DVM is described. The presentation starts with the BGK operator describing single component gases. Secondly, the method is applied to the McCormack kinetic model.

### 3.4.2 Single gases

The fully developed pressure driven flow of single component gas through a long channel with triangular cross section is considered. The gaseous flow is described by the Bhatnagar-Gross-Krook model applying the single relaxation time approximation [7]. Since the channel is long, the flow can be described in a cross section of the channel. For the considered problem, the BGK equation can be written by

$$\mathbf{c} \cdot \nabla f^{(t+1/2)}(c, \theta, \mathbf{x}) + \delta f^{(t+1/2)}(c, \theta, \mathbf{x}) = \delta F_{0,0}^{(t)}(\mathbf{x}) + S(\mathbf{x}). \quad (3.56)$$

In this equation,  $f^{(t+1/2)}(c, \theta, \mathbf{x})$  denotes the reduced distribution function,  $\mathbf{c} = (c, \theta)$  is the molecular velocity given in polar coordinates,  $\mathbf{x} = (x_1, x_2)$  is the two-dimensional position vector defined in Cartesian coordinates in the cross section sheet,  $F_{0,0}^{(t)}(\mathbf{x})$  is the velocity of the gas along the channel axis,  $S(\mathbf{x})$  is a source term, which is  $S(\mathbf{x}) = -1/2$  for the Poiseuille flow considered here, and  $t$  is the iteration index in the procedure of the solution. In addition,  $\delta$  is the rarefaction parameter.

The above equation is supplemented with the expression of the macroscopic velocity obtained as the moment of the distribution function

$$F_{0,0}^{(t+1)}(\mathbf{x}) = \frac{1}{\pi} \int_0^{2\pi} \int_0^\infty f^{(t+1/2)}(c, \theta, \mathbf{x}) \exp(-c^2) c d c d \theta. \quad (3.57)$$

At the channel walls, the diffuse boundary condition is applied for the distribution function

$$f(\mathbf{c}, \mathbf{x}_b) = 0, \quad \text{for } \mathbf{c} \cdot \mathbf{n} > 0, \quad (3.58)$$

where  $\mathbf{x}_b$  denotes a boundary point and  $\mathbf{n}$  is the normal vector pointing to the gas phase at the wall.

In this development, there is a special focus on the dimensionless flow rate, which has major practical importance, defined as

$$G = \frac{2}{A} \iint_A F_{0,0}(\mathbf{x}) d x_1 d x_2, \quad (3.59)$$

where  $A$  denotes the cross section of the channel.

The BGK kinetic equation is solved in an iterative manner as denoted by the iteration index  $t$ . The distribution function is calculated in the iteration step  $t + 1/2$  by solving Eq. (3.56) with the assumption of the known velocity field at the iteration stage  $t$  on the right hand side. This solution is carried out by discretizing the velocity and coordinate spaces and using the finite-difference method. On the basis of the obtained distribution function  $f^{(t+1/2)}(c, \theta, \mathbf{x})$ , the velocity field is calculated in the next iteration step  $t + 1$  from Eq. (3.57). The iteration is repeated until a convergent result is obtained. A convergence criterion is established by using the dimensionless flow rate. The flow rate in each iteration step is denoted by  $G^t$ . The solution procedure terminates by fulfilling the following condition  $|G^{t+1} - G^t| < \epsilon$ , where  $\epsilon$  is a predefined threshold for the convergence. This procedure is the standard iteration for the solution of the kinetic equation.

The standard iteration is improved by introducing the accelerated iteration of the kinetic equation. In this way, the relatively slow performance

of the standard iteration can be overcome. In the accelerated method, a moment equation, which is solved in parallel with the BGK equation, is introduced. The moment equation can be derived from the BGK one by taking its velocity moments and manipulating the resulting expressions. The additional moment equation is given by

$$\begin{aligned} \Delta F_{0,0}^{(t+1)}(\mathbf{x}) = & \\ & - \frac{1}{2} \partial_{x_1}^2 F_{2,0}^{(t+1/2)}(\mathbf{x}) - \frac{1}{2} \partial_{x_2}^2 F_{0,2}^{(t+1/2)}(\mathbf{x}) - \partial_{x_1} \partial_{x_2} F_{1,1}^{(t+1/2)}(\mathbf{x}) - \delta S(\mathbf{x}). \end{aligned} \quad (3.60)$$

On the right hand side of Eq. (3.60), the quantities  $F_{2,0}$ ,  $F_{0,2}$  and  $F_{1,1}$  are the Hermite moments of the distribution function

$$F_{m,n}^{(t+1/2)}(\mathbf{x}) = \frac{1}{\pi} \int_0^{2\pi} \int_0^\infty f^{(t+1/2)}(c, \theta, \mathbf{x}) H_{m,n}(\mathbf{c}) \exp(-c^2) c dc d\theta, \quad (3.61)$$

where  $m + n > 0$  and  $H_{m,n}(\mathbf{c})$  denotes the two-dimensional (m,n)-order Hermite polynomials. They can be defined from the one-dimensional n-order polynomials  $H_n(x)$  such that  $H_{m,n}(\mathbf{c}) = H_m(c \cos(\theta)) H_n(c \sin(\theta))$ . For completeness purposes, the first few elements of these polynomial are given by

$$H_0(\eta) = 1, \quad (3.62)$$

$$H_1(\eta) = 2\eta, \quad (3.63)$$

$$H_2(\eta) = 4\eta^2 - 2. \quad (3.64)$$

In the accelerated method, the iteration procedure performs as described as follows. In each iteration step, the distribution function at stage  $t + 1/2$  is calculated as in the standard iteration. Then, the higher moments of the distribution function are calculated according to Eq. (3.61). By using these moments, the additional moment equation, Eq. (3.60), is solved to yield the velocity in the next step,  $F_{0,0}^{(t+1)}(\mathbf{x})$ . The iteration terminates by fulfilling the same criterion as in the case of the standard iteration.

The accelerated method requires the solution of Eq. (3.61), which is carried out by an over-relaxation solver on the same spatial grid as used for the BGK equation. Finally, it is mentioned that the boundary nodes are not accelerated in the present scheme. However, it does not introduce significant change in the performance, since the number of these nodes is negligible compared to the interior part of the domain.

### Discretization

The solution of the kinetic and moment equations are carried out by the discrete velocity method. The spatial and velocity coordinates are discretized. The spatial variable is discretized by using a triangular grid, which is fitted to the boundary of the cross section. The triangular grid is shown in Figure 3.2. The discretized spatial coordinate is denoted by  $\boldsymbol{x}_p$ , where  $p$  is the  $p$ -th node on the grid with  $1 \leq p \leq L$ , where  $L$  is the total number of nodes. The velocity variable is given in polar coordinate system. The magnitude of the velocity vector and the polar angle are discretized as  $c_q$  and  $\theta_r$  with  $1 \leq q \leq M$  and  $1 \leq r \leq N$ , where  $M$  and  $N$  are the number of nodes used in the corresponding discretization.

Figure 3.3 presents a computational cell on the triangular grid. A central node denoted by  $A$  with coordinate  $\boldsymbol{x}_p$  and its six surrounding neighbours are shown. The six neighbours are connected to the center node via the vectors  $\boldsymbol{r}_j$ ,  $j = 1..6$ . The coordinates of the neighbours are given by  $\boldsymbol{x}_p + \boldsymbol{r}_j$ . An arbitrary velocity vector  $\boldsymbol{c}$  with velocity magnitude  $c_q$  and polar angle  $0 \leq \theta_r \leq 2\pi$  is also presented in the figure.

### Standard iteration

The BGK equation, Eq. (3.56), is transformed into a discrete equation by approximating the spatial derivative on the left hand side by finite-difference

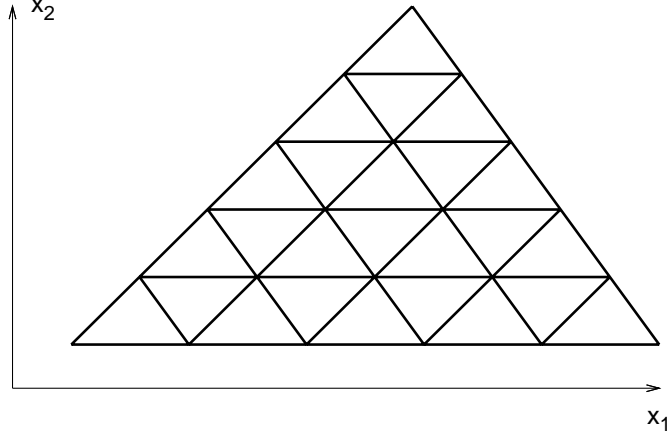


Figure 3.2: The triangular grid used in the discretization of the spatial coordinates.

forms

$$\frac{c_q}{\Delta(\theta_r)} [f^{(t+1/2)}(c_q, \theta_r, \mathbf{x}_p) - \sum_{j=1}^6 a_j(\theta_r) f^{(t+1/2)}(c_q, \theta_r, \mathbf{x}_p + \mathbf{r}_j)] + \delta f^{(t+1/2)}(c_q, \theta_r, \mathbf{x}_p) = \delta F_{0,0}^{(t)}(\mathbf{x}_p) + S(\mathbf{x}_p). \quad (3.65)$$

The bracketed term on the left hand side of this equation represents the discrete form of the advection operator of the BGK equation. The spatial derivative is calculated by an upwind finite difference approximation using the information on the central node  $A$  and the upwind point  $B$ , Figure 3.3. The spacing between these two points is denoted by  $\Delta(\theta_r)$ . The scheme works in such a way that by using the information on the nodes 4 and 5, the distribution function is linearly extrapolated to the point  $B$ . In the scheme,  $a_j(\theta_r)$  are weight functions describing the interpolation and the differential form. For every angle  $\theta_r$ , there are only two non-zero  $a_i(\theta_r)$  weights from the six-element set. The weights and the distance between  $A$  and  $B$  are

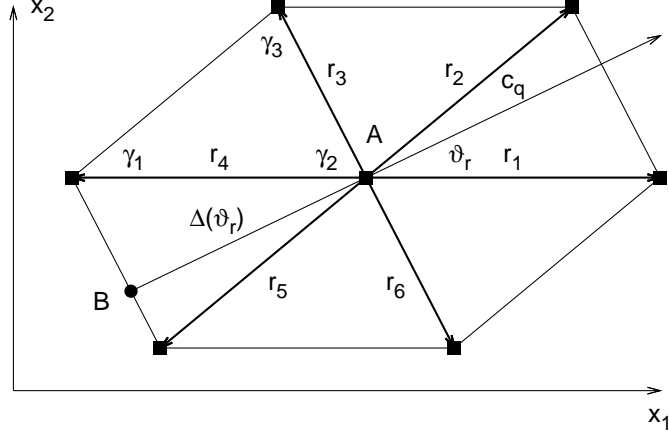


Figure 3.3: The computational cell for one node on the triangular grid.

defined in a compact form. These quantities can be determined by using the vector  $\beta_i = [\gamma_1, \gamma_1 + \gamma_3, \pi, \pi + \gamma_1, \pi + \gamma_1 + \gamma_3, 2\pi]$  and the sine theorem for the geometry given in Figure 3.3. It is seen that the six elements of  $\beta_i$  are the upper bounds of the six polar angle sectors of  $\theta_r$ .

The weights  $a_i(\theta_r)$  are periodic with respect to  $\theta_r$ ,  $a_i(\theta_r) = a_i(\theta_r + 2\pi)$ , and they have the following property  $a_i(\theta_r) = a_{i+3}(\theta_r - \pi)$  for  $i = 1, 2, 3$ . These properties make the definition easier. The weights are defined only in the  $\pi \leq \theta_r < 2\pi$  angle interval. There are two elements from  $a_i(\theta_r)$  which are non-zero for each  $\theta_r$ . These elements are defined by

$$a_i(\theta_r) = \frac{\sin(\theta_r - \beta_i) r_{i+1}}{\sin(\theta_r - \beta_{i+1}) r_{i+2}} \quad (3.66)$$

and

$$a_{i+1}(\theta_r) = \frac{\sin(\theta_r - \beta_{i+2}) r_{i+3}}{\sin(\theta_r - \beta_{i+1}) r_{i+2}}, \quad (3.67)$$

for  $\beta_{i+2} \leq \theta_r < \beta_{i+3}$ , where  $i = 1, 2, 3$ .

The distance function between node A and the extrapolated node B,  $\Delta(\theta_r)$ , is also periodic with respect to the angle  $\theta_r$ . It is convenient to

define the distance function for the angle interval  $\pi \leq \theta_r < 2\pi$  covered with the indices  $i = 4, 5, 6$  in  $\beta_i$ . After straightforward calculation, the distance function for the selected interval can be determined such that

$$\Delta(\theta_r) = \frac{\sin(\beta_{i-1} - \beta_{i-2})}{\sin(\theta_r - \beta_{i-2})} r_i, \quad \text{for } \beta_{i-1} \leq \theta_r < \beta_i. \quad (3.68)$$

Finally, the discretized form of the macroscopic velocity, Eq. (3.57), is discussed. By using the discrete angles in the discretization of the velocity space, the macroscopic gas velocity can be determined by applying quadrature approximation of the integrals

$$F_{0,0}^{(t+1)}(\mathbf{x}_p) = \frac{2}{N} \sum_{q=1}^M \sum_{r=1}^N w_q f^{(t+1/2)}(c_q, \theta_r, \mathbf{x}_p) c_q. \quad (3.69)$$

Here, the quantity  $w_q$  denotes the associated quadrature weights.

### Accelerated iteration

In this section, the solution of the diffuse-type moment equation, Eq. (3.60), is discussed. The solution is again based on the finite-difference approximation of the spatial derivative on the triangular grid. The finite-difference approximation of the Laplace operator on the central node  $A$ , Figure 3.2, uses the information on the six surrounding nodes.

The discrete moment equation is written by

$$\begin{aligned} \sum_{j=1}^6 [b_{1,j} + b_{2,j}] [F_{0,0}^{(t+1)}(\mathbf{x}_p + \mathbf{r}_j) - F_{0,0}^{(t+1)}(\mathbf{x}_p)] = \\ -\frac{1}{2} \sum_{j=1}^6 b_{1,j} [F_{2,0}^{(t+1/2)}(\mathbf{x}_p + \mathbf{r}_j) - F_{2,0}^{(t+1/2)}(\mathbf{x}_p)] - \\ \frac{1}{2} \sum_{j=1}^6 b_{2,j} [F_{0,2}^{(t+1/2)}(\mathbf{x}_p + \mathbf{r}_j) - F_{0,2}^{(t+1/2)}(\mathbf{x}_p)] - \\ \sum_{j=1}^6 b_{3,j} [F_{1,1}^{(t+1/2)}(\mathbf{x}_p + \mathbf{r}_j) - F_{1,1}^{(t+1/2)}(\mathbf{x}_p)] - \delta S(\mathbf{x}_p). \quad (3.70) \end{aligned}$$

On the left hand side of this equation, the finite-difference approximation applies the weights  $b_{p,j}$ . The present approximation is second-order with respect to the grid spacing. However, it is mentioned that second-order accuracy is needed since the spatial derivatives are second-order in the moment equation. The  $b_{p,j}$  weights are obtained by using the Taylor expansion of the velocity around the central node  $A$ .

By considering the second-order Taylor expansion of an arbitrary function  $g(\mathbf{x})$  around the central node  $A$  with coordinate  $\mathbf{x}_p$ , the function at the six surrounding nodes can be written as

$$g(\mathbf{x}_p + \mathbf{r}_1) = g(\mathbf{x}_p) + \partial_{x_1}g(\mathbf{x}_p)r_{1x_1} + \frac{1}{2}\partial_{x_1}^2g(\mathbf{x}_p)r_{1x_1}^2, \quad (3.71)$$

$$g(\mathbf{x}_p + \mathbf{r}_2) = g(\mathbf{x}_p) + \partial_{x_1}g(\mathbf{x}_p)r_{2x_1} + \partial_{x_2}g(\mathbf{x}_p)r_{2x_2} + \frac{1}{2}\partial_{x_1}^2g(\mathbf{x}_p)r_{2x_1}^2 + \frac{1}{2}\partial_{x_2}^2g(\mathbf{x}_p)r_{2x_2}^2 + \partial_{x_1}\partial_{x_2}g(\mathbf{x}_p)r_{2x_1}r_{2x_2}, \quad (3.72)$$

$$g(\mathbf{x}_p + \mathbf{r}_3) = g(\mathbf{x}_p) + \partial_{x_1}g(\mathbf{x}_p)r_{3x_1} + \partial_{x_2}g(\mathbf{x}_p)r_{3x_2} + \frac{1}{2}\partial_{x_1}^2g(\mathbf{x}_p)r_{3x_1}^2 + \frac{1}{2}\partial_{x_2}^2g(\mathbf{x}_p)r_{3x_2}^2 + \partial_{x_1}\partial_{x_2}g(\mathbf{x}_p)r_{3x_1}r_{3x_2}, \quad (3.73)$$

$$g(\mathbf{x}_p + \mathbf{r}_4) = g(\mathbf{x}_p) + \partial_{x_1}g(\mathbf{x}_p)r_{4x_1} + \frac{1}{2}\partial_{x_1}^2g(\mathbf{x}_p)r_{4x_1}^2, \quad (3.74)$$

$$g(\mathbf{x}_p + \mathbf{r}_5) = g(\mathbf{x}_p) + \partial_{x_1}g(\mathbf{x}_p)r_{5x_1} + \partial_{x_2}g(\mathbf{x}_p)r_{5x_2} + \frac{1}{2}\partial_{x_1}^2g(\mathbf{x}_p)r_{5x_1}^2 + \frac{1}{2}\partial_{x_2}^2g(\mathbf{x}_p)r_{5x_2}^2 + \partial_{x_1}\partial_{x_2}g(\mathbf{x}_p)r_{5x_1}r_{5x_2}, \quad (3.75)$$

$$g(\mathbf{x}_p + \mathbf{r}_6) = g(\mathbf{x}_p) + \partial_{x_1}g(\mathbf{x}_p)r_{6x_1} + \partial_{x_2}g(\mathbf{x}_p)r_{6x_2} + \frac{1}{2}\partial_{x_1}^2g(\mathbf{x}_p)r_{6x_1}^2 + \frac{1}{2}\partial_{x_2}^2g(\mathbf{x}_p)r_{6x_2}^2 + \partial_{x_1}\partial_{x_2}g(\mathbf{x}_p)r_{6x_1}r_{6x_2}. \quad (3.76)$$

In these equations, the quantities  $r_{ix_1}$  and  $r_{ix_2}$  with  $i = 1, 2$  denote the coordinates of the space vectors  $\mathbf{r}_i$ . These quantities can be determined from a trigonometrical calculation with respect to the cell in Figure 3.3.

The Laplace operator in the momentum equation can be expressed by taking the suitable linear combination of Eqs. (3.71)-(3.76) such that

$$\partial_{x_1}^2 g(\mathbf{x}_p) = \sum_{i=1}^6 b_{1,i} [g(\mathbf{x}_p + \mathbf{r}_i) - g(\mathbf{x}_p)], \quad (3.77)$$

$$\partial_{x_2}^2 g(\mathbf{x}_p) = \sum_{i=1}^6 b_{2,i} [g(\mathbf{x}_p + \mathbf{r}_i) - g(\mathbf{x}_p)], \quad (3.78)$$

$$\partial_{x_1} \partial_{x_2} g(\mathbf{x}_p) = \sum_{i=1}^6 b_{3,i} [g(\mathbf{x}_p + \mathbf{r}_i) - g(\mathbf{x}_p)]. \quad (3.79)$$

The expression of the weights  $b_{p,i}$  can be obtained from Eqs. (3.71)-(3.76). The weights have the following property  $b_{p,i} = b_{p,i+3}$  for  $i = 1, 2, 3$ . The nonzero elements of the weights  $b_{p,i}$  for  $i = 1, 2, 3$  are given by

$$b_{1,1} = 1/r_1^2, \quad (3.80)$$

$$b_{2,1} = -\cos(\gamma_1) \cos(\gamma_2) / [r_1^2 \sin(\gamma_1) \sin(\gamma_2)], \quad (3.81)$$

$$b_{2,2} = \cos(\gamma_2) / [r_1 r_2 \sin(\gamma_1) \sin(\gamma_2)], \quad (3.82)$$

$$b_{2,3} = \cos(\gamma_1) / [r_1 r_2 \sin^2(\gamma_1)], \quad (3.83)$$

$$b_{3,1} = [r_3 \cos(\gamma_2) - r_2 \cos(\gamma_1)] / [2r_1^2 r_2 \sin(\gamma_1)], \quad (3.84)$$

$$b_{3,2} = 1 / [2r_1 r_2 \sin(\gamma_1)], \quad (3.85)$$

$$b_{3,3} = -1 / [2r_1 r_2 \sin(\gamma_1)]. \quad (3.86)$$

In order to complete the discretization procedure, the integral expression of the Hermite moments are determined in the discretized formulation. The integrals are replaced by the following quadrature approximation

$$F_{m,n}^{(t+1/2)}(\mathbf{x}_p) = \frac{2}{N} \sum_{q=1}^M \sum_{r=1}^N w_q f^{(t+1/2)}(c_q, \theta_r, \mathbf{x}_p) H_{m,n}(c_q, \theta_r) c_q. \quad (3.87)$$

It is mentioned that only the higher order moments,  $F_{2,0}^{(t+1)}$ ,  $F_{0,2}^{(t+1)}$  and  $F_{1,1}^{(t+1)}$ , are calculated from Eq. (3.87). The velocity itself,  $F_{0,0}^{(t+1)}$ , is obtained by solv-

ing the moment equation. The solution is carried out by using a successive over-relaxation solver.

### Discrete stability analysis

The discrete stability analysis is employed to study the convergence behaviour of both the kinetic and accelerated iterations. The investigation is based on the Fourier stability analysis. The evolution of some modes in the iteration schemes is examined. In this way, information can be obtained about the convergence speed of the methods. Also, the convergence rate can be examined as a function of the rarefaction parameter. Mathematically, the analysis results into an eigenvalue problem. The specific modes are eigenvectors (eigenfunctions) in the iteration procedure, while the eigenvalues describe the convergence rates. In the stability analysis, the spectral radius, the maximum of the eigenvalues, is defined. That is a main quantity and describes the overall convergence behaviour of the iteration schemes.

In the analysis, the difference of the distribution function and the macroscopic velocity between two subsequent iteration stages is considered. Since the equations are linear, this is equivalent with the consideration of the functions  $f^{(t)}(c_q, \theta_r, \mathbf{x}_p)$  and  $F_{m,n}^{(t)}(\mathbf{x}_p)$  as perturbations satisfying the discrete equations with zero source term  $S(\mathbf{x}_p) = 0$ .

The distribution function is considered as a Fourier mode in the discrete equations

$$f^{(t+1/2)}(c_q, \theta_r, \mathbf{x}_p) = \omega(\mathbf{k})^t f_F(c_q, \theta_r, \mathbf{k}) \exp(i\mathbf{k}\mathbf{x}_p), \quad (3.88)$$

where  $f_F(c_q, \theta_r, \mathbf{k})$  is the Fourier amplitude and  $\omega(\mathbf{k})$  is the eigenvalue for the wave-number  $\mathbf{k}$ . The corresponding macroscopic velocity is written by

$$F_{0,0}^{(t)}(\mathbf{x}_p) = \omega(\mathbf{k})^t \exp(i\mathbf{k}\mathbf{x}_p). \quad (3.89)$$

Following Eq. (3.89), the macroscopic velocity in the iteration stage  $t + 1$

can be written by

$$F_{0,0}^{(t+1)}(\mathbf{x}_p) = \omega(\mathbf{k})F_{0,0}^{(t)}(\mathbf{x}_p) = \omega(\mathbf{k})^{t+1} \exp(i\mathbf{k}\mathbf{x}_p). \quad (3.90)$$

The goal of the stability analysis is to derive a closed form expression to the eigenvalues  $\omega(\mathbf{k})$  for both iteration methods. In addition, the spectral radius as the upper bound for the eigenvalue  $\omega(\mathbf{k})$  according to

$$\sigma = \sup|\omega(\mathbf{k})|. \quad (3.91)$$

is determined. As a consequence, information about the convergence behavior of both schemes is presented.

### Eigenvalues of the standard iteration

The analysis starts with the standard iteration method. By substituting the expression of the distribution function and the macroscopic velocity of the Fourier mode, Eqs. (3.88)-(3.89), into Eq. (3.65) with zero source term  $S(\mathbf{x}_p) = 0$ , the Fourier mode eigenvector is obtained by

$$f_F(c_q, \theta_r, \mathbf{k}) = \left[ \frac{c_q}{\delta\Delta(\theta_r)} (1 - A(\theta_r, \mathbf{k})) + 1 \right]^{-1}, \quad (3.92)$$

where for convenience the following function is introduced

$$A(\theta_r, \mathbf{k}) = \sum_{j=1}^6 a_j(\theta_r) \exp(i\mathbf{k}\mathbf{r}_j). \quad (3.93)$$

The eigenvalue is determined by substituting Eqs. (3.88), with the Fourier mode  $f_F$  given by Eq. (3.92), and (3.93) into Eq. (3.69) and using Eq. (3.90) such that

$$\omega_K(\mathbf{k}) = \frac{2}{N} \sum_{r=1}^N \sum_{q=1}^M w_q \left[ \frac{c_q}{\delta\Delta(\theta_r)} (1 - A(\theta_r, \mathbf{k})) + 1 \right]^{-1} c_q, \quad (3.94)$$

where the  $K$  index has been introduced to denote the eigenvalue for the kinetic iteration scheme.

## Eigenvalues of the accelerated iteration

Secondly, the eigenvalues of the accelerated method are investigated. It can be shown that the Fourier mode eigenvector  $f_F$  is the same as for the standard iteration and defined by Eqs. (3.92) and (3.93). First, the higher order Hermite moments are expressed by substituting Eq. (3.88) into Eq. (3.87) such that

$$F_{m,n}^{(t+1/2)}(\mathbf{x}_p) = \omega(\mathbf{k})^t \Phi_{m,n}(\mathbf{k}) \exp(i\mathbf{k}\mathbf{x}_p), \quad (3.95)$$

where

$$\Phi_{m,n}(\mathbf{k}) = \frac{2}{N} \sum_{r=1}^N \sum_{q=1}^M w_q f_F(c_q, \theta_r, \mathbf{k}) H_{m,n}(c_q, \theta_r) c_q \quad (3.96)$$

for  $m, n = 0, 1, 2$  and  $m + n = 2$ . Secondly, the expression of the updated velocity, Eq. (3.90), and the higher moments, Eqs. (3.95) and (3.96), are substituted into the discrete momentum equation, Eq. (3.70). In this way, after some routine manipulations, the eigenvalues for the synthetic iteration scheme can be deduced as

$$\omega_S(\mathbf{k}) = -\frac{1}{2} \left[ B_1(\mathbf{k})\Phi_{2,0}(\mathbf{k}) + B_2(\mathbf{k})\Phi_{0,2}(\mathbf{k}) + 2B_3(\mathbf{k})\Phi_{1,1}(\mathbf{k}) \right] \times \left[ B_1(\mathbf{k}) + B_2(\mathbf{k}) \right]^{-1}, \quad (3.97)$$

where for convenience the following function is introduced

$$B_p(\mathbf{k}) = \sum_{j=1}^6 b_{p,j} [\exp(i\mathbf{k}\mathbf{r}_j) - 1] \quad (3.98)$$

with  $p = 1, 2, 3$ . The  $S$  index in Eq. (3.98) denotes the eigenvalue for the (synthetic) accelerated iteration method.

## Properties of eigenvalues

In previous sections, closed analytical expressions have been derived for the eigenvalues for both the standard and accelerated iterations. Following the analysis, some mathematical properties of the eigenvalues are deduced.

It can be shown that the eigenvalues of the discrete equations are always real. First, the eigenvalue of the standard iteration is considered. In view of Eq. (3.94), the complex nature of the eigenvalue is encoded in the following quantity

$$\xi(\theta_r, \mathbf{k}) = \frac{1 - A(\theta_r, \mathbf{k})}{\Delta(\theta_r)}. \quad (3.99)$$

Having the mathematical properties  $a_i(\theta_r) = a_{i+3}(\theta_r - \pi)$  and  $\mathbf{r}_i = -\mathbf{r}_{i+3}$  for  $i = 1, 2, 3$ , it can be deduced that

$$\text{Re}[A(\theta_r, \mathbf{k})] = \text{Re}[A(\theta_r + \pi, \mathbf{k})] \quad (3.100)$$

$$\text{Im}[A(\theta_r, \mathbf{k})] = -\text{Im}[A(\theta_r + \pi, \mathbf{k})]. \quad (3.101)$$

By using these equations together with periodicity property of the distance function,  $\Delta(\theta_r) = \Delta(\theta_r + \pi)$ , one can show that

$$\text{Re}[\xi(\theta_r, \mathbf{k})] = \text{Re}[\xi(\theta_r + \pi, \mathbf{k})] \quad (3.102)$$

$$\text{Im}[\xi(\theta_r, \mathbf{k})] = -\text{Im}[\xi(\theta_r + \pi, \mathbf{k})]. \quad (3.103)$$

By substituting Eqs. (3.102) and (3.103) into the expression of the eigenvalue, Eq. (3.94), it can be deduced that the eigenvalue is real.

In the case of the accelerated iteration, the eigenvalue is given by Eq. (3.97). Considering the symmetry of the problem, one can deduced that

$$\text{Im}[B_p(\mathbf{k})] = 0 \quad (3.104)$$

for  $p = 1, 2, 3$ . On the other hand, the higher order Hermite polynomials are also periodic with respect to the angle variable

$$H_{m,n}(c_q, \theta_r) = H_{m,n}(c_q, \theta_r + \pi) \quad (3.105)$$

for  $m, n = 0, 1, 2$  and  $m + n = 2$ . It follows from Eqs. (3.104), (3.105) and (3.102), (3.103) that the eigenvalue for the accelerated method is real. It is noted that the eigenvalues are also real in the continuous case. As a result, this property is valid in both the continuous and discrete cases.

Finally, the continuous limit of the eigenvalues is deduced. This limit can be reached by letting the resolution infinitely fine. The base of the spatial resolution is defined by  $h = r_1$ . In order to obtain the continuous limit of the eigenvalues, the quantity of  $\xi(\theta_r, \mathbf{k})$ , which is responsible for the discrete effects, is analyzed. Mathematically, the continuous limit can be deduced by using the Taylor expansion with respect to  $h$  in the relevant expressions and taking the limit  $h \rightarrow 0$ . All spatial vectors in the computational cell have the same order as  $r_1$ , i.e.  $r_j \sim O(h)$ ,  $j = 1, \dots, 6$ . By using Taylor expansion,  $\exp(i\mathbf{k}\mathbf{r}_j)$  is expanded up to  $O(h^2)$  by

$$\exp(i\mathbf{k}\mathbf{r}_j) = 1 + i\mathbf{k}\mathbf{r}_j + O(h^2). \quad (3.106)$$

As a result, one can obtain that

$$A(\theta_r, \mathbf{k}) = 1 + \sum_{j=1}^6 a_j(\theta_r) i\mathbf{k}\mathbf{r}_j + O(h^2). \quad (3.107)$$

The continuous limit of  $\xi(\theta_r, \mathbf{k})$  as  $h \rightarrow 0$  is given such that

$$\lim_{h \rightarrow 0} \xi(\theta_r, \mathbf{k}) = \lim_{h \rightarrow 0} \frac{1 - A(\theta_r, \mathbf{k})}{\Delta(\theta_r)} = -\frac{\sum_{j=1}^6 a_j(\theta_r) i\mathbf{k}\mathbf{r}_j}{\Delta(\theta_r)} = i\mathbf{k}\mathbf{e}, \quad (3.108)$$

where  $\mathbf{e} = [\cos(\theta_r), \sin(\theta_r)]$  is the unit vector in the direction of the molecular velocity  $\mathbf{c}$ . Furthermore, the continuous limit requires  $M, N \rightarrow \infty$ . By using Eq. (3.108) in the expressions of the eigenvalues, Eqs. (3.94) and (3.97), the continuum limit of the eigenvalues is obtained by

$$\omega_K(\mathbf{k}) = \frac{1}{\sqrt{\pi}} \int_{-\infty}^{\infty} \frac{e^{-c^2}}{c^2(k/\delta)^2 + 1} dc \quad (3.109)$$

and

$$\omega_S(\mathbf{k}) = \frac{1}{\sqrt{\pi}} \int_{-\infty}^{\infty} \frac{1 - 2c^2}{c^2(k/\delta)^2 + 1} e^{-c^2} dc \quad (3.110)$$

for the standard and accelerated iterations, respectively.

### **Analysis of convergence rates**

In the previous section, the theoretical value of the converge rates for both the standard and accelerated iterations have been derived. These quantities provide information about the converge behaviour of the schemes. The smaller convergence rate provides better convergence, since the change of the Fourier modes during one iteration is larger in that case; as a consequence, the scheme converges faster to the final solution. In the following, the theoretical convergence rates are presented as a function of the rarefaction parameter, the wavelength and the discretization parameters,  $h$  and  $M \times N$ . The spectral radius, the maximum of the convergence rate as a function of the wave-number, is also studied. The wave-number is pointed to the direction of  $x_1$  with Cartesian components  $(k, 0)$ .

First, the spectral radius is studied because of its importance. The spectral radius for the standard iteration is unity. Table 3.1 shows the spectral radius for the accelerated scheme as a function of the rarefaction parameter at different spatial discretizations,  $h$ , and fixed velocity discretization  $16 \times 144$ . It can be seen that at all rarefaction parameters, the spectral radius converges to the exact analytical value 0.320. The convergence in terms of the discretization is faster at low value of the rarefaction parameter. These results justify that the accelerated scheme has a better convergence behaviour than that of the standard one.

Figures 3.4-3.6 show the dependence of the convergence rate on the rarefaction parameter,  $h$  and  $M \times N$  in the whole spectrum of the wave number. In Figure 3.4, the eigenvalues are shown for  $\delta$  equal to 1, 10 and 30. The

Table 3.1: Discrete spectral radius  $\sigma_S$  of the accelerated scheme.

$h$	$\delta$				
	0.1	1.0	5.0	10.0	50.0
$10^{-1}$	0.318	0.303	0.253	0.212	0.100
$10^{-2}$	0.319	0.318	0.311	0.303	0.253
$10^{-3}$	0.320	0.319	0.319	0.318	0.311
$10^{-4}$	0.320	0.320	0.319	0.319	0.319

resolution of the spatial grid and the molecular velocity space is fixed at  $h = 10^{-3}$  and  $M \times N = 16 \times 144$ . The effect of the rarefaction parameter on the eigenvalues is clearly observed. As the rarefaction parameter becomes larger and the system approaches the hydrodynamic limit, the convergence rate exhibits slower attenuation with increasing wave number. As a consequence, the convergence remains nearly the same as at  $k = 0$  in the relevant wave length spectrum. For the standard iteration, the convergence rate is nearly unity for all wave length and high rarefaction parameter. This is the reason of the slow convergence of the standard iteration in the hydrodynamic limit. On the contrary, the convergence rate of the accelerated iteration never exceeds the limiting value of 0.320. As a consequence, much faster iteration performance is expected for the accelerated method.

In Figure 3.5, the effect of the spatial discretization is examined. Results are presented for three different resolutions, a coarse grid ( $h = 10^{-1}$ ), a fine grid ( $h = 10^{-3}$ ) and for the limiting situation, the continuous case  $h \rightarrow 0$ . The rarefaction parameter and the resolution of the molecular velocity space are given by  $\delta = 10$  and  $M \times N = 16 \times 144$ . It can be seen that the large scale behaviour of the curves is similar at different values of the spatial resolution. However, it is observed that the curves approach the limiting case  $\rightarrow 0$  as the resolution tends to zero. For the fine grid, the difference between the

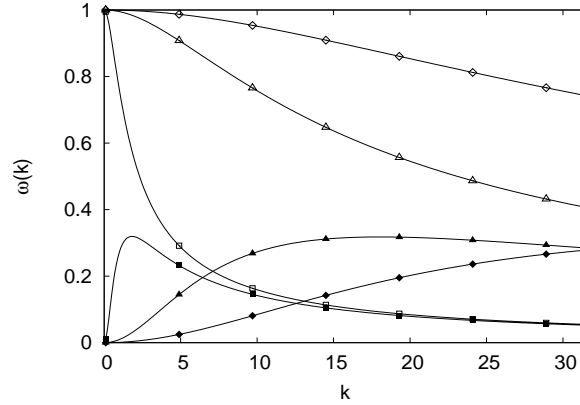


Figure 3.4: Eigenvalues  $\omega(\mathbf{k})$  as a function of the wave number  $\mathbf{k}$  at different values of the rarefaction parameter  $\delta$ . The resolution is fixed at  $h = 10^{-3}$  and  $M \times N = 16 \times 144$ . Symbols  $\square, \triangle, \diamond$  represent the results of the standard iteration for  $\delta = 1, 10$  and  $30$ , while  $\blacksquare, \blacktriangle, \blacklozenge$  represent the corresponding results of the accelerated scheme.

eigenvalue and its continuous counterpart is already invisible. This indicates that the discrete scheme converges to the continuous model as the spatial resolution becomes smaller.

Finally, Figure 3.6 shows the effects of the resolution of the molecular velocity space at  $M \times N = 16 \times 144$  and  $8 \times 24$ . The rarefaction parameter and the spatial resolution are given by  $\delta = 3$  and  $h = 10^{-3}$ . With respect to the different discretizations of the molecular velocity space, only small change can be observed on the eigenvalues. It can be seen that the difference slightly increases as the wavelength becomes larger. However, it can be concluded that there is a little effect of the discretization of the molecular velocity space on the convergence rates.

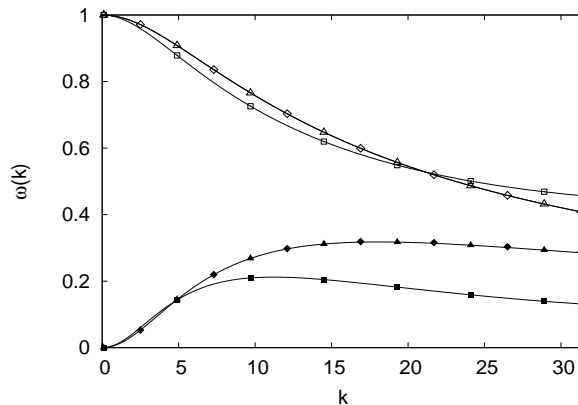


Figure 3.5: Eigenvalues  $\omega(\mathbf{k})$  as a function of the wave number  $\mathbf{k}$  at different values of spatial resolution  $h$ . The rarefaction parameter and the angular resolution are fixed at  $\delta = 10$  and  $N \times M = 16 \times 144$ , respectively. Symbols  $\square, \triangle, \diamond$  represent the results of the standard iteration for  $h = 10^{-1}, 10^{-3}$  and  $h \rightarrow 0$  (continuous limit), while  $\blacksquare, \blacktriangle, \blacklozenge$  represent the corresponding results of the accelerated scheme.

### Computational performance

In order to study the computational performance of the scheme, pressure driven gas flow through a long channel with equilateral cross section is studied. In the simulations, the flow rate  $G$  through the cross section is computed. In order to obtain the pressure driven (or Poiseuille) flow, the source term is chosen by  $S(\mathbf{x}) = -1/2$ . In the simulations, the following parameters are used  $L = 500500$ ,  $M = 16$  and  $N = 72$  and convergence error  $\epsilon = |G^{(t+1)} - G^{(t)}| < 10^{-8}$ .

Table 3.2 presents the required number of iterations, the computational time for both standard and accelerated schemes. The flow rate,  $G$ , obtained from the accelerated scheme is also presented. It is clearly seen that the accelerated method has a better computational performance. By comparing the second and third columns, it can be deduced that the required number of

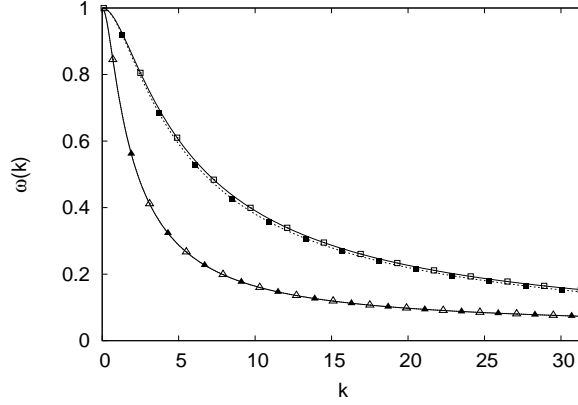


Figure 3.6: Eigenvalues  $\omega(\mathbf{k})$  as a function of the wave number  $\mathbf{k}$  at different values of the angular resolution  $M \times N$ . The rarefaction parameter and the spatial resolution are fixed at  $\delta = 3$  and  $h = 10^{-3}$ , respectively. Symbols  $\square, \triangle$  represent the results of the standard iteration for  $M \times N = 16 \times 144$  and  $8 \times 24$ , while  $\blacksquare, \blacktriangle$  represent the corresponding results of the accelerated scheme.

iterations is drastically reduced for the accelerated scheme as the rarefaction parameter becomes larger. For the standard method, the number of iteration monotonically increases as the rarefaction parameter becomes larger. On the contrary, it starts to increase for the accelerated scheme, reaches a maximum  $I = 35$  and then starts to decrease. It is noted that in the hydrodynamic limit, the iteration number decreases for the accelerated scheme because the diffusion equation provides the hydrodynamic description of the flow, so that the diffusion solver provides rapidly the hydrodynamic solution. In terms of the required computational time, it can be deduced that the accelerated scheme requires smaller computational time in the whole range of the rarefaction expect the nearly free molecular limit, where the diffusion solver may require some computational effort. The flow rate is presented in the 6th and 7th columns. At the present resolution, there are minor differences between

Table 3.2: Computational performance of the standard ( $S$ ) and accelerated ( $A$ ) schemes.

$\delta$	<i>Iterations</i>		<i>CPUtime(sec)</i>		$-G$		$-G_s$
	$S$	$A$	$S$	$A$	$S$	$A$	
0.0	2	2	87	90	0.9287	0.9287	
0.1	9	9	394	1246	0.8712	0.8712	
1.0	25	22	1126	3613	0.8320	0.8321	
3.0	62	33	2814	5383	0.9292	0.9305	
5.0	111	35	5007	5724	1.0560	1.0595	
7.0	171	35	7719	5728	1.1905	1.1969	
10.0	283	35	12441	5719	1.3977	1.4095	
30.0	1692	35	75773	5704	2.7996	2.8800	
50.0	4154	35	184735	5721	4.1605	4.3709	4.3556
100.0		34		4439		8.1190	8.1076
500.0		31		3901		3.8139(+1)	3.8109(+1)

the two results. At high values of the rarefaction degree, the results are compared to the slip flow solution. It can be seen that the slip flow solution is very close to the computed results. Practically, an excellent agreement is reached at rarefaction parameter 500.

The computational performance in terms of the number of iterations and computational time as a function of the convergence error  $\epsilon$  is also investigated. Figures 3.7 and 3.8 shows the required number of iterations and the CPU time for both iteration methods versus  $\epsilon$  at rarefaction parameters  $\delta = 3$  and 50. It can be seen that both the required number of iterations and the computational time increase with decreasing convergence error. More importantly, it is observed that the generally fewer iterations are needed for the accelerated than standard method. However, it is found that the required

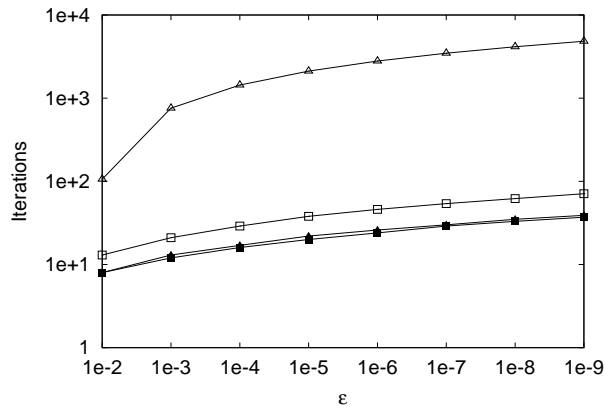


Figure 3.7: Number of iterations versus convergence criterion ( $\epsilon$ ). Symbols  $\square, \triangle$  represent kinetic results for  $\delta = 3$  and  $50$ , while  $\blacksquare, \blacktriangle$  represent the corresponding accelerated results.

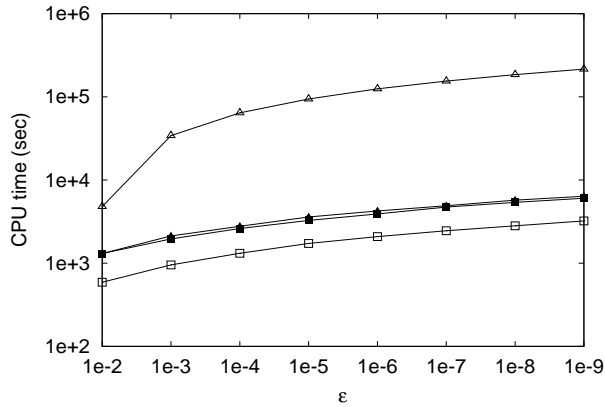


Figure 3.8: CPU time in seconds versus convergence criterion ( $\epsilon$ ). Symbols  $\square, \triangle$  represent kinetic results for  $\delta = 3$  and  $50$  while  $\blacksquare, \blacktriangle$  represent the corresponding accelerated results.

computational time is smaller only in the case of the large rarefaction parameter. The reason of this behaviour is that CPU time is required also for solving the moment equation. However, at high rarefaction parameter, the

accelerated method is clearly superior compared to the standard one. The required computational time is reduced with an order of two. Practically, for rarefaction parameters larger than 5, it is advised to use the accelerated method for a better computation.

### 3.4.3 Gaseous mixtures

For gas mixtures, the McCormack model equations [45] are solved by an accelerated discrete velocity method. In this case, the kinetic equations for the two reduced distribution functions are written by

$$c_{\alpha x} \frac{\partial \Phi_{\alpha}^{(i)}}{\partial x} + c_{\alpha y} \frac{\partial \Phi_{\alpha}^{(i)}}{\partial y} + \gamma_{\alpha} \omega_{\alpha} \Phi_{\alpha}^{(i)} = -\frac{1}{2} \sqrt{\frac{m}{m_{\alpha}}} \eta_{\alpha}^{(i)} + \omega_{\alpha} \sum_{\beta=1}^2 \left[ A_{\alpha\beta}^{(i)} + 2B_{\alpha\beta x}^{(i)} c_{\alpha x} + 2B_{\alpha\beta y}^{(i)} c_{\alpha y} + \frac{2}{5} C_{\alpha\beta}^{(i)} (c_{\alpha x}^2 + c_{\alpha y}^2 - 1) \right] \quad (3.111)$$

and

$$c_{\alpha x} \frac{\partial \Psi_{\alpha}^{(i)}}{\partial x} + c_{\alpha y} \frac{\partial \Psi_{\alpha}^{(i)}}{\partial y} + \gamma_{\alpha} \omega_{\alpha} \Psi_{\alpha}^{(i)} = -\frac{3}{4} \sqrt{\frac{m}{m_{\alpha}}} \eta_{\alpha}^{(i)} + \omega_{\alpha} \sum_{\beta=1}^2 \left[ \frac{3}{2} A_{\alpha\beta}^{(i)} + 3B_{\alpha\beta x}^{(i)} c_{\alpha x} + 3B_{\alpha\beta y}^{(i)} c_{\alpha y} + \frac{3}{5} C_{\alpha\beta}^{(i)} (c_{\alpha x}^2 + c_{\alpha y}^2) \right] \quad (3.112)$$

with  $\alpha = 1, 2$ .

The quantities of  $A_{\alpha\beta}^{(i)}$ ,  $B_{\alpha\beta j}^{(i)}$  and  $C_{\alpha\beta}^{(i)}$  on the right hand side of these equations are defined by Eqs. (3.49)-(3.51). The macroscopic quantities, the velocities, the heat-fluxes and the pressure tensors are obtained by taking

the appropriate moments of the reduced distribution functions

$$u_\alpha^{(i)} = \frac{1}{\pi} \int_{-\infty}^{\infty} \int_{-\infty}^{\infty} \Phi_\alpha^{(i)} e^{-c_{\alpha x}^2 - c_{\alpha y}^2} dc_{\alpha x} dc_{\alpha y}, \quad (3.113)$$

$$q_\alpha^{(i)} = \frac{1}{\pi} \int_{-\infty}^{\infty} \int_{-\infty}^{\infty} \left[ \Psi_\alpha^{(i)} + \left( c_{\alpha x}^2 + c_{\alpha y}^2 - \frac{5}{2} \right) \Phi_\alpha^{(i)} \right] e^{-c_{\alpha x}^2 - c_{\alpha y}^2} dc_{\alpha x} dc_{\alpha y}, \quad (3.114)$$

$$p_{\alpha jz}^{(i)} = \frac{1}{\pi} \sqrt{\frac{m}{m_\alpha}} \int_{-\infty}^{\infty} \int_{-\infty}^{\infty} c_{\alpha j} \Phi_\alpha^{(i)} e^{-c_{\alpha x}^2 - c_{\alpha y}^2} dc_{\alpha x} dc_{\alpha y}. \quad (3.115)$$

The kinetic equations, Eqs. (3.111)-(3.112), are solved in an iterative manner. In the iteration procedure, the right hand sides of these equations are calculated at the iteration step  $t$ . Then, the equations are solved yielding the distribution functions at the left hand sides at the iteration step  $t + 1/2$ . Finally, using the updated value of the distribution functions, the new macroscopic quantities are calculated at  $t + 1$ .

This standard iteration can be accelerated by supplementing the kinetic equations with two diffusion type equations. These moment equations are derived from the original equations by taking their Hermite moments. In the formalism, the following Hermite moments are introduced

$$U_{mn}^\alpha = \frac{1}{\pi} \int_{-\infty}^{\infty} \int_{-\infty}^{\infty} H_m(c_{\alpha x}) H_n(c_{\alpha y}) \Phi_\alpha e^{-c_{\alpha x}^2 - c_{\alpha y}^2} dc_{\alpha x} dc_{\alpha y}, \quad (3.116)$$

$$Q_{mn}^\alpha = \frac{1}{\pi} \int_{-\infty}^{\infty} \int_{-\infty}^{\infty} H_m(c_{\alpha x}) H_n(c_{\alpha y}) \times \left[ \Psi_\alpha + \left( c_{\alpha x}^2 + c_{\alpha y}^2 - \frac{5}{2} \right) \Phi_\alpha \right] e^{-c_{\alpha x}^2 - c_{\alpha y}^2} dc_{\alpha x} dc_{\alpha y}. \quad (3.117)$$

It is noticed that the moments  $U_{00}^\alpha$  and  $Q_{00}^\alpha$ , as special members of the general expression, are the velocity and the heat flow vectors for component  $\alpha = 1, 2$ , respectively. In order to obtain the equations of the accelerated method, the moment system with  $m + n \leq 2$  is used.

By taking the zeroth and first order Hermitian moments of the kinetic equations and manipulating the resulting equations, the following diffusion

equations are obtained

$$\begin{aligned}
& \frac{\partial^2 U_{00}^\alpha}{\partial x^2} + \frac{\partial^2 U_{00}^\alpha}{\partial y^2} - 2\omega_\alpha^2 (\nu_{\alpha\alpha}^{(3)} + \nu_{\alpha\beta}^{(3)} - \nu_{\alpha\alpha}^{(4)}) F_{\alpha\beta} + \\
& 2\omega_\alpha \omega_\beta \sqrt{\frac{m_\beta}{m_\alpha}} \nu_{\alpha\beta}^{(4)} G_{\alpha\beta} = -\frac{1}{2} \frac{\partial^2 U_{20}^\alpha}{\partial x^2} - \frac{1}{2} \frac{\partial^2 U_{02}^\alpha}{\partial y^2} - \frac{\partial^2 U_{11}^\alpha}{\partial x \partial y} + \\
& \omega_\alpha \sqrt{\frac{m}{m_\alpha}} [(S_\alpha - \nu_{\alpha\beta}^{(4)}) X_P + (S_\alpha \eta_\alpha - \nu_{\alpha\beta}^{(4)} \eta_\beta) X_C] \quad (3.118)
\end{aligned}$$

and

$$\begin{aligned}
& \frac{\partial^2 Q_{00}^\alpha}{\partial x^2} + \frac{\partial^2 Q_{00}^\alpha}{\partial y^2} + 2\omega_\alpha^2 \left[ -(\nu_{\alpha\alpha}^{(5)} + \nu_{\alpha\beta}^{(5)} - \nu_{\alpha\alpha}^{(6)}) Q_{00}^\alpha + \sqrt{\frac{m_\beta}{m_\alpha}} \nu_{\alpha\beta}^{(6)} Q_{00}^\beta - \right. \\
& \left. \frac{5}{4} \nu_{\alpha\beta}^{(2)} (U_{00}^\alpha - U_{00}^\beta) \right] + 2\omega_\alpha^2 (\gamma_\alpha - \nu_{\alpha\alpha}^{(3)} - \nu_{\alpha\beta}^{(3)} + \nu_{\alpha\alpha}^{(4)}) F_{\alpha\beta} + \\
& 2\omega_\alpha \omega_\beta \sqrt{\frac{m_\beta}{m_\alpha}} \nu_{\alpha\beta}^{(4)} G_{\alpha\beta} = -\frac{1}{2} \frac{\partial^2 U_{20}^\alpha}{\partial x^2} - \frac{1}{2} \frac{\partial^2 U_{02}^\alpha}{\partial y^2} - \frac{\partial^2 U_{11}^\alpha}{\partial x \partial y} - \\
& \omega_\alpha \sqrt{\frac{m}{m_\alpha}} [(\gamma_\alpha - S_\alpha + \nu_{\alpha\beta}^{(4)}) X_P + (\gamma_\alpha \eta_\alpha - S_\alpha \eta_\alpha + \nu_{\alpha\beta}^{(4)} \eta_\beta) X_C]. \quad (3.119)
\end{aligned}$$

In these equations,

$$F_{\alpha\beta} = \nu_{\alpha\beta}^{(1)} (U_{00}^\alpha - U_{00}^\beta) + \frac{\nu_{\alpha\beta}^{(2)}}{2} \left( Q_{00}^\alpha - \frac{m_\alpha}{m_\beta} Q_{00}^\beta \right), \quad (3.120)$$

$$G_{\alpha\beta} = \nu_{\alpha\beta}^{(1)} (U_{00}^\beta - U_{00}^\alpha) + \frac{\nu_{\alpha\beta}^{(2)}}{2} \left( Q_{00}^\beta - \frac{m_\beta}{m_\alpha} Q_{00}^\alpha \right) \quad (3.121)$$

with  $\alpha, \beta = [1, 2]$  and  $\alpha \neq \beta$ .

In the accelerated scheme, the iteration procedure works in such a way that the kinetic equation is solved first to yield the reduced distribution functions at the stage  $t + 1/2$ . By using this information, the higher-order Hermite moments in the diffusion equations are calculated. Finally, the diffusion equations are solved to provide the velocity  $U_{00}^\alpha$  and heat flow vectors  $Q_{00}^\alpha$  on the left hand side at stage  $t + 1$ .

The kinetic and diffusion equations are solved by using the finite-difference method. Both the spatial coordinates and the velocity spaces are discretized.

The discretization of the spatial space is carried out on the same triangular grid as for the BGK equation mentioned earlier. For the triangular cross section, the number of nodes along the base is set equal to 1000 for  $\delta \leq 1$  and to 1400 for  $\delta > 1$ , while for the trapezoidal cross section, the number of nodes along the large base  $B$  is set equal to 1500 for all values of  $\delta$ . The discretization of the molecular space is carried out in polar coordinate system. The number of discrete velocities is set to  $M \times N = 16 \times 300$  for  $\delta < 1$  and  $M \times N = 16 \times 72$  for  $\delta \geq 1$ . Here,  $M$  and  $N$  denote the number of magnitudes and polar angles of the discrete velocity vector. The convergence of the scheme is measured by calculating the absolute difference between subsequent values of the dimensionless flow rates. The iteration process is terminated when the absolute difference is less than  $10^{-6}$ .

### 3.5 Kinetic coefficients

Tables 3.3-3.5 show the kinetic coefficients in the whole range of the rarefaction and the concentration for  $Ne/Ar$  and  $He/Xe$  mixtures for an isosceles triangular and two isosceles trapezoidal channels with acute angle  $\omega = 54.74^\circ$ . The mass ratios of these mixtures are given by  $m_1/m_2 = [20.183/39.948, 4.0026/131.30]$ , respectively. In the following, first, the case of the triangular channel is examined. The  $\Lambda_{PP}$  coefficient describes the total flow rate of the mixture for the pressure driven flow. From the data for  $\Lambda_{PP}$ , it can be seen that the mixture exhibits the Knudsen minimum phenomenon. The flow rate has a minimum in the transition region. for all concentrations. The  $\Lambda_{CP}$  coefficient describes the diffusion of the components for the pressure driven flow. This coefficient increases as the gas becomes more rarefied. As a consequence, the diffusion effects become stronger with increasing rarefaction. In the hydrodynamic limit, there is no diffusion because of the strong intermolecular collisions. The same situation is observed for the  $\Lambda_{CC}$  coefficient,

Table 3.3: Kinetic coefficients for the isosceles triangular channel ( $\omega = 54.74^0$ ).

$\delta$	$C$	Ne/Ar			He/Xe		
		$\Lambda_{PP}$	$\Lambda_{CP}$	$\Lambda_{CC}$	$\Lambda_{PP}$	$\Lambda_{CP}$	$\Lambda_{CC}$
0	0.0	0.934	0.000	0.000	0.934	0.000	0.000
0.1	0.0	0.878	0.000	0.000	0.878	0.000	0.000
0.5	0.0	0.839	0.000	0.000	0.839	0.000	0.000
1	0.0	0.844	0.000	0.000	0.844	0.000	0.000
5	0.0	0.107(+1)	0.000	0.000	0.107(+1)	0.000	0.000
10	0.0	0.142(+1)	0.000	0.000	0.142(+1)	0.000	0.000
50	0.0	0.438(+1)	0.000	0.000	0.438(+1)	0.000	0.000
100	0.0	0.813(+1)	0.000	0.000	0.813(+1)	0.000	0.000
0	0.2	0.959	0.722(-1)	0.294	0.163(+1)	0.793	0.100(+1)
0.1	0.2	0.901	0.660(-1)	0.263	0.153(+1)	0.732	0.922
0.5	0.2	0.859	0.526(-1)	0.209	0.139(+1)	0.615	0.775
1	0.2	0.860	0.427(-1)	0.173	0.132(+1)	0.528	0.667
5	0.2	0.108(+1)	0.165(-1)	0.735(-1)	0.133(+1)	0.258	0.331
10	0.2	0.143(+1)	0.900(-2)	0.424(-1)	0.160(+1)	0.155	0.202
50	0.2	0.439(+1)	0.188(-2)	0.956(-2)	0.446(+1)	0.364(-1)	0.482(-1)
100	0.2	0.813(+1)	0.943(-3)	0.486(-2)	0.819(+1)	0.185(-1)	0.246(-1)
0	0.5	0.975	0.165	0.975	0.225(+1)	0.158(+1)	0.225(+1)
0.1	0.5	0.916	0.150	0.865	0.211(+1)	0.147(+1)	0.208(+1)
0.5	0.5	0.871	0.118	0.679	0.190(+1)	0.124(+1)	0.176(+1)
1	0.5	0.871	0.946(-1)	0.554	0.178(+1)	0.107(+1)	0.152(+1)
5	0.5	0.109(+1)	0.353(-1)	0.228	0.161(+1)	0.541	0.779
10	0.5	0.144(+1)	0.191(-1)	0.130	0.181(+1)	0.329	0.480
50	0.5	0.439(+1)	0.399(-2)	0.290(-1)	0.458(+1)	0.779(-1)	0.116
100	0.5	0.814(+1)	0.201(-2)	0.147(-1)	0.830(+1)	0.397(-1)	0.592(-1)
0	0.8	0.962	0.236	0.314(+1)	0.212(+1)	0.167(+1)	0.344(+1)
0.1	0.8	0.904	0.213	0.275(+1)	0.199(+1)	0.155(+1)	0.317(+1)
0.5	0.8	0.861	0.165	0.212(+1)	0.182(+1)	0.132(+1)	0.270(+1)
1	0.8	0.862	0.131	0.171(+1)	0.173(+1)	0.116(+1)	0.236(+1)
5	0.8	0.109(+1)	0.470(-1)	0.675	0.166(+1)	0.619	0.126(+1)
10	0.8	0.143(+1)	0.253(-1)	0.380	0.188(+1)	0.386	0.787
50	0.8	0.439(+1)	0.528(-2)	0.839(-1)	0.468(+1)	0.935(-1)	0.192
100	0.8	0.814(+1)	0.266(-2)	0.425(-1)	0.840(+1)	0.479(-1)	0.985(-1)
0	1.0	0.934	0.270		0.934	0.771	
0.1	1.0	0.878	0.242		0.878	0.701	
0.5	1.0	0.839	0.185		0.839	0.600	
1	1.0	0.844	0.145		0.844	0.533	
5	1.0	0.107(+1)	0.508(-1)		0.107(+1)	0.306	
10	1.0	0.142(+1)	0.272(-1)		0.142(+1)	0.199	
50	1.0	0.438(+1)	0.570(-2)		0.438(+1)	0.512(-1)	
100	1.0	0.813(+1)	0.287(-2)		0.813(+1)	0.265(-1)	

which describes the diffusion for the concentration driven flow. It starts to increase as the rarefaction parameter becomes smaller.

Table 3.4: Kinetic coefficients for the isosceles trapezoidal channel ( $\omega = 54.74^0$ ,  $b/h = 0.5$ ).

$\delta$	$C$	Ne/Ar			He/Xe		
		$\Lambda_{PP}$	$\Lambda_{CP}$	$\Lambda_{CC}$	$\Lambda_{PP}$	$\Lambda_{CP}$	$\Lambda_{CC}$
0	0.0	0.904	0.000	0.000	0.904	0.000	0.000
0.1	0.0	0.852	0.000	0.000	0.852	0.000	0.000
0.5	0.0	0.816	0.000	0.000	0.816	0.000	0.000
1	0.0	0.821	0.000	0.000	0.821	0.000	0.000
5	0.0	0.104(+1)	0.000	0.000	0.104(+1)	0.000	0.000
10	0.0	0.138(+1)	0.000	0.000	0.138(+1)	0.000	0.000
50	0.0	0.427(+1)	0.000	0.000	0.427(+1)	0.000	0.000
100	0.0	0.792(+1)	0.000	0.000	0.792(+1)	0.000	0.000
0	0.2	0.928	0.699(-1)	0.284	0.158(+1)	0.768	0.971
0.1	0.2	0.874	0.640(-1)	0.256	0.148(+1)	0.711	0.896
0.5	0.2	0.835	0.514(-1)	0.205	0.135(+1)	0.600	0.756
1	0.2	0.837	0.419(-1)	0.170	0.129(+1)	0.517	0.653
5	0.2	0.105(+1)	0.164(-1)	0.733(-1)	0.130(+1)	0.256	0.329
10	0.2	0.139(+1)	0.895(-2)	0.423(-1)	0.156(+1)	0.155	0.201
50	0.2	0.428(+1)	0.188(-2)	0.956(-2)	0.435(+1)	0.364(-1)	0.482(-1)
100	0.2	0.793(+1)	0.942(-3)	0.486(-2)	0.799(+1)	0.185(-1)	0.246(-1)
0	0.5	0.944	0.160	0.944	0.218(+1)	0.153(+1)	0.218(+1)
0.1	0.5	0.889	0.145	0.841	0.205(+1)	0.142(+1)	0.202(+1)
0.5	0.5	0.847	0.115	0.665	0.185(+1)	0.121(+1)	0.171(+1)
1	0.5	0.847	0.929(-1)	0.545	0.174(+1)	0.105(+1)	0.149(+1)
5	0.5	0.106(+1)	0.351(-1)	0.227	0.158(+1)	0.537	0.774
10	0.5	0.140(+1)	0.190(-1)	0.130	0.176(+1)	0.328	0.479
50	0.5	0.428(+1)	0.399(-2)	0.290(-1)	0.447(+1)	0.778(-1)	0.116
100	0.5	0.793(+1)	0.200(-2)	0.147(-1)	0.809(+1)	0.397(-1)	0.592(-1)
0	0.8	0.932	0.229	0.304(+1)	0.205(+1)	0.162(+1)	0.333(+1)
0.1	0.8	0.877	0.207	0.268(+1)	0.193(+1)	0.150(+1)	0.308(+1)
0.5	0.8	0.837	0.161	0.208(+1)	0.177(+1)	0.129(+1)	0.263(+1)
1	0.8	0.839	0.128	0.168(+1)	0.169(+1)	0.114(+1)	0.232(+1)
5	0.8	0.106(+1)	0.467(-1)	0.673	0.162(+1)	0.615	0.125(+1)
10	0.8	0.139(+1)	0.252(-1)	0.380	0.184(+1)	0.385	0.785
50	0.8	0.428(+1)	0.528(-2)	0.839(-1)	0.456(+1)	0.935(-1)	0.192
100	0.8	0.793(+1)	0.265(-2)	0.425(-1)	0.819(+1)	0.479(-1)	0.985(-1)
0	1.0	0.904	0.262		0.904	0.746	
0.1	1.0	0.852	0.235		0.852	0.681	
0.5	1.0	0.816	0.181		0.816	0.586	
1	1.0	0.821	0.143		0.821	0.522	
5	1.0	0.104(+1)	0.505(-1)		0.104(+1)	0.305	
10	1.0	0.138(+1)	0.271(-1)		0.138(+1)	0.199	
50	1.0	0.427(+1)	0.569(-2)		0.427(+1)	0.512(-1)	
100	1.0	0.792(+1)	0.287(-2)		0.792(+1)	0.265(-1)	

In this framework, the geometrical effects on the kinetic coefficients are also investigated. The results for the trapezoidal channel with  $\omega = 54.74^0$  are

Table 3.5: Kinetic coefficients for the isosceles trapezoidal channel ( $\omega = 54.74^0$ ,  $b/h = 3$ ).

$\delta$	$C$	Ne/Ar			He/Xe		
		$\Lambda_{PP}$	$\Lambda_{CP}$	$\Lambda_{CC}$	$\Lambda_{PP}$	$\Lambda_{PC}$	$\Lambda_{CC}$
0	0.0	0.965	0.000	0.000	0.965	0.000	0.000
0.1	0.0	0.892	0.000	0.000	0.892	0.000	0.000
0.5	0.0	0.830	0.000	0.000	0.830	0.000	0.000
1	0.0	0.818	0.000	0.000	0.818	0.000	0.000
5	0.0	0.965	0.000	0.000	0.965	0.000	0.000
10	0.0	0.123(+1)	0.000	0.000	0.123(+1)	0.000	0.000
50	0.0	0.354(+1)	0.000	0.000	0.354(+1)	0.000	0.000
100	0.0	0.649(+1)	0.000	0.000	0.649(+1)	0.000	0.000
0	0.2	0.991	0.746(-1)	0.304	0.169(+1)	0.819	0.104(+1)
0.1	0.2	0.916	0.675(-1)	0.267	0.156(+1)	0.748	0.941
0.5	0.2	0.850	0.530(-1)	0.208	0.139(+1)	0.617	0.775
1	0.2	0.834	0.427(-1)	0.170	0.130(+1)	0.524	0.659
5	0.2	0.975	0.166(-1)	0.727(-1)	0.122(+1)	0.254	0.325
10	0.2	0.124(+1)	0.905(-2)	0.422(-1)	0.140(+1)	0.155	0.200
50	0.2	0.355(+1)	0.188(-2)	0.956(-2)	0.362(+1)	0.364(-1)	0.482(-1)
100	0.2	0.649(+1)	0.944(-3)	0.486(-2)	0.655(+1)	0.185(-1)	0.246(-1)
0	0.5	0.101(+1)	0.170	0.101(+1)	0.233(+1)	0.164(+1)	0.233(+1)
0.1	0.5	0.932	0.153	0.879	0.216(+1)	0.150(+1)	0.212(+1)
0.5	0.5	0.863	0.119	0.674	0.190(+1)	0.124(+1)	0.176(+1)
1	0.5	0.845	0.947(-1)	0.544	0.175(+1)	0.107(+1)	0.151(+1)
5	0.5	0.982	0.355(-1)	0.226	0.150(+1)	0.533	0.765
10	0.5	0.124(+1)	0.192(-1)	0.130	0.161(+1)	0.327	0.476
50	0.5	0.356(+1)	0.399(-2)	0.290(-1)	0.374(+1)	0.778(-1)	0.116
100	0.5	0.650(+1)	0.201(-2)	0.147(-1)	0.665(+1)	0.398(-1)	0.592(-1)
0	0.8	0.995	0.244	0.325(+1)	0.219(+1)	0.173(+1)	0.356(+1)
0.1	0.8	0.919	0.217	0.279(+1)	0.203(+1)	0.158(+1)	0.323(+1)
0.5	0.8	0.852	0.166	0.210(+1)	0.182(+1)	0.132(+1)	0.269(+1)
1	0.8	0.837	0.131	0.168(+1)	0.170(+1)	0.115(+1)	0.233(+1)
5	0.8	0.978	0.472(-1)	0.669	0.154(+1)	0.607	0.123(+1)
10	0.8	0.124(+1)	0.254(-1)	0.379	0.168(+1)	0.382	0.780
50	0.8	0.355(+1)	0.528(-2)	0.839(-1)	0.383(+1)	0.935(-1)	0.192
100	0.8	0.650(+1)	0.266(-2)	0.425(-1)	0.674(+1)	0.479(-1)	0.985(-1)
0	1.0	0.965	0.279		0.965	0.797	
0.1	1.0	0.892	0.246		0.892	0.712	
0.5	1.0	0.830	0.185		0.830	0.593	
1	1.0	0.818	0.145		0.818	0.519	
5	1.0	0.965	0.510(-1)		0.965	0.296	
10	1.0	0.123(+1)	0.273(-1)		0.123(+1)	0.195	
50	1.0	0.354(+1)	0.570(-2)		0.354(+1)	0.512(-1)	
100	1.0	0.649(+1)	0.287(-2)		0.649(+1)	0.265(-1)	

compared to the ones of rectangular channels [54]. The comparison is based on the equality of the channel height and the hydrodynamic diameter. The

Table 3.6: Geometrical effects on the kinetic coefficients,  $He/Xe$  mixture with  $C = 0.5$ . The results are denoted by T and R for trapezoidal and rectangular channels, respectively.

$h/w$	$\delta^h$	$\Lambda_{PP}$		$\Lambda_{CP}$		$\Lambda_{CC}$	
		T	R	T	R	T	R
1	0	0.219(+1)	0.203(+1)	0.154(+1)	0.142(+1)	0.219(+1)	0.202(+1)
1	1	0.174(+1)	0.165(+1)	0.105(+1)	0.101(+1)	0.149(+1)	0.143(+1)
1	10	0.177(+1)	0.170(+1)	0.329	0.327	0.479	0.477
0.5	0	0.224(+1)	0.209(+1)	0.157(+1)	0.147(+1)	0.224(+1)	0.209(+1)
0.5	1	0.169(+1)	0.162(+1)	0.975	0.943	0.138(+1)	0.134(+1)
0.5	10	0.185(+1)	0.180(+1)	0.260	0.259	0.380	0.379
0.1	0	0.278(+1)	0.264(+1)	0.196(+1)	0.186(+1)	0.278(+1)	0.264(+1)
0.1	1	0.160(+1)	0.159(+1)	0.879	0.873	0.124(+1)	0.123(+1)
0.1	10	0.172(+1)	0.172(+1)	0.198	0.198	0.290	0.291

trapezoidal and rectangular channels have the same height and hydrodynamic diameter. The overall problem is characterized by the height to width ratio of the rectangular channel,  $h/w$ , and the rarefaction parameter  $\delta_h$  on the basis of the height. In order to compare the two results, the rarefaction parameter in the present formalism is converted to the one of the rectangular channel. The kinetic coefficient for the rectangular channel is converted to our formalism. Table 3.6 shows the kinetic coefficients for the simulation case  $He/Xe$  with the concentration  $C = 0.5$ . It can be seen that as the height to width ratio decreases the results of the two types of channel tend to each other. This demonstrates that as the height to width ratio becomes smaller the two channels provides the same result. In the limiting case, the two cross section becomes identical with each other.

In addition to the geometrical effects, the hydrodynamic limit of the results is also studied. For a single gas, the Poiseuille number is calculated and compared to the results of the slip flow solution [49]. The Poiseuille number is the Fanning friction factor times the Reynolds number. In the present calculation, the Poiseuille number is given by  $Po = \delta/\Lambda_{PP}$  and the  $\Lambda_{PP}$  is

Table 3.7: The Poiseuille number for triangular and trapezoid channels as a function of  $Kn_v$  for a single gas ( $C = 0$ ). The symbols K and S stand for the kinetic and slip solutions, respectively.

$Kn_v$	$Po$					
	$b/h = 0$		$b/h = 0.5$		$b/h = 2$	
	K	S	K	S	K	S
0.100	0.710(+1)	0.748(+1)	0.729(+1)	0.767(+1)	0.784(+1)	0.828(+1)
0.075	0.809(+1)	0.838(+1)	0.830(+1)	0.860(+1)	0.902(+1)	0.937(+1)
0.050	0.936(+1)	0.954(+1)	0.961(+1)	0.979(+1)	0.106(+2)	0.108(+2)
0.025	0.110(+2)	0.111(+2)	0.113(+2)	0.114(+2)	0.127(+2)	0.127(+2)
0.010	0.123(+2)	0.123(+2)	0.126(+2)	0.126(+2)	0.143(+2)	0.143(+2)

evaluated for the single gas case  $C = 0$  (or  $C = 1$ ). The rarefaction degree is described by a modified Knudsen number,  $Kn_v$ . This definition includes the effect of the first order slip coefficient. It is related to the rarefaction parameter such that  $Kn_v = \alpha_s/\delta$ , where  $\alpha_s = 1.018$  is the slip coefficient of the S kinetic model. It is mentioned that the McCormack model reduces to the S kinetic model for a single gas. Table 3.7 presents the kinetic and slip results for three types of channel with  $\omega = 54.74^0$ , a triangular and two trapezoidal ones, as a function of the  $Kn_v$ . It can be seen that the kinetic results converge to the slip solution with decreasing  $Kn_v$ . This demonstrates that the present results recover the slip solution as a limiting case.

## 3.6 Flow rates

### 3.6.1 General expressions

In practical applications, the flow rate through the microsystem is an important quantity. Basically, the flow rate can be defined as mass or molar flow rate. For single component gases, the two quantities in dimensionless form are the same because the mass of the gas is proportional to its molar

amount. However, for gaseous mixtures the two quantities are different since the flow is usually affected by diffusion effects, and the concentration is a varying quantity. Both quantities can be determined by using the present methodologies.

In this section, the mass flow rate is deduced for the gaseous mixture. When a gaseous mixture flows through a microchannel, the components have usually different average velocities at the cross section because of the gas diffusion. Usually, the lighter particle has larger average speed; as a result, the gas tends to separate. Even if the concentration of the gas is the same at the two ends of the channel, it may vary significantly along its axis. The flow of the mixture through the channel is a complex phenomenon, and the separation effect should be taken into account. However, if the gaseous diffusion is negligible, an approximation of the mass flow rate can be developed. The discussion on the flow rate starts with the development of approximated formulas by neglecting the separation effect. This consideration may be useful in engineering applications.

To begin with, the mass flow rate of the gas through the channel is considered as

$$\dot{M} = \iint_{A'} (n_1 m_1 u'_1 + n_2 m_2 u'_2) dx' dy'. \quad (3.122)$$

This quantity is constant along the channel at every cross section because of the particle and mass conservation. The mass flow rate can be rewritten by using the two thermodynamic fluxes  $J_P$  and  $J_C$  introduced earlier such that

$$\dot{M} = -m J_P + (m_2 - m_1)(1 - C) J_C. \quad (3.123)$$

The thermodynamic fluxes can be connected to the local pressure and concentration gradients via the kinetic coefficients. It is emphasized that the kinetic coefficients and the gradients of the pressure and the concentration are local quantities. The kinetic coefficients depend on the local rarefaction

parameter and the concentration. Now, the discussion is divided into two parts, whether pressure or concentration driven flow is considered.

### 3.6.2 Pressure driven flow

For the pressure driven flow, the gaseous diffusion is neglected in the present approximated formalism. As a consequence, the concentration gradient is taken to be zero. In addition, the mass flow rate is written as a function of the global pressure gradient. By neglecting the concentration gradient, the local mass flow rate can be written as

$$\dot{M} = \left[ -\Lambda_{PP} + \frac{m_2 - m_1}{m}(1 - C)\Lambda_{PC} \right] \frac{A' dP}{v dz}. \quad (3.124)$$

By using the global pressure difference with the assumption that the pressures in the upstream and downstream reservoirs are  $P_A$  and  $P_B$ , the mass flow rate can be reformulated as

$$\dot{M} = \left[ -\Lambda_{PP}^* + \frac{m_2 - m_1}{m}(1 - C)\Lambda_{PC}^* \right] \frac{A' P_B - P_A}{v L} D_h, \quad (3.125)$$

where  $\Lambda_{PP}^*$  and  $\Lambda_{PC}^*$  are the average kinetic coefficients.

By equalizing Eqs. (3.124) and (3.125), an expression for the average kinetic coefficients can be obtained such that

$$\Lambda_{PP} \frac{dP}{P_B - P_A} = \Lambda_{PP}^* dz \frac{D_h}{L}, \quad (3.126)$$

$$\Lambda_{PC} \frac{dP}{P_B - P_A} = \Lambda_{PC}^* dz \frac{D_h}{L}. \quad (3.127)$$

The average kinetic coefficients can be deduced by using the relation  $dP/(P_B - P_A) = d\delta/(\delta_B - \delta_A)$ , these equations are integrated to yield

$$\Lambda_{PP}^* = \frac{1}{\delta_B - \delta_A} \int_{\delta_A}^{\delta_B} \Lambda_{PP} d\delta, \quad (3.128)$$

$$\Lambda_{PC}^* = \frac{1}{\delta_B - \delta_A} \int_{\delta_A}^{\delta_B} \Lambda_{PC} d\delta. \quad (3.129)$$

If the kinetic coefficients are known for the considered rarefaction interval and concentration value, the average kinetic coefficients can be deduced and the mass flow rate can be calculated from Eq. (3.125). It is noted that the average kinetic coefficients have been used earlier for single gases [75]. Now, it is used with the assumption that the concentration is constant.

It is interesting to elaborate on the single gas limit of the pressure driven gas case. In this situation, the gas has only one component which can be obtained by either the condition  $C = 1$  or  $C = 0$ . Both choices provide the same result. By using the concentration  $C = 1$  in Eq. (3.125), the mass flow rate is obtained by

$$\dot{M} = -\Lambda_{PP}^* \frac{A'}{v} \frac{P_B - P_A}{L} D_h, \quad (3.130)$$

where  $\Lambda_{PP}^*$  is given by

$$\Lambda_{PP}^* = \frac{1}{\delta_B - \delta_A} \int_{\delta_A}^{\delta_B} \Lambda_{PP} d\delta. \quad (3.131)$$

It can be seen that the flow rate is proportional with the average kinetic coefficient and some other factors related to the dimension of the channel. This means that the dependence of the mass flow rate on the flow parameters is rather complex. The flow rate in dimensionless units, i.e. the average kinetic coefficient, is determined by the inlet and outlet rarefaction parameters. If these later quantities are fixed, the dimensional flow rate is proportional to the area of the cross section and the hydrodynamic diameter. In actual calculations, the inlet and outlet rarefaction parameters together with the average kinetic coefficient must be determined first, then the flow rate is obtained by the multiplication of the factors given in Eq. (3.130).

### 3.6.3 Concentration driven flow

In the case of the concentration driven flow, the movement of the gas is caused by the concentration gradient between the two ends of the channel

by assuming the same pressure everywhere along the channel. As a result, the pressure gradient is taken to be zero in this situation.

By assuming zero pressure gradient, the local mass flow rate can be written by

$$\dot{M} = \left[ -\Lambda_{CP} + \frac{m_2 - m_1}{m(C)}(1 - C)\Lambda_{CC} \right] \frac{nm(C)A'v(C)}{2C} \frac{dC}{dz}. \quad (3.132)$$

This equation can be reformulated by using the global concentration difference. Assuming that the concentrations in the upstream and downstream reservoirs are  $C_A$  and  $C_B$ , the mass flow rate can be written by

$$\dot{M} = \left[ -\Lambda_{CP}^* + \frac{m_2 - m_1}{m_a}(1 - C_a)\Lambda_{CC}^* \right] \frac{nm_a A' v_a}{2C_a} \frac{C_{II} - C_I}{L} D_h. \quad (3.133)$$

Here,  $L_{CP}^*$  and  $L_{CC}^*$  are the average kinetic coefficients. It is noted that for the concentration driven flow a reference concentration  $C_a$  and the corresponding reference mass  $m_a$  and reference molecular velocity  $v_a$  must be introduced. These quantities are needed because the concentration is a varying quantity along the axis of the channel. In the present work, the reference concentration and a reference molecular velocity is introduced as  $C_a = (C_A + C_B)/2$  and  $v_a = (v_A + v_B)/2$ .

By equalizing Eqs. (3.132) and (3.133), it can be deduced that

$$\Lambda_{CP} \frac{dC}{C_{II} - C_I} \frac{C_a}{C} \frac{mv}{m_a v_a} = \Lambda_{CP}^* dz \frac{D_h}{L}, \quad (3.134)$$

$$\Lambda_{CC} \frac{dC}{C_{II} - C_I} \frac{C_a}{C} \frac{1 - C}{1 - C_a} \frac{v}{v_a} = \Lambda_{CC}^* dz \frac{D_h}{L}. \quad (3.135)$$

By using the same scenario as for the pressure driven flow, integrating these equations, the average kinetic coefficients are obtained by

$$\Lambda_{CP}^* = \frac{1}{C_{II} - C_I} \int_{C_I}^{C_{II}} \frac{C_a}{C} \frac{mv}{m_a v_a} \Lambda_{CP} dC, \quad (3.136)$$

$$\Lambda_{CC}^* = \frac{1}{C_{II} - C_I} \int_{C_I}^{C_{II}} \frac{1 - C}{1 - C_a} \frac{C_a}{C} \frac{v}{v_a} \Lambda_{CC} dC. \quad (3.137)$$

If the kinetic coefficients are known, the average kinetic coefficients can be calculated and the mass flow rate can be deduced from (3.133) as in the case of the pressure driven flow.

### 3.6.4 Separation effect

In the previous sections, the flow rates have been deduced by neglecting the separation phenomenon. The obtained expressions are only approximations. In this section, a general formalism is developed in order to properly calculate the flow rate through the channel. In addition, both pressure and concentration distributions are deduced. It is noted that the flow rate has earlier been calculated by including the gas separation by applying a different treatment using the gas densities as primitive variables [72], [32]. However, in the present work, the problem is formulated in terms of the pressure and the concentration instead of the densities. The present formulation is considered more straightforward because it is based on directly measurable quantities.

To begin with, the mass flow rate of the components is introduced

$$\dot{M}_\alpha = n_\alpha m_\alpha \iint_{A'} u'_\alpha dy' dz'. \quad (3.138)$$

It is noted that these quantities are constant along the axis of the channel at every cross section. This happens due to the mass conservation, which is hold for each specie of the gaseous mixture. The goal of the formulation is to express the component mass flow rates as a function of the local pressure and concentration gradients. For this purpose, the mass flow rates are converted into the terms of the thermodynamic fluxes. Straightforward calculation shows that the component flow rates can be expresses as

$$\dot{M}_1 = -m_1 (C J'_P + (1 - C) J'_C), \quad (3.139)$$

$$\dot{M}_2 = -m_2 (1 - C) (J'_P - J'_C). \quad (3.140)$$

In the following, the dimensionless mass flow rates are introduced by

$$J_\alpha = \frac{2L}{m_\alpha n_A A' v_A D_h} \dot{M}_\alpha. \quad (3.141)$$

The normalization refers to the upstream reservoirs. The quantities,  $n_A, v_A$ , denote the number density and the characteristic velocity in the upstream reservoir. By using the balance equations for the thermodynamic fluxes,  $J_P, J_C$ , the dimensionless mass flow rates are obtained by

$$J_1 = -\frac{nvL}{n_A v_A D_h} \times [(C\Lambda_{PP} + (1-C)\Lambda_{CP}) X_P + (C\Lambda_{PC} + (1-C)\Lambda_{CC}) X_C], \quad (3.142)$$

$$J_2 = -\frac{nvL}{n_A v_A D_h} (1-C) [(\Lambda_{PP} - \Lambda_{CP}) X_P + (\Lambda_{PC} - \Lambda_{CC}) X_C]. \quad (3.143)$$

These equations can be more simplified by using the expression of the pressure and concentration gradients, the ideal gas law and the definition of the characteristic velocity such that

$$J_1 = -\frac{P}{P_A} \sqrt{\frac{m(C_A)}{m(C)}} \times \left[ (C\Lambda_{PP} + (1-C)\Lambda_{CP}) \frac{\partial P}{\partial \hat{z}} \frac{1}{P} + (C\Lambda_{PC} + (1-C)\Lambda_{CC}) \frac{\partial C}{\partial \hat{z}} \frac{1}{C} \right], \quad (3.144)$$

$$J_2 = -\frac{P}{P_A} \sqrt{\frac{m(C_A)}{m(C)}} \times (1-C) \left[ (\Lambda_{PP} - \Lambda_{CP}) \frac{\partial P}{\partial \hat{z}} \frac{1}{P} + (\Lambda_{PC} - \Lambda_{CC}) \frac{\partial C}{\partial \hat{z}} \frac{1}{C} \right]. \quad (3.145)$$

Here, the dimensionless coordinate along the axis of the channel  $\hat{z} = z'/L$  has been introduced. Obviously,  $\hat{z}$  takes the value of  $0 \leq \hat{z} \leq 1$ .

Eqs. (3.144) and (3.145) are the basic differential equations for the mass flow rates, including the separation phenomenon. The mass flow rates on the left hand sides are constant along the channel. These equations are

supplemented with the boundary conditions at the walls

$$P(0) = P_A, \quad P(1) = P_B, \quad (3.146)$$

$$C(0) = C_A, \quad C(1) = C_B. \quad (3.147)$$

In order to obtain the flow rates and the pressure and concentration distributions, the above equations are solved numerically. The solution is carried out by using the finite difference method. The dimensionless coordinate along the channel axis is discretized. The spatial spacing  $\Delta\hat{z} = 1/500$  has been applied in all cases. The standard Euler method is used to integrate Eqs. (3.144) and (3.145). The solution procedure starts at the inlet of the channel with the initial values of  $P_A$  and  $C_A$  dictated by the boundary condition. Assuming the mass flow rates  $J_\alpha$ , the equations are integrated to yield the pressure and concentration distributions. The values of the pressure and concentration distributions at the outlet of the channel are used to check against the outlet boundary conditions. If the boundary conditions are not satisfied, then the integrations are repeated with an updated value of  $J_\alpha$ . The iteration is terminated when an absolute convergence criterion of  $10^{-5}$  is satisfied for the downstream values of  $P(1)$  and  $C(1)$ . Practically, a doubled bisection root finding method is used to determine the proper values of the mass flow rates together the pressure and the concentration distributions [90].

In the following, a test case of binary gas flow is investigated. The mass flow rates and the pressure and concentration distributions are determined. The flow of  $He/Xe$  mixture through a channel is investigated. The channel has triangular cross section with the acute angle of  $54.74^\circ$ . The kinetic coefficients  $\Lambda_{PP}, \Lambda_{PC}, \Lambda_{CC}$  obtained earlier for this flow configuration are used in the study.

The investigated case refers to pressure ratio  $\Pi = P_A/P_B = 3$  and  $6$  and for inlet rarefaction parameter  $\delta_A = 1$  and  $10$ . The concentrations are selected as  $C_A = C_B = 0.5$  and  $C_A = C_B = 0.8$ . It is noted that the pressure ratio and the inlet rarefaction parameter ultimately determines the outlet

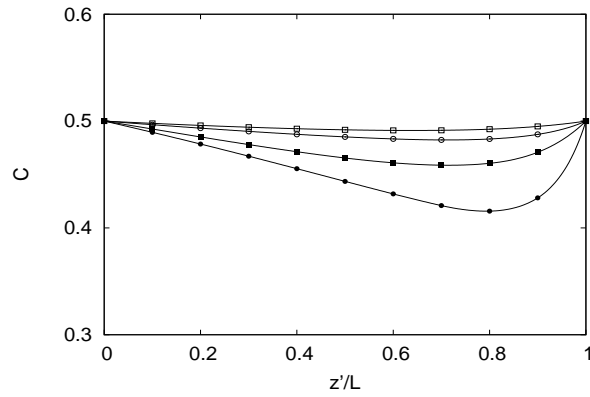


Figure 3.9: Concentration distribution along the isosceles triangular channel for the  $He/Xe$  mixture with  $C_I = C_{II} = 0.5$ . Symbols  $\square, \circ$  represent the results for  $\delta_I = 1$  and  $10$ , respectively, with pressure ratio  $\Pi = 3$ , while  $\blacksquare, \bullet$  represent the corresponding results with pressure ratio  $\Pi = 6$ .

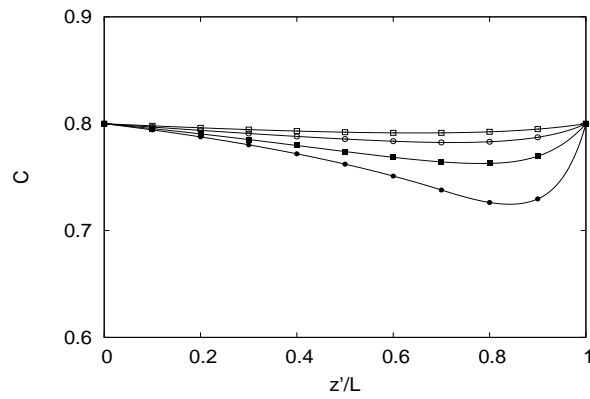


Figure 3.10: Concentration distribution along the isosceles triangular channel for the  $He/Xe$  mixture with  $C_I = C_{II} = 0.8$ . Symbols  $\square, \circ$  represent the results for  $\delta_I = 1$  and  $10$ , respectively, with pressure ratio  $\Pi = 3$ , while  $\blacksquare, \bullet$  represent the corresponding results with pressure ratio  $\Pi = 6$ .

rarefaction parameter. The above values of the pressure ratio, the rarefaction parameter and the concentrations are typical values for an experiment

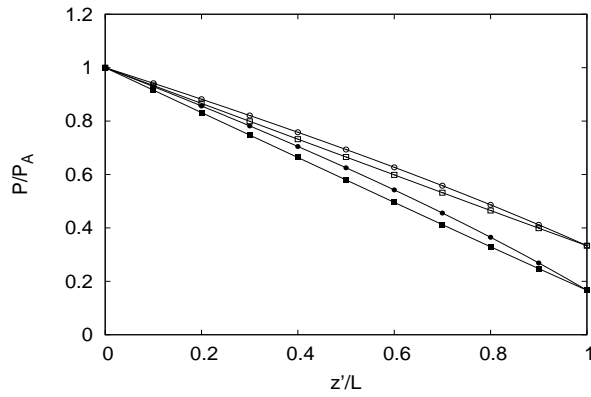


Figure 3.11: Pressure distribution along the isosceles triangular channel for the *He/Xe* mixture with  $C_I = C_{II} = 0.5$ . Symbols  $\square, \circ$  represent the results for  $\delta_I = 1$  and 10, respectively, with pressure ratio  $\Pi = 3$ , while  $\blacksquare, \bullet$  represent the corresponding results with pressure ratio  $\Pi = 6$ .

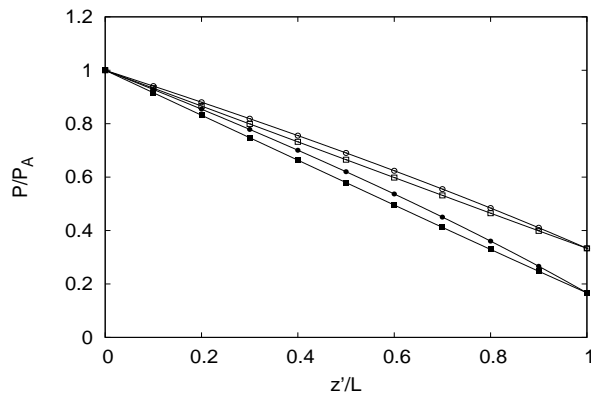


Figure 3.12: Pressure distribution along the isosceles triangular channel for the *He/Xe* mixture with  $C_I = C_{II} = 0.8$ . Symbols  $\square, \circ$  represent the results for  $\delta_I = 1$  and 10, respectively, with pressure ratio  $\Pi = 3$ , while  $\blacksquare, \bullet$  represent the corresponding results with pressure ratio  $\Pi = 6$ .

with microchannels. Figures 3.9 and 3.10 show the concentration distribution along the channel for the cases  $C_A = C_B = 0.5$  and  $C_A = C_B = 0.8$ ,

Table 3.8: Normalized fluxes and mass flow rates with and without separation effects ( $He/Xe$ ,  $C_I = C_{II} = 0.5$ ).

$\Pi$	$\delta_I$	$J_1$	$J_2$	$J_1^*$	$J_2^*$	$J_M$	$J_M^*$	$\Delta(\%)$
5	0.1	0.147(+1)	0.263	0.147(+1)	0.263	0.597	0.597	0.0
	1	0.124(+1)	0.271	0.125(+1)	0.270	0.599	0.597	0.3
	5	0.905	0.370	0.961	0.357	0.772	0.750	2.8
	10	0.801	0.485	0.883	0.460	0.989	0.944	4.5
	30	0.966	0.876	0.104(+1)	0.835	0.176(+1)	0.168(+1)	4.4
10	0.1	0.166(+1)	0.296	0.166(+1)	0.296	0.673	0.673	0.0
	1	0.141(+1)	0.304	0.142(+1)	0.302	0.673	0.671	0.4
	5	0.103(+1)	0.411	0.111(+1)	0.391	0.857	0.826	3.7
	10	0.891	0.535	0.102(+1)	0.497	0.109(+1)	0.103(+1)	6.0
	30	0.104(+1)	0.942	0.115(+1)	0.886	0.189(+1)	0.179(+1)	5.4

respectively. It is clearly seen in the figures that the concentrations are not constant along the channel. The concentrations start to decrease after the inlet, takes its minimum near the outlet and finally reaches the outlet value. The smaller value of the concentration in the channel indicates the separation phenomenon in the microchannel. The light species propagates faster than the heavier one, which results into the concentration drop in the channel. The non-uniformity of the concentration is stronger if the pressure ratio is larger. It is also found that the separation phenomenon is the strongest in the transition region. This is explained by the fact that in the hydrodynamic region the diffusion is negligible. On the other hand, in the free molecular domain there are fewer collisions between the molecules, so that the components of the gas become independent. This indicates that even if the flow speed of the components is different, the concentration is constant along the channel. The corresponding pressure distributions are shown in Figures 3.11 and 3.12. It can be seen that the pressure distributions are non-linear, and the non-linearity increases in the hydrodynamic domain. In the free molecular limit, the distributions are rather linear. A similar behavior is observed for single component gases as well.

Table 3.9: Normalized fluxes and mass flow rates with and without separation effects ( $He/Xe$ ,  $C_I = C_{II} = 0.8$ ).

$\Pi$	$\delta_I$	$J_1$	$J_2$	$J_1^*$	$J_2^*$	$J_M$	$J_M^*$	$\Delta(\%)$
5	0.1	0.156(+1)	0.708(-1)	0.156(+1)	0.708(-1)	0.528	0.528	0.0
	1	0.136(+1)	0.833(-1)	0.137(+1)	0.821(-1)	0.556	0.552	0.7
	5	0.113(+1)	0.144	0.120(+1)	0.131	0.794	0.747	5.8
	10	0.112(+1)	0.200	0.120(+1)	0.180	0.105(+1)	0.965	7.6
	30	0.154(+1)	0.362	0.160(+1)	0.340	0.182(+1)	0.173(+1)	4.9
10	0.1	0.176(+1)	0.797(-1)	0.176(+1)	0.797(-1)	0.594	0.594	0.0
	1	0.154(+1)	0.929(-1)	0.156(+1)	0.911(-1)	0.623	0.618	0.9
	5	0.127(+1)	0.160	0.137(+1)	0.142	0.885	0.818	7.6
	10	0.124(+1)	0.222	0.136(+1)	0.193	0.116(+1)	0.104(+1)	9.8
	30	0.166(+1)	0.390	0.175(+1)	0.360	0.196(+1)	0.184(+1)	6.2

Finally, Tables 3.8 and 3.9 present the flow rates with and without the inclusion of the separation as determined from the calculation for  $C_I = C_{II} = 0.5$  and  $C_I = C_{II} = 0.8$ , respectively. The pressure ratio and the rarefaction parameter are selected as  $\Pi = 5$  and 10 and  $\delta_I = 0.1, 1, 5, 10$  and 30. It is observed that for  $\delta_I = 0.1$  and 1, the differences between  $J_M$  and  $J_M^*$  are negligible. In this cases, the separation effects are not so important and may be ignored. However, for  $\delta_I = 10, 5$  and 30, there are some discrepancies. It is seen that in the case of the large pressure ratio the relative error defined as  $\Delta = (J_M - J_M^*)/J_M$  varies between 3.7 – 7.6% for  $\delta_I = 5$ , 6.0 – 9.8% for  $\delta_I = 10$  and 5.4 – 6.2% for  $\delta_I = 30$ .

# Chapter 4

## Simulation of binary gas flows through microchannels of finite length

### 4.1 Introduction

The flow in short channels basically differs from the case of long channels. In this situation, the length of the channel compared to its diameter is relatively small. The usual length to hydrodynamic diameter ratio is in the range of 0 – 10. Because of the shorter length, the velocities of the gas components are generally larger for finite pressure drops between the inlet and the outlet of the channel. The gas velocity can be as high as the molecular velocity of the components. The velocity can even become larger than this value in specific situations. Under these conditions, the gas is far out of absolute equilibrium and the flow is non-linear. In order to simulate rarefied gas flows under these conditions, the full non-linear Boltzmann equation needs to be solved. The solution of the problem can be obtained by the DSMC method [8]. On the other hand, the inlet and outlet effects can not be neglected

for short channels. As a consequence, the total geometrical configuration involving the channel and the upstream and downstream reservoirs have to be considered in the numerical simulations.

In the present investigation, the flow through short tubes [92], [94] including the orifice, which is a short tube with zero length, and slits is examined. The case of tubes has cylindrical symmetry. The cylindrical configuration of flows through short tubes can be projected into the two dimensional sheet spanned by the channel axis and the radial coordinate. The flow through a slit is also a two-dimensional configuration. In this situation, the relevant coordinate directions refer to the center line of the slit and the transverse coordinate along its height.

## 4.2 Flow configuration

### 4.2.1 Flow through short tubes

The flow of gaseous mixtures through short tubes having radius  $R$  and length  $L$  is simulated. The channel axis lies in the  $x'$  direction while the radial coordinate is denoted by  $r'$ . The characteristic length of the problem is chosen as the radius of the tube. The channel is located between upstream (A) and downstream (B) cylindrical containers having radii  $R_A, R_B$  and length  $L_A, L_B$ .

The mixture consists of two components  $\alpha = 1, 2$  having molecular masses  $m_\alpha$  and molecular diameters  $d_\alpha$ . It is always assumed that the first species is the lighter component. The number densities of the components are denoted by  $n_\alpha$ . The total number density of the mixture is given by  $n = n_1 + n_2$ . The mixture composition is characterized by the concentration of the first component

$$C = \frac{n_1}{n}. \quad (4.1)$$

The concentration is a local quantity and generally varies in the geometry of the flow. The concentration in the upstream reservoir  $C_A$  is used as a reference value, while  $C_B$  is the concentration in the downstream reservoir. The concentrations in the two reservoirs are taken to be equal  $C_A = C_B$ . The pressure of the gas is denoted by  $P$ . The pressures in the upstream and downstream reservoirs are  $P_A$  and  $P_B$ , respectively. The flow is driven by the pressure difference between the two containers, and it is assumed that  $P_A > P_B$ ; as a result, the gas flows from container A towards container B. The temperature is denoted by  $T$  and its values in the two reservoirs  $T_A$  and  $T_B$  are taken to be equal to a reference temperature  $T_0$  as  $T_A = T_B = T_0$ .

The gas rarefaction is characterized by the rarefaction parameter

$$\delta = \frac{PR}{\mu(C)v(C)}. \quad (4.2)$$

Here,  $\mu(C)$  denotes the mixture viscosity and  $v(C)$  is the characteristic molecular velocity defined by

$$v(C) = \sqrt{\frac{2kT}{m(C)}}, \quad (4.3)$$

where  $k$  is the Boltzmann constant and  $m(C) = Cm_1 + (1 - C)m_2$  is the average mass of the mixture. The rarefaction parameter is also a local quantity in the geometrical configuration. Its value in the upstream reservoir

$$\delta_A = \frac{P_A R}{\mu_0(C_A)v_0(C_A)} \quad (4.4)$$

is introduced as a reference quantity to characterize the flow problem. In this formulation, the reference characteristic velocity  $v_0(C_A) = \sqrt{2kT_0/m(C_A)}$  and the viscosity  $\mu_0(C_A)$  are introduced on the basis of the reference upstream concentration  $C_A$  and temperature  $T_0$ .

The main macroscopic quantities of the problem are the species densities  $n_\alpha$ , velocities  $\mathbf{u}'_\alpha$  and the temperature  $T$ . Another important quantity of the

flow problem is the component flow rates through the tube  $J'_\alpha$  defined as

$$J'_\alpha = \int_{A'} n_\alpha u'_{\alpha x} dA', \quad (4.5)$$

where  $u'_{\alpha x}$  is the axial component of the macroscopic gas velocity of species  $\alpha$  and the integration refers to the inlet cross section  $A' = R^2\pi$ . For later purposes, the dimensionless flow rates are introduced by

$$J_\alpha = \frac{J'_\alpha}{n_A A' v_0(C_A)}, \quad (4.6)$$

where  $n_A$  is the total number density in the upstream reservoir. The total flow rate of the mixture is obtained by  $J = J_1 + J_2$ .

## 4.2.2 Flow through slits

The flow of gaseous mixtures is considered through a slit having height  $H$  between upstream (A) and downstream (B) rectangular reservoirs, which have lengths  $L_A, L_B$  and heights  $2H_A, 2H_B$ , respectively. The height of the channel  $H$  is chosen as the characteristic length of the problem. The normal vector of the slit lies in the  $x'$  direction, while the tangential one in the  $y'$  direction. The center of the slit is in the origin of the coordinate system.

The characterization of the mixture and the flow is similar to that of the short tube problem. The concentration of the mixture is defined by Eq. (4.1), while its value  $C_A$  in container A is used as a reference quantity. The definition of the rarefaction parameter is based on the channel height such that

$$\delta = \frac{PH}{\mu(C)v(C)}. \quad (4.7)$$

In the same manner, its value  $\delta_A$  in the upstream reservoir is used to characterize the problem.

The flow rates of the species are defined by

$$J'_\alpha = \int_{-H/2}^{H/2} n_\alpha u'_{\alpha x} dy', \quad (4.8)$$

where the integration refers to the transverse coordinate  $y'$  along the slit. The dimensionless flow rates are introduced according to

$$J_\alpha = \frac{J'_\alpha}{n_A H v_0 (C_A)}. \quad (4.9)$$

## 4.3 The DSMC algorithm for binary gas flows

### 4.3.1 General considerations

The direct simulation Monte-Carlo method is a particle based approach to simulate the dynamics of gases [8]. It is more suitable in the rarefied region, where there are relatively fewer collisions between the molecules and the Mach-number is higher, which indicates larger signal to noise ratio. The DSMC is a gas model, where the individual motion of model particles is simulated in the real geometry and the relevant macroscopic quantities are obtained as averages of the microscopic motion. It was revealed that the DSMC provides the solution of the Boltzmann equation in the limit of dense resolution of the spatial and temporal scales and by using infinite model particles [102].

In the approach, model particles mimic the motion of the real molecules. undergoing streaming and collision. The geometry of the configuration is divided into a collection of cells. In order to simulate the gas dynamics, the time-splitting approach is applied in the Boltzmann equation. The continuous time evolution is replaced by a discrete time-marching scheme with a finite time step. Here, the No Time Counter scheme, which assumes constant time step, is adopted [8]. The dynamics is divided into moving and collision steps. In the moving part, the particles move along free trajectories

corresponding to their speeds. Upon colliding with the boundaries of the domain, they may undergo specific boundary treatments. In the collision step, the collisions between the molecules are modeled in a probabilistic manner. Only binary collisions are considered as in the Boltzmann equation. Some molecule pairs are selected in each cell for collision with given distribution regarding molecular types and velocities, and the pairs collide as defined by the molecular interaction. In the present work, the hard-sphere (HS) [8], the variable hard-sphere (VHS) [8] and the variable soft-sphere (VSS) [37] models are considered to describe the interaction. The difference between these models is that they produce different transport coefficients of the gas. For nearly isothermal binary gases, the viscosity and the diffusion are the two primary coefficients. The ratio of these two quantities, the Schmidt number, is fixed for the HS model, while it is variable in the VSS model. The post-collisional velocities of the molecules are calculated in accordance with the interaction law. It is noted that this calculation also contains probabilistic elements. The impact parameter of the two colliding particles is selected in a probabilistic manner. Finally, a sampling stage is applied in each time step in order to calculate the macroscopic quantities. In each cell, these macroscopic quantities of the gas are deduced as the averages of the corresponding quantities of the particles residing in the cell. To summarize, in the actual algorithm, the following steps are applied repeatedly

- Moving
- Boundary conditions
- Collision
- Sampling

The detailed description of the computational domain for the investigated flow configurations and the elements of the algorithm is provided in the forthcoming sections.

### 4.3.2 Computational domain and grid

In the DSMC, the geometry consisting of the short channel and the connecting reservoirs is considered as the computational domain. In all cases, three-level grid-size distribution is used, which provides finer resolution around the channel, where a stronger change of the macroscopic quantities of the gas is expected. In addition, weighting zones are adopted to increase the efficiency of the DSMC. In these zones, the particles have different weights. Regions with smaller weights represent the same particle density with larger model particle density. As a consequence, the statistical scattering may be reduced by multiplying the model particles in the different zones if it is necessary. In the following, the computational grid and the zones are discussed in all situations.

#### Short tube

Since the short tube problem is axial symmetric, the simulation refers to the  $x', r'$  two-dimensional coordinate sheet. The computational geometry with the cell distribution is show in Figure 4.1. There are rectangular cells in the  $x', r'$  sheet. The second-level grid is applied in the zone  $-R < x' < R + L$  and  $0.5R < y' < 2R$  outside the tube or  $0.5R < y' < R$  inside the tube. The third-level grid is utilized in the region  $-0.25R < x' < 0.25R + L$  and  $0.75R < y' < 1.25R$  outside the tube or  $0.75R < y' < R$  inside the tube. In addition to the grid refinement, weighting zones are introduced. This technique is applied for the downstream reservoir, where there could be smaller amount of particles than in the upstream one due to the large pressure drop. On the other hand, radial weighting zones are applied in the whole configuration. By the aid of this solution, the model particle density is increased near the axis in order to balance the density reduction caused by the cylindrical projection. The boundaries of the axial and radial zones are at  $x' = 0$  and  $y' = [0.25R, 0.5R, 0.75R, R, 2R, 3R]$ .

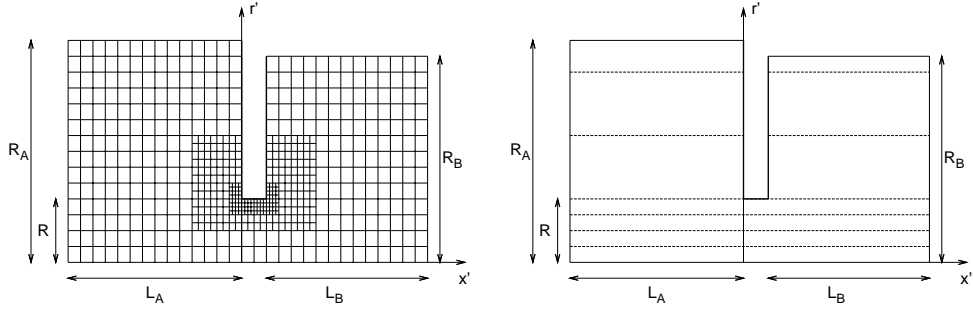


Figure 4.1: The computational domain (left) and the weighting zones (right) for the short tube problem. Thick lines denote the physical walls.

### Slit

The simulation of the motion of the particles is considered in the  $x', y'$  coordinate sheet. This computational domain is similar to the short tube case by exchanging the radial coordinate  $r'$  with  $y'$ . The geometry is presented in Figure 4.2 for completeness purposes. As it can be seen, the computational domain refers to the half of the entire domain in the direction of  $y'$  because of the mirror-symmetry regarding the  $y' = 0$  coordinate plate. The delimiters of the grids with different levels are exactly the same as for the short tube problem with the exchange of  $R \leftrightarrow H/2$  and setting  $L = 0$ . Weighing zone is also applied at  $x' = 0$ , where the downstream reservoir having the gas at a smaller pressure connects to the slit.

### 4.3.3 Moving

In the moving step of the algorithm, the particles move along free trajectories without collisions. Without external forces the velocity of the molecules,  $v'_{\alpha k}$  for the  $k$ -th molecule from component  $\alpha$ , are kept constant, while their

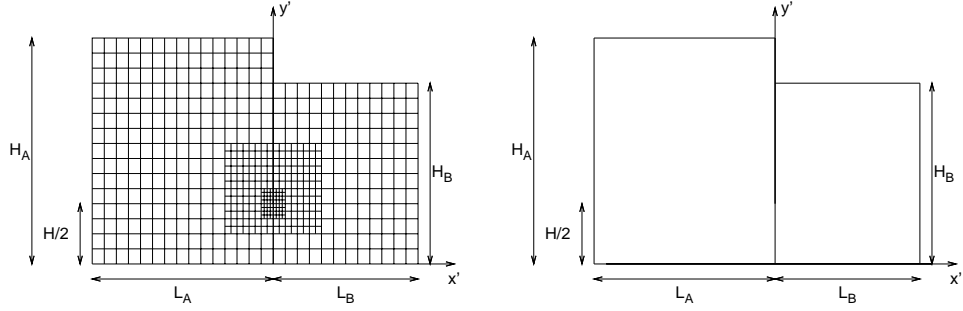


Figure 4.2: The computational domain (left) and the weighting zones (right) for the slit flow problem. Thick lines denote the physical walls.

coordinates  $\mathbf{r}'_{\alpha k}$  are updated according to

$$\mathbf{r}'_{\alpha k}(t + \Delta t) = \mathbf{r}'_{\alpha k}(t) + \mathbf{v}'_{\alpha k}(t)\Delta t \quad (4.10)$$

in each time step  $\Delta t$ .

### 4.3.4 Boundary conditions

In the computational domain, there are three types of boundaries: physical walls, where the particles collide with a real solid surface, open walls at the external side of the containers, where molecules leave and enter the domain freely, and symmetry boundaries, where the domain is delimited because of the mirror symmetry of flow configuration. Each of these boundary conditions is described in the following.

At the solid walls, the diffuse reflection boundary condition is applied. For silicon materials, this boundary condition is sufficient because the accommodation coefficient is nearly unity for this type of matter [87]. When colliding with the wall, the particle is immediately emitted in accordance with the Maxwell equilibrium distribution with temperature  $T_0$ . These solid walls in Figures 4.1 and 4.2 are presented with thick lines.

On the open surfaces of the reservoirs, the particles leave the domain freely and new particles are generated with the equilibrium distribution for the corresponding gas pressure, concentration and temperature  $T_0$ . The number of particles entering through the unit surface of the domain during time step  $\Delta t$  for components  $\alpha = [1, 2]$  in the reservoirs  $i = [A, B]$  can be determined from the equilibrium conditions such that

$$N_{Ent,1}^{(i)} = n_A \frac{P_i}{P_A} C_A \sqrt{\frac{m(C_A)}{m_1} \frac{v_0(C_A)}{2\sqrt{\pi}}} \Delta t, \quad (4.11)$$

$$N_{Ent,2}^{(i)} = n_A \frac{P_i}{P_A} (1 - C_A) \sqrt{\frac{m(C_A)}{m_2} \frac{v_0(C_A)}{2\sqrt{\pi}}} \Delta t. \quad (4.12)$$

On symmetry boundaries due to the mirror symmetry, the specular reflection (or symmetric) boundary condition is used. This boundary condition is applied at the bottom surface at  $y' = 0$  for the slit flow problem.

### 4.3.5 Collision modeling

In the collision step, the intermolecular collisions between the molecules are simulated in each cell. Molecule pairs are chosen in a probabilistic manner. In accordance with the Boltzmann equation, the probability of the collision between two molecules is proportional to the scattering cross section and the absolute relative velocity of the molecules. The distribution can be reproduced by pre-selecting some particles for collisions and applying an acceptance rejection method for the final distribution.

For gaseous mixtures, the selection of the particles for collision depends on the types of the particles. The selection is group dependent, where there are three collisional groups for collisions between molecules with type 1 – 1, 1 – 2 and 2 – 2. In the first group, the particle from the first component collides with the particle from the first one. In the second group, the particle from the first component collides with the particle from the second one. Finally,

in the third group, the particle from the second component collides with the particle from the second one.

In the present work, the No-Time-Counter scheme [8] is applied for the selection of the particles for collision. Accordingly, first, some particles are preselected for collision. Their number for component  $\alpha$  and  $\beta$  during time step  $\Delta t$  in the cell is given by

$$N_{\alpha\beta} = \frac{1}{2V_C} N_\alpha \bar{N}_\beta (\sigma_{T,\alpha\beta} v_{R,\alpha\beta})_{max} \Delta t, \quad (4.13)$$

where  $V_C$  is the volume of the cell,  $N_\alpha$  is the total number of particles from component  $\alpha$  in the cell,  $\bar{N}_\beta$  is the average number of particles for component  $\beta$  in the cell in the previous time steps,  $\sigma_{T,\alpha\beta}$  is the total collision cross section and  $v_{R,\alpha\beta}$  is the relative velocity between the molecules. From this preliminary selection, the collision is finally selected by using an acceptance-rejection method which reproduces the true distribution of the colliding particles. The detailed formulation of the collision treatment will be outlined in the forthcoming sections.

At this point, it is mentioned that it may also be possible to select the particles for collision independently of their types. In this case, the selection is group independent, and the correct distribution of the colliding particles with respect to their types is obtained in a probabilistic manner. Although the group dependent and independent selection mechanisms are identical by taking the continuous limit with very large number of particles, in the present work, the group dependent collision algorithm is used because, in that case, the collision rate for the species is free from statistical scattering and exactly reproduced.

### Hard-sphere model

In the hard-sphere interaction model, the particles are assumed to be spheres with diameters  $d_\alpha$  for component  $\alpha$ . The collisions are elastic and the mechanics of the collision follow the collision of two mechanically rigid spheres.

Generally, the collision cross section is determined from the diameters of the molecules. However, these quantities should be expressed by the relevant spatial scale of the problem through the rarefaction parameter.

In the present situation, the cross section for collisions between the particles of the first component is derived. For the hard-sphere interaction, this quantity is obtained from the dynamic viscosity of the first species  $\mu(1)$  [56] such that

$$\sigma_{T,11} = 1.016034 \frac{5}{16} \frac{\sqrt{\pi m_1 k_B T_0}}{\mu(1)}. \quad (4.14)$$

By using the definition of the rarefaction parameter, the characteristic velocity and the ideal gas law, the cross section is obtained by

$$\sigma_{T,11} = 1.016034 \frac{5}{16} \sqrt{2\pi} \sqrt{\frac{m_1}{m(C_A)}} \frac{\delta_A}{n_A L_C} \frac{\mu_0(C_A)}{\mu_0(1)}. \quad (4.15)$$

where  $L_C$  is the characteristic length of the problem, appearing in the definition of the rarefaction parameter. The collision cross section defined by Eq. (4.15) depends on the ratio of the viscosities  $\mu(1)/\mu(C_A)$ , which can be obtained in a standard manner for hard-sphere gases [53]. The viscosity for the binary gas can be written as  $\mu(C) = \mu_1 + \mu_2$ , where  $\mu_\alpha$  is given by

$$\mu_\alpha = P_{0\alpha} \frac{\Psi_\beta + \nu_{\alpha\beta}^{(4)}}{\Psi_\alpha \Psi_\beta - \nu_{\alpha\beta}^{(4)} \nu_{\beta\alpha}^{(4)}}, \quad (4.16)$$

where

$$\Psi_\alpha = \nu_{\alpha\alpha}^{(3)} - \nu_{\alpha\alpha}^{(4)} + \nu_{\alpha\beta}^{(3)} \quad (4.17)$$

with  $\alpha = [1, 2]$  and  $\alpha \neq \beta$ . In the above expression,  $P_{0\alpha} = n_{0\alpha} k T_0$  is the partial pressure with  $n_{0\alpha}$  denoting the component densities and  $\nu_{\alpha\beta}^{(k)}$  are the collision frequencies, expressions of which can be deduced for hard spheres. By using Eq. (4.16), the viscosity ratio is calculated. It is noted that  $\mu(1) = \mu_1$  and  $\mu(0) = \mu_2$ . From  $\sigma_{T,11}$  given by Eq. (4.15) in terms of

the defining quantities of the flow problem, the remaining components of the collision cross section are obtained by  $\sigma_{T,12} = \sigma_{T,21} = \sigma_{T,11}(d_{12}/d_{11})^2$  and  $\sigma_{T,22} = \sigma_{T,11}(d_{22}/d_{11})^2$ . Substituting the expressions of the total collision cross sections into Eq. (4.13), the number of preselected particles in the cell can be deduced.

The final selection for collision is obtained by applying the acceptance-rejection method for the molecular velocity since the cross section is constant in Eq. (4.13). The preselected pair is accepted (or not) for collision on the basis of the probability  $p = v_{R,\alpha\beta}/(v_{R,\alpha\beta})_{max}$ .

The post-collisional velocities of the particles can be deduced from elementary mechanics. Two colliding particles with masses  $m_\alpha, m_\beta$  and initial velocities  $\boldsymbol{\xi}_\alpha, \boldsymbol{\xi}_\beta$  are considered. The velocity of the center of mass is given by

$$\mathbf{u}_A = \frac{m_\alpha \boldsymbol{\xi}_\alpha + m_\beta \boldsymbol{\xi}_\beta}{m_\alpha + m_\beta}. \quad (4.18)$$

This quantity is a collisional invariant and takes the same value before and after the collision. The main quantities in the calculation are the relative particle velocities respect to the centre of mass

$$\hat{\mathbf{u}}_\alpha = \boldsymbol{\xi}_\alpha - \mathbf{u}_A, \quad \hat{\mathbf{u}}_\beta = \boldsymbol{\xi}_\beta - \mathbf{u}_A. \quad (4.19)$$

The hard-sphere collision for binary mixtures is isotropic. As a consequence, the post-collisional relative velocities can be obtained from an isotropic rotation of the pre-collisional relative velocities. The post-collisional values can be written by

$$\hat{\mathbf{u}}'_\alpha = |\mathbf{u}_\alpha| \mathbf{e}, \quad \hat{\mathbf{u}}'_\beta = -|\mathbf{u}_\beta| \mathbf{e}, \quad (4.20)$$

where  $\mathbf{e}$  is a randomly selected unit vector with equal probability for all spherical angles. Finally, the post-collisional particle velocities can be obtained by moving back to the real, laboratory coordinate system

$$\boldsymbol{\xi}'_\alpha = \hat{\mathbf{u}}'_\alpha + \mathbf{u}_A, \quad \boldsymbol{\xi}'_\beta = \hat{\mathbf{u}}'_\beta + \mathbf{u}_A. \quad (4.21)$$

### Variable hard-sphere

The usefulness of the hard-sphere model is its relatively simplicity for practical implementation. It is also physically acceptable for nearly isothermal simulations. However, the model provides a temperature dependence of the viscosity as  $(T/T_0)^{1/2}$ . In realistic application, the exponent should be around 0.75. To overcome this difficulty, the VHS model [8] can be used, where the diameter of the molecule depends on the relative velocity, but the deflection angle of the collision is the same as for the HS model. By using this idea, an arbitrary temperature exponent in the viscosity can be achieved. However, in the present work, this model is not used because the flow is nearly isothermal.

### Variable soft-sphere

The VSS model was developed to obtain a variable ratio for the viscosity and the diffusion coefficient [37], [8]. In the method, the molecular diameter depends on the relative velocity of the molecules in the same manner as for the VHS model. In addition, the deflection angle for the collision is slightly modified compared to the HS model.

The total cross section for similar particles  $\sigma_{\alpha\alpha}$  with  $\alpha = 1, 2$  can be connected to the viscosity of the individual components. In terms of the viscosity, the cross section can be written by

$$\sigma_{\alpha\alpha} = \pi \frac{5(a_\alpha + 1)(a_\alpha + 2)\sqrt{m_\alpha/\pi}(kT_0)^{\omega_\alpha}}{16a\Gamma(9/2 - \omega_\alpha)\mu_\alpha E_t^{\omega_\alpha - 1/2}}, \quad (4.22)$$

where  $a_\alpha$  and  $\omega_\alpha$  are the coefficient for the deflection angle and the temperature exponent for the viscosity, which can be obtained from databases for each species. In addition,  $E_t$  is the translational energy with regard to the relative velocity. This relationship can be used to determine the cross section in units of the relevant spatial scale through the rarefaction parameter as in

the case of the HS model such that

$$\sigma_{\alpha\alpha} = \sqrt{2\pi} \frac{5(a_\alpha + 1)(a_\alpha + 2)}{16a\Gamma(9/2 - \omega_\alpha)} \times \left( \frac{m_\alpha}{m(C_A)} \right)^{1-\omega_\alpha} \frac{\delta_A}{n_A L_C} \left( \frac{v_r}{v_0(C_A)} \right)^{(1-2\omega_\alpha)} \frac{\mu_0(C_A)}{\mu_0(\alpha)}. \quad (4.23)$$

It is noted that the HS result can be obtained by using the HS data,  $a_\alpha = 1$  and  $\omega_\alpha = 1/2$ .

The total cross section for unlike molecules  $\sigma_{12}$  can be deduced from the diffusion coefficient such that

$$\sigma_{12} = \pi \frac{3(a_{12} + 1)(2kT_0)^{\omega_{12}}}{16\Gamma(7/2 - \omega_{12})(\pi m_r)^{1/2} n_A D_{12} (2E_t)^{\omega_{12}-1/2}}, \quad (4.24)$$

where  $a_{12}, \omega_{12}$  are the corresponding parameters for the deflection angle and the viscosity. If these parameters are not available in tabulated forms, the average of the single gas results may be used. In addition,  $m_r = m_1 m_2 / (m_1 + m_2)$  is the reduced mass of the components, and  $D_{12}$  is the diffusion coefficient. This expression can be reformulated in the units of the problem by using the rarefaction parameter and the definition of the reference Schmidt number in container A,  $Sc_A = \mu(C_A) / (m(C_A) n_A D_{12})$  as

$$\sigma_{12} = 2\sqrt{\pi} \frac{3(a_{12} + 1)}{16\Gamma(7/2 - \omega_{12})} \frac{Sc_A \delta_A}{n_A L_C} \left( \frac{v_r}{v_0(C_A)} \right)^{(1-2\omega_\alpha)}. \quad (4.25)$$

Eqs. (4.23) and (4.25) are used to determine the number of preselected pairs in the DSMC algorithm.

The final selection for collision is obtained by applying the acceptance-rejection method for both the cross section and the molecular velocity. The preselected pair is accepted (or not) for collision based on the probability  $p = \sigma_{\alpha\beta} v_{R,\alpha\beta} / (\sigma_{\alpha\beta} v_{R,\alpha\beta})_{max}$ .

The post-collisional velocities in the collision treatment can be obtained from the deflection angle for the interaction. As it has been mentioned, this expression differs from the corresponding one for HS gas. The particular expression for the post-collisional velocities is given in Ref. [8].

### 4.3.6 Sampling of macroscopic quantities

The macroscopic quantities in the cell, the density, the velocity and the temperature, are obtained in the sampling procedure. The determination of these quantities follows from their microscopic definition. The sampling step in the DSMC provides the instant value of the macroscopic quantities in the cells. However, for steady state simulations, the averaging can be extended for the whole simulation time, which produces the ensemble average of the quantities being identical with the physical values.

The number density of the components in the cell can be obtained by

$$\frac{n_\alpha}{n_0} = \frac{\overline{N}_\alpha V_A}{N_A V_C}, \quad (4.26)$$

where  $N_A$  denotes the total number of particles initially distributed in the upstream reservoir and  $V_A$  is the volume of the upstream reservoir. The bar denotes the operation of the time average.

The dimensionless macroscopic velocity vector for the components is determined by

$$\frac{\mathbf{u}'_\alpha}{v_0(C_A)} = \frac{1}{N_{T\alpha}} \sum_{i=1}^{N_{T\alpha}} \mathbf{v}_{\alpha i}, \quad (4.27)$$

where  $N_{T\alpha}$  is the total number of particles from component  $\alpha$  in the cell during the sampling time and  $\mathbf{v}_{\alpha i}$  is the dimensionless velocity of the  $i$ -th molecule from component  $\alpha$  in the cell.

In the same manner, the dimensionless temperature of the gas can be obtained such that

$$\frac{T}{T_0} = \frac{2}{3} \frac{1}{N_T} \sum_{\alpha=1}^2 \sum_{i=1}^{N_{T\alpha}} \frac{m_\alpha}{m(C_A)} (\mathbf{v}_{\alpha i} - \mathbf{u})^2 \quad (4.28)$$

where  $N_T = N_{T1} + N_{T2}$  is the total number of particles in the cell during the sampling period. In addition, the dimensionless macroscopic velocity of the mixture is given by  $\mathbf{u} = (n_1 m_1 \mathbf{u}_1 + n_2 m_2 \mathbf{u}_2) / (n_1 m_1 + n_2 m_2)$  with  $\mathbf{u}_\alpha = \mathbf{u}'_\alpha / v_0(C_A)$ .

### 4.3.7 Computational details

Some details of the implementation of the computational algorithm in the DSMC code is discussed in the following. The code applies the routines: 1. initialization, 2. moving, 3. indexing, 4. colliding, 5. sampling. After initialization, the code repeatedly uses the moving, indexing, colliding and sampling routines.

The code starts with the initialization routine. In this part of the code, the basic elements of the scheme are defined. This involves setting up the cell structure, with the coordinates of the vertexes of the cells. The cells are numbered in accordance with their positions in the spatial domain. The cell number can be recalculated from an arbitrary point of the cell. Then, the initial particles are distributed in the cells in accordance with the macroscopic quantities.

After the initialization routine, the program switches to the moving step, when the coordinates of the particles are updated. The boundary conditions are also enforced. In the moving step, the effect of the weighting zone is also considered. Finally, the cell number for a particle is updated if the particle moves from one cell to another. The cell number of each particle is stored in the memory.

In the next stage, the scheme enters the indexing step. When the particles are selected for collision, the identifiers of the particles residing in the cell are to be known. After the moving step, the particles are arranged into tables, which contain the particles in sequences by their occurrence in the cells. In the present DSMC, a doubled particle table is used for the two components of the mixture.

In the colliding step, the intermolecular collisions are simulated. For each cell, the actual preselected pairs for collision are determined for the different collision groups. After the pre-selection, the final distribution is obtained by using the acceptance-rejection method. The post-collisional velocities of the

particles are calculated from the collision rule.

Finally, the macroscopic quantities are calculated in the sampling step.

## 4.4 Results and discussions

### 4.4.1 Flows through short tubes and orifices

In this section, the results for the short tube problem in terms of the flow rates and the axial distribution of the macroscopic quantities are presented and discussed. The parameters of the simulations are chosen as follows. The size of the inlet and outlet reservoirs is given by  $L_A = L_B = R_A = R_B = 8R$ . The total number of particles is  $4 \times 10^7$ , which slightly varies during the simulation. Initially,  $10^7$  particles is used, then, this value is doubled two times to reach the final number of particles. The time step is  $\Delta t = 0.005R/v_0(C_A)$  and the largest grid spacing is  $R/20$ . The simulations are terminated by using a constraint in terms of the total flow rate. The statistical scattering for the short tube problem is estimated as  $\epsilon = \sqrt{N^+}/(N^+ - N^-)$ , where  $N^+$  and  $N^-$  denote the total numbers of particles crossing through the inlet cross section from the upstream reservoir to the tube and in the reverse direction, respectively. The simulation terminates with fulfilling the constrain  $\epsilon < 0.004$ . The achieved accuracy for the total flow rate is better than  $\pm 0.5\%$ . Test simulations have been managed for flows through a short tube with  $L/R = 0.1$  and  $P_B/P_A = 0.1$  at rarefaction parameters  $\delta_A = 1, 10, 50$  for a single gas. The flow rates have been compared to corresponding values in Ref. [101]. The difference between the results is less than  $\pm 0.5\%$ . Test simulations have also been carried out for flows through an orifice with  $P_B/P_A = 0.1$  at rarefaction parameters  $\delta_A = 1, 10, 100$  for the single gas case. The flow rate has been compared to the result of Ref. [64]. The difference between the two results is less than  $\pm 0.5\%$ .

Simulations have been carried out for  $He/Ar$  and  $Ne/Ar$  mixtures by

using the hard-sphere molecular model. The mass and diameter ratios of  $He/Xe$  and  $Ne/Ar$  are given by  $m_1/m_2 = [4.0026/131.30, 20.183/39.948]$  and  $d_1/d_2 = [1/2.226, 1/1.406]$ , respectively. The simulations refer to different values of the channel length, the concentration, the pressure ratio and the reference rarefaction parameter. It is noted that the simulations have been executed on a cluster having difference processors. The simulation time is in the range from a few days to one and a half months. The required time increases with increasing pressure ratio and channel length.

### Flow rates through short tubes

Tables 4.1-4.4 show the flow rates of the components  $J_\alpha$ , the ratio  $J_1/J_2$  and the total flow rate for different flow configurations. The  $J_1/J_2$  ratio is used to examine the separation phenomenon, which means that the components have different average flow speeds due to the different molecular velocities. In some cases, the flow rates for a single gas are also provided for comparative purposes.

In Table 4.1, these quantities are tabulated for  $He/Xe$  mixture flowing through a channel with  $L/R = 1$  at  $P_B/P_A = 0.1$  in terms of the reference rarefaction parameter in the range of  $0 \leq \delta_A \leq 100$ . Three concentration values  $C_A = [0.25, 0.5, 0.75]$  are examined. In addition, the total flow rate for a single component gas  $J^*$  from Ref. [101] is shown. The single gas result denoted by  $W$  in Ref. [101] is converted to the present formalism according to  $J = W/(2\sqrt{\pi})$ . In Table 4.1, the dependency of the flow rates on  $\delta_A$  and  $C_A$  can be observed. As  $\delta_A$  increases, the flow rate of the lighter species  $J_1$  decreases up to  $\delta_A = 50$  and then it increases, while the flow rate of the heavier species  $J_2$  steadily increases. Furthermore, the ratio  $J_1/J_2$  monotonically increases as  $\delta_A$  decreases due to the gas separation. In the hydrodynamic limit, where separation is diminishing, the ratio  $J_1/J_2$  tends to the limiting value of  $C_A/(1-C_A)$ . The separation phenomenon becomes more

and more important with increasing gas rarefaction (i.e. with decreasing  $\delta_A$ ). In this situation, the gas components become more independent of each other due to the reduction of intermolecular collisions. The total flow rates are quite different from the corresponding ones of the single gas, except in the case of large values of  $\delta_A$ , where all dimensionless total flow rates are approaching each other. This situation occurs because the gas becomes so dense in the viscous limit that diffusion effects become negligible and the mixture tends to behave like a single gas. In addition, it can be seen that the dependency of the total flow rate  $J$  on  $\delta_A$  is not monotonic. As  $\delta_A$  increases, the flow rate is initially reduced and then after some critical value of  $\delta_A$ , the flow rate increases. A type of a Knudsen minimum shows up although such a minimum is not present in the corresponding single gas flow.

Table 4.2 presents the component and total flow rates in terms of  $\delta_A$  for *He/Xe* with  $C_A = 0.5$ ,  $P_B/P_A = 0.1$  and  $L/R = 5, 10$ . Therefore, the results of this table in connection with the corresponding ones, Table 4.1 with  $C_A = 0.5$ , may provide a description of the dependency of the flow rates on the length of the channel. The available corresponding single gas results are also tabulated from Ref. [101]. It can be clearly seen that the flow rates decrease as the channel becomes longer. This behavior is easily explained by the fact that the local pressure gradient becomes smaller with increasing channel length at constant overall pressure drop. However, the qualitative behavior of the component and total flow rates with respect to  $\delta_A$  is similar as before. With regard to the dependency of the separation on  $L/R$ , it can be seen that for the same values of  $\delta_A$ , as we are moving from  $L/R = 1$  to  $L/R = 5$ , the ratio  $J_1/J_2$  is nearly the same but initially increases and then decreases for  $L/R = 10$ .

It is interesting to examine whether the specific behavior of the flow rates versus the gas rarefaction is still observed at a smaller pressure drop. Therefore, in Table 4.3, the normalized flow rates and the ratio  $J_1/J_2$  are

Table 4.1: Dimensionless flow rates of  $He/Xe$  through short tubes in terms of  $\delta_A$  for  $P_B/P_A = 0.1$ ,  $L/R = 1$  and  $C_A = [0.25, 0.5, 0.75]$  (top, center and bottom).

$\delta_A$	$J_1$	$J_2$	$J_1/J_2$	$J$	$J^*$
0	0.213	0.111	1.91	0.324	0.171
0.1	0.210	0.114	1.85	0.324	0.173
0.5	0.200	0.123	1.62	0.323	0.183
1	0.188	0.134	1.40	0.322	0.194
5	0.134	0.193	0.694	0.327	0.258
10	0.112	0.225	0.496	0.337	0.296
50	0.0948	0.274	0.347	0.368	0.361
100	0.0973	0.286	0.341	0.383	0.381
0	0.351	0.0613	5.73	0.412	0.171
0.1	0.348	0.0631	5.51	0.411	0.173
0.5	0.335	0.0709	4.72	0.406	0.183
1	0.320	0.0801	3.99	0.400	0.194
5	0.243	0.129	1.88	0.373	0.258
10	0.212	0.154	1.38	0.366	0.296
50	0.188	0.185	1.02	0.374	0.361
100	0.193	0.191	1.01	0.384	0.381
0	0.383	0.0223	17.2	0.405	0.171
0.1	0.381	0.0233	16.4	0.404	0.173
0.5	0.375	0.0281	13.4	0.404	0.183
1	0.367	0.0339	10.9	0.401	0.194
5	0.314	0.0657	4.78	0.380	0.258
10	0.290	0.0804	3.61	0.371	0.296
50	0.283	0.0937	3.02	0.377	0.361
100	0.289	0.0962	3.01	0.386	0.381

tabulated in terms of  $\delta_A$  for the binary mixture of  $He/Xe$  with  $C_A = 0.5$  and  $P_B/P_A = 0.4$ . By comparing the corresponding results of Tables 4.1 and 4.3, it is clearly seen that the magnitudes of all flow rates are reduced with decreasing pressure drop. However, again, the ratios  $J_1/J_2$  increase, as we are moving from the continuum to the free molecular regime. The flow rates  $J_1$  and  $J_2$ , which are very close to each other at  $\delta_A = 100$ , also start to depart from each other as  $\delta_A$  decreases with the largest deviation occurring at  $\delta_A = 0$ . With regard to the total flow rate,  $J$  first decreases up to  $\delta_A = 1$ , where the minimum flow rate is obtained, and then it increases

Table 4.2: Dimensionless flow rates of  $He/Xe$  through short tubes in terms of  $\delta_A$  for  $P_B/P_A = 0.1$ ,  $L/R = [5, 10]$  (top and bottom) and  $C_A = 0.5$ .

$\delta_A$	$J_1$	$J_2$	$J_1/J_2$	$J$	$J^*$
0	0.162	0.0272	5.95	0.189	0.0787
0.1	0.160	0.0280	5.69	0.188	0.0793
0.5	0.150	0.0313	4.81	0.182	0.0821
1	0.141	0.0352	4.01	0.176	0.0858
5	0.105	0.0604	1.74	0.165	0.116
10	0.101	0.0799	1.26	0.181	0.149
50	0.131	0.129	1.02	0.261	0.258
100	0.147	0.147	1.00	0.294	0.302
0	0.0996	0.0174	5.72	0.117	0.0480
0.1	0.0973	0.0175	5.55	0.115	
0.5	0.0914	0.0200	4.57	0.111	0.0482
1	0.0843	0.0219	3.84	0.106	
5	0.0615	0.0370	1.66	0.0985	
10	0.0612	0.0496	1.23	0.111	0.0906
50	0.0999	0.0982	1.02	0.198	
100	0.120	0.120	1.00	0.240	

Table 4.3: Dimensionless flow rates of  $He/Xe$  through short tubes in term of  $\delta_A$  for  $C_A = 0.5$ ,  $P_B/P_A = 0.4$  and  $L/R = 1$ .

$\delta_A$	$J_1$	$J_2$	$J_1/J_2$	$J$
0	0.234	0.0406	5.78	0.275
0.1	0.231	0.0425	5.43	0.273
0.5	0.221	0.0491	4.51	0.271
1	0.211	0.0569	3.71	0.268
5	0.180	0.104	1.73	0.284
10	0.176	0.133	1.32	0.308
50	0.177	0.175	1.01	0.353
100	0.185	0.185	1.00	0.370

up to  $\delta_A = 100$ .

In Table 4.4, the flow rates and the ratio  $J_1/J_2$  of the two different gas mixtures  $He/Xe$  and  $Ne/Ar$  are shown for  $C_A = 0.5$ ,  $L/R = 0.3$  and  $P_B/P_A = [0.1, 0.4, 0.7]$ . Starting the comparison with the corresponding flow rates of the light species, it is seen that as  $\delta_A$  increases the flow rate of  $He$  decreases in all cases except for  $P_A/P_B = 0.7$  and  $\delta_A \geq 10$ , while the

Table 4.4: Dimensionless flow rates through short tubes for  $He/Xe$  and  $Ne/Ar$  in terms of  $\delta_A$  for  $C_A = 0.5$ ,  $P_B/P_A = [0.1, 0.4, 0.7]$  (top, center and bottom) and  $L/R = 0.3$ .

$\delta_A$	$He/Xe$				$Ne/Ar$			
	$J_1$	$J_2$	$J_1/J_2$	$J$	$J_1$	$J_2$	$J_1/J_2$	$J$
0	0.454	0.0796	5.70	0.533	0.135	0.0961	1.40	0.231
0.1	0.451	0.0821	5.50	0.533	0.136	0.0981	1.38	0.234
0.5	0.436	0.0917	4.76	0.528	0.140	0.107	1.31	0.246
1	0.418	0.104	4.04	0.522	0.145	0.117	1.24	0.261
5	0.317	0.164	1.94	0.481	0.170	0.163	1.05	0.333
10	0.265	0.190	1.40	0.455	0.183	0.182	1.00	0.364
50	0.215	0.210	1.02	0.426	0.202	0.203	1.00	0.404
100	0.212	0.211	1.01	0.424	0.206	0.207	0.994	0.413
0	0.302	0.0525	5.76	0.355	0.0894	0.0637	1.40	0.153
0.1	0.299	0.0550	5.44	0.354	0.0908	0.0656	1.38	0.156
0.5	0.289	0.0638	4.54	0.353	0.0945	0.0733	1.29	0.168
1	0.277	0.0742	3.73	0.351	0.100	0.0825	1.21	0.183
5	0.237	0.134	1.77	0.370	0.141	0.136	1.04	0.276
10	0.221	0.164	1.35	0.384	0.165	0.163	1.01	0.328
50	0.201	0.195	1.03	0.397	0.194	0.194	1.00	0.388
100	0.201	0.200	1.00	0.401	0.200	0.200	1.00	0.400
0	0.151	0.0264	5.72	0.178	0.0447	0.0319	1.40	0.0766
0.1	0.149	0.0279	5.35	0.177	0.0456	0.0331	1.38	0.0787
0.5	0.143	0.0330	4.34	0.176	0.0481	0.0379	1.27	0.0859
1	0.137	0.0396	3.47	0.177	0.0515	0.0434	1.19	0.0949
5	0.131	0.0830	1.57	0.214	0.0859	0.0832	1.03	0.169
10	0.144	0.115	1.25	0.259	0.117	0.116	1.01	0.233
50	0.160	0.155	1.03	0.315	0.156	0.156	1.01	0.312
100	0.162	0.162	1.00	0.325	0.162	0.163	1.00	0.325

flow rate of  $Ne$  always increases. The corresponding flow rates of the heavy species, i.e.  $Xe$  and  $Ar$ , steadily increase in all cases with increasing  $\delta_A$ . It is seen that there are not only quantitative but also qualitative differences with regard to the light species of the two mixtures. The ratios  $J_1/J_2$  in both mixtures monotonically decrease as the reference rarefaction parameter increases and finally approach unity as the viscous limit is reached. Thus, the separation phenomenon is present in both mixtures. However, since the values of  $J_1/J_2$  of  $He/Xe$  are much higher than the corresponding ones for

Table 4.5: Dimensionless flow rates through orifices for  $He/Xe$  in terms of  $\delta_A$  for various values of  $C_A$  and  $P_B/P_A = 0.1$ .

$\delta_A$	$J_1$	$J_2$	$J_1/J_2$	$J$	$J^*$
0.1	0.314	0.170	1.85	0.483	0.257
0.5	0.300	0.184	1.63	0.484	
1	0.284	0.200	1.42	0.484	0.291
5	0.203	0.279	0.728	0.482	
10	0.162	0.309	0.524	0.472	0.405
50	0.116	0.332	0.348	0.448	
100	0.113	0.331	0.340	0.444	0.430
0.1	0.518	0.0945	5.49	0.613	0.257
0.5	0.503	0.106	4.77	0.609	
1	0.483	0.119	4.05	0.602	0.291
5	0.366	0.186	1.97	0.552	
10	0.300	0.213	1.41	0.514	0.405
50	0.233	0.229	1.02	0.462	
100	0.227	0.226	1.01	0.453	0.430
0.1	0.568	0.0345	16.5	0.603	0.257
0.5	0.563	0.0418	13.5	0.605	
1	0.554	0.0499	11.1	0.604	0.291
5	0.467	0.0939	4.97	0.561	
10	0.411	0.112	3.67	0.523	0.405
50	0.356	0.118	3.02	0.474	
100	0.345	0.115	2.99	0.460	0.430

$Ne/Ar$ , except at large values of  $\delta_A$ , where both ratios are close to one, there is a clear indication that separation is stronger for the mixture with the larger molecular mass ratio. With regard to the total flow rates, it can be seen that  $J$  monotonically increases as  $\delta_A$  increases in the case of  $Ne/Ar$ , while the dependency on the rarefaction parameter is quite different in the case of  $He/Xe$ . This latter behaviour is quite close to the one previously observed of the other  $L/R$ . It is interesting to note that the Knudsen minimum previously observed does not show up at all for  $P_B/P_A = 0.1$  and it is very shallow for  $P_B/P_A = 0.4$  and  $0.7$  in the present case of the  $He/Xe$  flow through this very short tube.

Table 4.6: Dimensionless flow rates through orifices for  $He/Xe$  in terms of  $\delta_A$  for  $C_A = 0.5$  and  $P_B/P_A = 0.4$ .

$\delta_A$	$J_1$	$J_2$	$J_1/J_2$	$J$
0.1	0.346	0.0628	5.51	0.409
0.5	0.333	0.0733	4.54	0.406
1	0.320	0.0851	3.75	0.405
5	0.273	0.152	1.79	0.425
10	0.246	0.183	1.35	0.429
50	0.211	0.205	1.03	0.416
100	0.204	0.205	1.00	0.409

Table 4.7: Dimensionless flow rate through orifices for  $He/Xe$  in terms of  $P_B/P_A$  for  $\delta_A = 1$  and  $C_A = 0.5$ .

$P_B/P_A$	$J_1$	$J_2$	$J_1/J_2$	$J$
0	0.537	0.129	4.16	0.666
0.1	0.483	0.119	4.05	0.602
0.4	0.320	0.0851	3.75	0.405
0.7	0.158	0.0455	3.48	0.204
0.9	0.0531	0.0158	3.37	0.0689

Table 4.8: Dimensionless flow rates through orifices for  $Ne/Ar$  in terms of  $\delta_A$  for  $C_A = 0.5$  and  $P_B/P_A = 0.1$ .

$\delta_A$	$J_1$	$J_2$	$J_1/J_2$	$J$	$J^*$
0.1	0.156	0.113	1.38	0.269	0.257
0.5	0.161	0.123	1.31	0.283	
1	0.166	0.134	1.24	0.300	0.291
5	0.194	0.185	1.05	0.378	
10	0.205	0.203	1.01	0.408	0.405
50	0.214	0.216	0.992	0.431	
100	0.216	0.215	1.00	0.431	0.430

### Flow rates through orifices

In this section, Tables 4.5-4.8 present some results for flows through orifices  $L/R = 0$  at various flow parameters. In Table 4.5, the flow rates are tabulated for  $He/Xe$  mixture with reference concentrations  $C_A = [0.25, 0.5, 0.75]$  and pressure ratio  $P_B/P_A = 0.1$  for  $0.1 \leq \delta_A \leq 100$ . It can be seen that  $J_1$

monotonically increases while  $J_2$  initially increases up the  $\delta_A = 50$  then it decreases in all cases with decreasing rarefaction parameter. This behavior is similar to the short tube case  $L/R = 0.3$  in Table 4.4 for  $He/Xe$  at the same pressure ratio, except  $J_2$  in the range of  $\delta_A = 50 - 100$ . The gaseous separation  $J_1/J_2$  has nearly the same structure as in Tables 4.1 and 4.4. The total flow rate increases with decreasing rarefaction parameter and always larger than the corresponding single gas results  $J^*$  obtained from Ref. [64].

Table 4.6 shows the flow rates for  $He/Xe$  mixture with  $C_A = 0.5$  at larger pressure ratio  $P_B/P_A = 0.4$ . It can be seen that the flow rates are generally smaller than in Table 4.5 due to the reducing driving force. However, the gaseous separation is nearly the same as for  $P_B/P_A = 0.1$ . Table 4.7 presents the results at  $\delta_A = 1$  and different values of the pressure ratio. It is confirmed that the flow rates become smaller at larger pressure ratio. In addition, the gaseous separation is intensified by increasing pressure drop. Finally, in Table 4.8, the flow rates are shown for  $Ne/Ar$  mixture with  $C_A = 0.5$  and  $P_B/P_A = 0.1$ . In this case, the flow rates follow the typical pattern of the single gas situation and the dependence on the rarefaction parameter is similar as for the corresponding tendency given in Table 4.4. It is also shown that the separation is stronger for the mixture with larger mass ratio.

### Overview on the flow rates

Closing this section on the flow rates, it may be useful to have a visual description of the dependency of the total flow rate of the gas mixture of  $He/Xe$  in terms of gas rarefaction and tube length. In Figure 4.3, the total flow rate  $J$  of  $He/Xe$  as a function of  $\delta_A$  is presented for  $C_A = 0.5$ ,  $P_B/P_A = 0.1$  and  $L/R = [0, 0.3, 1, 5, 10]$ . As  $L/R$  is increased the flow rate is decreased. In addition, it is seen that for very short channels with  $L/R \leq 0.3$ , the flow rate monotonically decreases with increasing  $\delta_A$ , while for longer channels, with  $L/R \geq 1$ , the dependency of the flow rate is not monotonic and the

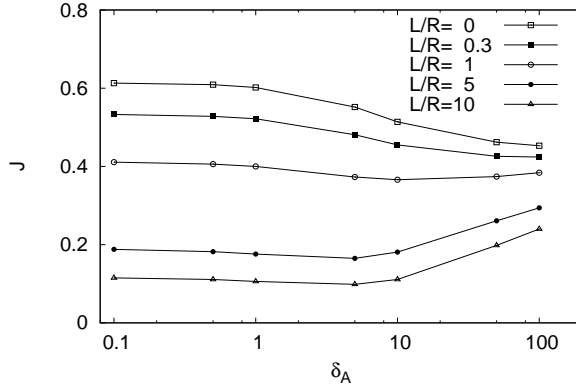


Figure 4.3: Dimensionless total flow rate for  $He/Xe$  as a function of  $\delta_A$  for  $C_A = 0.5$ ,  $P_B/P_A = 0.1$  and various values of  $L/R$  for short tubes.

so-called Knudsen minimum appears.

### Axial distributions of macroscopic quantities

Axial distributions of the density of the mixture components are presented in Figures 4.4-4.6. In Figure 4.4, the densities are shown for  $He/Xe$  with  $C_A = 0.5$ ,  $P_B/P_A = 0.1$ ,  $L/R = [1, 5, 10]$ , and  $\delta_A = [0.1, 1, 10]$ . It can be seen that the component densities vary between the upstream and downstream reference values, exhibiting a rapid change in the zone of the tube. In the free-molecular limit, the corresponding density profiles of the two species are nearly the same; however, the densities are component dependent at larger values of the rarefaction parameter. Because of the difference in the density of the components, there is a concentration variation along the tube, which is caused by the separation effect. The lighter particle has larger molecular speed than that of the heavier one due to the smaller molecular mass. The pressure gradient accelerates the flow along the channel, and the lighter particle acquires larger flow speed. This mechanism eventually results into the gas separation. Figure 4.5 presents the axial distributions

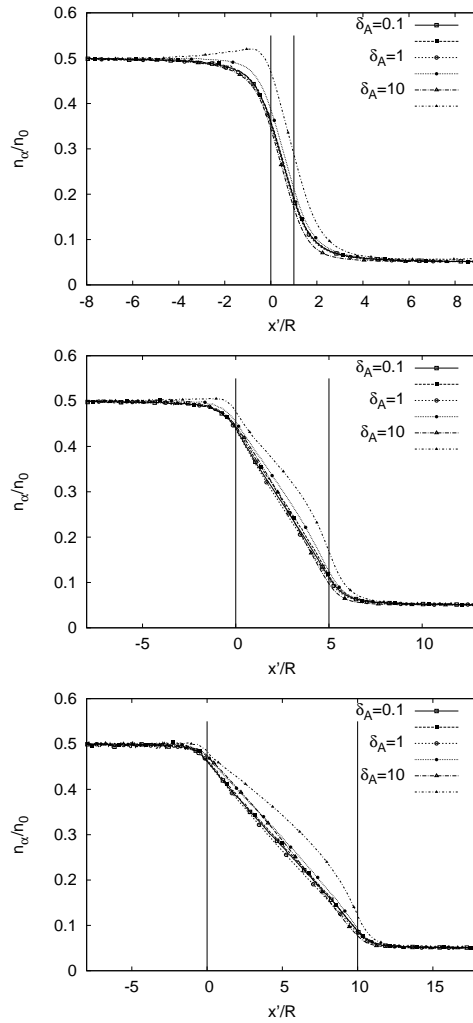


Figure 4.4: Axial distributions of the density of each species of  $He/Xe$  for  $C_A = 0.5$ ,  $P_B/P_A = 0.1$ ,  $\delta_A = [0.1, 1, 10]$  and  $L/R = [1, 5, 10]$  (from top to bottom) for short tubes. Filled and empty symbols stand for  $He$  and  $Xe$ , respectively.

of the density of the components for  $He/Xe$  at two different values of the concentration  $C_A = [0.25, 0.75]$  with  $L/R = 1$ ,  $P_B/P_A = 0.1$  and  $\delta_A = 10$ . It can be seen that the density curves exhibit the expected behaviour.

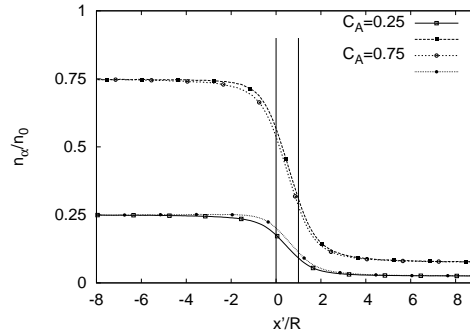


Figure 4.5: Axial distributions of the density of each species of  $He/Xe$  for  $L/R = 1$ ,  $\delta_A = 1$ ,  $P_B/P_A = 0.1$  and  $C_A = [0.25, 0.75]$  for short tubes. Filled and empty symbols stand for  $He$  and  $Xe$ , respectively.

Starting at the inlet reference value, they decrease in the zone of the tube and finally reach the outlet reference density. A comparison between the density distributions of  $He/Ar$  and  $Ne/Ar$  with  $L/R = 0.3$ ,  $C_A = 0.5$ ,  $\delta_A = 1$  and  $P_B/P_A = [0.1, 0.4, 0.7]$  is shown in Figure 4.6. Here, the effect of the type of the mixture may be observed. The differences between the density distributions of the species of each mixture are larger for the  $He/Xe$  mixture, which of course has the larger molecular mass ratio. This is again due to the separation phenomenon which is expected to be more dominant for mixtures with larger mass ratios.

Figures 4.7 and 4.8 present the velocity distributions along the axis of the channel. In Figures 4.7, the axial velocity distributions of each species are plotted for  $He/Xe$  with  $C_A = 0.5$ ,  $P_B/P_A = 0.1$ ,  $\delta_A = [0.1, 1, 10]$  and  $L/R = [1, 5, 10]$ . In all cases, the velocities of  $He$  are larger than the velocities of  $Xe$ . The velocity difference between the components becomes larger as the rarefaction parameter decreases. This is due to the fact that the components tend to propagate with their own molecular speeds as the gas becomes more rarefied and intermolecular collisions are less important. In the inlet region and along the channel the velocities steadily increase reaching their

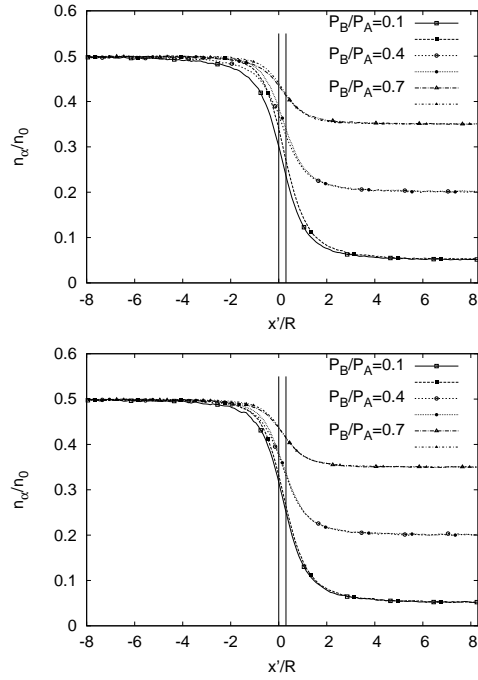


Figure 4.6: Axial distributions of the density of each species of *He/Xe* (top) and *Ne/Ar* (bottom) for  $C_A = 0.5$ ,  $L/R = 0.3$ ,  $\delta_A = 1$  and  $P_B/P_A = [0.1, 0.4, 0.7]$  for short tubes. Filled and empty symbols stand for the lighter and heavier components, respectively.

maximum values after the exit of the tube and then they gradually decrease in the outlet section. It is also seen that the velocities become smaller as the channel becomes longer. This is a consequence of the smaller average pressure gradient available with longer channel. Figure 4.8 shows the axial velocity profiles of the species of the two mixtures under investigation with  $C_A = 0.5$ ,  $\delta_A = 5$ ,  $L/R = 0.3$  and  $P_B/P_A = [0.1, 0.4, 0.7]$ . The velocity difference between the components of *Ne/Ar* is smaller than the one of *He/Xe*.

The temperature distribution for *He/Xe* with  $C_A = 0.5$ ,  $P_B/P_A = 0.1$ ,  $\delta_A = [0.1, 1, 10]$  and  $L/R = [1, 5, 10]$  is shown in Figure 4.9. A temperature

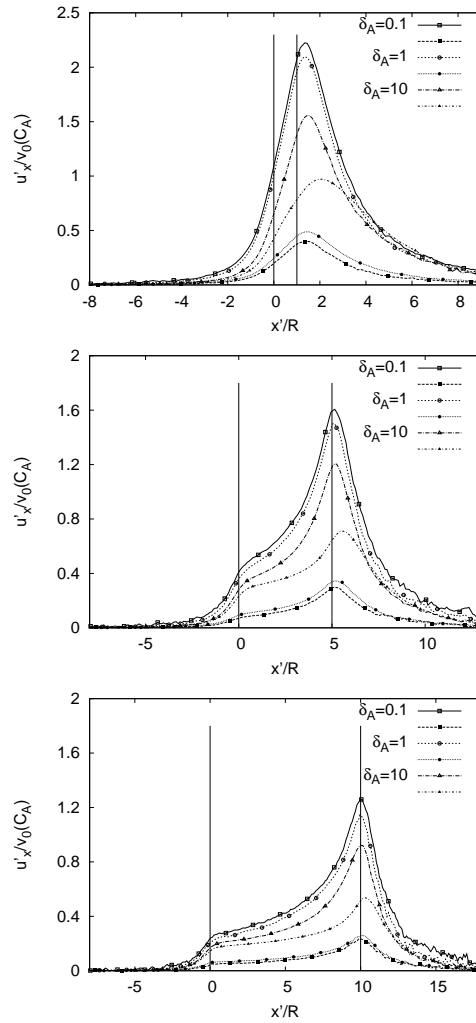


Figure 4.7: Distributions of axial velocities of each species of  $He/Xe$  for  $C_A = 0.5$ ,  $P_B/P_A = 0.1$ ,  $\delta_A = [0.1, 1, 10]$  and  $L/R = [1, 5, 10]$  (from top to bottom) for short tubes. Filled and empty symbols stand for  $He$  and  $Xe$ , respectively.

drop having its maximum after the exit of the channel is observed. This is due to the strong expansion of the gaseous mixture in the low pressure environment. The temperature drop generally decreases as the channel becomes

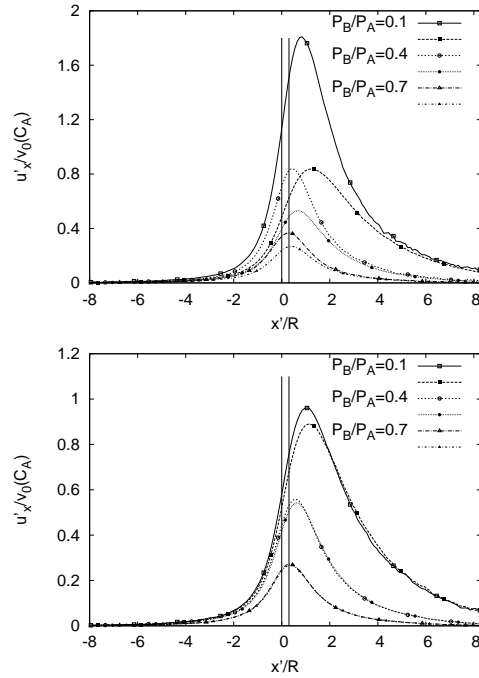


Figure 4.8: Distributions of axial velocities of each species of *He/Xe* (top) and *Ne/Ar* (bottom) for  $C_A = 0.5$ ,  $L/R = 0.3$ ,  $\delta_A = 5$  and  $P_B/P_A = [0.1, 0.4, 0.7]$  for short tubes. Filled and empty symbols stand for the lighter and heavier components, respectively.

longer. For longer channels, the flow rates are reduced so the expansion becomes weaker, which eventually causes smaller temperature drop.

Finally, Figure 4.10 shows the axial distribution of the local rarefaction parameter and the Mach number for *He/Xe* with  $L/R = 0.3$ ,  $C_A = 0.5$  and  $\delta_A = 1$  and various values of the pressure drop. The Mach number is defined as  $Ma = \sqrt{6/5}u'/v_0(C_A)$ , where  $u'$  is the absolute value of the mass-density average velocity. It can be seen that the rarefaction parameter shows strong variation along the axis of the tube. It starts at the inlet reference value, then decreases in the tube, and finally reaches the outlet value, which is  $(P_B/P_A)\delta_A$  in accordance with the pressure drop. This variation is very

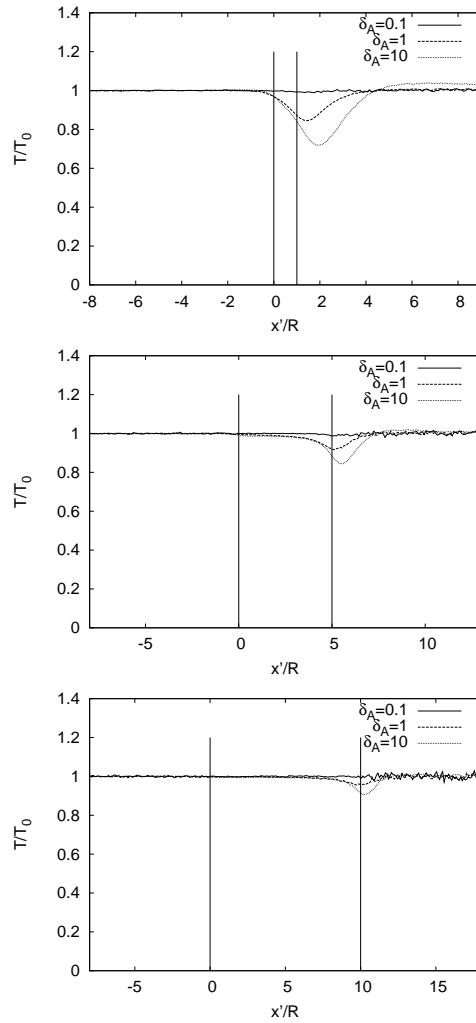


Figure 4.9: Axial distribution of the temperature of  $He/Xe$  for  $C_A = 0.5$ ,  $P_B/P_A = 0.1$ ,  $\delta_A = [0.1, 1, 10]$  and  $L/R = [1, 5, 10]$  (from top to bottom) for short tubes.

similar to the variation of the number density. With regard to the Mach number, it can be seen that it increases along the flow in the tube, reaching its maximum value just after the exit of the tube, and then starts to decrease. As the pressure drop becomes larger the Mach number increases due to the

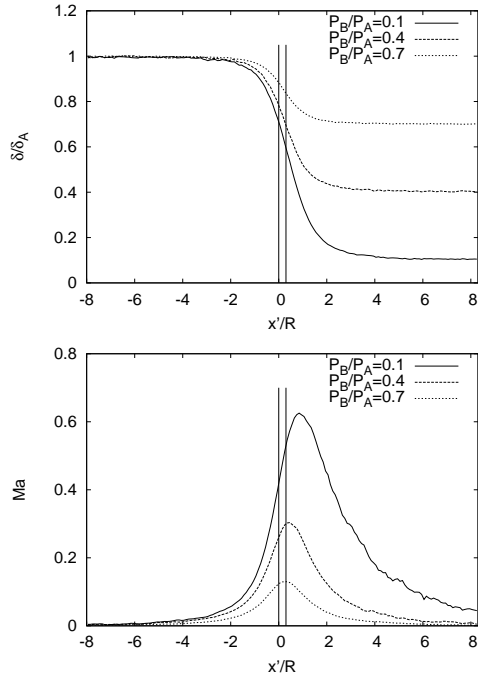


Figure 4.10: Axial distributions of the local rarefaction parameter (top) and the Mach number (bottom) of  $He/Xe$  for  $C_A = 0.5$ ,  $L/R = 0.3$ ,  $\delta_A = 1$  and  $P_B/P_A = [0.1, 0.4, 0.7]$  for short tubes.

stronger acceleration of the gas.

#### 4.4.2 Flows through slits

In this section, the results of flow of binary gases through slits are discussed. In the simulations, different upstream and downstream reservoir sizes, depending on the rarefaction degree of the gas, are used. The length  $L_A$  and the height  $H_A$  of the upstream reservoir is chosen as  $30H$  for all rarefaction parameters. The size of the downstream container is chosen as  $L_B = H_B = 8H$ . The time step is  $\Delta t = 0.005R/v_0(C_A)$  and the largest grid spacing is  $H/40$ . The total number of particle is  $8 \times 10^7$  in the simulations. Initially, the num-

ber of particle is  $2 \times 10^7$ , which is doubled two times at the beginning of the simulation to reach the final value. For terminating the simulations, a criterion is formulated in terms of the total flow rate. In the present case, the statistical scattering is estimated as  $\epsilon = 1/(\sqrt{N^+} - \sqrt{N^-})$ , where  $N^+$  and  $N^-$  are the total number of particles entering the downstream and upstream containers through the slit. The simulations are terminated when the condition  $\epsilon < 0.004$  is fulfilled. The achieved accuracy for the total flow rate is better than  $\pm 0.5\%$ . Test simulations have been performed for a single gas with  $P_B/P_A = 0.1$  and rarefaction parameters  $\delta_A = 1, 10, 50$ . The flow rates have been compared to the results of Ref. [74]. The difference between the results is less than  $\pm 1\%$ .

Simulations have been performed for *He/Xe* and *Ne/Ar* mixtures. The same molecular parameters are used as for the short tube problem. The flow is investigated at different values of the concentration, the pressure ratio and the inlet rarefaction parameter. The simulations have been executed on different processors of the cluster. The required simulation time is in the range from a few days to two months. It is found that the simulation time increases with increasing pressure ratio.

### Flow rates

Tables 4.9-4.11 show the flow rate of the components and the mixture through the slit for different flow parameters. In Table 3.5, the flow rates are presented for the *He/Xe* mixture at the reference concentration  $C_A = 0.25, 0.5$  and  $0.75$  for flow into vacuum,  $P_B/P_A = 0$ , as a function of the rarefaction parameter. It can be seen that the relative flow rates  $J_1/J$  and  $J_2/J$  in the hydrodynamic limit reach the limiting values of  $C_A$  and  $1 - C_A$  defined by the molar weights of the components. With decreasing rarefaction parameter,  $\delta_A \rightarrow 0$ , the flow rate of the lighter component monotonically increases in all cases. This behaviour is caused by the larger molecular speed of the lighter

Table 4.9: Flow rates through slits for  $He/Xe$  mixture at different values of the concentration and  $P_B/P_A = 0$ .

$\delta_A$	$C_A = 0.25$			$C_A = 0.5$			$C_A = 0.75$		
	$J_1$	$J_2$	$J$	$J_1$	$J_2$	$J$	$J_1$	$J_2$	$J$
0.1	0.352	0.189	0.541	0.577	0.105	0.682	0.632	0.0393	0.672
0.5	0.327	0.208	0.535	0.545	0.121	0.667	0.616	0.0489	0.665
1	0.289	0.228	0.518	0.498	0.140	0.638	0.586	0.0605	0.646
5	0.179	0.300	0.479	0.332	0.208	0.540	0.443	0.110	0.553
10	0.141	0.329	0.470	0.274	0.233	0.506	0.400	0.124	0.524
50	0.119	0.344	0.462	0.237	0.239	0.476	0.370	0.123	0.493
100	0.114	0.342	0.455	0.234	0.234	0.468	0.355	0.120	0.475

Table 4.10: Flow rates through slits for  $Ne/Ar$  mixture at  $C_A = 0.5$  and  $P_B/P_A = 0$ .

$\delta_A$	$J_1$	$J_2$	$J$
0.1	0.175	0.125	0.300
0.5	0.181	0.138	0.319
1	0.183	0.150	0.334
5	0.200	0.194	0.393
10	0.211	0.210	0.421
50	0.221	0.222	0.443
100	0.220	0.222	0.442

component. When the rarefaction is increased, the effect of the intermolecular collisions becomes less important, and the flows of the two components become independent of each other. The larger molecular speed of the lighter component results into the increasing flow rate  $J_1$  with decreasing rarefaction parameter. The flow rate of the heavier component  $J_2$  initially increases up to  $\delta_A = 50$  for  $C_A = [0.25, 0.5]$  and  $\delta_A = 10$  for  $C_A = 0.75$  then monotonically decreases as the rarefaction parameter becomes smaller. The net effect of the behaviour of the component flow rates is a monotonically increasing total flow rate with decreasing rarefaction parameter. However, the rarefaction dependence of the total flow rate is opposite as for the single gas due to the inverted flow rate of the lighter particle.

Table 4.10 presents the flow rates for the  $Ne/Ar$  mixture at  $C_A = 0.5$

Table 4.11: Flow rates through slits for  $He/Xe$  and  $Ne/Ar$  mixture at  $C_A = 0.5$  and  $P_B/P_A = [0.4, 0.7]$  (top and bottom).

$\delta_A$	$He/Xe$			$Ne/Ar$		
	$J_1$	$J_2$	$J$	$J_1$	$J_2$	$J$
0.1	0.349	0.0634	0.413	0.106	0.0754	0.182
0.5	0.328	0.0773	0.406	0.113	0.0871	0.200
1	0.299	0.0932	0.392	0.117	0.0989	0.216
5	0.239	0.163	0.402	0.161	0.158	0.319
10	0.228	0.194	0.422	0.187	0.187	0.374
50	0.214	0.213	0.427	0.206	0.205	0.411
100	0.210	0.212	0.422	0.205	0.206	0.411
0.1	0.181	0.0315	0.212	0.0545	0.0374	0.0920
0.5	0.170	0.0394	0.210	0.0591	0.0446	0.104
1	0.153	0.0493	0.203	0.0625	0.0518	0.114
5	0.135	0.0982	0.234	0.0973	0.0951	0.192
10	0.152	0.132	0.284	0.130	0.129	0.260
50	0.164	0.163	0.327	0.160	0.161	0.321
100	0.162	0.164	0.326	0.163	0.161	0.323

and  $P_B/P_A = 0$  at different values of the rarefaction parameter. With regard to the hydrodynamic limit, similar observation can be made as for the corresponding results in Table 4.9. The relative flow rates  $J_1/J$  and  $J_2/J$  tend to the values of  $C_A$  and  $1 - C_A$  as the gaseous rarefaction approaches the continuum regime. However, at higher rarefactions there are major differences between the two mixtures,  $He/Xe$  and  $Ne/Ar$ . The  $Ne/Ar$  mixture has an opposite dependence of the total flow rate on the rarefaction parameter. Actually, all of the flow rates,  $J_1$ ,  $J_2$  and  $J$ , slightly increase up to  $\delta_A = 50$  then monotonically decreases with decreasing rarefaction. The difference between the two composition is caused by the different mass ratios of the two mixtures. The differences between the molecular speeds of the lighter and heavier components for the  $Ne/Ar$  mixture is not as large as for the  $He/Xe$  mixture. Hence, the flow rate rarefaction parameter function is similar to the single gas case.

Finally, Table 4.11 shows the flow rates for the two types of mixtures with

$C_A = 0.5$  and finite pressure ratios  $P_B/P_A = 0.4$  and  $0.7$ . As it can be seen the  $J_1$  flow rate for the  $He/Xe$  mixture follows the new, inverted flow rate dependence in a wide range of the rarefaction parameter for  $P_B/P_A = 0.4$  and from  $\delta_A = 5$  with decreasing rarefaction parameter for  $P_B/P_A = 0.7$ . At larger pressure ratio, the pressure gradient is not so large to accelerate the lighter particle to produce the inverted flow rate in the whole range of the rarefaction spectrum. The flow rate dependence of  $J_2$  is similar to what is observed in Tables 4.9 and 4.10. The flow rate generally decreases with decreasing rarefaction parameter; however, it initially increases up to  $\delta_A = 50$  for  $P_B/P_A = 0.4$ . The total flow rate has a complex behaviour in both cases. These findings indicate that the inverted flow rate is pronounced for large pressure drops, when there is sufficient pressure gradient to accelerate the lighter particle. With regard to the  $Ne/Ar$  mixture, it is found that all flow rates generally decrease as the rarefaction parameter becomes smaller, except the case of  $P_B/P_A = 0.4$  where  $J_1$  initially increases up to  $\delta_A = 50$  then it starts to decrease. In addition to the above results, it is more important to note that the flow rates become smaller as the pressure drop is reduced. This outcome is caused by the fact that the driving force is smaller in that case.

### **Axial distribution of macroscopic quantities**

Figures 4.11-4.18 show the distribution of the densities, the axial velocities and the temperature together with the rarefaction parameter and the Mach number. Figure 4.11 presents the density profiles of the components for the two mixtures with  $C_A = 0.5$  and  $P_B/P_A = 0$ . The density curves show strong variation near the orifice. Generally, the densities start to decrease from the inlet values and then tend to the outlet zero value after the slit. However, the density of the heavier particle for the case of  $He/Xe$  mixture with  $\delta_A = 5$  and  $10$  slightly increases near the slit, takes its maximum then starts to decrease. It can be seen that the density profiles are strongly component dependent.

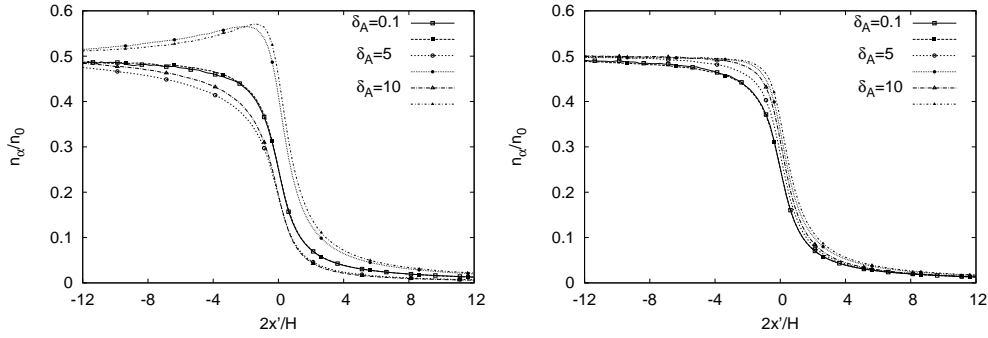


Figure 4.11: The distribution of the density for *He/Xe* (left) and *Ne/Ar* (right) mixtures with  $C_A = 0.5$  and  $P_B/P_A = 0$  at different values of the rarefaction parameter for slit flows. Filled and empty symbols stand for the lighter and heavier components, respectively.

From the density curves, it can be deduced that gas separation strongly affects the flow. Near the free molecular limit, the density curves are nearly identical. In this case, the dynamics of the gas components are independent. The dynamics of both components follows the universal behavior of the single gas. However, at intermediate values of the rarefaction parameter, there are differences between the density profiles due to the gas separation. With regard to the mixture composition, it can be seen that the separation is larger for the *He/Xe* mixture than for the *Ne/Ar* one.

Figure 4.12 presents the density profiles for the *He/Xe* mixture at different concentrations  $C_A = 0.25$  and  $0.75$ ,  $\delta_A = 10$  and  $P_B/P_A = 0$ . The density distributions show the decreasing character across the slit. The gas flow is also affected by the gas separation.

In order to compare the results at different pressure ratios, Figure 4.13 shows the density profiles for the two types of mixture at  $C_A = 0.5$ ,  $\delta_A = 1$  and  $P_B/P_A = 0, 0.4$  and  $0.7$ . It can be seen that the densities tend to the finite outlet conditions for finite pressure drops; however, the outlet densities are zero for flow into vacuum. It is clearly seen that the separation

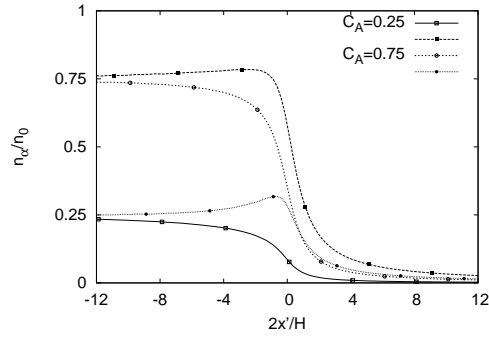


Figure 4.12: The distribution of the density for  $He/Xe$  mixture with  $C_A = [0.25, 0.75]$  and  $\delta_A = 10$  at  $P_B/P_A = 0.1$  for slit flows. Filled and empty symbols stand for the lighter and heavier components, respectively.

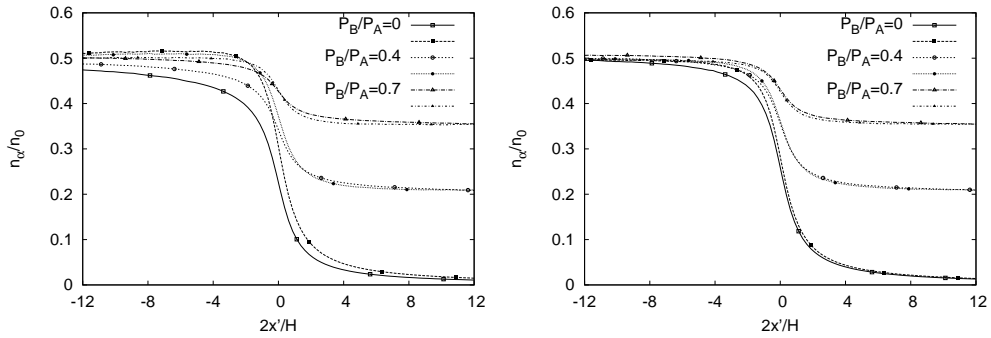


Figure 4.13: The distribution of the density for  $He/Xe$  (left) and  $Ne/Ar$  (right) mixtures with  $C_A = 0.5$  and  $\delta_A = 1$  at different values of the pressure ratio for slit flows. Filled and empty symbols stand for the lighter and heavier components, respectively.

becomes stronger as the pressure drop becomes larger. As a consequence, the separation is intensified with the larger pressure drop. It can be deduced that the separation is stronger for the mixture with larger mass ratio. In that case, the difference between the molecular velocities is larger, which intensifies the separation.

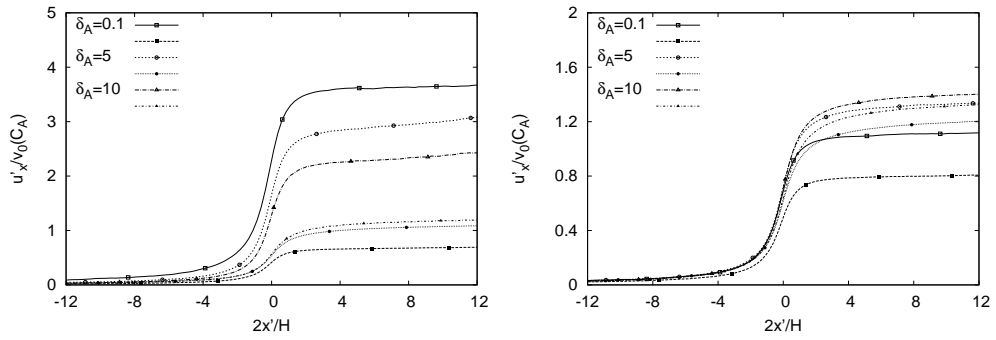


Figure 4.14: The distribution of the axial velocity for *He/Xe* (left) and *Ne/Ar* (right) mixtures with  $C_A = 0.5$  and  $P_B/P_A = 0$  at different values of the rarefaction parameter for slit flows. Filled and empty symbols stand for the lighter and heavier components, respectively.

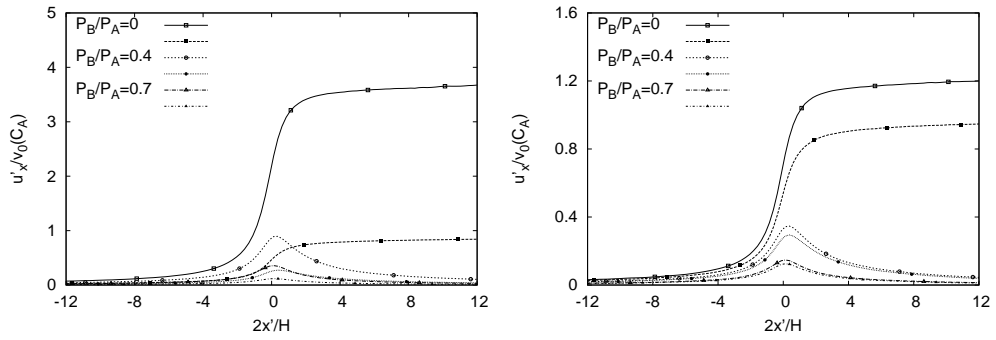


Figure 4.15: The distribution of the axial velocity for *He/Xe* (left) and *Ne/Ar* (right) mixtures with  $C_A = 0.5$  and  $\delta_A = 1$  at different values of the pressure ratio for slit flows. Filled and empty symbols stand for the lighter and heavier components, respectively.

In Figure 4.14, the velocity profiles are shown for two different mixtures at  $C_A = 0.5$ ,  $P_B/P_A = 0$ . For both cases, the velocities start to increase as approaching the zone of the slit. The tendency of increasing velocity is maintained after the slit as well. This behavior happens because the flow

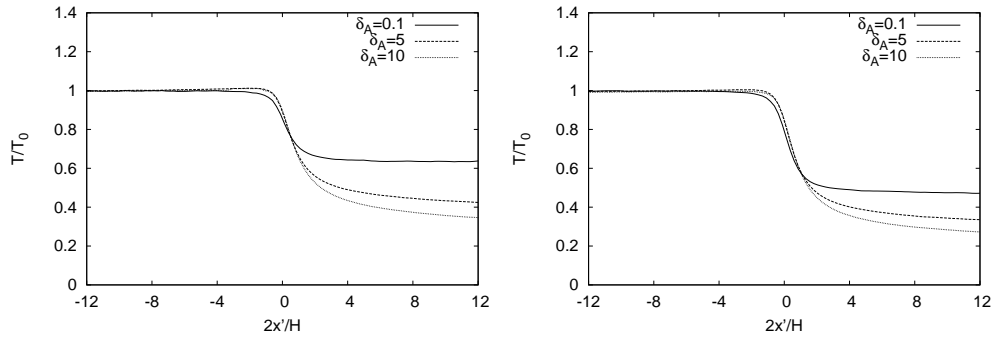


Figure 4.16: The distribution of the temperature for *He/Xe* (left) and *Ne/Ar* (right) mixtures with  $C_A = 0.5$  and  $P_B/P_A = 0$  at different values of the rarefaction parameter for slit flows.

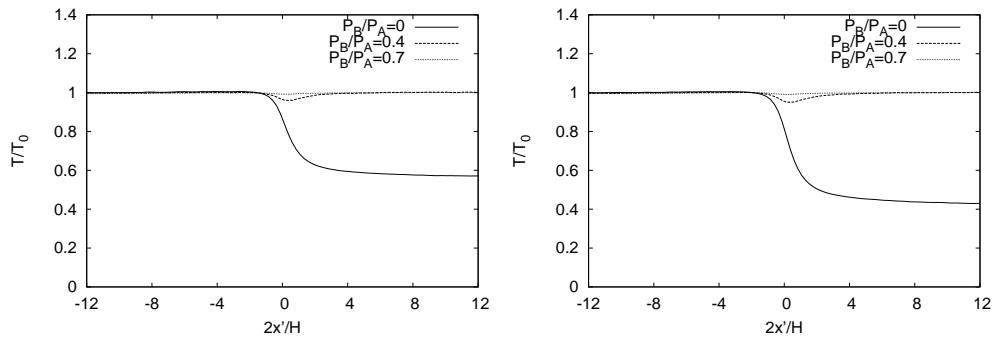


Figure 4.17: The distribution of the temperature for *He/Xe* (left) and *Ne/Ar* (right) mixtures with  $C_A = 0.5$  and  $\delta_A = 1$  at different values of the pressure ratio for slit flows.

is into vacuum. It is observed that significant differences can appear between the velocities of the components. The difference becomes larger as the gas is more rarefied. This is caused by the increasing gas separation as the rarefaction parameter becomes smaller. There are qualitative differences between the two types of mixture. The velocity of the lighter component monotonically increases as the gas is more rarefied for the *He/Xe* mixture,

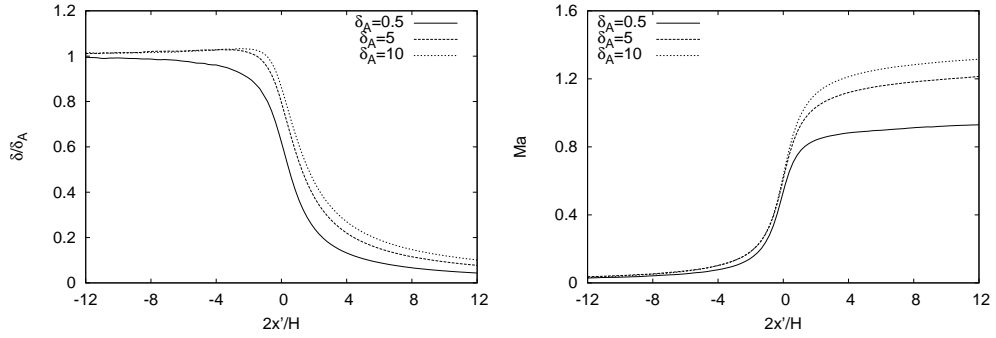


Figure 4.18: Normalized rarefaction parameter (left) and Mach number (right) for  $He/Xe$  mixture with  $C_A = 0.5$  and  $P_B/P_A = 0$  at different values of rarefaction parameter for slit flows.

while an opposite situation occurs for the  $Ne/Ar$  composition, the velocity of the lighter species decreases as the rarefaction parameter decreases. These findings are in accordance with the behavior of the flow rates.

Figure 4.15 shows the velocity curves for the two species at  $C_A = 0.5$ ,  $\delta_A = 1$  and different values of the pressure drop. There are qualitative differences between the zero and finite pressure ratio cases. The velocities increase along the  $x'$  axis for flow into vacuum. However, they take a maximum near the slit for the finite pressure ratio cases. The reduction of the velocities in the latter situation is caused by the background gas in the downstream reservoir. The magnitude of the velocities become smaller if the pressure drop is reduced.

To examine the temperature, Figure 4.16 presents the temperature profiles versus the rarefaction parameter. The two types of mixture are studied at  $C_A = 0.5$ ,  $P_B/P_A = 0$ . The temperature shows a decreasing character, which starts near the slit and still continues in the downstream reservoir. The temperature drop is caused by the rapid extension of the gas into vacuum. It is interesting to note that the temperature drop is larger for the  $Ne/Ar$  mixture. This happens because the mixture temperature is affected by the mass-density average gas velocity, which is larger for the  $Ne/Ar$  mixture.

Figure 4.17 shows the temperature profiles for the two mixtures at  $C_A = 0.5$ ,  $\delta_A = 1$  and different values of the pressure drop. The temperature has different behaviors at zero and finite pressure ratios. For zero pressure drop, the temperature steadily decreases, while for the finite pressure ratio, it reaches a minimum in the downstream container, then it starts to tend to the value of the outflow condition. Generally, the temperature variation is larger if the pressure drop is larger. This is in accordance with our expectation since the flow is more out of equilibrium if the driving force is larger. On the other hand, it is found that the temperature variation is larger for the *Ne/Ar* mixture, which is caused by the larger mass-average velocity of this mixture.

Finally, in Figure 4.18, the distributions of the local normalized rarefaction parameter and Mach number are presented for *He/Xe* mixture with  $C_A = 0.5$  and  $P_B/P_A = 0$  at different values of the reference rarefaction parameter. The Mach number is defined by  $Ma = \sqrt{6/5}u'/v_0(C_A)$ , where  $u'$  is the absolute value of the mass-density average gas velocity. It is observed that the rarefaction parameter rapidly decreases near the slit. Finally, it tends to the zero outflow value, which corresponds to the vacuum condition. The Mach number starts increasing near the slit by moving from the upstream to downstream reservoirs. The Mach number increases if the rarefaction parameter becomes smaller.

# Chapter 5

## Experimental study of binary gas flows through long microchannels and comparison to kinetic calculation

### 5.1 Introduction

The properties of rarefied gases can be measured by different experimental techniques. With regard to flows through microchannels, the flow rate is an important quantity and it has been studied by many researchers [6],[3], [105],[44],[18], [19]. By using the flow rate, the average gas speed in the channel can be estimated. The experimental flow rates can be compared to different theoretical approaches. The slip coefficients have been determined, for example, in Refs. [4], [16]. For mixtures, it is interesting to see the effect of the gas separation, which has a significant impact on the flow rate. The flow rate can be measured by the constant volume and bubble-tracking methods. However, the constant volume method can be considered as the

most accurate. In the experimental part of the thesis, this technique is used for the measurement of the flow rate through different microchannels.

This chapter is dedicated to the flow rate measurement of binary gases through long rectangular [87], [88], [93], [86] and trapezoidal channels and comparison to the kinetic calculation. In the first section, the description of the constant volume method and the experimental setup is provided. The method is based on the measurement of the changes of the pressure in the upstream and downstream containers during the gas flow process. The experimental setup consists of a thermally insulated chamber containing the inlet and outlet reservoirs, the microsystem, connecting facilities and pressure and temperature sensors. The experiments are carried out under isothermal conditions. In the forthcoming sections, the results are compared to the computational flow rates, which are obtained from the solution of the McCormack kinetic model [45] and the application of the flow rate calculation developed in the computational part of the thesis [90].

## 5.2 Definition of the problem

In the flow rate measurement, the gas of binary mixtures flows through microchannels. The channel axis lies in the  $z'$  coordinate direction, while the cross section is in the  $x', y'$  coordinate sheet. The characteristic length of the problem  $L_C$  is chosen by as the height of the microchannel for rectangular channels and the hydrodynamic diameter  $D_h$  for other geometries. Dimensionless coordinates are introduced by  $x = x'/L_C$ ,  $y = y'/L_C$  and  $z = z'/L_C$ .

The channel is located between upstream A and downstream B reservoirs. The gaseous mixture has two components  $\alpha = 1, 2$ . The pressures and the concentrations of the gas in the reservoirs are denoted by  $P_A, P_B$  and  $C_A, C_B$ . The temperature is  $T_0$  in the reservoirs and the channel. The rarefaction

degree of the gas is described by the rarefaction parameter such that

$$\delta = \frac{PL_C}{\mu(C)v(C)}, \quad (5.1)$$

where  $P$  is the local pressure,  $\mu(C)$  is the viscosity and  $v(C) = \sqrt{2kT_0/m}$  is the characteristic molecular speed. In addition,  $m = Cm_1 + (1 - C)m_2$  is the average mass. Here,  $m_1$  and  $m_2$  are the masses of the components. The flow may be classified by the inlet rarefaction parameter  $\delta_A$  as a reference value. The average Knudsen number in the channel is introduced by  $Kn_0 = 2/(\delta_A + \delta_B)$ . Under these conditions, we are interested in the molar flow rates defined by

$$J_\alpha = \int_{A'} n_\alpha u'_{\alpha z} dA', \quad (5.2)$$

where  $A'$  denotes the cross section,  $n_\alpha$  is the molar density of component  $\alpha$  and  $u'_{\alpha z}$  is the axial velocity of component  $\alpha$ . The total flow rate is defined as  $J = J_1 + J_2$ .

## 5.3 The experimental approach

### 5.3.1 Experimental setup

The overall experimental setup, which was described in detail in Refs. [58], [57], [87], is located in a thermally insulated plastic chamber kept at constant temperature, as it is shown in Figure 5.1. Inside the chamber, there are upstream A and downstream B reservoirs with volumes  $V_A = 1.708e - 4m^3$  and  $V_B = 1.685e - 4m^3$ . The volumes are determined with an uncertainty of  $\pm 1.3\%$ . The microsystem  $\mu S$  is placed between the two containers. The reservoirs A and B can be connected to an external gas bottle G and a vacuum pump VP to clean the system. During the flow rate measurement, the pressure inside each reservoir is measured by Inficon capacitance diaphragm

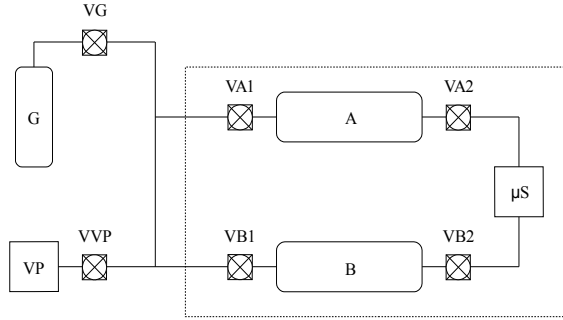


Figure 5.1: The layout of the flow rate setup.

gauges (CDG025D) and the flow rate is deduced from the pressure change in the reservoirs. The accuracy of the pressure measurements by the capacitance pressure gauges is  $\pm 0.2\%$  of reading. In order to maintain isothermal conditions, the interior part of the setup is thermally regulated by Peltier modules, which allow maintaining constant temperature inside the setup. The temperature is accurately measured during the operations with PT100 temperature sensors with  $0.15K$  accuracy. Most of the setup is made of stainless steel, aluminum or glass, and the connections are well-insured to avoid any leakage during low pressure operation. Leakage has been checked by means of helium detection, with a portable leak detector.

In the experiment, the flow rate is determined from the pressure variations in the inlet and outlet reservoirs. However, for the actual measurement a three-step process is applied by taking into account the effect of possible leakage or outgassing. Initially, the gas circuit, including the reservoirs A, B and the microchannels, in the interior part of the setup is filled up with the gas mixture at the downstream pressure  $P_B$ . Then, valve  $VA2$  is closed and the possible leakage or outgassing flow rate  $J_B^o$  is measured in circuit B. In the second step, reservoir A is filled up with the mixture at pressure  $P_A$ . After thermal regulation is reached, valve  $VA2$  is opened, allowing the gas

to flow through the microsystem. From the pressure variations in container A and B, the flow rates are determined as  $J'_A$  and  $J'_B$ . In the final step, the overall circuit is filled up with the gas at the actual upstream pressure. Then, valve  $VB2$  is closed and the possible leakage or outgassing flow rate  $J_A^o$  is determined in circuit A. The leakage or outgassing flow rates are used to correct the quantities  $J'_A$  and  $J'_B$  to yield  $J_A$  and  $J_B$  as the final flow rates [87]. In all cases, the deviation between  $J_A$  and  $J_B$  is less than the experimental uncertainty, which justifies the correctness of the measurement. The experimental flow rate is then defined by  $J = (J_A + J_B)/2$ .

### 5.3.2 Determination of the flow rates

On the basis of the pressure variations in each reservoir, the flow rates can be deduced as

$$J_A^e = -\frac{dN_A}{dt} = -\frac{V_A}{R_g} \frac{d}{dt} \left( \frac{P_A}{T_A} \right), \quad (5.3)$$

$$J_B^e = \frac{dN_B}{dt} = \frac{V_B}{R_g} \frac{d}{dt} \left( \frac{P_B}{T_B} \right), \quad (5.4)$$

where  $t$  is the time,  $R_g = 8.3143 \text{ J}/(\text{molK})$  is the global gas constant,  $N_A$  and  $N_B$  are the amount of gas molecules in mol unit in the upstream and downstream reservoirs, respectively,  $P_A$  and  $T_A$ ,  $P_B$  and  $T_B$  the pressures and temperatures in the reservoirs.

It is noticed that the definition of the flow rate is given in molar unit, which is a useful choice for the measurement instead of the mass flow rate. The molar (or particle) and mass flow rates are two different quantities. For gaseous mixtures, the mass flow rate does not typify well the flow rate since the masses of the components are different, and the actual concentration of the gas portion flowing through the microsystem is not known [87]. The difference between the two types of flow rates is explained in the following.

The mass flow rate  $dM/dt$  is commonly introduced in single gases. Since, in general,  $M = N \times m^*$ , with  $m^*$  denoting the average molecular mass of

the particles flowing through the channel during the experiment, the mass flow rate can be written by

$$\frac{dM}{dt} = \pm \frac{V}{RT} \frac{dP}{dt}, \quad (5.5)$$

where,  $R = k/m^*$  is the specific gas constant with  $k$  denoting the Boltzmann constant. For single component gases, the average mass  $m^*$  is equal to the molecular mass. However, for gaseous mixtures,  $m^*$  can not be defined, since it refers to that gas portion which has flowed through the channel during the experiment. Because of the diffusion effects, that is the lighter particle has larger velocity than the heavier one, the concentration of this gas portion, denoted by  $C^*$ , is different from the concentrations in the two reservoirs ( $C_A$  and  $C_B$ ) and it is not determined. In fact, this concentration can be expressed as  $C^* = J_1/(J_1 + J_2)$  and then the average mass is obtained by  $m^* = C^*m_1 + (1 - C^*)m_2$ . However, the component fluxes,  $J_1$  and  $J_2$  and consequently  $m^*$ , can not be determined from the present experimental approach. They are estimated only from the computational approach. Therefore, the experimental results and the comparative study is based on the molar and not on the mass flow rates.

From Eqs. (5.3)-(5.4), the total molar flow rate through the channel can be expressed by

$$J_A^e = -\frac{dN_A}{dt} = -\frac{V_A}{R_g T_A} \frac{dP_A}{dt} \left( 1 - \frac{dT_A/T_A}{dP_A/P_A} \right), \quad (5.6)$$

$$J_B^e = \frac{dN_B}{dt} = \frac{V_B}{R_g T_B} \frac{dP_B}{dt} \left( 1 - \frac{dT_B/T_B}{dP_B/P_B} \right). \quad (5.7)$$

High thermal stability is ensured by temperature-regulation in the system. The relative temperature variation  $dT_{A,B}/T_{A,B}$  is of the order of  $4 \times 10^{-4}$  and the relative pressure variation is  $dP_{A,B}/P_{A,B} \simeq 2 \times 10^{-2}$ . As a consequence,

Eqs. (5.6)-(5.7) can be written as

$$J_A^e = -\frac{V_A}{R_g T_A} a_A c_A, \quad (5.8)$$

$$J_B^e = \frac{V_B}{R_g T_B} a_B c_B, \quad (5.9)$$

where  $a_{A,B} = dP_{A,B}/dt$  is calculated from a least-square linear fit of the upstream or downstream measured pressure

$$P_A(t) = a_A t + b_A, \quad (5.10)$$

$$P_B(t) = a_B t + b_B, \quad (5.11)$$

and  $c_{A,B} = 1 - (dT_{A,B}/T_{A,B}) / (dP_{A,B}/P_{A,B}) = 1 \pm 2\%$ . The standard deviation of coefficient  $a_{A,B}$  is found to be less than 0.5%. To summarize, the overall uncertainty of the flow rate measurement is calculated such that

$$\frac{\Delta J_{A,B}^e}{J_{A,B}^e} = \frac{\Delta V}{V} + \frac{\Delta T_{A,B}}{T_{A,B}} + \frac{\Delta a_{A,B}}{a_{A,B}} + \frac{\Delta c_{A,B}}{c_{A,B}} \quad (5.12)$$

and less than  $\pm(1.3 + 0.2 + 0.5 + 2)\% = \pm 4\%$ .

### 5.3.3 Specification of microchannels

The microsystems consist of a series of parallel microchannels connected to the same inlet and the same outlet in order to increase the total flow rate through the system and make the measurement more efficient. In the experiments, flows through rectangular and trapezoidal microchannels are measured. The first rectangular microchannels (R1) have dimensions as height  $H = 1.88 \pm 0.1 \mu m$ , width  $W = 21.2 \pm 0.3 \mu m$  and length  $L = 5 mm$ <sup>1</sup> The bunch contains 45 parallel channels. The second rectangular channel (R2) have dimensions  $H = 1.15 \mu m$ , width  $W = 21 \mu m$  and length  $L = 5 mm$ .

---

<sup>1</sup>It is noted that these experimental results are taken from J. Pitakarnnop's PhD thesis for the comparison for channel R1 [57].

The bunch contains 380 parallel channels. The trapezoidal channel (T1) has acute angle  $54.74^\circ$  and other dimensions, depth  $h = 1.90 \pm 0.013\mu m$ , longer base  $B = 5.38 \pm 0.019\mu m$  and length  $L = 5mm$ . The microsystem contains 400 parallel channels. The bunch of channels are prepared by etching in silicon and covered by a glass plate made by anodic bonding. The accommodation coefficient of the channels is very close to unity. In fact, the accommodation coefficients on the silicon and glass surfaces may not be the same exactly. However, the diffuse reflection boundary condition is adequate for these channels, as it was confirmed in Refs. [58] and also [87]. Hence, in the present work, the diffuse reflection boundary condition is used for all flow configurations.

## 5.4 Kinetic calculation of the flow rates

The calculation is rest on the methodology developed in section 3.6.4. The deduction of the flow rates is divided into two parts. First, the kinetic coefficients are determined for a wide range of the gas rarefaction and the concentration for the particular mixture by solving the McCormack model [54], [90]. The realistic potential is used in all calculation [35] and Appendix A.1. It is mentioned that the kinetic coefficients provided by the realistic potential or the hard-sphere molecular system are different. A discussion on the effect of the two different interactions may be found in Ref. [53] for flows between two parallel plates. It was verified that the  $\Lambda_{PP}$  coefficient is nearly the same, but there could be some differences between the values of the coefficients  $\Lambda_{CP}, \Lambda_{CC}$  provided by the two potentials. Since the realistic potential is derived from experimental measurements, that is the suitable choice, which takes into account the transports in the gaseous mixture well, and, consequently, used in the present work. For the rectangular channels, the height  $L_C = H$ , while for the trapezoidal channels, the hydrodynamic

diameter  $L_C = D_h$  is chosen as the characteristic length.

In the second step, the flow rates are calculated by using the expressions of Eqs. (3.144)-(3.147). However, in the present case, the molar flow rates are deduced. The corresponding equations for the molar flow rates are given by

$$J_1 = -\frac{PAL_C}{mvL} \times \left[ (C\Lambda_{PP} + (1-C)\Lambda_{CP}) \frac{\partial P}{\partial \hat{z}} \frac{1}{P} + (C\Lambda_{PC} + (1-C)\Lambda_{CC}) \frac{\partial C}{\partial \hat{z}} \frac{1}{C} \right], \quad (5.13)$$

$$J_2 = -\frac{PAL_C}{mvL} \times (1-C) \left[ (\Lambda_{PP} - \Lambda_{CP}) \frac{\partial P}{\partial \hat{z}} \frac{1}{P} + (\Lambda_{PC} - \Lambda_{CC}) \frac{\partial C}{\partial \hat{z}} \frac{1}{C} \right], \quad (5.14)$$

where  $\hat{z} = z'/L$  is the dimensionless coordinate along the channel axis. In these equations, the kinetic coefficients depend on the rarefaction parameter, which is determined from the local pressure and the experimental viscosity. The procedure of deducing the viscosity function is described in Appendix A.2. Equations (5.13) and (5.14) are supplemented by the boundary condition

$$P(0) = P_A, \quad P(1) = P_B, \quad (5.15)$$

$$C(0) = C_A, \quad C(1) = C_B. \quad (5.16)$$

In the experiments, these boundary conditions are justified by the fact that the volume of the upstream and downstream containers are significantly larger than the volume of the microsystem, and the pressure variation in the containers is sufficiently small. Consequently, the variation of the pressure and the concentration can be neglected during the experiment. Eqs. (5.13)-(5.16) are solved with the same numerical treatment and parameters as described in section 3.6.4.

## 5.5 Comparative study for binary gas flows in rectangular and trapezoidal channels

### 5.5.1 Flow rates for channel R1

Computational and experimental results are provided for the flow of *He/Ar* gaseous mixture through the rectangular microchannels R1. The molar masses of the components of the mixture are  $m_{He} = 4.003g/mol$  and  $m_{Ar} = 39.95g/mol$ . The reference concentration  $C_A$  of the gas mixture takes the following values  $C_A = [0.0, 0.1017, 0.3012, 0.5010, 0.7019, 0.9014, 1.0]$ , which includes the single gas cases *He*  $C_A = 1$  and *Ar*  $C_A = 0$  as well. These values cover the whole range of the concentration interval. For these cases, the concentration uncertainty is  $[0, \pm 0.002, \pm 0.006, \pm 0.01, \pm 0.006, \pm 0.002, 0]$ , respectively. The effect of the uncertainty of the concentration is checked on the flow rates, and it is less than  $\pm 0.5\%$ . The temperature is  $T = 298.5K$ . Two values of the outlet pressure  $P_B \simeq 15kPa$  and  $P_B \simeq 2kPa$  are considered in the experiment, while the pressure ratio is in the range of  $P_A/P_B = 3 - 7$ .

Table 5.1 and 5.2 show the experimental and computational flow rates together with the flow parameters for  $P_B \simeq 15kPa$  and  $P_B \simeq 2kPa$ , respectively, at different values of the inlet concentration and pressure ratio. For the case R1, the exact downstream pressures can be found in Ref. [57], but they are nearly  $15kPa$  and  $2kPa$ . It is noted that the flow rate through one single channel is shown. In the first table, the columns from the first one to the last one contain the pressure ratio, the average Knudsen number, the computed flow rate of the first component  $J_1$ , the corresponding flow rate for the second component  $J_2$ , the total computational flow rate  $J$ , the experimental flow rate  $J^e$  and the deviation between the computational and experimental flow rates  $\Delta = 100(J - J^e)/J$ . In the second table, two additional columns, the seventh and eights, present the experimental uncertainties,  $\Delta_A$  and  $\Delta_B$ , for the  $J_A^e$  and  $J_B^e$  flow rates. In the case of the lower outlet pressure, there was

Table 5.1: Flow rates for  $He/Ar$  mixture at different values of the concentration and pressure ratio at  $P_B \simeq 15kPa$  through channels R1.

$P_A/P_B$	$Kn_0$	$J_1(mol/s)$	$J_2(mol/s)$	$J(mol/s)$	$J^e(mol/s)$	$\Delta$
$C_A = 0.0$						
3.06	0.175	0.00	7.57e-11	7.57e-11	7.28e-11	3.82
4.06	0.165	0.00	1.26e-10	1.26e-10	1.21e-10	3.50
5.06	0.159	0.00	1.86e-10	1.86e-10	1.79e-10	3.29
6.01	0.154	0.00	2.51e-10	2.51e-10	2.43e-10	3.34
7.00	0.151	0.00	3.28e-10	3.28e-10	3.13e-10	4.67
$C_A \simeq 0.1$						
3.03	0.197	8.80e-12	6.70e-11	7.58e-11	7.56e-11	0.23
4.08	0.184	1.42e-11	1.14e-10	1.29e-10	1.29e-10	-0.77
5.04	0.178	1.99e-11	1.65e-10	1.85e-10	1.94e-10	-5.03
6.01	0.173	2.64e-11	2.23e-10	2.50e-10	2.49e-10	0.15
7.04	0.169	3.44e-11	2.94e-10	3.28e-10	3.26e-10	0.50
$C_A \simeq 0.3$						
3.04	0.225	2.85e-11	5.62e-11	8.48e-11	8.38e-11	1.15
4.02	0.212	4.39e-11	9.20e-11	1.36e-10	1.36e-10	0.19
5.03	0.203	6.27e-11	1.35e-10	1.98e-10	2.00e-10	-0.80
6.04	0.197	8.37e-11	1.84e-10	2.68e-10	2.70e-10	-0.50
7.00	0.194	1.06e-10	2.37e-10	3.43e-10	3.42e-10	0.24
$C_A \simeq 0.5$						
3.10	0.262	5.40e-11	4.54e-11	9.93e-11	9.80e-11	1.54
4.09	0.246	8.28e-11	7.42e-11	1.57e-10	1.59e-10	-0.84
5.05	0.237	1.14e-10	1.05e-10	2.20e-10	2.16e-10	1.59
6.02	0.231	1.51e-10	1.41e-10	2.92e-10	2.90e-10	0.69
7.00	0.226	1.91e-10	1.82e-10	3.73e-10	3.73e-10	0.05
$C_A \simeq 0.7$						
3.05	0.309	8.49e-11	3.02e-11	1.15e-10	1.07e-10	6.75
4.03	0.291	1.31e-10	4.91e-11	1.80e-10	1.73e-10	3.99
5.02	0.280	1.82e-10	7.11e-11	2.53e-10	2.39e-10	5.38
5.98	0.272	2.38e-10	9.45e-11	3.32e-10	3.15e-10	5.30
7.01	0.267	3.03e-10	1.22e-10	4.25e-10	4.09e-10	3.81
$C_A \simeq 0.9$						
2.99	0.402	1.28e-10	1.16e-11	1.40e-10	1.38e-10	1.22
4.04	0.376	2.05e-10	1.97e-11	2.24e-10	2.23e-10	0.79
5.03	0.361	2.85e-10	2.83e-11	3.13e-10	3.11e-10	0.57
6.09	0.351	3.79e-10	3.87e-11	4.18e-10	4.17e-10	0.04
6.96	0.345	4.63e-10	4.78e-11	5.11e-10	5.09e-10	0.45
$C_A = 1.0$						
3.03	0.511	1.65e-10	0.00	1.65e-10	1.68e-10	-2.20
4.00	0.481	2.55e-10	0.00	2.55e-10	2.57e-10	-0.94
5.01	0.461	3.58e-10	0.00	3.58e-10	3.65e-10	-1.93
6.01	0.449	4.70e-10	0.00	4.70e-10	4.77e-10	-1.44
6.94	0.440	5.83e-10	0.00	5.83e-10	6.00e-10	-2.82

Table 5.2: Flow rates for  $He/Ar$  mixture at different values of the concentration and pressure ratio at  $P_B \simeq 2kPa$  through channels R1.

$P_A/P_B$	$Kn_0$	$J_1(mol/s)$	$J_2(mol/s)$	$J(mol/s)$	$J^e(mol/s)$	$\Delta_A$	$\Delta_B$	$\Delta$
$C_A = 0.0$								
3.10	1.31	0.00	6.56e-12	6.56e-12	6.51e-12	9.67	9.58	0.82
4.02	1.26	0.00	9.31e-12	9.31e-12	8.86e-12	8.59	8.56	4.78
4.79	1.18	0.00	1.22e-11	1.22e-11	1.20e-11	7.30	7.76	1.89
5.96	1.17	0.00	1.59e-11	1.59e-11	1.51e-11	6.84	7.50	4.73
6.61	1.11	0.00	1.89e-11	1.89e-11	1.83e-11	6.03	6.55	2.99
$C_A \simeq 0.1$								
3.02	1.48	1.47e-12	5.85e-12	7.32e-12	6.96e-12	9.24	9.14	4.94
3.96	1.39	2.05e-12	8.68e-12	1.07e-11	1.03e-11	7.42	7.22	3.52
5.21	1.32	2.73e-12	1.25e-11	1.52e-11	1.44e-11	5.95	7.09	5.55
6.08	1.29	3.18e-12	1.53e-11	1.85e-11	1.78e-11	5.40	5.88	3.78
6.62	1.28	3.44e-12	1.71e-11	2.05e-11	1.97e-11	5.50	6.25	4.15
$C_A \simeq 0.3$								
3.07	1.68	4.76e-12	5.00e-12	9.76e-12	8.82e-12	7.90	8.33	9.57
4.03	1.58	6.67e-12	7.44e-12	1.41e-11	1.27e-11	6.44	6.95	9.71
5.00	1.52	8.43e-12	9.98e-12	1.84e-11	1.75e-11	5.75	5.60	5.07
5.94	1.50	9.94e-12	1.24e-11	2.23e-11	2.12e-11	5.39	5.53	5.03
6.67	1.45	1.13e-11	1.47e-11	2.60e-11	2.40e-11	5.19	5.83	7.55
$C_A \simeq 0.5$								
3.03	1.97	8.38e-12	3.78e-12	1.22e-11	1.13e-11	6.12	6.35	6.72
4.06	1.85	1.21e-11	5.80e-12	1.79e-11	1.66e-11	5.20	5.66	7.02
5.03	1.78	1.54e-11	7.81e-12	2.32e-11	2.11e-11	4.80	5.27	8.99
5.91	1.73	1.82e-11	9.72e-12	2.79e-11	2.54e-11	4.67	5.11	9.23
6.42	1.71	1.98e-11	1.09e-11	3.07e-11	2.83e-11	4.71	4.92	7.70
$C_A \simeq 0.7$								
3.06	2.32	1.29e-11	2.50e-12	1.54e-11	1.41e-11	5.63	5.78	8.44
3.94	2.20	1.78e-11	3.67e-12	2.15e-11	2.00e-11	4.92	5.22	6.59
5.42	2.07	2.58e-11	5.77e-12	3.16e-11	2.90e-11	4.59	4.95	8.19
5.87	2.05	2.81e-11	6.43e-12	3.46e-11	3.13e-11	4.50	4.89	9.57
6.33	2.03	3.05e-11	7.15e-12	3.77e-11	3.41e-11	4.46	4.83	9.44
$C_A \simeq 0.9$								
3.01	3.01	1.78e-11	8.97e-13	1.87e-11	1.80e-11	5.47	5.53	3.50
3.95	2.83	2.56e-11	1.37e-12	2.70e-11	2.60e-11	4.86	5.05	3.65
5.20	2.70	3.56e-11	2.06e-12	3.77e-11	3.56e-11	4.66	5.18	5.46
5.88	2.64	4.11e-11	2.46e-12	4.35e-11	4.08e-11	4.43	4.74	6.26
6.31	2.62	4.45e-11	2.71e-12	4.72e-11	4.53e-11	4.27	4.61	3.95
$C_A = 1.0$								
3.12	3.95	2.12e-11	0.00	2.12e-11	1.95e-11	6.63	6.44	8.29
3.92	3.61	2.99e-11	0.00	2.99e-11	2.77e-11	5.58	5.96	7.24
4.97	3.44	4.04e-11	0.00	4.04e-11	3.82e-11	5.05	5.34	5.39
5.83	3.40	4.83e-11	0.00	4.83e-11	4.62e-11	4.83	5.02	4.22
6.81	3.34	5.76e-11	0.00	5.76e-11	5.45e-11	4.52	4.92	5.43

non-negligible leakage or outgassing flow rate, which effects the experimental error [58], [87].

It can be concluded that the average Knudsen number is within the range of 0.151 – 0.511 and 1.11 – 3.95 in the first and second tables. In addition, the flow rate is about one order of magnitude larger at higher outlet pressures. The reason of this behavior is that the gas is more dense at higher pressures, which results into the larger flow rate. The discrepancy between the computational and experimental results  $\Delta$  in Table 5.1 varies between  $-5.03\%$  and  $6.75\%$  with an average value of  $1.03\%$ , while in Table 5.2 it is between  $0.82\%$  and  $9.71\%$  with the average value of  $5.98\%$ . It can be seen that the deviation  $\Delta$  is generally much smaller for larger outlet pressure. For  $P_B \simeq 15kPa$ ,  $\Delta$  is almost within the range of the experimental uncertainty  $\pm 4\%$ , however, for  $P_B \simeq 2kPa$ , the discrepancy can exceed the level of the corresponding experimental uncertainties. This suggests that the agreement between the computational and experimental results is better at smaller Knudsen numbers. This is explained by the fact that the rarefaction effects are less important at higher pressures. As a consequence, the behaviour of the gas is more close to hydrodynamics. In the zero Knudsen number limit, the McCormack model results into a hydrodynamic description with the correct transport coefficients obtained from the realistic potential. In this case, good agreement is expected between theory and experiment. At smaller pressures, the flow is affected by rarefaction effects more significantly, which can results into the slight mismatch between the computational and experimental results. However, the overall agreement between the experimental and computational results are considered as very good. It can be seen that the flow rates increase with increasing pressure drop. In addition, the flow rate is larger at larger *He* concentration. This behavior is explained by the larger molecular speed for the lighter component.

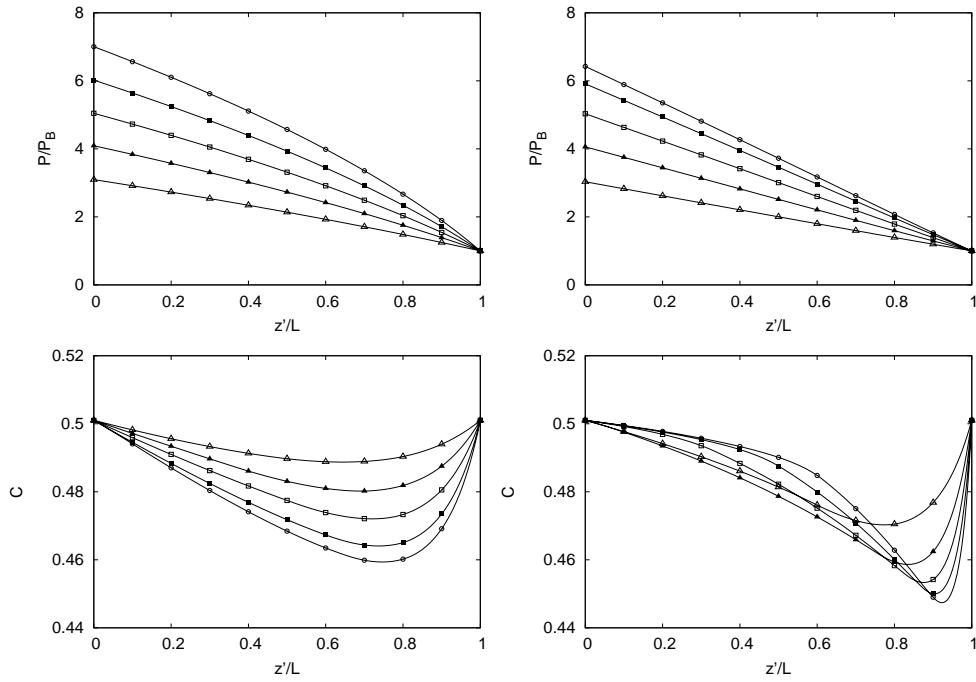


Figure 5.2: Distributions of the pressure (up) and concentration (down) for  $He/Ar$  mixture with  $C_A = 0.5010$  along the axis of the channel for  $P_B \simeq 15kPa$  (right) and  $P_B \simeq 2kPa$  (left) for channel R1. The symbols  $\Delta, \blacktriangle, \square, \blacksquare, \circ$  represent the results for  $P_A/P_B = [3.01, 4.09, 5.04, 6.02, 7.00]$  and  $[3.03, 4.06, 5.03, 5.91, 6.42]$  for the larger and smaller outlet pressures, respectively.

### 5.5.2 Distribution of macroscopic quantities for R1

The pressure and concentration distributions along the axis of the channel are also computed by solving the McCormack model. The typical distributions of these quantities are shown in Figure 5.2. The flow parameters correspond the data in Tables 5.1 and 5.2 for the case  $C_A = 0.5$  and outlet pressures  $P_B \simeq 15kPa$  and  $P_B \simeq 2kPa$ , respectively. The distributions for the five different values of the pressure ratio are plotted. The pressure profiles for the larger

outlet pressure are non-linear, which is caused by the compression effects on the dimensionless flow rates. The pressure starts at the value  $P(0)$  at the inlet of the channel then reaches the outlet value  $P(1)$  at the outlet of the channel. The corresponding pressure for the smaller outlet pressure has a more linear character. This feature is caused by the fact that the dimensionless flow rate becomes independent of the rarefaction as approaching the free molecular limit. It can be seen that the corresponding concentration profiles are non-uniform, and there is a significant concentration variation, which can be as large as 10%, along the axis of the channel. It can be seen that the variation increases with increasing pressure drop and it is generally larger for the more rarefied atmosphere. These features are justified by the fact that the gas separation is intensified with larger pressure drop and larger Knudsen number.

### 5.5.3 Flow rates for channel R2

Flow rate results are presented for  $He/Ar$  and  $He/Kr$  gaseous mixtures through the rectangular microchannels R2. The masses of the species of the  $He/Kr$  mixture are  $m_{He} = 4.003g/mol$  and  $m_{Ar} = 39.95g/mol$ . The reference concentration of the  $He/Ar$  mixtures is the same as for the experiments for channels R1. The concentration for the  $He/Kr$  mixture is  $C_A = 0.501$ . The uncertainty of the concentration is  $\pm 0.01$ . The temperature in the experiments is  $T = 299.2K$ . Experiments have been performed at downstream pressures  $P_B \simeq 15.2kPa$ ,  $P_B \simeq 8kPa$  and  $P_B \simeq 4.1kPa$ . In the latter case, only single gases are considered. The pressure ratio is in the range of 3 – 7 for  $P_B \simeq 15.2kPa$  and 4 – 7 for  $P_B \simeq 8kPa$ ,  $P_B \simeq 4.1kPa$ , respectively.

Table 5.3: Flow rates for  $He/Ar$  at different values of the concentration as the function of the pressure ratio at  $P_B \simeq 15.2kPa$  through channels R2.

$P_A(kPa)$	$P_B(kPa)$	$P_A/P_B$	$Kn_0$	$J_A^c(mol/s)$	$J_B^c(mol/s)$	$J^e(mol/s)$	$\Delta^e$	$J(mol/s)$	$\Delta$
$C_A = 0.0$									
45908	15200	3.02	0.23	2.26e-11	2.24e-11	2.25e-11	-1.02	2.25e-11	-0.03
59198	15200	3.89	0.19	3.60e-11	3.47e-11	3.53e-11	-3.69	3.46e-11	-2.12
73582	15200	4.84	0.16	4.91e-11	4.88e-11	4.89e-11	-0.45	4.94e-11	0.86
89571	15200	5.89	0.13	7.18e-11	6.94e-11	7.06e-11	-3.45	6.79e-11	-3.94
104238	15200	6.86	0.12	8.95e-11	8.89e-11	8.92e-11	-0.62	8.69e-11	-2.65
$C_A \simeq 0.1$									
45809	15201	3.01	0.24	2.40e-11	2.34e-11	2.37e-11	-2.84	2.40e-11	1.31
59232	15200	3.90	0.20	3.71e-11	3.75e-11	3.73e-11	1.01	3.68e-11	-1.56
73603	15200	4.84	0.17	5.13e-11	5.12e-11	5.13e-11	-0.06	5.20e-11	1.47
89424	15199	5.88	0.14	7.26e-11	7.09e-11	7.17e-11	-2.52	7.08e-11	-1.26
104225	15202	6.86	0.12	9.33e-11	9.27e-11	9.30e-11	-0.67	9.04e-11	-2.82
$C_A \simeq 0.3$									
44327	15199	2.92	0.28	2.59e-11	2.54e-11	2.56e-11	-2.27	2.63e-11	2.62
59292	15200	3.90	0.23	4.36e-11	4.21e-11	4.28e-11	-3.43	4.19e-11	-2.27
74553	15200	4.90	0.19	6.19e-11	6.17e-11	6.18e-11	-0.28	5.95e-11	-3.88
89629	15200	5.90	0.16	8.17e-11	7.90e-11	8.03e-11	-3.43	7.87e-11	-2.12
104034	15200	6.84	0.14	9.84e-11	9.82e-11	9.83e-11	-0.22	9.88e-11	0.47
$C_A \simeq 0.5$									
45217	15200	2.97	0.33	3.13e-11	3.06e-11	3.09e-11	-2.51	3.22e-11	3.93
60197	15201	3.96	0.26	4.86e-11	4.78e-11	4.82e-11	-1.81	4.98e-11	3.23
74279	15201	4.89	0.22	6.59e-11	6.60e-11	6.60e-11	0.27	6.79e-11	2.90
89125	15200	5.86	0.19	9.00e-11	8.90e-11	8.95e-11	-1.13	8.86e-11	-1.09
104034	15200	6.84	0.16	1.13e-10	1.11e-10	1.12e-10	-1.26	1.11e-10	-0.80
$C_A \simeq 0.7$									
45823	15200	3.01	0.39	3.92e-11	3.79e-11	3.85e-11	-3.36	4.00e-11	3.72
59504	15200	3.91	0.32	5.82e-11	5.67e-11	5.74e-11	-2.61	5.89e-11	2.53
74071	15200	4.87	0.27	7.97e-11	7.80e-11	7.89e-11	-2.11	8.05e-11	1.99
89356	15200	5.88	0.23	1.02e-10	1.00e-10	1.01e-10	-1.63	1.05e-10	3.72
104103	15200	6.85	0.20	1.30e-10	1.27e-10	1.29e-10	-2.57	1.30e-10	1.05
$C_A \simeq 0.9$									
45671	15199	3.00	0.51	4.95e-11	4.77e-11	4.86e-11	-3.74	5.05e-11	3.80
59550	15200	3.92	0.42	7.22e-11	7.21e-11	7.22e-11	-0.18	7.47e-11	3.35
74267	15199	4.89	0.35	1.03e-10	1.00e-10	1.02e-10	-2.67	1.02e-10	0.20
90106	15200	5.93	0.29	1.37e-10	1.37e-10	1.37e-10	-0.52	1.33e-10	-3.27
104329	15201	6.86	0.26	1.65e-10	1.61e-10	1.63e-10	-2.63	1.62e-10	-0.19
$C_A = 1.0$									
45673	15200	3.00	0.64	5.68e-11	5.73e-11	5.71e-11	0.87	5.81e-11	1.79
59241	15200	3.90	0.52	8.89e-11	8.60e-11	8.75e-11	-3.35	8.58e-11	-1.99
74048	15200	4.87	0.43	1.20e-10	1.19e-10	1.20e-10	-1.29	1.18e-10	-1.67
89282	15200	5.87	0.37	1.60e-10	1.54e-10	1.57e-10	-3.67	1.52e-10	-3.07
103915	15200	6.84	0.33	1.96e-10	1.90e-10	1.93e-10	-2.91	1.88e-10	-2.86

Table 5.4: Flow rates for  $He/Kr$  at  $C_A = 0.5010$  as the function of the pressure ratio at  $P_B \simeq 15.2kPa$  through channels R2.

$P_A(kPa)$	$P_B(kPa)$	$P_A/P_B$	$Kn_0$	$J_A^e(mol/s)$	$J_B^e(mol/s)$	$J^e(mol/s)$	$\Delta^e$	$J(mol/s)$	$\Delta$
$C_A \simeq 0.5$									
45278	15199	2.98	0.26	2.60e-11	2.52e-11	2.56e-11	-3.08	2.64e-11	3.19
59797	15200	3.93	0.21	4.07e-11	4.05e-11	4.06e-11	-0.59	4.04e-11	-0.44
73618	15204	4.84	0.18	5.70e-11	5.51e-11	5.60e-11	-3.56	5.47e-11	-2.40
87696	15201	5.77	0.15	7.29e-11	7.07e-11	7.18e-11	-3.03	7.05e-11	-1.83
104033	15200	6.84	0.13	9.42e-11	9.11e-11	9.27e-11	-3.46	9.08e-11	-2.02

Tables 5.3, 5.4, 5.5, 5.6 and 5.7 present the experimental and numerical results and the flow parameters for the three outlet pressures. In the tables, the columns from the first one to the last one present the exact inlet and outlet pressures, the pressure ratio, the average Knudsen number, the  $J_A^e$  and  $J_B^e$  flow rates, the experimental flow rate, the deviation between  $J_A^e$  and  $J_B^e$  defined by  $\Delta_e = (1 - J_A^e/J_B^e)$ , the computational flow rate, and the discrepancy between the computational and experimental flow rates  $\Delta = 100(J - J^e)/J$ .

It can be seen in Tables 5.3, 5.4 and 5.5, 5.6 that the average Knudsen number is in the range of 0.12 – 0.64 and 0.22 – 0.98 for downstream pressures  $P_B \simeq 15.2kPa$  and  $P_B \simeq 8kPa$ , respectively. The leakage or outgassing flow rate is negligible; as a result, the experimental uncertainty is  $\pm 4\%$ . In all cases, the discrepancy between the upstream and downstream flow rates is within the range of the experimental error, which justifies the good performance of the experiment. The deviation between the numerical and experimental results is less than the experimental uncertainty for both outlet pressures. This can be considered as a very good agreement between the two approaches. The agreement is even better than in the case of the experiments for channels R1. The better agreement is caused by the subsequent improvement of the experimental facility, which consists of the replacement of the connecting facility of the microchannels. In previous experiments for channels R1, the microchannels were placed between two plastic plates, which

Table 5.5: Flow rates for  $He/Ar$  at different values of the concentration as the function of the pressure ratio at  $P_B \simeq 8kPa$  through channels R2.

$P_A(kPa)$	$P_B(kPa)$	$P_A/P_B$	$Kn_0$	$J_A^c(mol/s)$	$J_B^c(mol/s)$	$J^e(mol/s)$	$\Delta^e$	$J(mol/s)$	$\Delta$
$C_A = 0.0$									
31822	8000	3.98	0.35	1.57e-11	1.62e-11	1.60e-11	3.14	1.56e-11	2.23
40113	8000	5.01	0.29	2.26e-11	2.29e-11	2.27e-11	1.44	2.20e-11	-3.17
47964	8000	6.00	0.25	3.00e-11	2.95e-11	2.97e-11	-1.80	2.86e-11	-3.88
55969	8002	6.99	0.22	3.52e-11	3.39e-11	3.46e-11	-3.78	3.59e-11	3.55
$C_A \simeq 0.1$									
31989	8000	4.00	0.37	1.70e-11	1.65e-11	1.67e-11	-3.04	1.72e-11	2.85
40346	8000	5.04	0.31	2.46e-11	2.42e-11	2.44e-11	-1.76	2.41e-11	-1.55
47949	8000	5.99	0.27	3.10e-11	3.06e-11	3.08e-11	-1.48	3.07e-11	-0.20
56125	8000	7.02	0.23	3.91e-11	3.84e-11	3.87e-11	-1.86	3.84e-11	-0.85
$C_A \simeq 0.3$									
31977	8000	4.00	0.42	2.05e-11	2.00e-11	2.02e-11	-2.76	2.07e-11	2.10
40290	8000	5.04	0.35	2.79e-11	2.82e-11	2.81e-11	1.26	2.83e-11	1.00
47968	8000	6.00	0.30	3.52e-11	3.40e-11	3.46e-11	-3.28	3.58e-11	3.23
56000	8000	7.00	0.26	4.50e-11	4.35e-11	4.38e-11	-3.34	4.39e-11	0.41
$C_A \simeq 0.5$									
31781	7997	3.97	0.49	2.53e-11	2.46e-11	2.49e-11	-3.11	2.49e-11	-0.18
40109	8000	5.01	0.41	3.30e-11	3.19e-11	3.25e-11	-3.52	3.38e-11	3.85
47854	8000	5.98	0.35	4.10e-11	4.06e-11	4.08e-11	-1.04	4.24e-11	3.70
55934	8000	6.99	0.31	5.04e-11	4.97e-11	5.01e-11	-1.32	5.16e-11	2.84
$C_A \simeq 0.7$									
31909	8000	3.99	0.60	3.07e-11	3.00e-11	3.02e-11	-2.58	3.11e-11	2.70
40266	8001	5.03	0.49	4.08e-11	3.93e-11	4.01e-11	-3.97	4.17e-11	3.95
48003	8000	6.00	0.42	5.10e-11	4.98e-11	5.04e-11	-2.38	5.20e-11	2.96
55984	8000	7.00	0.37	6.22e-11	6.02e-11	6.12e-11	-3.21	6.28e-11	2.64
$C_A \simeq 0.9$									
31947	8000	3.99	0.78	3.92e-11	3.80e-11	3.86e-11	-3.18	3.95e-11	2.22
40176	8000	5.02	0.64	5.35e-11	5.19e-11	5.27e-11	-3.15	5.39e-11	2.29
47888	8000	5.99	0.56	6.62e-11	6.54e-11	6.58e-11	-1.25	6.59e-11	0.17
55820	8000	6.98	0.49	7.71e-11	7.81e-11	7.76e-11	1.17	7.96e-11	2.55
$C_A = 1.0$									
31691	8000	3.96	0.98	4.47e-11	4.37e-11	4.42e-11	-2.19	4.46e-11	0.86
40047	8000	5.01	0.81	6.32e-11	6.24e-11	6.28e-11	-1.36	6.07e-11	-3.50
47739	8000	5.97	0.70	7.64e-11	7.68e-11	7.66e-11	0.50	7.59e-11	-0.91
55917	8000	6.99	0.61	9.36e-11	9.69e-11	9.53e-11	3.43	9.25e-11	-3.00

have been replaced by metal plates. In addition, the previous plastic connecting pipes have also been replaced by metal pipes. The new connection is made by Swagelok Ultra-Torr components. By using the improved connection facility, a better insulation has been reached. On the basis of the experiments for channels R2, it can be concluded that the flow rate is larger

Table 5.6: Flow rates for  $He/Kr$  at  $C_A = 0.5010$  as the function of the pressure ratio at  $P_B \simeq 8kPa$  through channels R2.

$P_A(kPa)$	$P_B(kPa)$	$P_A/P_B$	$Kn_0$	$J_A^e(mol/s)$	$J_B^e(mol/s)$	$J^e(mol/s)$	$\Delta^e$	$J(mol/s)$	$\Delta$
$C_A \simeq 0.5$									
31914	8000	3.99	0.40	2.06e-11	2.11e-11	2.08e-11	2.40	2.07e-11	-0.54
40232	8000	5.03	0.33	2.74e-11	2.64e-11	2.69e-11	-3.67	2.78e-11	3.27
48055	8000	6.01	0.28	3.43e-11	3.32e-11	3.37e-11	-3.40	3.48e-11	3.02
55928	8000	6.99	0.25	4.27e-11	4.30e-11	4.28e-11	0.67	4.20e-11	-2.03

Table 5.7: Flow rates of  $He$  and  $Ar$  gases as the function of the pressure ratio at  $P_B \simeq 4.1kPa$  through rectangular channels R2.

$P_A(kPa)$	$P_B(kPa)$	$P_A/P_B$	$Kn_0$	$J_A^e(mol/s)$	$J_B^e(mol/s)$	$J^e(mol/s)$	$\Delta^e$	$J(mol/s)$	$\Delta$
<i>He</i>									
16572	4100	4.04	1.88	2.39e-11	2.37e-11	2.38e-11	-1.16	2.40e-11	0.99
20431	4100	4.98	1.58	3.05e-11	3.03e-11	3.04e-11	-0.71	3.12e-11	2.48
24281	4100	5.92	1.37	3.77e-11	3.62e-11	3.70e-11	-3.96	3.84e-11	3.73
28400	4100	6.93	1.19	4.59e-11	4.44e-11	4.52e-11	-3.23	4.62e-11	2.17
<i>Ar</i>									
16738	4100	4.08	0.67	7.29e-12	7.49e-12	7.39e-12	2.56	7.61e-12	2.88
20691	4100	5.05	0.57	1.03e-11	1.05e-11	1.04e-11	2.68	1.01e-11	-2.45
24527	4100	5.98	0.49	1.27e-11	1.31e-11	1.29e-11	2.90	1.27e-11	-1.30
28910	4100	7.05	0.43	1.61e-11	1.61e-11	1.61e-11	0.11	1.58e-11	-2.30

at larger pressure drops and increases with increasing  $He$  concentration. It can also be seen that the  $He/Kr$  mixture has smaller flow rate at the same concentration  $C_A = 0.501$  than that of the  $He/Ar$  mixture. This feature is explained by the larger average mass of the  $He/Kr$  mixture.

Table 5.7 shows the results for single gases  $He$  and  $Ar$  for  $P_B \simeq 4.1kPa$ . The average Knudsen number is in the range of 0.43 – 1.88. Again, it can be seen that the difference between the inlet and outlet flow rates is less than the experimental uncertainty  $\pm 4\%$ . This justifies that possible outgassing or leakage flow rates are taken into account well. The deviation between the experimental and kinetic flow rates is smaller than the experimental uncertainty. Hence, a very good agreement between the experimental and numerical results is obtained.

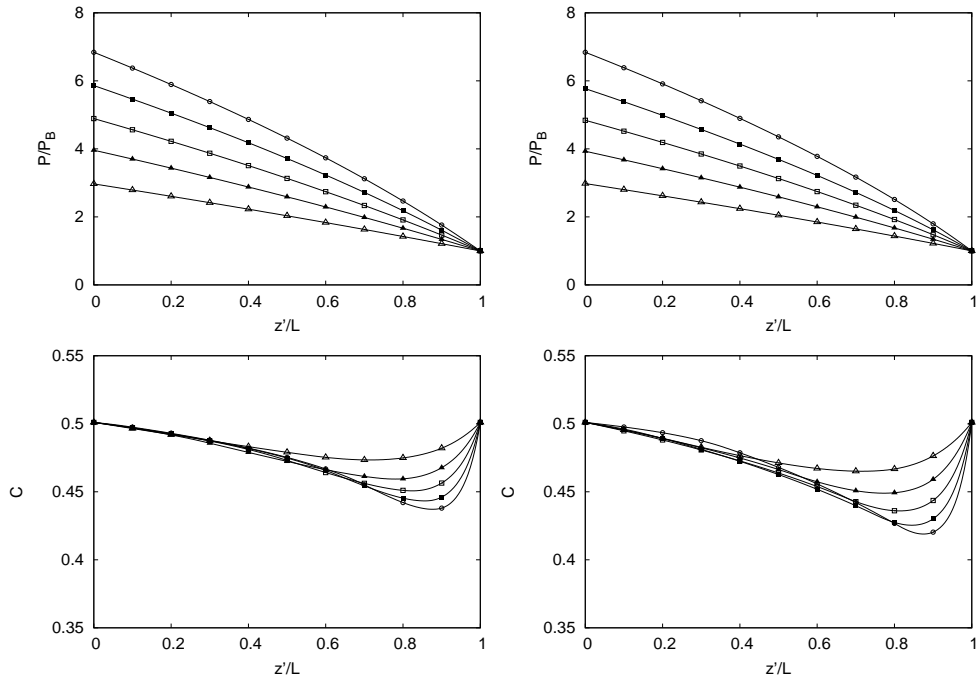


Figure 5.3: Distributions of the pressure (up) and the concentration (down) for  $He/Ar$  (left) and  $He/Kr$  (right) mixtures with  $C_A = 0.5010$  along the axis of the channel at  $P_B \simeq 15.2kPa$  for channels R2. The symbols  $\Delta, \blacktriangle, \square, \blacksquare, \circ$  represent the results for  $P_A/P_B = [2.97, 3.96, 4.89, 5.86, 6.84]$  and  $[2.98, 3.93, 4.84, 5.77, 6.84]$  for the  $He/Ar$  and  $He/Kr$  mixtures, respectively.

#### 5.5.4 Distribution of macroscopic quantities for R2

Figures 5.3 and 5.4 show the typical profiles of the pressure and the concentration along the axis of the channel for  $He/Ar$  and  $He/Kr$  mixtures, respectively, at  $C_A = 0.501$ . It is concluded that at higher outlet pressure the pressure profiles have non-linear character, while at smaller outlet pressure, they are nearly linear functions of the axial coordinate. This is again explained by the different effects of the compressibility and the rarefaction

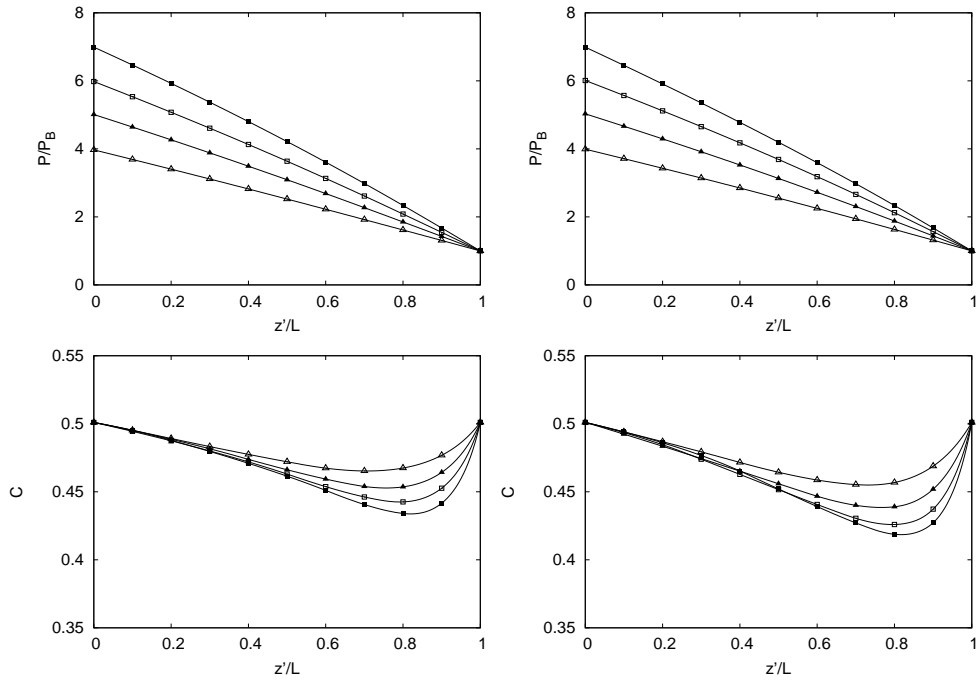


Figure 5.4: Distributions of the pressure (up) and the concentration (down) for  $He/Ar$  (left) and  $He/Kr$  (right) mixtures with  $C_A = 0.5010$  along the axis of the channel at  $P_B \simeq 8kPa$  for channels R2. The symbols  $\Delta, \blacktriangle, \square, \blacksquare$  represent the results for  $P_A/P_B = [3.97, 5.01, 5.98, 6.99]$  and  $[3.99, 5.03, 6.01, 6.99]$  for the  $He/Ar$  and  $He/Kr$  mixtures, respectively.

on the flow rate. The concentration profiles are non-uniform and exhibit a drop of the concentration in the second half of the channel. This is the direct evidence of the gas separation in the microchannel. The non-uniformity of the concentration increases with increasing pressure drop. In addition, it can be concluded that the concentration drop is larger for smaller outlet pressure and for the  $He/Kr$  mixture, which has larger molecular mass ratio. The separation is stronger in a gas mixture, which has gas components with larger mass ratio.

### 5.5.5 Flow rates for channel T1

Experiments have been carried out in order to measure the flow rate through the T1 trapezoidal channels as well. The experiment is performed in the same scenario as in the case of channels R2. The measurement refers to  $He/Ar$  and  $He/Kr$  mixtures with the same concentrations as for channels R2. The temperature is fixed at  $T = 299.5K$ . Two values of the downstream pressure  $P_B \simeq 15.1kPa$  and  $P_B \simeq 8.05kPa$  are investigated. The pressure ratios are in the range of 3 – 7 and 4 – 7 for the larger and smaller outlet pressures.

In Tables 5.8, 5.9 and 5.10, 5.11, the measured and computed flow rates together with the relevant flow parameters are tabulated for the larger and smaller downstream pressures, respectively. The columns from the first to the last one present the exact upstream and downstream pressures, the pressure ratio, the average Knudsen number, the  $J_A^e$  and  $J_B^e$  experimental flow rates, the final experimental flow rate, the deviation between  $J_A^e$  and  $J_B^e$  defined by  $\Delta_e = (1 - J_A^e/J_B^e)$ , the computed flow rate, and the deviation between the computational and experimental flow rates  $\Delta = 100(J - J^e)/J$ .

The average Knudsen numbers are in the range of 0.05 – 0.30 and 0.11 – 0.36 for the larger and smaller outlet pressures. The Knudsen number is a bit smaller than in the case of channels R2. However, in the present situation, the definition of the rarefaction parameter and Knudsen number is based on the hydrodynamic diameter of the trapezoidal channel, while, in the case of the rectangular duct, they are based on the height of the channel. The experimental uncertainty is in the range of  $\pm 4\%$  for all cases. The difference between  $J_A^e$  and  $J_B^e$  is less than the experimental uncertainty; hence, the possible leakage or outgassing effects are taken into account well. The difference between the experimental and numerical results are also less than the experimental uncertainty, which indicates a very good agreement between the two approaches. It can be seen that the flow rates increase with increasing concentration, which is caused by the larger molecular velocity of the lighter

Table 5.8: Flow rates for  $He/Ar$  at different values of the concentration as the function of the pressure ratio at  $P_B \simeq 15.1kPa$  through channels T1.

$P_A(kPa)$	$P_B(kPa)$	$P_A/P_B$	$Kn_0$	$J_A^c(mol/s)$	$J_B^c(mol/s)$	$J^e(mol/s)$	$\Delta^e$	$J(mol/s)$	$\Delta$
$C_A = 0.0$									
45355	15100	3.00	0.11	1.01e-11	1.02e-11	1.02e-11	1.22	1.01e-11	-0.35
59422	15100	3.94	0.09	1.67e-11	1.65e-11	1.66e-11	-1.41	1.64e-11	-1.35
74977	15100	4.97	0.07	2.52e-11	2.46e-11	2.49e-11	-2.45	2.45e-11	-1.75
90110	15100	5.97	0.06	3.44e-11	3.35e-11	3.39e-11	-2.63	3.36e-11	-0.90
105010	15100	6.95	0.05	4.37e-11	4.44e-11	4.41e-11	1.66	4.38e-11	-0.67
$C_A \simeq 0.1$									
45328	15100	3.00	0.12	1.05e-11	1.03e-11	1.04e-11	-2.16	1.06e-11	2.37
59944	15100	3.97	0.09	1.75e-11	1.78e-11	1.76e-11	1.64	1.74e-11	-1.58
74994	15100	4.97	0.08	2.52e-11	2.59e-11	2.56e-11	2.59	2.54e-11	-0.73
90439	15100	5.99	0.07	3.49e-11	3.54e-11	3.51e-11	1.61	3.48e-11	-0.93
105938	15100	7.02	0.06	4.72e-11	4.65e-11	4.69e-11	-1.50	4.53e-11	-3.47
$C_A \simeq 0.3$									
45340	15100	3.00	0.13	1.15e-11	1.16e-11	1.15e-11	0.76	1.19e-11	2.88
59885	15100	3.97	0.11	1.86e-11	1.87e-11	1.86e-11	0.52	1.90e-11	2.05
74925	15100	4.96	0.09	2.83e-11	2.79e-11	2.81e-11	-1.38	2.75e-11	-2.41
90251	15100	5.98	0.08	3.84e-11	3.73e-11	3.79e-11	-2.96	3.73e-11	-1.64
105761	15100	7.00	0.07	4.94e-11	4.89e-11	4.91e-11	-1.07	4.85e-11	-1.27
$C_A \simeq 0.5$									
45200	15100	2.99	0.15	1.41e-11	1.38e-11	1.40e-11	-2.52	1.36e-11	-2.49
59840	15100	3.96	0.12	2.15e-11	2.07e-11	2.11e-11	-3.79	2.15e-11	1.89
74731	15100	4.95	0.10	3.15e-11	3.05e-11	3.10e-11	-3.23	3.06e-11	-1.12
90368	15100	5.98	0.09	4.10e-11	4.08e-11	4.09e-11	-0.39	4.13e-11	1.06
105126	15100	6.96	0.08	5.24e-11	5.19e-11	5.21e-11	-0.89	5.26e-11	0.78
$C_A \simeq 0.7$									
45082	15100	2.99	0.19	1.55e-11	1.56e-11	1.55e-11	0.37	1.61e-11	3.35
60203	15100	3.99	0.15	2.49e-11	2.53e-11	2.51e-11	1.41	2.54e-11	1.24
75204	15100	4.98	0.12	3.59e-11	3.46e-11	3.52e-11	-3.85	3.57e-11	1.41
90316	15101	5.98	0.11	4.78e-11	4.60e-11	4.69e-11	-3.84	4.72e-11	0.72
105449	15100	6.98	0.09	6.09e-11	5.88e-11	5.99e-11	-3.49	5.99e-11	-0.02
$C_A \simeq 0.9$									
45255	15100	3.00	0.24	1.94e-11	1.97e-11	1.95e-11	1.82	2.01e-11	2.57
59883	15100	3.97	0.19	3.06e-11	2.98e-11	3.02e-11	-2.80	3.12e-11	3.08
74922	15100	4.96	0.16	4.32e-11	4.29e-11	4.30e-11	-0.59	4.36e-11	1.37
90239	15100	5.98	0.14	5.74e-11	5.54e-11	5.64e-11	-3.63	5.75e-11	1.95
105660	15100	7.00	0.12	7.24e-11	7.10e-11	7.17e-11	-1.96	7.28e-11	1.50
$C_A = 1.0$									
45482	15101	3.01	0.30	2.32e-11	2.25e-11	2.29e-11	-3.07	2.32e-11	1.35
60343	15101	4.00	0.24	3.50e-11	3.63e-11	3.57e-11	3.70	3.63e-11	1.70
75293	15100	4.99	0.20	4.96e-11	4.91e-11	4.94e-11	-0.90	5.07e-11	2.66
89976	15100	5.96	0.17	6.47e-11	6.61e-11	6.54e-11	2.01	6.61e-11	1.05
105450	15100	6.98	0.15	8.30e-11	8.15e-11	8.23e-11	-1.93	8.37e-11	1.77

Table 5.9: Flow rates for  $He/Kr$  at  $C_A = 0.5010$  as the function of the pressure ratio at  $P_B \simeq 15.1kPa$  through channels T1.

$P_A(kPa)$	$P_B(kPa)$	$P_A/P_B$	$Kn_0$	$J_A^e(mol/s)$	$J_B^e(mol/s)$	$J^e(mol/s)$	$\Delta^e$	$J(mol/s)$	$\Delta$
$C_A \simeq 0.5$									
45275	15100	3.00	0.12	1.12e-11	1.09e-11	1.11e-11	-3.32	1.13e-11	1.87
59875	15100	3.97	0.10	1.81e-11	1.79e-11	1.80e-11	-0.89	1.78e-11	-1.24
74947	15100	4.96	0.08	2.57e-11	2.50e-11	2.53e-11	-2.84	2.54e-11	0.18
90320	15100	5.98	0.07	3.56e-11	3.45e-11	3.50e-11	-3.29	3.41e-11	-2.62
105832	15100	7.01	0.06	4.46e-11	4.40e-11	4.43e-11	-1.50	4.40e-11	-0.56

Table 5.10: Flow rates for  $He/Ar$  at different values of the concentration as the function of the pressure ratio at  $P_B \simeq 8.05kPa$  through channels T1.

$P_A(kPa)$	$P_B(kPa)$	$P_A/P_B$	$Kn_0$	$J_A^e(mol/s)$	$J_B^e(mol/s)$	$J^e(mol/s)$	$\Delta^e$	$J(mol/s)$	$\Delta$
$C_A \simeq 0.1$									
31974	8050	3.97	0.17	7.63e-12	7.38e-12	7.50e-12	-3.50	7.29e-12	-2.88
40237	8050	5.00	0.14	1.04e-11	1.02e-11	1.03e-11	-1.97	1.04e-11	1.32
47965	8050	5.96	0.12	1.34e-11	1.33e-11	1.33e-11	-0.77	1.34e-11	0.74
56065	8050	6.96	0.11	1.68e-11	1.69e-11	1.68e-11	0.46	1.70e-11	1.03
$C_A \simeq 0.3$									
32038	8050	3.98	0.20	8.52e-12	8.64e-12	8.58e-12	1.48	8.43e-12	-1.82
40155	8050	4.99	0.16	1.16e-11	1.16e-11	1.16e-11	-0.11	1.18e-11	1.14
47940	8050	5.96	0.14	1.47e-11	1.49e-11	1.48e-11	1.22	1.52e-11	2.80
56086	8050	6.97	0.12	1.93e-11	1.92e-11	1.92e-11	-0.66	1.91e-11	-0.56
$C_A \simeq 0.5$									
32063	8050	3.98	0.23	9.82e-12	9.72e-12	9.77e-12	-1.02	1.00e-11	2.50
40143	8050	4.99	0.19	1.33e-11	1.37e-11	1.35e-11	2.62	1.38e-11	2.14
47955	8050	5.96	0.16	1.72e-11	1.72e-11	1.72e-11	-0.07	1.77e-11	2.53
55789	8050	6.93	0.14	2.24e-11	2.21e-11	2.23e-11	-1.54	2.18e-11	-1.96
$C_A \simeq 0.7$									
31879	8050	3.96	0.28	1.20e-11	1.17e-11	1.18e-11	-2.76	1.20e-11	1.24
40248	8050	5.00	0.23	1.62e-11	1.61e-11	1.61e-11	-0.54	1.66e-11	2.57
47842	8050	5.94	0.20	2.07e-11	2.03e-11	2.05e-11	-2.04	2.10e-11	2.03
55793	8050	6.93	0.17	2.59e-11	2.51e-11	2.55e-11	-3.54	2.58e-11	1.10
$C_A \simeq 0.9$									
31945	8050	3.97	0.36	1.48e-11	1.49e-11	1.48e-11	0.26	1.50e-11	1.26
40188	8050	4.99	0.30	2.02e-11	1.97e-11	1.99e-11	-2.62	2.06e-11	3.35
47947	8050	5.96	0.26	2.61e-11	2.60e-11	2.60e-11	-0.29	2.62e-11	0.62
55821	8050	6.93	0.23	3.17e-11	3.20e-11	3.18e-11	0.91	3.21e-11	0.85

species. The flow rates increase with increasing pressure drop. By comparing the results of the two mixtures at the same concentration  $C_A = 0.5$ , it is concluded that the flow rates of  $He/Kr$  are smaller than the corresponding values of  $He/Ar$  due to the larger mass of  $Kr$  compared to  $Ar$ .

Table 5.11: Flow rates for  $He/Kr$  at  $C_A = 0.5010$  as the function of the pressure ratio at  $P_B \simeq 8.05kPa$  through channels T1.

$P_A(kPa)$	$P_B(kPa)$	$P_A/P_B$	$Kn_0$	$J_A^e(mol/s)$	$J_B^e(mol/s)$	$J^e(mol/s)$	$\Delta^e$	$J(mol/s)$	$\Delta$
$C_A \simeq 0.5$									
31971	8050	3.97	0.19	7.97e-12	8.02e-12	7.99e-12	0.64	8.30e-12	3.70
40264	8050	5.00	0.15	1.13e-11	1.10e-11	1.11e-11	-2.13	1.14e-11	2.34
47974	8050	5.96	0.13	1.45e-11	1.40e-11	1.43e-11	-3.37	1.46e-11	2.03
55979	8050	6.95	0.12	1.77e-11	1.74e-11	1.76e-11	-2.14	1.75e-11	-0.21

### 5.5.6 Distribution of macroscopic quantities for T1

Figures 5.5 and 5.6 show the axial distributions of the pressures and the concentrations for  $He/Ar$  and  $He/Kr$  mixtures with  $C_A = 0.5010$  at downstream pressures  $P_B \simeq 15.1kPa$  and  $P_B \simeq 8.05kPa$ , respectively. The pressure profiles exhibit a nearly non-linear character at  $P_B \simeq 15.1kPa$ , which is caused by the compressibility effects, i.e. the dependence of the dimensionless flow rate on the rarefaction parameter. The concentration profiles exhibit a concentration drop near the end of the channel in a similar manner as for the rectangular ducts. Hence, the gaseous separation is also present in this case. In the case of the smaller outlet pressure, Figure 5.6, the pressure profiles are more linear compared to Figure 5.5, but they are not as linear as in the case of channels R2. The reason of this difference is the different range of the Knudsen number. The mixture exhibits the concentration drop also at the smaller outlet pressure. Generally, the concentration drop is stronger at larger pressure drops due to the larger driving force, which accelerates the flow. The drop is also larger for  $He/Kr$  than  $He/Ar$ , as it is observed in the case of channels R2. This feature is caused by the larger mass ratio of the  $He/Kr$  mixture. In this case, the gaseous separation is expected to be stronger.

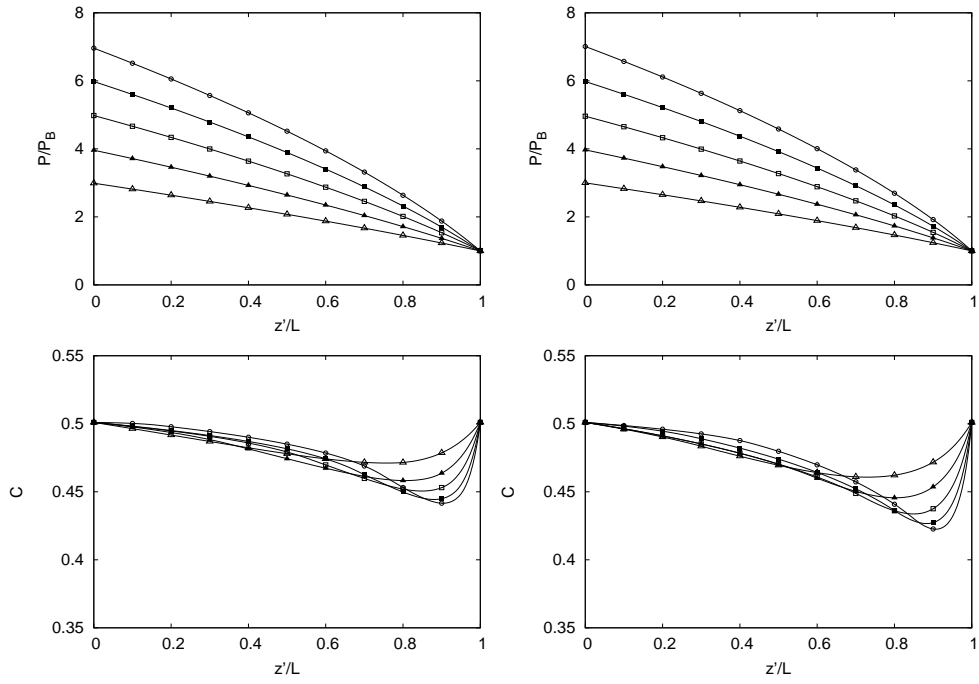


Figure 5.5: Distributions of the pressure (up) and the concentration (down) for  $He/Ar$  (left) and  $He/Kr$  (right) mixtures with  $C_A = 0.5010$  along the axis of the channel for  $P_B \simeq 15.1kPa$  for channels T1. The symbols  $\Delta, \blacktriangle, \square, \blacksquare, \circ$  represent the results at  $P_A/P_B = [2.99, 3.96, 4.95, 5.98, 6.69]$  and  $[3.00, 3.97, 4.96, 5.98, 7.01]$  for  $He/Ar$  and  $He/Kr$  mixtures, respectively.

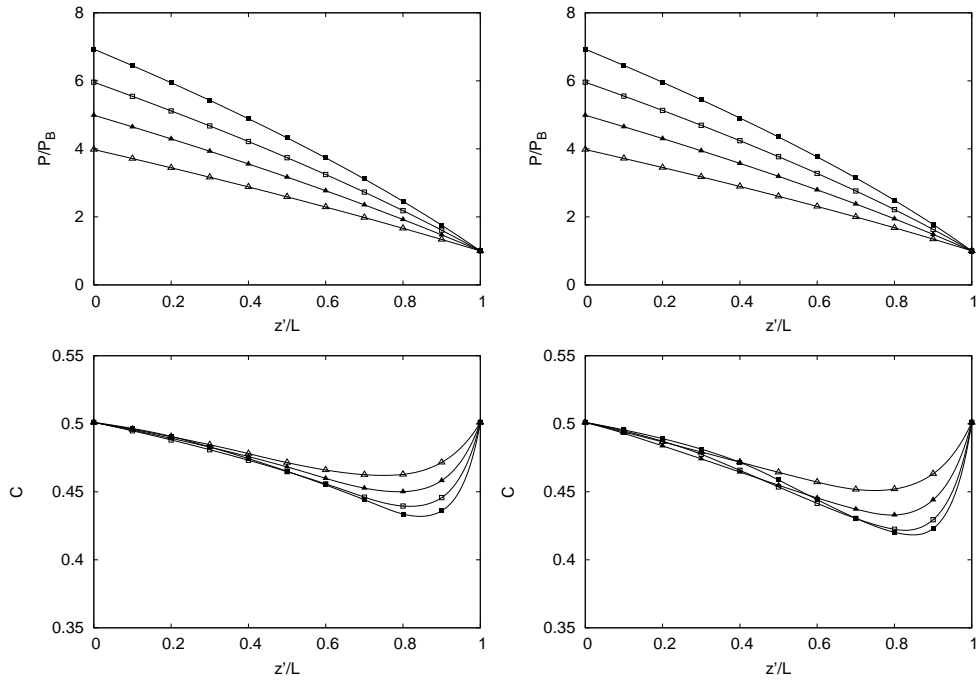


Figure 5.6: Distributions of the pressure (up) and the concentration (down) for *He/Ar* (left) and *He/Kr* (right) mixtures with  $C_A = 0.5010$  along the axis of the channel for  $P_B \simeq 8.05kPa$  for channels T1. The symbols  $\triangle, \blacktriangle, \square, \blacksquare$  represent the results at  $P_A/P_B = [3.98, 4.99, 5.96, 6.93]$  and  $[3.97, 5.00, 5.96, 6.95]$  for *He/Ar* and *He/Kr* mixtures, respectively.

# Chapter 6

## Conclusions

The scope of the thesis is the computational and experimental study of flows of gas mixtures in microchannels. In the computational part, the flows through long and short channels are considered in the whole range of the gas rarefaction. The experimental part focuses on the flow rate measurement of gas mixtures in various long microchannels in the transition and early transition regions. The results are compared to the kinetic solution of the flow problems.

The flows through long channels are described by the McCormack linearized kinetic model. An accelerated discrete velocity method has been developed in order to solve the kinetic equations on triangular grids, which is used for the description of flows in triangular and trapezoidal channels. First, the prototype of the model has been developed for single gases described by the linearized BGK operator. A stability analysis has been established for the discrete equations in the accelerated discrete velocity method in order to study the computational performance of the scheme. The stability analysis and computer simulations have revealed that the accelerated method has better computational performance near the hydrodynamic and in a significant part of the transition regions than the standard one. By using the

method, significant improvement is reached in terms of computational time in the simulations. The accelerated method has been adopted for the simulation of flows of gas mixtures defined by the McCormack model through triangular and trapezoidal channels. The McCormack model provides the local information on the flow at a given cross section of the channel. To deduce the global flow behaviours of gas mixtures, approximating and exact flow rate calculators have been developed. These calculators use the kinetic coefficients obtained from the local solution of the McCormack model. Typical flows of  $Ne/Ar$  and  $He/Xe$  have been simulated. The flow rates and the axial distributions of the pressure and the concentration have been deduced. It is shown that the flow exhibits the gaseous separation.

Flows through short channels are described by the non-linear Boltzmann equation, which has been solved by the Direct Simulation Monte Carlo method. Upgraded codes have been developed for the simulation of the flows of gas mixtures through orifices, short tubes and slits. The codes use three-level grids near the short channels and weighting zones for obtaining better resolution and more uniform model particle density, respectively. By using the codes, simulations have been executed for flows of  $Ne/Ar$  and  $He/Xe$  mixtures at a wide range of flow parameters. The results are obtained for the hard-sphere molecular model. The component and total flow rates have been deduced in the simulations. It is shown that the gas separation has a significant impact on the flow. As the rarefaction increases, the lighter species acquires larger speed than that of the heavier one. There are different dependencies of the flow rates on the rarefaction for mixtures with smaller and larger mass ratios. In the study, the axial distributions of the densities and the velocities of the species together with the temperature, the rarefaction parameter and the Mach number have also been deduced. Generally, these quantities exhibit rapid changes near the short channel. The flow can be high-speed at large values of the pressure drop.

In the experimental part of the thesis, the flow rates of  $He/Ar$  and  $He/Kr$  gaseous mixtures have been measured through long microchannels with rectangular and trapezoidal cross sections. The flow rate measurement is based on the constant volume method. The microchannels are placed between upstream and downstream reservoirs having different pressures. The flow rate is determined from the pressure variations in the reservoirs. Measurements have been carried out for a wide range of the concentration for  $He/Ar$  and for a fixed concentration value for  $He/Kr$  mixtures. The pressure ratio is in the range of 3 – 7. The total flow rates have been compared to the solution of the McCormack model on the basis of the methodology developed in the computational part of the thesis. A very good agreement has been reached between the experimental and numerical flow rates, which justifies that the McCormack kinetic model can be considered as a reliable approach for the description of isothermal flows of gas mixtures in the considered parameter range. The typical axial distributions of the pressure and the concentration of the mixtures have also been deduced. The pressure profiles are nearly non-linear, while the concentration distributions are non-uniform. This latter behavior is the clear manifestation of the non-negligible gaseous separation in the microchannels.

# Appendix A

## Collision integrals and viscosity function

In the thesis, the realistic potential is used to define the transport properties of gaseous mixtures [35]. Here, the procedure of deducing the collision integrals and the viscosity is presented.

### A.1 Collision integrals

The improved principle of corresponding states [35] postulates that the interaction potential between molecules of species  $\alpha$  and  $\beta$  may be written as

$$V_{\alpha\beta}(r) = \epsilon_{\alpha\beta} f \left( \frac{r}{\sigma_{\alpha\beta}}, C_{6,\alpha\beta}^*, \rho_{\alpha\beta}^*, V_{0,\alpha\beta}^* \right), \quad (\text{A.1})$$

where  $f(\cdot)$  is an universal function,  $\epsilon_{\alpha\beta}$  and  $\sigma_{\alpha\beta}$  are the characteristic energy minimum of the potential and the associated distance. The remaining quantities  $C_{6,\alpha\beta}^*, \rho_{\alpha\beta}^*, V_{0,\alpha\beta}^*$  are dimensionless material parameters. The intermolecular potential together with the density, the concentration and the temperature of the mixture defines the collision integrals  $\Omega_{\alpha\beta}^{ij}$ . The parameters and the defining expressions in Ref. [35] are used to calculate the scaled

collision integrals  $\Omega_{\alpha\beta}^{ij*}$ , which are converted to the dimensionless forms of  $\Omega_{\alpha\beta}^{ij}$ . These latter quantities are applied to deduce the collision frequencies in the McCormack model. In all cases, the solution of the McCormack model is carried out at temperature  $T = 300K$ .

## A.2 Viscosity function

The viscosity for the mixtures  $He/Ar$  and  $He/Kr$  is also deduced from the aforementioned ansatz. The values of the viscosity are used in the experimental part of the thesis. The viscosity of a given mixture can be obtained in accordance with Ref. [53] such that

$$\mu(C) = nkT \left( \frac{C}{\gamma_1} + \frac{1-C}{\gamma_2} \right). \quad (\text{A.2})$$

By using this expression and the dimensionless collision integrals  $\Omega_{\alpha\beta}^{ij}$ , the ratio of the mixture viscosity  $\mu(C)$  and the reference viscosity of helium  $\mu_{He}$ , ( $C = 1$ ), is calculated for a particular mixture. The dimensional viscosity is deduced by  $\mu'(C) = [\mu(C)/\mu_{He}] \mu_{He}^{Exp}$ , where  $\mu_{He}^{Exp}$  is the experimental viscosity of helium on the basis of Ref. [35]. The interpolated value of  $\mu_{He}^{Exp}$  is used at the valid temperature in the flow rate measurements. This treatment is used for obtaining the viscosity for gas mixtures. For demonstrative purposes, the viscosity function for  $He/Ar$  and  $He/Kr$  mixtures at various concentrations and  $T = 299.2K$  is presented in Table A.1.

Table A.1: Viscosity of *He/Ar* and *He/Kr* mixtures at different helium concentrations  $C$ .

$C$	$\mu'(C) \times 10^6 \text{ Pa s}$	
	<i>He/Ar</i>	<i>He/Kr</i>
0.0	22.78	25.55
0.1	23.09	25.96
0.2	23.30	26.24
0.3	23.48	26.52
0.4	23.64	26.78
0.5	23.73	26.99
0.6	23.72	27.08
0.7	23.54	26.94
0.8	23.06	26.28
0.9	22.03	24.51
1.0	20.00	20.00

# Bibliography

- [1] P. Andries, K. Aoki, B. Perthame, A consistent BGK-type model for gas mixtures, *J. Stat. Phys.*, 106, 993-1018, 2002.
- [2] V.V. Aristov, *Direct Methods for Solving the Boltzmann Equation and Study of Nonequilibrium Flows*, Kluwer Academic Publishers, Dordrecht, The Netherlands, 2001.
- [3] E.B. Arkilic, K.S. Breuer, M.A. Schmidt, Mass flow and tangential momentum accommodation in silicon micromachined channels, *J. Fluid. Mech.*, 437, 29-43, 2001.
- [4] C. Aubert, S. Colin, High-order boundary conditions for gaseous flows in rectangular microchannels, *Microscale Therm. Eng.*, 5, 41-54, 2001.
- [5] J.A. Bentz, R.V. Tompson, S.K. Loyalka, Measurement of viscosity, velocity slip coefficients, and tangential momentum accommodation coefficients using a modified spinning rotor gauge, *J. Vac. Sci. Technol. A*, 19, 317-324, 2001.
- [6] M. Bergoglio, A. Calcatelli, G. Rumiano, Gas flow rate measurement for leak calibration, *Vacuum*, 46, 763-765, 1995.
- [7] P.L. Bhatnagar, E.P. Gross, M. Krook, A model for collision processes in gases. I. Small amplitude processes in charged and neutral one-component systems, *Phys. Rev.*, 94, 511-525, 1954.

- [8] G.A. Bird, *Molecular Gas Dynamics and the Direct Simulation of Gas Flows*, Oxford University Press, 1994.
- [9] G.A. Bird, *The DS2V/3V Program Suite for DSMC Calculations*, RGD24, AIP Conf. Proc., 762, 541-546, 2005.
- [10] G. Breyiannis, S. Varoutis, D. Valougeorgis, *Rarefied gas flow in concentric annular tube: Estimation of the Poiseuille number and the exact hydraulic diameter*, Eur. J. Mech, B/Fluids, 27, 609-622, 2008.
- [11] S.F. Borisov, I.G. Neudachin, B.T. Porodnov, P.E. Suetin, *Flow of rarefied gases through an orifice for small pressure drop*, Zh. Tekh. Fiz., 43, 1735-1739, 1973.
- [12] L. Carlomusto, L.M. Socio, *Poiseuille flow of a rarefied gas mixture*, J. Appl. Math. Phys., 29, 206-216, 1978.
- [13] C. Cercignani, *Theory and application of the Boltzmann equation*, Scottish Academic Press, 1975.
- [14] C. Cercignani, *Slow Rarefied flows: Theory and Applications to Micro-electro-mechanical systems*, Birkhauser Verlag, 2006.
- [15] S. Chapman, T.G. Cowling, *The mathematical theory of non-uniform gases*, Cambridge University Press, 1970.
- [16] S. Colin, P. Lalonde, R. Caen, *Validation of a second-order slip flow model in rectangular microchannels*, Heat Transfer Eng., 25, 23-30, 2004.
- [17] S. Dietrich, I.D. Boyd, *Scalar and parallel optimized implementation of the direct simulation Monte Carlo method*, J. Comp. Phys., 126, 328-342, 1996.

- [18] T. Ewart, P. Perrier, I. Graur, J.G. Meolans, Mass flow rate measurement in gas micro flows, *Exp. Fluids*, 41, 487-498, 2006.
- [19] T. Ewart, P. Perrier, I.A. Graur, J.G. Meolans, Mass flow rate measurements in a microchannel from hydrodynamic to near free molecular regimes, *J. Fluid Mech.*, 584, 337-356, 2007.
- [20] T. Fujimoto, M. Usami, Rarefied gas flow through a circular orifice and short tubes, *Trans. ASME: J. Fluids Eng.*, 106, 367-373, 1984.
- [21] R.D.M. Garcia, C.E. Siewert, Channel flow of a binary mixture of rigid spheres described by the linearized Boltzmann equation and driven by temperature, pressure, and density gradients, *SIAM J. Appl. Math.*, 67, 1041-1063, 2007.
- [22] R.D.M. Garcia, C.E. Siewert, Couette flow of a binary mixture of rigid-sphere gases described by the linearized Boltzmann equation, *Eur. J. Mech. B/Fluids*, 27, 823-836, 2008.
- [23] V. Garzó, A. Santos, J.J. Brey, A kinetic model for a multicomponent gas, *Phys. Fluids*, 1, 380-383, 1989.
- [24] H. Grad, On the kinetic theory of rarefied gases, *Commun. Pur. Appl. Math.*, 2, 331-407, 1949.
- [25] I. Graur, F. Sharipov, Gas flow through an elliptical tube over the whole range of the gas rarefaction, *Eur. J. Mech. B/Fluids*, 27, 335-345, 2008.
- [26] J. Gumbel, Rarefied gas flows through meshes and implications for atmospheric measurements, *Ann. Geophys.*, 19, 563-569, 2001.
- [27] F. Hamad, K. C. Khulbe, and T. Matsuura, Comparison of gas separation performance and morphology of homogeneous and composite PPO membranes, *J. Membr. Sci.*, 256, 29, 2005.

- [28] B.B Hamel, Kinetic model for binary gas mixtures, *Phys. Fluids*, 8, 418-425, 1965.
- [29] R.W. Hanks, H.L. Weissberg, Slow viscous flow of rarefied gases through short tubes, *J. Appl. Phys.*, 35, 142-144, 1964.
- [30] C.M. Ho, Y.C. Tai, Micro-electro-mechanical systems (MEMS) and fluid flows, *Annu. Rev. Fluid Mech.*, 30, 579-612, 1998.
- [31] M.S. Ivanov, S.V. Rogazinskii, Statistical simulation of rarefied-gas flows on the basis of Majorant frequency principle, *Dokl Akad Nauk SSSR*, 312, 315-320, 1990.
- [32] D. Kalempa, F. Sharipov, Flows of rarefied gaseous mixtures with a low mole fraction. Separation phenomenon, *Eur. J. Mech. B/Fluids*, 30, 466-473, 2011.
- [33] S.G. Kandlikar, S. Garimella, D. Li, S. Colin, M.R. King, *Heat transfer and fluid flow in minichannels and microchannels*, Elsevier, 2006.
- [34] G.E. Karniadakis, A. Beskok, *Microflows: Fundamentals and simulation*, Springer, 2001.
- [35] J. Kestin, K. Knierim, E.A. Mason, B. Najafi, S.T. Ro, M. Waldman, Equilibrium and transport properties of the noble gases and their mixture at low densities, *J. Phys. Chem. Ref. Data*, 13, 229-303, 1984.
- [36] S. Kosuge, Model Boltzmann equation for gas mixtures: Construction and numerical comparison, *Eur. J. Mech. B/Fluids*, 28, 170-184, 2009.
- [37] K. Koura, H. Matsumoto, Variable soft sphere molecular-model for inverse-power-law of Lennard-Jones potential, *Phys. Fluids*, 3, 2459-2465, 1991.

- [38] J. Lihnaropoulos, S. Naris, D. Valougeorgis, Formulation and stability analysis of rapidly convergent iteration schemes for the 2-D linearized BGK equation, *Transp. Theory Statist. Phys.*, 36, 513-528, 2007.
- [39] T.C. Lilly, S.F. Gimelshein, A.D. Ketsdever, G.N. Markelov, Measurements and computations of mass flow and momentum flux through short tubes in rarefied gases, *Phys. Fluids*, 18, 093601/1-11, 2006.
- [40] D.A. Lockerby, J.M. Reese, On the modeling of isothermal gas flows at the micro scale, *J. Fluid Mech.*, 604, 235-261, 2008.
- [41] D.A. Lockerby, J.M. Reese, D.R. Emerson, R.W. Barber, The velocity boundary condition at solid walls in rarefied gas calculations, *Phys. Rev. E*, 70, 017303/1-4, 2004.
- [42] D.A. Lockerby, J.M. Reese, M.A. Gallis, The usefulness of higher-order constitutive relations for describing the Knudsen layer, *Phys. Fluids*, 17, 100609/1-6, 2005.
- [43] L.S. Luo, S.S. Girimaji, Lattice Boltzmann model for binary mixtures, *Phys. Rev. E*, 66, 035301, 2002.
- [44] J. Maurer, P. Tabeling, P. Joseph, H. Willaime, Second-order slip laws in microchannels for helium and nitrogen, *Phys. Fluids*, 15, 2613-2621, 2003.
- [45] F.J. McCormack, Construction of linearized kinetic models for gaseous mixtures and molecular gases, *Phys. Fluids*, 16, 2095-2105, 1973.
- [46] L. Mieussens, Discrete-velocity models and numerical schemes for the Boltzmann-BGK equation in plane and axisymmetric geometries, *J. Comput. Phys.*, 162, 429-466, 2000.

- [47] N.K. Mitra, M. Fiebig, W. Swann, Quasi-one-dimensional nozzle flows of disparate mixtures, *Phys. Fluids*, 27, 2424-2428, 1984.
- [48] G.L. Morini, M. Lorenzini, M. Spiga, A criterion for experimental validation of slip-flow models for incompressible rarefied gases through microchannels, *Microfluid. Nanofluid.*, 1, 190-196, 2005.
- [49] G. L. Morini, M. Spiga, P. Tartarini, The rarefaction effect on the friction factor of gas flow in microchannels, *Superlattices Microstruct.*, 35, 587-599, 2004.
- [50] T.F. Morse, Kinetic model equations for a gas mixture, *Phys. Fluids*, 7, 2012-2013, 1964.
- [51] K. Nanbu, Velocity slip and temperature difference of gas mixtures in quasi-one-dimensional nozzle flows, *Phys. Fluids*, 22, 998-999, 1978.
- [52] S. Naris, D. Valougeorgis, Rarefied gas flow in a triangular duct based on a boundary fitted lattice, *Eur. J. Mech. B/Fluids*, 27, 810-822, 2008.
- [53] S. Naris, D. Valougeorgis, D. Kalempa, F. Sharipov, Gaseous mixture flow between two parallel plates in the whole range of the gas rarefaction, *Physica A*, 336, 294-318, 2004.
- [54] S. Naris, D. Valougeorgis, D. Kalempa, F. Sharipov, Flows of gaseous mixtures through rectangular microchannel driven by pressure, temperature and concentration gradients, *Phys. Fluids*, 17, 100607, 2005.
- [55] S. Naris, D. Valougeorgis, F. Sharipov, D. Kalempa, Discrete velocity modelling of gaseous mixture flows in MEMS, *Superlattices Microstruct.*, 35, 629-643, 2004.

- [56] C.L. Pekeris, Z. Alterman, Solution of the Boltzmann-Hilbert integral equation. II. The coefficients of viscosity and heat conduction, *Proc. Natl Acad. Sci.*, 43, 998–1007, 1957.
- [57] J. Pitakarnnop, *Analyse expérimentale et simulation numérique d'écoulements raréfiés de gaz simples et de mélanges gazeux dans les microcanaux*, Ph.D. thesis, University of Toulouse, 2009.
- [58] J. Pitakarnnop, S. Varoutis, D. Valougeorgis, S. Geoffroy, L. Baldas, S. Colin, A novel experimental setup for gas microflows, *Microfluid. Nanofluid.*, 8, 57-72, 2010.
- [59] B.T. Porodnov, P.E. Suetin, S.F. Borisov, V.D. Akinshin, Experimental investigation of rarefied gas flow in different channels, *J. Fluid Mech.*, 64, 417-437, 1974.
- [60] P. Raghuraman, P. Davidovits, Velocity slip of gas mixtures in free jet expansions, *Phys. Fluids*, 21, 1485-1489, 1978.
- [61] E.M. Shakov, Generalization of the Krook kinetic equation, *Fluid Dyn.*, 3, 95-96, 1968.
- [62] F. Sharipov, Onsager-Casimir reciprocity relations for open gaseous systems at arbitrary rarefaction III. Theory and its application for gaseous mixtures, *Physica A*, 209, 457-476, 1994.
- [63] F. Sharipov, Rarefied gas flow through a long rectangular channel, *J. Vac. Sci. Technol. A*, 17, 3062-3066, 1999.
- [64] F. Sharipov, Numerical simulation of rarefied gas flow through a thin orifice, *J. Fluid Mech.*, 518, 35-60, 2004.
- [65] F. Sharipov, Data on the velocity slip and temperature jump on a gas-solid interface. *J. Phys. Chem. Ref. Data*, 40, 023101-28, 2011.

- [66] F. Sharipov, L.M.G. Cumin, D. Kalempa, Plane Couette flow of binary gaseous mixture in the whole range of the Knudsen number, *Eur. J. Mech. B/Fluids*, 23, 899-906, 2004.
- [67] F. Sharipov, L.M.G. Cumin, D.Kalempa, Heat flux through a binary gaseous mixture over the whole range of the Knudsen number, *Physica A*, 378, 183-193, 2007.
- [68] F. Sharipov and D. Kalempa, Gaseous mixture flow through a long tube at arbitrary Knudsen numbers, *J. Vac. Sci. Technol. A*, 20, 814-822, 2002.
- [69] F. Sharipov, D. Kalempa, Velocity slip and temperature coefficients for gaseous mixtures. I. Viscous slip coefficient, *Phys. Fluids*, 15, 1800-1806, 2003.
- [70] F. Sharipov, D. Kalempa, Velocity slip and temperature coefficients for gaseous mixtures. II. Thermal slip coefficient, *Phys. Fluids*, 16, 759-764, 2004.
- [71] F. Sharipov, D. Kalempa, Velocity slip and temperature coefficients for gaseous mixtures. III. Diffusion slip coefficient, *Phys. Fluids*, 16, 3779-3785, 2004.
- [72] F. Sharipov, D. Kalempa, Separation phenomena for gaseous mixture flowing through a long tube into vacuum, *Phys. Fluids*, 17, 127102/1-8, 2005.
- [73] F. Sharipov, D. Kozak, Rarefied gas flow through a thin slit into vacuum simulated by the Monte Carlo method over the whole range of the Knudsen number, *J. Vac. Sci. Technol. A*, 27, 479-484, 2009.
- [74] F. Sharipov, D. Kozak, Rarefied gas flow through a thin slit at an arbitrary pressure ratio, *Eur. J. Mech. B/Fluids*, 30, 543-549, 2011.

- [75] F. Sharipov, V. Seleznev, Data on internal rarefied gas flows, *J. Phys. Chem. Ref. Data*, 27, 657-706, 1998.
- [76] H. Shinagawa, H. Setyawan, T. Asai, An experimental and theoretical investigation of rarefied gas flow through circular tube of finite length, Y. Yuuichi, K. Okuyama, K., *Chem. Eng. Sci.*, 57, 4027-4036, 2002.
- [77] C.E. Siewert, D. Valougeorgis, The McCormack model: channel flow of a binary gas mixture driven by temperature, pressure and density gradients , *Eur. J. Mech. B/Fluids*, 23, 645-664, 2004.
- [78] C.E. Siewert, D. Valougeorgis, Concise and accurate solutions to half-space binary-gas flow problems defined by the McCormack model and specular diffuse reflection, *Eur. J. Mech. B/Fluids*, 23, 709-726, 2004.
- [79] L. Sirovich, Kinetic modeling of gas mixtures, *Phys. Fluids*, 5, 908-918, 1962.
- [80] A.K. Sreekanth, Transition flow through short circular tubes, *Phys. Fluids*, 8, 1951-1956, 1965.
- [81] L. Szalmas, Slip-flow boundary condition for straight walls in the lattice Boltzmann model, *Phys. Rev. E*, 73, 066710/1-5, 2006.
- [82] L. Szalmas, Multi-relaxation time lattice Boltzmann method for the finite Knudsen number region, *Physica A*, 379, 401-408, 2007.
- [83] L. Szalmas, Variable slip coefficient in binary lattice Boltzmann models, *C. Eur. J. Phys.*, 6, 786-791, 2008.
- [84] L. Szalmas, Lattice Boltzmann model as an innovative method for microfluidics, in *Micro-electromechanical Systems (MEMS): Technology, Fabrication Processes and Applications*, Nova Science Publishers, 2011.

- [85] L. Szalmas, DSMC simulation of binary rarefied gas flows between parallel plates and comparison to other methods, RGD27, AIP Conf. Proc., 1333, 348-353, 2011.
- [86] L. Szalmas, S. Colin, D. Valougeorgis, Flow rate measurement of rarefied binary gases in long rectangular microchannels, Proceedings of the 3rd Micro and Nanoflow Conference, 5, 1-9, 2011.
- [87] L. Szalmas, J. Pitakarnnop, S. Geoffroy, S. Colin, D. Valougeorgis, Comparative study between computational and experimental results for binary gas flows through long microchannels, *Microfluid. Nanofluid.*, 9, 1103-1114, 2010.
- [88] L. Szalmas, J. Pitakarnnop, S. Geoffroy, S. Colin, D. Valougeorgis, Computational and experimental investigation of binary gas flows through rectangular microchannels, Proceedings of the 2nd GASMEMS Workshop, DY01, 1-8, 2010
- [89] L. Szalmas, D. Valougeorgis, Investigation of pressure driven rarefied binary gas flow through a triangular channel, Proceedings of the 1st GASMEMS Workshop, 1, 1-7, 2009.
- [90] L. Szalmas, D. Valougeorgis, Rarefied gas flow of binary mixtures through long channels with triangular and trapezoidal cross sections, *Microfluid. Nanofluid.*, 9, 471-487, 2010.
- [91] L. Szalmas, D. Valougeorgis, A fast iterative model for discrete velocity calculations on triangular grids, *J. Comp. Phys.*, 229, 4315-4326, 2011.
- [92] L. Szalmas, D. Valougeorgis, DSMC simulation of pressure driven binary gas flow through a short microtube, Proceedings of the 2nd European Conference on Microfluidics, 17, 1-10, 2010.

- [93] L. Szalmas, D. Valougeorgis, S. Colin, Flow rate measurement of binary gases through long rectangular microchannels, Proceedings of the 3rd GASMEMS Workshop, 2, 1-8, 2011.
- [94] L. Szalmas, D. Valougeorgis, S. Colin, DSMC simulation of pressure driven binary gas flow through short microtubes, Proceedings of the 9th ASME International Conference on Nanochannels, Microchannels and Minichannels, 58022, 1-10, 2011.
- [95] F. Tcheremissine, Direct numerical solution of the Boltzmann equation, RGD24, AIP Conf. Proc., 762, 677-685, 2005.
- [96] M. Usami, K. Okuyama, Molecular simulation of rarefied supersonic free jets by DSMC method, J. B-Fluids and Thermal Eng., 42, 369-376, 1999.
- [97] D. Valougeorgis, Couette-flow of a binary gas-mixture, Phys. Fluids, 31, 521-524, 1988.
- [98] D. Valougeorgis, S. Naris, Acceleration schemes of the discrete velocity method: gaseous flows in rectangular microchannels, SIAM J. Sci. Comput., 25, 534-552, 2003.
- [99] S. Varoutis, S. Naris, V. Hauer, C. Day, D. Valougeorgis, Experimental and computational investigation of gas flows through long channels of various cross sections in the whole range of the Knudsen number, J. Vac. Sci. Technol. A, 27, 89-100, 2009.
- [100] S. Varoutis, D. Valougeorgis, O. Sazhin, F. Sharipov, Rarefied gas flow through short tubes into vacuum, J. Vac. Sci. Technol. A, 26, 228-238, 2008.

- [101] S. Varoutis, D. Valougeorgis, F. Sharipov, Gas flow through tubes of finite length over the whole range of the rarefaction for various pressure drop ratios, *J. Vac. Sci. Technol. A*, 27, 1377-1391, 2009.
- [102] W. Wagner, A convergence proof for Bird's direct simulation Monte Carlo method for the Boltzmann equation, *J. Stat. Phys.*, 66, 1011-1044, 1992.
- [103] E.L. Walker, B.S. Tanenbaum, Investigation of kinetic models of gas mixtures, *Phys. Fluids*, 11, 1951-1954, 1968.
- [104] V.M. Zhdanov, Flow and diffusion of gases in capillaries and porous media, *Adv. Colloid Interface Sci.*, 66, 1-21, 1996.
- [105] Y. Zohar, S.Y.K. Lee, W.Y. Lee, L. Jiang, P. Tong, Subsonic gas flow in a straight and uniform microchannel, *J. Fluid Mech.*, 472, 125-151, 2002.

**Titre : Les écoulements des mélanges gazeux dans les microcanaux**

**Résumé :** La sujet de la thèse est l'étude numérique et expérimentale des écoulements des mélanges gazeux dans les microcanaux. Dans la partie calculatoire de la thèse, les écoulements dans les canaux longs et courts sont considérés. La description de l'écoulement dans les microcanaux longs est effectuée en utilisant le modèle cinétique de McCormack. Une méthode accélérée de vitesse discrète est développée pour résoudre le modèle de McCormack pour les microcanaux avec des sections transversales triangulaires et trapézoïdales. En utilisant la méthode, les écoulements de mélange gazeux,  $Ne/Ar$ ,  $He/Xe$ ,  $He/Ar$  et  $He/Kr$ , sont simulés pour différents paramètres de l'écoulement. Les débits des différentes configurations sont calculés. Les écoulements de mélanges gazeux dans les microcanaux courts sont simulés en utilisant la simulation directe Monte Carlo. Des codes avancés sont développés pour simuler l'écoulement de mélanges gazeux,  $Ne/Ar$  et  $He/Xe$ , dans les microcanaux courts. Les débits des espèces gazeuses et du mélange et la distribution axiale de densité, de vitesse et de température sont déduits des simulations. La partie expérimentale est axée sur la mesure des débits de mélange gazeux,  $He/Ar$  et  $He/Kr$ , dans les microcanaux rectangulaires et trapézoïdaux longs en utilisant la méthode de volume constant. Les débits sont comparés à des calculs cinétiques. Un très bon accord entre les débits théoriques et expérimentaux est obtenu. Le bon accord démontre l'utilité du modèle de McCormack pour décrire l'écoulement isotherme dans les microcanaux. Il est démontré que le mélange se sépare dans le canal.

**Mots-Clés :** micro-écoulements gazeux, mélanges gazeux, modèle cinétique de McCormack, simulation directe Monte Carlo, mesure du débit, méthode de volume constant, régime de transition